HIGH FREQUENCY MODELING OF POWER TRANSFORMERS

STRESSES AND DIAGNOSTICS

by

Eilert Bjerkan

Doctoral Thesis
for the degree of Doctor Ingeniør

Trondheim, May 2005

Faculty of Information Technology,
Matematics and Electrical Engineering

NTNU
Norwegian University of
Science and Technology

Department for Electrical Power Engineering
O.S.Bragstads pl. 2F
7491 Trondheim
ISBN: 82-471-6925-8 (printed version)
ISBN: 82-471-6923-1 (electronic version)
Trondheim 2005

PREFACE

This work has been a part of the project “Transformer winding ageing, condition control and condition assessment” at SINTEF Energy Research (SEfAS). The project is financed by SEfAS together with Norwegian utilities and the Norwegian Research Council. This work was accomplished at the Norwegian University of Science and Technology, Department of Electrical Power Engineering in the period 2000-2005.

I would like to express my gratitude to my supervisor Associate Professor Hans Kristian Høidalen for being supportive, and giving me guidance and inspiration during my work. I would also like to thank all my colleagues at the Department of Electrical Power Engineering and the Materials Science group at SEfAS for all the help and assistance when needed. Gratitude is also expressed to Professor Jarle Sletbak for proofreading most of the thesis.

I would also like to thank ABB for supporting my work, especially Svein Ola Løvlien at ABB, Drammen for helping out with constructional details on the test-object in this thesis and for increasing my constructional knowledge on a general basis. I would also like to express my thankfulness to Egil Henriksen at ABB, Drammen for valuable discussions and guidance regarding the importance of the core in transformer models.

I am also grateful for the T3 Buran transformer (main testobject) supplied by TEV (Trondheim Energiverk), since they were upgrading the network and scrapping this unit.

Thanks are also rewarded to Eilin Guillot, Olivier Moreau and Guy Dos-Santos at the R&D dept. of EdF in Clamart/Paris for arranging the 5 months stay in 2003 and for giving me training and guidance in transformer modeling using SUMER.

Support and encouragement from Nortroll AS in Levanger is also deeply appreciated.

Finally I would like express my gratitude to my love, dear friend and wife to be; Vigdis Aakerholm and also my two daughters Emma, born in 1999 and Åse Johanne, born in 2002. Vigdis have been patient and understanding during my work and has always been supportive and encouraging. Emma and Åse Johanne has given me strength during difficult periods being a source of constant inspiration and motivation. I am also grateful to the rest of my family and friends for being supportive and interested in my work during these years.

Trondheim, May 2005

Eilert Bjerkan

“Inductance is best measured with a measuring-tape”
O.Heaviside

ABSTRACT

In this thesis a reliable, versatile and rigorous method for high frequency power transformer modeling is searched and established. The purpose is to apply this model to sensitivity analysis of FRA (Frequency Response Analysis) which is a quite new diagnostic method for assessing the mechanical integrity of power transformer windings on-site. The method should be versatile in terms of being able to estimate internal and external overvoltages and resonances. Another important aspect is that the method chosen is suitable for real transformer geometries. In order to verify the suitability of the model for real transformers, a specific test-object is used. This is a 20MVA transformer, and details are given in chapter 1.4.

The high frequency power transformer model is established from geometrical and constructional information from the manufacturer, together with available material characteristics. All circuit parameters in the lumped circuit representation is calculated based on these data. No empirical modifications need to be performed. Comparison shows capability of reasonable accuracy in the range from 10 kHz to 1 MHz utilizing a disc-to-disc representation. A compromise between accuracy of model due to discretisation and complexity of the model in a turn-to-turn representation is inevitable.

The importance of the iron core is emphasized through a comparison of representations with/without the core included. Frequency-dependent phenomena are accurately represented using an isotropic equivalent for windings and core, even with a coarse mesh for the FEM-model. This is achieved through a frequency-dependent complex permeability representation of the materials. This permeability is deduced from an analytical solution of the frequency-dependent magnetic field inside the conductors and the core.

The importance of dielectric losses in a transformer model is also assessed. Since published data on the high frequency properties of pressboard are limited, some initial measurements are done on impregnated pressboard at different temperatures and moisture-levels. $Tan\delta$ is found to be twice the corresponding value for impregnated paper at frequencies from 50 kHz to 1MHz. Moisture has a minor effect on the losses when frequency approaches 1MHz. Service-aged paper (impregnated) is also tested in order to investigate other ageing-effects than produced water, but the test show the same decreasing influence at higher frequencies as impregnated pressboard with moisture added. The following main conclusions were drawn from this work:

- A simple, analytical approach cannot be used to build a versatile high frequency power transformer model. The reason being mainly the lack of a proper representation of the iron core, since a FEM-representation without the core did not increase coherence to measurements significantly.

- A proper representation of the iron core is very important for the calculation of inductances. Losses mainly originate from the core at intermediate frequencies (10-200 kHz), and not only from eddy currents in the windings as traditionally assumed. The permeability seem to be of less importance as long as it is well above permeability for oil, since the internal resonances mainly depends on the leakage inductances. The core leg equivalent is important for the leakage field and determines the leakage inductances and winding losses.

- Using a frequency-dependent complex permeability in a FEM-simulation makes possible an accurate representation of core and windings using a coarse mesh. If coating resistivity is sufficiently low to create interlaminar currents/ losses, the iron laminates should be represented by a 2-dimensional complex permeability. Coating parameters are seldom available.

- Dielectric properties of power transformer insulating materials depend on frequency, temperature, moisture, ageing and pressure. Temperature has minor influence on FRA-signatures, other parameters have practically no influence.

- Impulse- and resonant overvoltages both internally and on terminals can be analysed using this method with sufficient accuracy, provided the discretisation of the winding is sufficiently refined regarding the frequencies involved. Since terminal behaviour is given by the internal geometry and material parameters, it is assumed that internal behaviour is related to the accuracy of the terminal behaviour.

- FRA sensitivity to axial displacement is 1.2% of total axial height. The sensitivity to radial deformation (forced buckling) is found to be a buckling depth of 9% of the radius of the winding. Turn-to-turn short-circuits could not be modeled correctly since the lumped elements includes several turns. Disc-to-disc short circuits are easily detected. Axial bending is not detectable. Detection of loose windings and aged insulation is improbable and will be dependent on the available sensitivity (mainly related to the repeatability of the measurements and the reference utilized for comparison).

The contributions in this work relates to different topics such as; Frequency-dependent iron core representation in FEM, study of interlaminar currents and its effect on the internal magnetic field, characterization of high frequency dielectric properties of impregnated pressboard and service-aged impregnated paper, procedure for evaluation of internal/external overvoltages, and finally sensitivity guidelines for the application of FRA to mechanical deformations.

Keywords: Power Transformer, High frequency model, Condition assessment, FEM, Lumped parameter model, FRA, Internal stresses, Overvoltages, Terminal stresses, Mechanical deformations, Frequency-dependent losses, Eddy currents.

TABLE OF CONTENTS

LIST OF SYMBOLS AND UNITS

ε^*	Complex permittivity
ε'	Real part of relative permittivity
ε''	Imaginary part of relative permittivity
ε_0	Permittivity of free space: $8,85 \times 10^{-9} F/m$
ε_r	Relative permittivity
$\tan\delta$	Dielectric loss factor
σ	Conductivity $[S/m]$
μ^*	Complex permeability
μ'	Real part of the relative permeability
μ''	Imaginary part of the relative permeability
μ_0	Permeability of free space: $4\pi \times 10^{-7} H/m$
μ_r	Relative permeability
Ω	Ohm
j	$\sqrt{-1}$, imaginary unity
ω	Angular frequency [rad/s]
s	Laplace-operator: $s = j\omega$
A	Magnetic vector potential
B	Magnetic flux density [T]
H	Magnetic field strength [A/m]
$\mathbf{R}(\omega)$	Frequency-dependent branch Resistance matrix
$\mathbf{L}(\omega)$	Frequency-dependent branch Inductance matrix
$\mathbf{G}(\omega)$	Frequency-dependent Conductance matrix
$\mathbf{C}(\omega)$	Frequency-dependent Capacitance matrix
$\mathbf{Z}$	Branch impedance matrix
$\mathbf{Y_B}$	Nodal admittance matrix description of the branch matrix
$\mathbf{Y_N}$	Admittance description of nodal elements
$\mathbf{Y_{sys}}(s)$	Nodal system description in Laplace-domain
$\tilde{\mathbf{Y}}$	Condensed/reduced system description
$\mathbf{V_e}$	Matrix of terminal voltages

$\mathbf{I_e}$	Matrix of terminal currents
$\mathbf{Y_{ee}}$	Matrix containing the part of system description that contains only the terminal nodes
$\mathbf{Y_{ei}}$	Lower left part of system description containing admittances between terminal nodes and internal nodes.
$\mathbf{Y_{ie}}$	Upper left part of system description containing admittances between terminal nodes and internal nodes.
$\mathbf{Y_{ii}}$	Matrix containing the part of system description that contains only the internal nodes
$\mathbf{A}$	Transformation matrix for branch to nodal transformation
$r(\alpha)$	Radius of buckled winding
r_0	Nominal radius of winding
b	Depth of deformation
c	Span of deformation
α	Angle
M_{12}	Mutual inductance between winding 1 & 2
R_{12}	Distance between filament 1 & 2
$\vec{A}$	Vector potential
$\nabla \cdot A$	Divergence of A
$\nabla \times A$	Curl of A
φ_j^*	Complex flux flowing through element j
S_j	Cross-sectional area of element j
$d\vec{S}$	Differential area
n_j	Number of turns in element j
Φ_j^*	Total complex flux through element j ($\Phi_j^* = n_j \cdot \varphi_j^*$)
I_j	Total current in element j
W_{mag}	Magnetic energy
Q	Charge
$\vec{D}$	Charge density
W_{el}	Electrostatic energy
V_j	Voltage on electrode j
$c_{i,j}$	Capacitance between electrode i and j

$H_z(x)$	Magnetic field-strength in z-direction with variation along x
$J_y(x)$	Current-density in y-direction with variation along x
$\vec{E}$	Electric field strength
H_0	Nominal magnetic field strength
$\overline{H}$	Conjugated field strength
$\|H\|$	Absolute value of field strength
γ	Stacking factor of core (usually around 0.95)
$\gamma_{Cooling}$	Amount of cooling ducts in the net iron area of the core.

ABBREVIATIONS

DGA	Dissolved Gas Analysis
DP	Degree of Polymerisation
FEM	Finite Element Method
FFT	Fast Fourier Transform
FRA	Frequency Response Analysis
FRSL	Frequency Response Stray Losses
HV	High Voltage
LV	Low Voltage
LVI	Low Voltage Impulse
OLTC	On-Line Tap-Changer
PD	Partial Discharges
SFRA	Swept Frequency Response Analysis

LIST OF FIGURES

LIST OF TABLES

1 INTRODUCTION

During the last decades there has been a great change in the general terms and conditions for power system utilities. Opening up for free competition has led to major restrictions regarding the development of one of the major infrastructures called electricity: Efficiency improvements, cutting costs and reducing investments. All this to comply with the competition.

In the same time, the demand for a reliable supply of energy has increased considerably requiring nearly a no-fault operation of power systems. Reliability may be increased by replacement of equipment based on age composition. Due to high initial cost and long lifetimes, components such as power transformers have condition-based replacements. The replacement-rate is lower than the total ageing-rate.

The age distribution of the Norwegian transformer population is entering a critical era. In a few years, 40% of the population will be older than 30 years. Most power transformers is operated well below nominal capacity and can, if maintained properly, stay in service for as much as 60-70 years (in some cases more). In practice the only reason for scrapping these units are due to upgrading of the network (for instance the voltage), or devaluating reliability due to age.

But some transformers subjected to overload conditions and/or accelerated ageing, might be near end-of-life at an earlier stage. The fault-rate is expected to increase in networks holding old units. Since todays methods for condition assessment cannot detect all fault-types, the need for more sophisticated methods of condition assessment is advancing, in order to keep the fault-rate as low as possible.

The FRA-method (Frequency Response Analysis) is one of the methods that seems promising because it appear to be sensitive in detecting mechanical deformations in transformer windings. This is a type of fault that can occur due to close-up secondary faults. Aged transformers have reduced short-circuit strength and are more likely to experience mechanical deformations. There are several outcomes from such faults: Severe deformations lead to an electrical fault which normally trip protection relays (otherwise easily detected). Less severe

deformations involve insulation rupture and partial discharges which after some time normally is discovered through oil analysis and/or tripping the bucholtz-relay. Minor deformations which show no significant change in the operational characteristics, where mechanical properties of the copper might be changed seriously risking rupture on next event. The impulse strength might also be reduced significantly due to damaged insulation and reduced distances.

FRA have showed to be promising in both real cases and laboratory investigations. There still seems to be little knowledge on why and how the method works, and how the results can be interpreted. Before making this method a standard test for condition assessment, all interpretational aspects should be investigated. This can either be done by experiments or calculations (using transformer models), or presumably a combination.

Transformer modeling has traditionally occupied alot of attention during the years due to its importance in power systems and also due to the complexity of the component. There is still disagreement in literature on which assumptions that should be allowed or not in order to make a good model.

Modeling from constructional data seems to be the best method, but the data is normally not available. Other than analysing the FRA-method, such models have a variety of applications.

1.1 Scope of Work

The work in this thesis is split in two areas, where the general topic is high frequency modeling of power transformers. The sub topic is condition assessment, where a specific method (FRA) is investigated using high frequency modeling as a tool to gain better understanding of aspects regarding interpretation.

In the modeling part, different methods of modeling are reviewed in respect of their advantages and disadvantages, their application and limitations. Later, a method appropriate for investigating FRA is chosen. The method would desirably also be well suited for investigating internal stresses and transformer-network interaction in transient calculations.

The main goal in this work is to develop high frequency models of power transformer windings. These models should be used to:

- Evaluate possible influence from core
- Study potential influence of frequency dependent material characteristics.
- Study 2D simplifications versus 3D phenomena.

Another subtarget is to employ the models developed to investigate the FRA-method in order to:

- Study influence of different mechanical deformations.
- Study sensitivity to different fault-types.
- Study other phenomena that might change the FRA-signature, such as connections, leads, tapchanger, ageing-effects etc.
- Study which fault-types changes which part of the signature.

The outcome of the above analysis will be used to increase the physical understanding of the FRA-method, in order to be able to interpret results.

The following hypotheses are investigated in this work:

1. *Deviations observed in FRA measurements can be related to actual winding deformations by means of a detailed high frequency model of the transformer.*

2. *Analytical methods are sufficient for simple/homogenous transformer geometries. A real transformer geometry complicates the analytical approach. Finite element methods would be an alternative for complex designs since details and variations may easily be included.*

3. *Iron core can be neglected and considered to behave like a perfect conducting screen above 10 kHz.*

4. *High frequency characteristics of insulating materials are independent of frequency, temperature, moisture, ageing etc. Ageing should therefore not change the FRA-signature.*

5. *High frequency transformer models can be established with high degree of conformity to terminal measurements, provided constructional information is available.*

In order to test the above hypotheses for real transformer geometries, a specific test-case is used during the work. This enable comparison to terminal measurements and the possibility of refining the model developed.

The first step is to find a method for modeling which suites all primary targets well. The next step is to develop a model that comply well with measurements and then it can be applied to the purpose of the subtarget (FRA).

1.2 Thesis Outline

The thesis has two principal parts: background information and contributions. Chapters 1-4 contains background material, state of the art knowledge and all necessary information for the decisions made in this work. Chapters 5-7 contains the contributions and results of this work.

The subdivision of this thesis reflects the progress of the work when it comes to the choice of methods. The work of Rahimpour [1]-[5] was considered "state of the art" regarding sensitivity analysis of FRA using transformer modeling. This have had influence on the initial choices due to the high resemblence between model-results and measurements reported in his work. Some of his initial assumptions have failed, but led to improvements of the methods used in this work.

In addition to the outline of the work in this chapter, the other chapters include:

Chapter 2 presents background material for condition assessment and transformer modeling.

Chapter 3 describes theory regarding analytical modeling, together with results from the analytical model developed. It also outlines analytical approaches to investigate the effect of buckling on inductance and capacitance.

Chapter 4 shows how a FEM-software calculates the elementary quantities used in a transformer model, and then presents a model established using SUMER, a FEM-based software for high frequency modeling of power transformers.

Chapter 5 describes theory covering frequency-dependent iron core characteristics and how to implement it into any FEM-based software. It gives relevant and simplified examples on how to apply the theory to elements inside a transformer model. A second phenomena that increase the displacement of the magnetic field, is introduced. This is related to interlaminar currents (in the gap between laminations). This is only presented as a future option to further improve the core representation.

Chapter 6 reviews theory and measurements on frequency-dependent dielectric characteristics and how the characteristics are applied in transformer modeling.

Chapter 7 shows the results of the complete model were all effects are included. Included applications are FRA, ageing studies, and transient analysis such as: transformer-network interaction, transferred overvoltages and studies of internal stresses are included.

Chapter 8 discusses the results and optional solutions.

Chapter 9 contains the main conclusions from this work regarding the hypothesis' defined in chapter 1.

Chapter 10 suggests topics for further research.

1.3 Publications

The main results from this work have been, or are to be published in the following journals and conference proceedings:

1. **Bjerkan, E., Høidalen, H.K., "Detailed High Frequency Power Transformer Modeling in ATP using FEM and Matlab", presented at the European EMTP-ATP Conference, 2004, 3-5 October, Trondheim, Norway**

2. **Bjerkan, E., Høidalen, H.K., "High Frequency FEM-based Power Transformer Modeling: Investigation on Internal Stresses due to Network-Initiated Overvoltages", to be presented at the 6th Int. Conf. on Power System Transients, June 19-23, 2005, Montréal, Canada**

3. **Bjerkan, E., Høidalen, H.K., Moreau, O., "Importance of a Proper Iron Core Representation in High Frequency Power Transformer Models", to be presented at: the 14th International Symposium in High Voltage Engineering (ISH2005), August 25-29, 2005, Beijing, China**

4. **Bjerkan, E., Høidalen, H.K., Moreau, O., "FRA Sensitivity Analysis using High Frequency Modeling of Power Transformers based on the Finite Element Method", to be presented at: the 14th International Symposium in High Voltage Engineering (ISH2005), August 25-29, 2005, Beijing, China**

5. **Bjerkan, E., Høidalen, H.K., "Accurate Representation of Laminated Iron Cores at High Frequencies Including Interlaminar Effects", To be published in: IEEE Transactions on Power Delivery.**

6. **Bjerkan, E., Hestad, Ø., Høidalen, H.K., "High Frequency Characterization of Impregnated Pressboard and its applicability to High Frequency Power Transformer Modeling and FRA", to be presented at: the 19th Nordic Symposium on Electrical Insulation (NORD-IS 2005), June 13-15, 2005, Trondheim, Norway.**

1.4 Test object

The test object used in this thesis is a quite typical transformer for the Norwegian distribution network. It is manufactured in 1969 at one of the previous Norwegian transformer factories. The transformer is a 20MVA 66/6,6 kV YNyn0 transformer with a 24-strand, 69 turns, double-start LV helical winding, a double-stranded continuously wound HV disc-winding with 564 turns, and an interleaved single layer regulating winding counting 110 turns. The magnetic circuit is a three legged stacked core. The test object is referenced by the cell-number and name of the substation: T3 Buran.

T3 Buran was scrapped during autumn 2001 due to its age and a planned voltage upgrade in the network. Terminal measurements in all combinations (admittances and voltage ratios) were taken before disassembling the unit. The windings were then removed from the core to be used in possible investigations later.

The idea was to apply controlled deformations, for comparison to computer models of the same winding. The effect of axial displacements without the core present, was studied by means of experiments. However, since the importance of the core is addressed later in this work, the experiments on these windings have afterwards been considered to be of less importance than first assumed.

The effect of radial displacements were not evaluated experimentally, since this is thoroughly studied by others.

As seen in fig. 1.1, the total height of the winding assembly is approximately 1.6 m. The core is a traditional 3-legged stacked core. Dimensions and other information on the test object is given in appendix A.

Figure 1.1: Disassembling the test object

All constructional details and drawings are supplied by ABB Transformers in Drammen, Norway. Together with the windings, this makes a good foundation for developing accurate models.

Four other winding geometries are also utilized in this work for minor comparison (details are given when used).

2 BACKGROUND

Introductions and historical aspects are given both for condition monitoring and transformer modeling. Methods are reviewed, purpose and applications are assessed. Conclusions from this chapter represent the foundation for the choice of method(s) used in the further work.

Power transformers are the largest, heaviest, and often the most expensive single piece of equipment in a power system. Obviously appropriate care is necessary in commissioning, operation and maintenance of power transformers. It is THE key component in power networks. Since repair-time is considerable and backup-units are not always available, it is important to assess the condition of each and every unit in the network. An international survey of CIGRE [6] on large power transformers, show a failure rate of 1-2% per year. This is not much, but a single failure on a large transformer usually results in large expenses for the utility. Since many manufacturers are merging or shutting down, the repair costs will increase in future due to increasing distances of transport. This leads to a growing importance of condition monitoring on power transformers, for early warning.

FRA is a fairly new diagnostic method for assessing mechanical integrity of transformer windings. This method is based on comparing FRA signatures to base-line measurements. Deviations may be attributed to mechanical deformations. In order to establish sensitivity guidelines for different mechanical faults, high frequency transformer modeling is utilized.

The transformer behaviour above operational frequencies has been subjected to research for nearly a hundred years, since the recognition of the capacitive behaviour at impulses [7]. Many different techniques of modeling have been developed since then, depending on the application of the model. Experimental work was the basis during the first 50 years. The introduction of computers led to possibilities of solving complex problems such as internal voltages inside a transformer winding at high frequencies.

A proper method of modeling is searched in order to investigate FRA and at the same time be able to evaluate stresses internally/externally.

2.1 Condition Monitoring - Purpose and practice

Attention to condition assessment of power transformers has increased the last decade. Asset- and life management have become important since economical considerations have changed the technical policies of power utilities. The maintenance-philosophy has moved from time-based to condition-based maintenance in order to reduce maintenance-costs, and at the same time extending lifetime of components past the designed lifetime in order to postpone investments.

Many power transformers will approach their originally designed lifetime in just a few years. It is therefore important to monitor the condition of these units in order to be able to benefit and determine the remaining lifetime, and at the same time avoid catastrophic accidents and long outages.

Problems related to power transformers can be characterized into three main categories:

- Defects or deficiencies that in time will represent incipient faults.
- Problems originating from ageing processes.
- Problems induced by operating conditions exceeding transformer capabilities.

It usually takes some time before such problems develop into failures.

Lifetime management has the purpose of “achieving true useful life of the equipment” and at the same time minizing life-cycle-costs including new investments. Condition assessment contributes to the life management process by enabling knowledge-based decisions regarding refurbishment, replacement and retirement.

Lifetime management requires a lifetime model to be established. There are multiple parameters affecting such a model. These parameters will have to be investigated in order to assess the condition of the component. For a transformer, the following factors should be considered:

- The main dielectric insulation system; DGA, particle contamination, partial discharges etc.
- Winding/conductor insulation; Mechanical strength/DP, cellulose structure, decomposition/ageing products.
- OLTC (On-line Tap Changer); Condition of mechanical drive system, Corrosion/pyrolytic carbon growth, Tie-in or transition resistors, Diverter switch, Seals etc.
- Core; Local overheating due to faulty grounding-leads, circulating currents, local short-circuits (defect insulation), overrated flux-levels.
- Mechanical condition of winding; Withstand strength, deformations, clamping force and supportive structure.
- Bushings; Pollution, oil-level, pd, gaskets.
- Tank and associated components (conservator, cooling etc.).

Several different diagnostic methods have been developed in order to assess the condition of the components in a transformer.

Several studies [6],[8]-[10] have been accomplished with the aim of establishing statistics for power transformer failures and the type of elements involved in these failures. An abstract of these are given in table 2.1:

Table 2.1: Percentage fault distribution for Power Transformer failures

Defective component	Fault Distribution in % of components involved				
	CIGRE[a] Survey[6]	CEA[b] Survey[8]	Doble clients[9]	ZTZ-Service clients[9]	South Africa[10]
Bushings/ accessories	29	29	35	45	14
Tap-changer	15	39	16	9	24
Major insulation	12	16	9	17	30
Winding ageing	31		16	12	17
Winding distortion			12	10	
Core	2	10	7	7	15
Leads	11	6	5	-	-

a. Forced and scheduled outages with on-line tap-changer (figure 12 in [6])
b. Failures due to cooling- and auxiliary equipment are excluded for comparison

Several methods (both electrical and chemical, direct and indirect) are developed in order to determine the condition of different transformer parts.

As seen from table 2.1, winding and core are involved in a large portion of the failures reported here. It is assumed that some dielectric failures are initiated by mechanical movements inside the winding, and these could have been avoided by assessing the mechanical condition of the winding and core at an early stage.

The mechanical integrity of a transformer winding is challenged by several mechanisms:

- Excessive short circuit forces due to close-up secondary faults.
- Excessive mechanical acceleration during transport (accidents).
- Dynamic forces in service, for instance vibration or seismic forces.
- Ageing reduce clamping force upon insulation and supportive structure, which in turn challenges the withstand strength against the above factors.

Many dielectric failures are a direct results of reduced dielectric strength due to deformations. It is therefore favourable to detect deformations as early as possible, before they lead to problems or failures. Mechanical deformations do not necessarily change the operational characteristics of the transformer.

The most common reason for mechanical deformations is short circuit forces due to secondary faults.

Theory on short-circuit forces and common fault-modes are reviewed in Appendix B: “Short circuit forces“.

The main primary fault-modes resulting from short-circuit forces are:

- Axial displacement
    - Displacement of the complete winding
    - Telescoping
    - Stretching
    - Bending
- Radial deformation (Buckling)
    - Forced mode buckling
    - Free mode buckling

The different modes are explained more in detail in Appendix B.

Secondary faults (accompanying faults) are normally disruption of strand and turn insulation, resulting in local short-circuits. This normally leads to hot-spots and, in time, gassing where DGA normally detects and classifies the fault. Other secondary faults might be partial discharges or strand rupture.

During factory acceptance tests, IEC [11] recommends measuring the leakage inductance of the transformer. It is stated that an inter-phase deviation less than 2% is acceptable. The conclusion is that conventional methods such as ratio-measurements or impedance- and inductance measurements, do not have the required sensitivity to identify winding deformations. The desired method should be sensitive to deformations and displacements within the winding. Since opening the transformer for inspection is rather costly, the method should depend upon terminal measurements requiring a minimum of outage-time and resources.

The FRA-method seems to fulfil these requirements for some applications.

2.2 FRA (Frequency Response Analysis)

Hypothesis 1.: *Deviations observed in FRA measurements can be related to actual winding deformations by means of a detailed high frequency model of the transformer.*

As outlined in Chapter 1, one of the targets in this work is investigating FRA as a diagnostic method for power transformers. FRA is used to discover winding deformations. No other methods have the required sensitivity.

A FRA-signature is generally a transfer function output/input as a function of frequency (50 Hz - 1 MHz), usually measured at very low voltages. Typically winding admittances, voltage ratio between windings, or the attenuation is measured. Measured signatures are compared to a reference. The reference is usually other phases (symmetric comparison), an earlier measurement (time-based comparison), or similar transformers (construction-based comparison). Assuming a detailed model based on constructional information is accurate, comparison would be possible also between model and measurement. Changes/differences are attributed to geometrical changes inside the winding.

In order to study the FRA-method in particular, it is therefore assumed that a detailed internal model is the best way to study sensitivity and influence of different types of fault.

The technique of impulse testing transformers and shunt reactors dates back 60 years, by investigating measured current records for faults [12]-[14]. FRA is actually an improvement of impulse testing and the LVI-method [15]. It was first proposed by Dick and Erven [16] in 1978. FRA did not attract very much interest until 10 years later [17].

Postmortem investigations allow changes in the transfer function to be correlated to the location and nature of the fault. These events are however rather rare, and it would take a large number of tests accumulated over many years for a quantitative evaluation of the sensitivity of the method. The faults investigated have usually developed into an electrical fault, masking the mechanical faults. These are reasons for testing sensitivity of the method with computer modeling.

2.2.1 Measurement techniques

Until now, FRA is not a standardized method, and a variety of setups are used throughout the world. Besides the two ways of measuring (LVI/SFRA), different techniques regarding termination, cable layout and combinations are used. Measurements are influenced by the setup. A standard measurement-setup should therefore be established in order to make comparisons and cooperation easier. A comparison of the two measurement-methods is elucidated in the following (mainly based on Tenbohlen/Ryder [18], and Kreβ/König [19]):

2.2.1.1 LVI (Low Voltage Impulse)

The LVI-method is a adapted from the initial impulse test-method. The applied voltage from the impulse generator is measured along with secondary voltages on other terminals or currents from terminals to ground. Several measurements can be done at the same time. The time-domain measurements are then transferred into the frequency-domain by a Fast Fourier Transform (FFT) and the transfer function is established from the ratio of the two transformed signals.

LVI advantages:

- Several channels/transfer functions can be measured at the same time, reducing outage time during revision.
- Fast compared to SFRA. One measurement is usually conducted in one minute (several impulses are applied to establish an average time series.).

LVI disadvantages:

- Fixed frequency resolution resulting in a low resolution at low frequencies. This might be a problem for the detection of electrical faults. In addition signals are usually high pass-filtered in order to reduce problems with window-functions of the FFT.
- Broad band noise cannot be filtered.
- Power spectrum of injected signal is frequency-dependent. The resulting precision across the frequency-range will then be frequency-dependent.
- Slowly decaying signals are not recorded. Window-function, zero-padding or high-pass filtering is necessary.
- Several pieces of equipment needed.
- Noise and errors related to digitizers.
- Accuracy dependent on the mathematical evaluation.

2.2.1.2 SFRA (Swept Frequency Response Analysis)

This method is much slower than the LVI-method since it sweeps the desired frequency-range using a single sinusoidal excitation.

SFRA advantages:

- High signal to noise ratio. Network-analysers usually use a very-narrow-band filter to cancel broad band noise/out-of-band noise.
- A wide frequency-range can be swept.
- The resolution can be controlled by the number of frequency points used. If a finer resolution is required, the range can be split up into several frequency bands to be measured. The distribution of points can usually be either linear or logarithmic.
- One single piece of equipment is usually sufficient.

SFRA disadvantages:

- Using a standard network analyser, simultaneous determination of several transfer functions is not possible.
- Each measurement takes long time: Up to several minutes depending on the number of points and the degree of filtering.
- Low signal amplitude
- Averaging techniques are very time-consuming.

SFRA is the method applied to the measurements performed in this work.

2.2.1.3 Comparison

A measurement can be compared to a number of different references:

- Time-based comparison: A fingerprint is obtained during factory acceptance test or at an earlier revision. This supplies the best sensitivity since it cancel out almost all natural differences. It sensitivity is limited to the accuracy and repeatability of the instrumentation and measurement setup. Possible ageing- and temperature effects may be seen with this method.
- Construction-based comparison: Measurements are compared to measurements from equal transformers (same construction). This comparison incorporates a lower sensitivity since differences between different units may be important. Small adjustments to the design, and differences in lead layout etc., will influence on the measurements.
- Comparison based on symmetry: This is the usual method for comparison since baseline measurements are not usually available. Full comparison is usually limited to Yy-connected transformers, but different admittances of Dy-connected transformers can be applied with success. OLTC is the usual source of discrepancy together with differences between outer and centre phase.
- Model-based comparison: Measurements compared to a computer model of the transformer would be a possible solution if accurate models could be developed. This approach is used in this work to determine sensitivity guidelines for interpretation of FRA measurements.

2.2.1.4 Connections/setup

The setup used so far in Norway [20] is the SFRA-method using a network analyser (HP4195A) with active probes (HP41800A) and double-screened coax-cables. The network analyser has a very good signal-to-noise ratio, when used correctly. Using active probes with high input impedance, eliminates the influence of the coax-cables running from the point of measurement to the network analyser.

For impedance-measurements, a Pearson current monitor [21] is used for the current measurement. As long as the measurement leads are short compared to the wave-length, no phasing-effects will occur. Series inductance in the measurement leads become prominent at higher frequencies. Using active probes instead of low impedance termination reduces the current flowing in the measurement leads and thus the voltage-drop due to the series inductance is minimized.

The measurement setup is further elucidated in appendix C.

2.2.2 International experience

Several FRA-related projects have been accomplished at the University of Stuttgart in Germany. They have exclusively been using the LVI-method:

- Leibfried [22], [23] studied the possibilities of measuring impulse excitation using switching operations. This led to an on-line monitoring system. The frequency-spectra of such switching operations are highly variable, and only the first phase connecting can be utilized. Just a small percentage of the switching operations can be used for FRA investigations. The wide tolerance-bands established by Leibfried masks the possibility of detecting minor deformations, which promotes the use of an off-line measurement technique (Minor deformations are believed to affect the upper part of the frequency range (several MHz)). These large tolerance-bands are mainly a function of the variation in the frequency-content of the excitation signal and the signal to noise level of the measurement-system.

- Christian reports [24], [25] time-based, construction-based and type-based comparisons between many transformers, establishing a good statistical foundation. He also presents an experimental setup used at the University of Stuttgart, where sensitivity to radial deformations and axial displacements were investigated. The overall sensitivity to axial displacement is 1-2% of the total axial height of the winding. Radial deformations have a limit of sensitivity at a buckling-depth of 3% of winding diameter along 10% of its height. These are the only quantified sensitivities found in literature. Admittance measurements were found to be less sensitive than voltage ratio-measurements.

- The sensitivities found by Christian were verified in high frequency models developed by Rahimpour [1]-[5], using the same constructional details as Christian. These laboratory models were reduced scale models, built to ease the application of radial deformations and axial displacements. The core has been replaced by a slit cylinder by assuming the core-flux can be neglected.

The University of Helsinki, Finland has performed numerous measurements on different transformers using measurements from factory acceptance tests (standard lightning impulse) at full and reduced voltage levels [26]. Testing at full voltage involves the use of dividers and this limits the applicable frequency range severely. Correlation and coherence functions are used to establish confidence limits. Different grounding topologies are tested; grounding each terminal at the flange or establishing one point of grounding.

Differences between similar transformers, different tapping positions and differences between phases are investigated, as well as the influence of different types of windings. All experiments utilizing artificial damages are done by adding capacitances to the winding rather than applying deformations. These experiments are arranged equally to the arrangements used in Stuttgart (as described above),

where tank and core is replaced with two metallic cylinders. But these artificial damages are not directly related to a degree of deformation and thus the application of these results is rather limited.

Vandermaar and Wang [27], [28] report large differences in measured admittance above 1 MHz before and after reclamping of different transformers (specially on a 630 MVA and a 140MVA unit). This was a result of a measurement program where FRA was measured before and after reclamping of a large number of transformers. The LVI-method was utilized with a front-chopped impulse. Loose windings during short-circuits may be detrimental and must be identified.

Another study conducted by Wang et al.[29] identify important aspects of FRA during field-measurements. When measuring admittance, the shunt impedance used for current measurements is important. Different values between 1 and 50 Ω is tested with the result that sensitivity increases with decreasing shunt impedance. This result promotes the use of a current transformer instead of a measuring shunt, since a 50Ω shunt dominates the measured response above 500 kHz, while a 10Ω shunt is sensitive up to 3 MHz. For a shunt impedance lower than 1Ω, the measurement will be sensitive up to 10 MHz.

Investigations [29] by Wang et al. on the effect of connecting cables at the top or bottom of the bushing shows some difference already below 1 MHz, and becomes prominent above 3 MHz. The difference with/without the neutral grounded show only small difference above 2 MHz, but major difference at low frequencies. Minor/local axial deformations are clearly detected above 4 MHz, while small radial deformations show only minor difference above 7 MHz. The biggest change is observed for different lengths of the measurement leads (above 1 MHz). Their conclusion was that the lengths of the measurement-leads should be as short as possible, and at the same time kept in the same position when repeating the measurements. The size of the transformer is important, because the size of the bushings limits the upper usable frequency due to the increasing length of the leads.

ERA [30] reports successful utilisation of FRA by using the LVI-method on winding collapse and distortion, axial displacement and winding slackness. Their experience emphasize the fact that extreme winding collapses do not always cause secondary effects such as broken conductors or low insulation resistance, and that substantial distortions can occur without detracting from the normal performance at power frequency. This underlines the need for FRA.

Doble is a supplier of instruments for diagnostic purposes, and in their user guide for one of the instruments [31] applicable to FRA-measurements, extensive experience is outlined. The application examples show both healthy and faulty transformers, which connections that should be applied and how to separate normal deviations from deviations due to mechanical- or electrical faults.

Høidalen et al. [20] reports low sensitivity to both axial and radial faults during an experiment on a 35 MVA single phase transformer (radial not detectable, axial hardly detectable). The radial buckling was performed very localised (1-3% of winding height), but the axial displacement was severe (outer winding displaced 5% of total winding height). One of the assumptions for the low sensitivity in this experiment is the complexity of the winding; Two identical sets of windings were mounted on each core leg and cross-connected in a certain order. They also investigated the effect of the bushings, the oil and the tank.

Coffeen et al. [32], [33] reports several successful cases of detection using FRA supported by a new method named OWA (Object Winding Asymmetry). They make use of the LVI-method, and the transfer function is formulated by using spectral density estimates. The technique improves detection when fingerprint-measurements are not available for comparison.

Core related problems such as circulating currents, faulty grounding, clamping problems have also been mentioned as detectable in literature.

Some even claim to be able to detect inter-strand short-circuits.

2.2.3 Alternatives

As mentioned earlier there are no traditional methods that can detect mechanical deformations with high degree of sensitivity. Methods such as turn ratio, stray inductance and impedance measurements incorporate inaccuracies of 2% or higher.

During the last few years, a new and simpler method to FRA have developed. It is called FRSL [34] (Frequency Response Stray Losses), and measures the stray losses in the frequency-range from 10Hz to 1kHz. This method is reported to be able to detect deformations and it also results in an easier interpretation of the measurements. It is less dependent on the measurement-setup than FRA due to the low frequency used.

Vibro-acoustic techniques to detect winding slackness and other clamping-problems related to the core and windings, are utilized to some extent [9], [35]-[37].

At last, a special application is mentioned to illustrate the evolved creativity in order to establish alternative methods: Application of ultrasonic measurements in service to detect radial deformations to the winding [38].

2.2.4 FRA Summary

As seen from the reviewed literature, there is a need for interpretational criteria and guidelines in using FRA. Most of the experiments reported are in-service failures of large transformers or artificial damages to quite small simplified transformers. There is a need for detailed studies on real transformer geometries preferably using a computer model in order to establish guidelines for interpreting FRA.

Another important factor is the standardization of a measurement method for FRA. Since different methods and different equipment are used, FRA is not adopted completely by the industry as a diagnostic method. It seems like small deformations can be detected at frequencies above 1 MHz. This promotes the use of the SFRA method since the LVI-method is limited (both in frequency and dynamic performance) in terms of noise and digitizer problems. Minimizing the loops of the measurement-leads connecting to the bushings is important.

The literature shows that most mechanical faults are detectable, with the limitation that minor damages are detected at frequencies where the measurement-setup influences more than the deviation itself. This is clearly a limitation and effort must be put into making measurements as reproducible as possible.

In order to verify or reject hypothesis 1, the approach used by Rahimpour seems to be the most appropriate way of investigating FRA influence of different types of faults.

2.3 Transformer modeling

> ***Hypothesis 2.:*** *Analytical methods are sufficient for simple/homogenous transformer geometries. A real transformer geometry complicates the analytical approach. Finite element methods would be an alternative for complex designs since details and variations may easily be included.*

Simple, analytical approaches have been used extensively for decades in transformer modeling. Such methods are assumed to have limitations regarding details in a real transformer geometry, but are examined due to their convenience for analysing deformed windings.

Regarding modeling, suitable methods for determining the elementary parameters have to be reviewed, with the aim of narrowing down to the most suitable method for the purposes of this work.

A historical review on the early years of transformer modeling is given in appendix D. This review presents a more detailed introduction to the methods used today.

Todays methods are listed together with their advantages and drawbacks, their applications and limitations, to make a better basis for choosing the proper method for further work. The frequency-range of interest for FRA/deformations is mainly 100kHz and above, but for high frequency modeling in general the lower frequency of interest would be around 10kHz.

Since the modeling of inductance is believed to be the most complex task in the process of transformer modeling, this point is emphasized:

2.3.1 Inductance Calculation

The main streams of inductance calculation for analysis and design of transformers in general, has traditionally been classified [1], [39] into the following categories:

- "Modeling based on self and mutual inductances". This is by far the most utilized method mostly since it is easily understood and utilized. A ladder-network was first proposed by Weed [40] in 1915 neglecting mutual inductances. This was improved by many others: The first analytical, computer-based attempt following this approach was presented by Rabins [41] employing an infinite permeability. This work was followed by many others such as Fergestad and Henriksen [42], [43] (Mainly based on Olaussen [45]). Their method was supported by experiments where empirical data was used to add losses and modify inductances. A recent improvement is made by Wilcox et al. [46], [47] (includes core and winding losses as well) and seems to be very accurate in the calculation of self and mutual inductances for the windings, sections, or turns of transformers. This is the method usually used

in high frequency models and is used in earlier sensitivity-analysis of FRA. Numerical values of the self and mutual inductances are very close at low frequencies and this results in ill-conditioned equations. There are however methods to avoid ill-conditioned matrices (during inversion), for instance the extraction of the leakage inductance:

- "Modeling based on leakage inductance". This approach was initiated by Blume [50] and improved by McWirther et al. [51] and Shipley et al. [52]. Brandwajn et al. [53] presented the three-phase multi-winding generalization. Dugan et al. [54] used the same technique for modeling multi-section transformers. Such models are frequently used to represent the leakage inductance of the transformer adequately at low frequencies (from nameplate short circuit data), but the low frequency core-properties are not properly included. This method is normally used at low frequencies when representing short-circuit data for a transformer. It could be extended to higher frequencies if the winding is discretizised to small parts as in the previous method.
- "Modeling based on the principle of duality". This approach was introduced by Cherry [55]. The iron core can be modeled accurately at low frequencies by using an equivalent circuit with a duality to the reluctance of the core. However, models based only on this approach have the inconvenience that the leakage inductances are not correctly represented (they are directly derived from the leakage flux neglecting the thickness of the windings). Edelmann [56] and Krähenbühl et al. [57] corrected this inaccuracy (assuming that the magnetic field is axial). Arturi [58] used this approach in the modeling of highly saturated conditions. This method is suitable for low- and intermediate frequencies, since details in the leakage field becomes important at higher frequencies.
- "Transmission Line Modeling": The winding is treated as a multiconductor transmission-line. The method was first proposed by Wagner [59]. This approach can only be applied on homogenous windings according to Al-Khayat [60]. Popov et. al. [61] seem to cope with this limitation by combining STL-(Single Transmission Line) models with MTL-(Multi Transmission Line) models. The STL-model describes each elementary unit such as discs, while the MTL-model is used to model the interaction between each elementary unit.
- "Modeling based on terminal measurements (black-box modeling)".This is not a suitable method when the purpose is to study geometrical effects such as mechanical deformations, since it is not a physical model. Still it is considered because it is feasible for implementing frequency domain models into time domain. A great number of high frequency transformer models have been derived from measurements; see for instance [62]-[65]. Tests are made for the determination of the model parameters in the frequency domain or time domain. Models obtained from measurements have the drawback that their performance can only be guaranteed for the tested transformers. Although some general trends can be inferred from the tests, according to design, size, manufacturer, etc., accurate predictions for non-tested transformers cannot be

assured. The main methods used for implementing black-box measurements are:

  - Modal analysis: Wilcox et al. [66]-[68] and Glaninger [69], [70].
  - Pole/zero-representation: Soysal et al. [71].
  - Vector fitting: Gustavsen et al. [62], [63].

- "Analysis based on electromagnetic fields". This is not a separate method but a tool for establishing the parameters of the above methods. Designers of large transformers use electromagnetic field approaches for the calculation of the design parameters. The technique of finite elements (FEM) is the most accepted numerical solution for field problems [72]. There are, however, other techniques available; see for instance [73]. There is general agreement that three-dimensional field analyses are necessary in the design process, for instance for evaluation of eddy-current stray losses. These methods are in most cases impractical for the calculation of transients since they give expensive simulations, at least for 3D-calculations. As computational resources are increasing, this method will gain popularity in near future. SUMER is a FEM-based software developed by EdF in France [74]. It is based on the method of self- and mutual inductances, and it is able to incorporate all types of frequency-dependencies including losses. This is made possible by a special technique reducing the mesh-size considerably.
- Combinations: Several publications have combined the methods above. The method of De Leon/Semlyen [75], [76] was derived from a combination of leakage inductances (based on image currents) and principle of duality. Gharehpetian et al. [77] combined the principle of self- and mutual inductances with the black-box method in order to extend the coherence of the model from a few hundred kHz to a few MHz.

The methods listed above concerns mainly the inductances in the transformer model, since this traditionally has been the biggest challenge in transformer modeling. Other important elements in a high frequency transformer model are briefly reviewed in the following.

2.3.2 Capacitance Calculation

The capacitances can be calculated either by using traditional analytical methods or by using computer methods such as the Finite Element Method where the material parameters and the geometry are important [78]. Shunt- or parallel capacitances (capacitance between windings or from winding to ground) can be calculated with simplified geometrical/analytical formulas or on a semi-empirical basis (additional capacitance to ground are introduced by connections, bushings, static plates and tap-changers. The series capacitance is the capacitance between different turns of the same winding and is a determinant for the electrostatic voltage distribution. Several contributions to the calculation of this parameter are made: (Stein [79], Okuyama [80] and Ambrozie [81], [82]). Special consideration must be taken when calculating the series capacitance of interleaved coils or coils with in-wound shields (See: Ambrozie [83], Pedersen [84], De [85], Moreau et al. [86], Del Vecchio et al. [87] and finally Seitlinger [88])

2.3.3 Losses

The losses in a detailed model are indispensable, particularly when internal stresses are evaluated in the design-stage of a transformer. Without the losses implemented, the stresses will be higher in the model than in reality and the design will become unnecessary cost-consuming and then less competitive, as stated by Mombello et al. [89].

The different loss-mechanisms in a transformer are:

- Series resistance in windings (DC-resistance)
- Frequency dependent losses in the conductors occur as eddy currents due to time-varying magnetic fields. The eddy currents cause an increase of the losses and a reduction in the net amount of magnetic flux. This is translated into an increase of the resistance and a reduction of the inductance of the equivalent impedance (reflected impedance) representing the winding.
    - Skin effect: Frequency-dependent current density distribution (eddy currents) due to the current in the conductor itself, as shown by De Leon et al. [90], [91].
    - Proximity effect: Eddy currents due to the external magnetic field generated from current in the other conductors, see [48], [49], [90]-[97].
- Eddy currents in core laminations (core reaction) due to magnetic field in the core. They are assumed important for low-and mid-frequency models. The eddy currents have a frequency dependent penetration depth, shown by Ferreira [98], [99].
- Dielectric losses within the insulation (both series- and shunt conductances) due to conductivity and different polarization mechanisms. Dielectric losses are normally not included in transformer models. As a first approximation, a constant value based on low-frequency measurements can be used.

2.3.4 Model Applications

The method to be preferred depends on the application. There are several different applications that incorporate transformer models:

- Determining impulse-overvoltages in windings, during both design-stage and when coordinating insulation-levels. The impulse strength is checked experimentally during factory acceptance tests. Detailed methods are necessary, see; McWirther et al. [51], Dent et al. [100], Okuyama [101] and Waldvogel et al. [102].
- Understanding measurements and propagation of signals in windings due to partial discharges (locating partial discharges). Such considerations are for instance made by Dong et al. [103] and Akbari et al. [104].
- Analysing overvoltages in transformers and power networks:
    - Lightning overvoltages: These usually correspond to fast wave fronts (Miki et al. [105]).
    - Switching overvoltages: These correspond to slower wave fronts, and can be generated by switching of lines, transformers, reactors, capacitors and by faults (Degeneff et al. [106]).
    - When oscillations due to switching operations, coincide with resonances in the transformer, large resonant overvoltages may occur.
- Understanding frequency response measurements when applied in diagnosis and condition assessment. According to Rahimpour et al. [2]-[4], the most suitable for this application, is the method of self- and mutual inductances using air core theory (see; [107], [108]).

2.4 Iron Core

Hypothesis 3.: *Iron core can be neglected and considered to behave like a perfect conducting screen above 10 kHz.*

Transformer modeling has divided into two different paths depending on the application. In the frequency-range of slow transients (from 50 Hz to some kHz), time-domain models have been developed in order to handle non-linear effects such as hysteresis and saturation in the core. High frequency models are usually established in the frequency-domain since it is assumed that transformers behave linearly at higher frequencies. The reason for this will be shown later.

The iron core has traditionally been neglected in high frequency transformer models [1], [100], [102], [105], [106], [109]-[112], still giving reasonable results. This is also a widespread assumption applied in the modeling of electrical machines [113], [114]. Others report influence due to the core [42], [46] but no agreement is achieved regarding the influence of the iron core and whether it is convenient to neglect it. In other words; none of them gives a transition/frequency where the core can be neglected.

10 kHz is selected as the transition to where the core can be neglected, based on [1], [109]-[111]. This frequency is pointed out by most of the publications neglecting the core. At the same time this is the frequency where time- and frequency-domain models approach, since core-related nonlinear effects decrease with increasing frequency.

The core is assumed to complicate the calculation of inductances and if hypothesis 3 is proved to be correct, it simplifies the calculations substantially. It is therefore of principal interest to establish an overview of the possible errors made by this assumption.

Several methods [115]-[118], are reported to include the core successfully where low frequency- and switching transients are the main topic. Common for these methods is the inclusion of nonlinearities which necessitates the use of time-domain simulations. Since high degree of conformity is observed when comparing full and reduced lightning impulse tests [44], the transformer is considered to behave linearly at higher frequencies. This enables the use of frequency-domain modeling instead of the more troublesome time-domain approach, and nonlinearities can be neglected.

2.5 Dielectric materials

> ***Hypothesis 4.:*** *High frequency characteristics of insulating materials are independent of frequency, temperature, moisture, ageing etc. Ageing should therefore not change the FRA-signature.*

Since there is limited data available regarding high frequency characteristics of insulating materials in transformers, high frequency transformer models usually use constant permittivity and neglect the dielectric losses. Another reason for neglecting the frequency-dependency of the dielectric parameters is that other parameters in a high frequency model seem to influence more than the dielectric characteristics.

Measurements are highly needed in order to investigate prospective effects influencing the dielectric parameters. If the dielectric characteristics do influence, it would be important to separate the influence due to ageing from the influence due to damages (deformations and displacements), by studying the changes in FRA-signatures in the two cases.

Buckow [109] included frequency-dependent dielectric losses. His data was based on measurements taken inside a real transformer geometry, both between turns, between discs and between windings. Since the measurements are performed on a real transformer winding, it must be pointed out that the measurement will be influenced by stray-effects and that high frequency-measurements done this way must be questioned. A linearized approximation of these measurements were utilized by Rahimpour [1]-[4].

Buckow and Rahimpour are so far the only approaches found in literature that have included such dependencies. The initial approach chosen in this work is to include dielectric losses based on measurements at 50 Hz.

The influence of the dielectric characteristics have evidently been considered less important than other loss mechanisms such as the skin- and proximity-effect in the winding structure.

Some influence due to ageing is reported at low frequencies, but in order to obtain detailed knowledge on high frequency characteristics, dielectric spectroscopy measurements are needed in order to disapprove or accept aspects around the above hypothesis.

2.6 Modeling accuracy

Hypothesis 5.: *High frequency transformer models can be established with high degree of conformity to terminal measurements, provided constructional information is available.*

Detailed internal transformer models are always established on the basis of constructional details. If an internal model is properly defined, including all relevant phenomena, it should also give a proper behaviour reflected to the terminals of the transformer. If not, there must be other elements of influence than the construction of the winding. This may be investigated by comparing terminal measurements with the terminal model.

Some influence from leads, connections, tap-changer etc. is to be expected, at least in the upper frequency-range. These effects may be difficult to account for.

The approach of Rahimpour [1], [5] is based on analytical air-core theory, since it is assumed that all flux is displaced from the core above 10 kHz. His approach seems to obtain a high degree of accuracy for his models compared to terminal measurements. This approach is tested on three different windings which are manufactured for investigating axial deformation, radial deformation and disc-to-disc-short-circuit (one for each application, in an experimental work done by Christian [24]). Rahimpour employs the models developed for FRA sensitivity analysis using an analytical approach. The results in this work show the highest agreement between model and measurements seen so far, and thus constitutes the starting-point for this work.

De Leon's approach [115] focus on a simple implementation based on analytical equations for the magnetic field. The leakage field is adjusted using mirror-currents inside the core, but this requires calibration. His method establishes turn-to-turn parameters which are reduced to a terminal equivalent. Losses are also calculated on a turn-to-turn basis but represented by a Foster-equivalent at the terminals. The accuracy of this approach is questioned since all terminal behaviour is dependent on the internal representation. His work is completed by a comparison to measurements on a small, simplified transformer with layer windings. The transfer function incorporates one resonance frequency, but agreement between measurement and model is not satisfactory. This approach seems to be suitable for simplified geometries but will probably fail at a real and complex transformer geometry.

There are other methods claiming to have good coherence to measurements. Most of them are time-domain models [116], [118], comparing simulated and measured time-domain responses. This gives no complete overview of the models ability to reproduce a broad frequency-spectrum of the transformer represented.

Fergestad [44] get close agreement comparing to time-domain responses, but empirical corrections are needed for the inductance calculation. In addition all losses are added on an empirical basis.

Wilcox et al. [46], [47] seem to obtain high degree of resemblence to measurements of inductances on iron cores, but his method needs measurements on each specific core in order to establish different parameters needed for the calculation. In addition the formulas seem to be difficult to implement numerically. Accurate formulas for inductance-calculation are also reported by Mombello [48], [49].

2.7 Conclusions

The increased focus on condition monitoring have led to new methods for detecting minor incipient faults such as mechanical deformations. Operational characteristics are usually not degraded by such faults, but withstand-strength to short circuits and overvoltages may be degraded severely. FRA is a fairly new method with several reports of successful detection of deformations. Little investigational work is done to reveal sensitivities and drawbacks of this method. Construction-based high frequency transformer modeling seems to be a proper approach for investigating sensitivities and behaviour of different faults to the FRA signature, referring to the work of Rahimpour [1].

The analysis in this chapter is made to reveal the most suitable method for modeling power transformer at high frequencies. This method must be suitable for both FRA investigations and other applications such as analysis of internal stresses, transferred overvoltages and possible resonances with the network. The most referenced method for inductance calculation is the method of self- and mutual inductances. This seems to be a proper starting-point since it is simple to implement, understand and also to compare for instance by using a FEM-based software. The other methods are either suited only for low-frequency analysis or homogenous windings, or they simply do not relate to the physics and geometry of the winding directly.

The chosen principle of inductance representation for further work is therefore the self- and mutual inductance description in a linear lumped parameter model, applying simple analytical equations at first.

3 BASIC CALCULATIONS

Hypothesis 2.: *Analytical methods are sufficient for simple/homogenous transformer geometries. A real transformer geometry complicates the analytical approach. Finite element methods would be an alternative for complex designs since details and variations may easily be included.*

As decided in the previous chapter, the method in this work is based on lumped parameter representation using self- and mutual inductances. With the high degree of conformity to measurements obtained by Rahimpour [1], the outlook for this approach is promising. In this chapter, all lumped parameters are calculated using analytical formulations.

Winding deformations can also be studied using basic analytical formulas. This enables the user to easily perform several degrees of deformations in order to study in detail, the sensitivity of FRA to different fault-types.

When dividing the transformer winding into elementary parts/lumped segments, the model will be limited in frequency due the discretisation. This is comparable to a pi-representation of a transmission line. Similarly a transformer winding can be regarded as a multiconductor transmission-line, represented by a number of lumped circuits (concentrated parameters) incorporating mutual coupling between elements.

It is often practical to use single or double discs as an elementary unit in the model (or an equivalent division for other winding types). This simplifies the modeling since the electrical elements are concentrated geometrically.

3.1 Lumped parameter description

Lumping several turns into one electrical element reduces the complexity of the model. Using a single disc as the smallest discretisation is usually sufficient up to 1MHz, sometimes even more, depending on the size of the transformer (no. of turns per disc and the circumference of the coil). The upper limit decreases with increasing size of the transformer. A turn-to-turn model would be unnecessary complex and require excessive computational resources. In reality the parameters are distributed so each and every turn has its own electrical and magnetic characteristics, such as inductance, losses and capacitance. When combining several turns to one electrical lumped element, these parameters are merged (and approximated). All mutual parameters are established for the disc as one element. For other types of winding, the principle is the same.

A subdivision is valid only if there is a linear voltage distribution inside each electrical element. This holds true below the upper frequency limit imposed by the subdivision. When the frequency approaches this limit the internal series capacitance will influence the voltage distribution, and the subdivision must be refined to hold true. All lumped parameters belonging to this particular element (for instance a disc) form a special elementary group of elements (like an advanced pi-element) as shown in figure 3.1

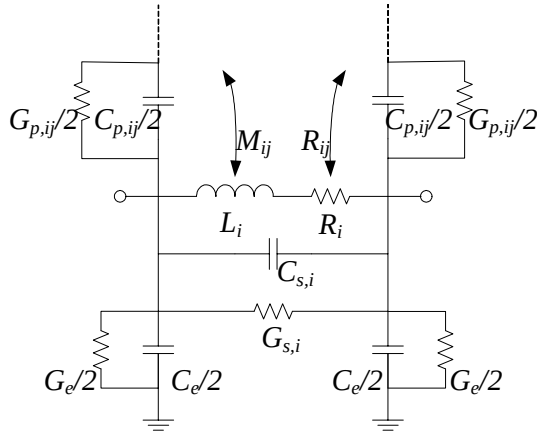

Figure 3.1: Lumped parameter equivalent of one electrical element

Figure 3.1 shows an equivalent of one electrical element. Mutual effects are shown both for inductance and resistance. Capacitance to other discs or windings is also shown as well as ordinary series and shunt capacitance. The different elementary parameters are described below:

R_i = Resistance due to DC- and eddy current losses.
L_i = Self inductance of the element (skin-effect included).
$C_{s,i}$ = Series capacitance along the element itself.
G_e = Dielectric losses to ground.
C_e = Capacitance from element to ground.

Mutual inductance between element i and other elements are designated M_{ij}, while R_{ij} describes the losses in other elements due to the current in element i (proximity losses). Parallel capacitance and conductance to other elements are represented by $C_{p,\,i}$ and $G_{p,\,i}$ respectively.

The objective is to establish an equivalent circuit model of the winding as illustrated in fig. 3.2, and represent it with a nodal admittance matrix as a function of frequency. Not all mutual effects are shown here, such as proximity losses (mutual effects incorporated into the series resistance), and different capacitive coupling. There will be coupling between all inductance and resistance elements.

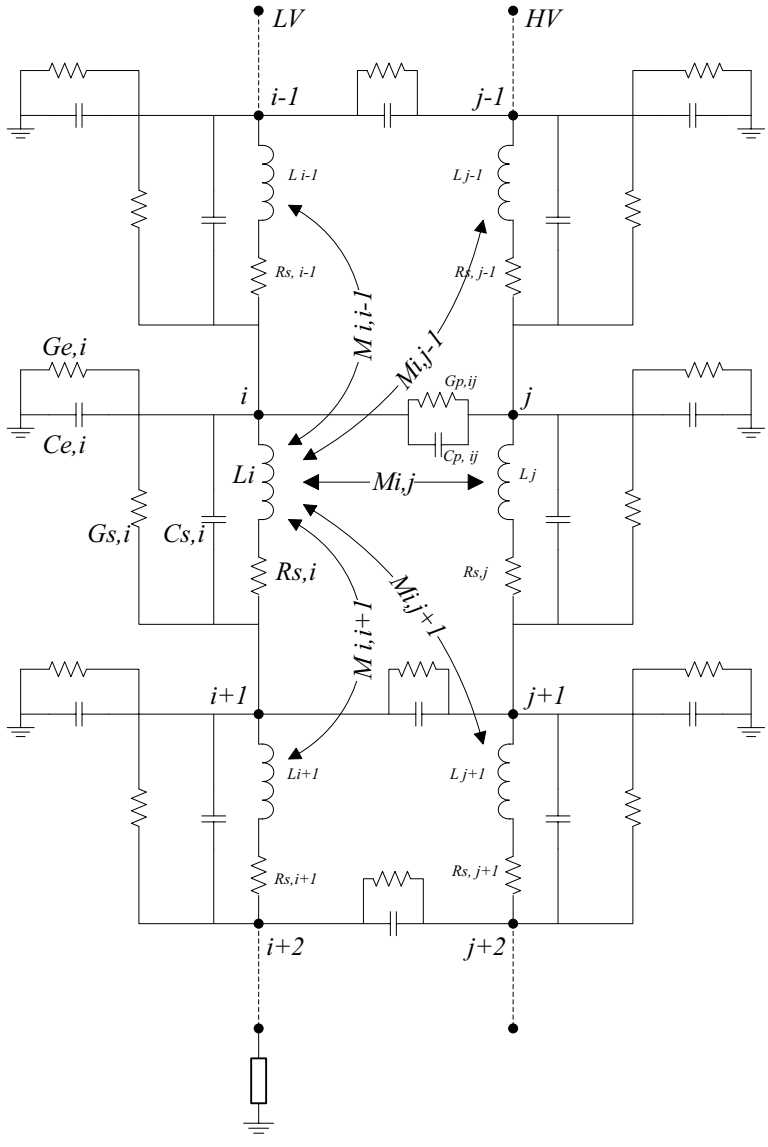

Figure 3.2: Equivalent circuit of high frequency transformer model

The series impedance matrix is:

$$\mathbf{Z} = \mathbf{R}(\omega) + j\omega \cdot \mathbf{L}(\omega) \tag{3.1}$$

and the shunt admittance matrix is:

$$\mathbf{Y_N} = \mathbf{G}(\omega) + j\omega \cdot \mathbf{C}(\omega) \tag{3.2}$$

The series impedance matrix $\mathbf{Z}$ is transformed into a nodal description $\mathbf{Y_B}$ by using the transformation matrices $\mathbf{A}$, and $\mathbf{A}^T$. These matrices describe the relation between branch-/nodal currents and branch/nodal voltages respectively. The transformation is explained in detail in appendix E.

$$\mathbf{Y_B} = \mathbf{A} \cdot \mathbf{Z}^{-1} \cdot \mathbf{A}^T \tag{3.3}$$

The nodal system-description can then be described by the following relation:

$$\mathbf{Y_{sys}}(\omega) = \mathbf{Y_N}(\omega) + \mathbf{Y_B}(\omega) \tag{3.4}$$

This is the detailed admittance matrix for the system. In order to handle the system referred to its terminals, it is reduced to the following condensed or reduced description of the system:

$$\tilde{\mathbf{Y}} \cdot \mathbf{V_e} = \mathbf{I_e} \tag{3.5}$$

$$\text{where } \tilde{\mathbf{Y}} = \mathbf{Y_{ee}} - (\mathbf{Y_{ei}} \cdot \mathbf{Y_{ii}^{-1}} \cdot \mathbf{Y_{ie}}) \tag{3.6}$$

This reduction is further described in appendix E.

3.2 Inductance

Since it is assumed (Hypothesis 3) that core-influence is neglectable, all initial calculation of the elementary parameters is based on core-less/air-core theory. In the following, air core theory is examined. This will not be equal to treating the core as a shield, but it is easy to implement as a first approach.

3.2.1 Self and mutual inductance

If all materials are assumed to be linear, the total magnetic flux through the winding segment is proportional to the current applied to the winding segment. The proportionality coefficient *L*, expresses the self inductance of the segment.

Mutual inductance *M*, between two segments indicates how much of the total magnetic flux from the energizing segment, that links the other segment. If *L* and *M* is approximately equal, it means that the linkage/connection between two winding parts is strong. The difference represents the leakage field set up by the first winding segment not linking the other.

A disc from a disc-winding is shown in figure 3.3. It shows parts of the magnetic flux in the air surrounding the disc. The colour indicates the flux density.

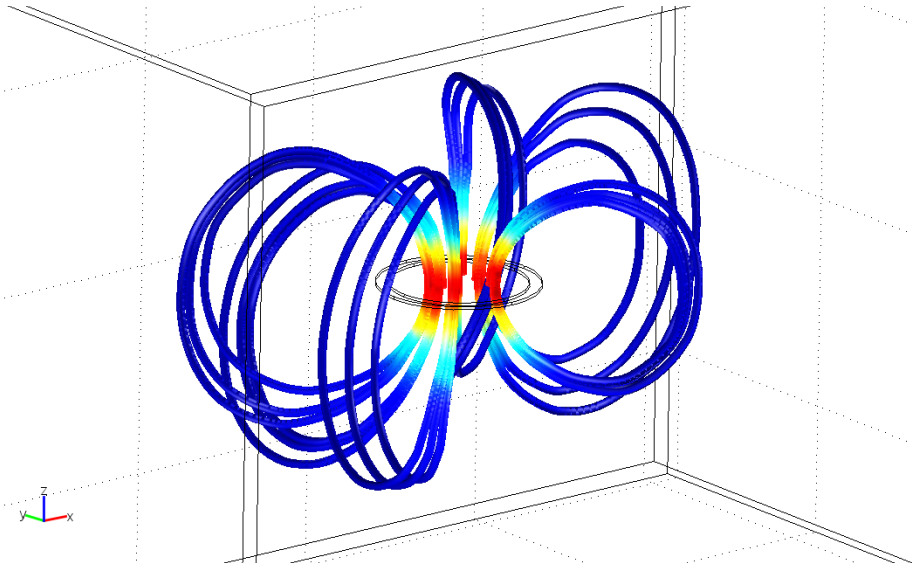

Figure 3.3: Magnetic field from a winding-segment in air

The next figure shows the principle of mutual inductance, were only a part of the magnetic field flows through the upper disc.

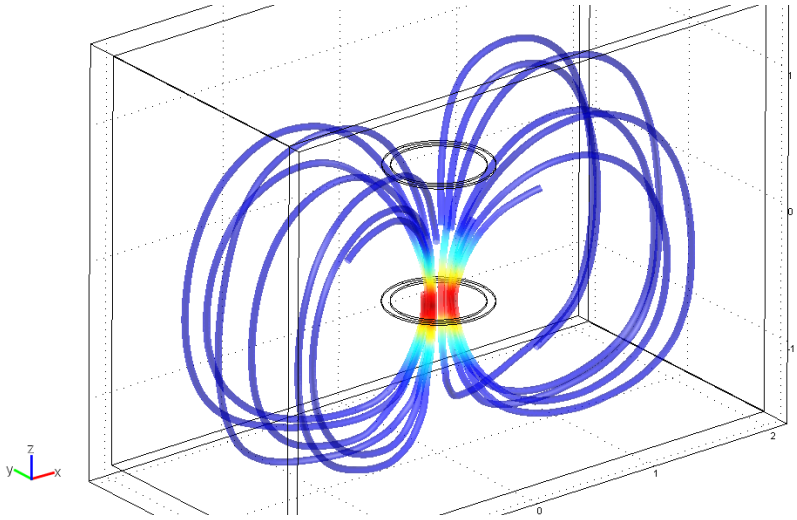

Figure 3.4: Principle of mutual inductance

Analytical formulas for the calculation of inductances are summarized in Appendix F: “Analytical formulations” on page 196. These parameters assumes circular windings. Inductance for buckled windings is not necessarily equal to non-buckled windings. This will be investigated later.

Hypothesis 3 approximates the core with a conducting screen, since the magnetic field is assumed to be completely displaced ($\mu_r = 0$). Using an air-core ($\mu_r = 1$) approach will not be equal to the conditions given by the hypothesis. Inductances (both self- and mutual-) will be overestimated compared to the approach suggested in the hypothesis. The result of the air-core approximation compared to the conditions in hypothesis 3 will be further discussed in chapter 4. Air-core theory is initially used for simplicity reasons.

3.3 Capacitance

Capacitance between the windings and from the windings to ground/core can be calculated assuming that the windings can be treated as cylindrical capacitors.

Detailed formulas for the calculation of elementary capacitances in different winding types are given in Appendix F.

The resulting relative permittivity for the winding insulation has to be calculated as shown in the following.

A typical transformer insulation mainly consist of oil and pressboard, and resulting permittivity can in most cases be calculated by means of the X-Y model of Gafvërt et al. [119].

If considering the paper as well, the dielectric structure will be as outlined in fig. 3.5, where the resulting permittivity is calculated by means of material data given in table 3.1 and eq. (3.7).

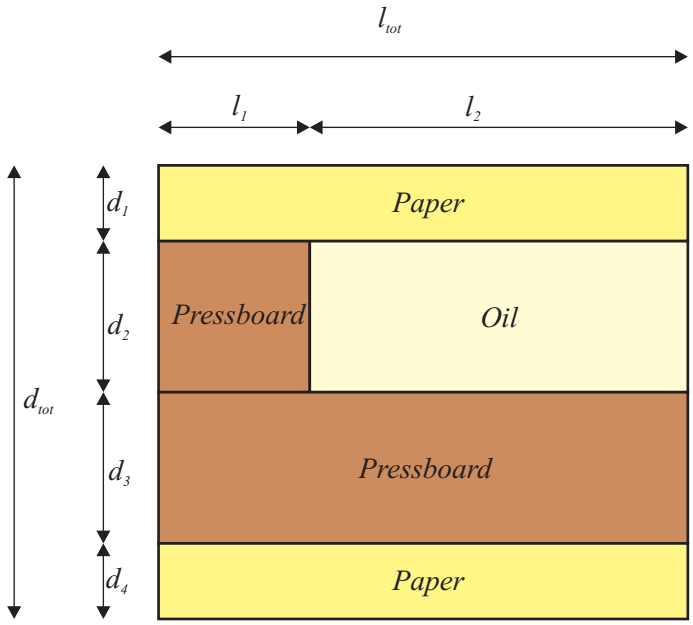

Figure 3.5: Structure of typical inter-winding transformer insulation

where l_{tot} represents the span between axial spacers, l_1 is the width of the axial pressboard spacer and l_2 is the width of the oil duct between the spacers. d_{tot} is the distance between the windings, d_1 & d_4 is the paper thickness of the two windings, d_2 is the thickness of the pressboard spacer/depth of the oil duct and d_3 is the total thickness of all pressboard cylinders between the windings.

The values given in table 3.1 have traditionally been used.

Table 3.1: Relative permittivity for different materials used in transformer insulation [44]

	Rel. permittivity - ε_r	
	Impregnated	Non-impregnated
Paper	3,3	2,2
Pressboard	4,4	3,5
Oil	2,2	

The resulting permittivity will in the case of fig. 3.5 be:

$$\frac{1}{\varepsilon_{res}} = \frac{1}{\varepsilon_{paper}} \cdot \frac{(d_1 + d_4)}{d_{tot}} + \frac{1}{\varepsilon_{PB} \cdot \frac{l_1}{l_{tot}} + \varepsilon_{oil} \cdot \frac{l_2}{l_{tot}}} \cdot \frac{d_2}{d_{tot}} + \frac{1}{\varepsilon_{PB}} \cdot \frac{d_3}{d_{tot}} \qquad (3.7)$$

This procedure is applicable to both the interwinding structure as well as internal (interdisc/inter layer etc.)

3.3.1 Series capacitance

The series-capacitance of an element in the model (for instance one disc), consists of a composition of several capacitances, between turns inside the disc and to turns in neighbouring discs. These capacitances forms a network of several different capacitances. In order to establish a lumped model for these elements, an equivalent series capacitance has to be calculated. This requires some assumptions regarding the voltage distribution inside and between the discs. Details on analytical calculation of series capacitance for different types of windings are given in appendix F.3

3.3.2 Shunt capacitance

Typical shunt-capacitances are capacitance from winding to ground or between windings, and also to neighbouring phases (between outer windings). They can be calculated as the geometric capacitance between circular electrodes as shown in appendix F.4. Capacitance between outer windings would only be important if assembling a three-phase model of a transformer. Only a single phase representation is implemented in this work. Capacitance from leads, tap-changer, static-plates and shields are implemented on an empirical basis. Bushing capacitance is added as lumped capacitance (based on data sheets/measurements/ typical values) on the terminals.

3.3.3 Core capacitance

Traditionally, the core has been replaced by a conducting cylinder with a radius equal to the radius of the circumscribed core radius. An examination by means of a 2D FEM model (fig. 3.6) showed deviation not exceeding 1% for the T3 Buran core. This means that the effective electrostatic radius is close to the outer/ circumscribed radius of the core, and that the cylinder approach is valid.

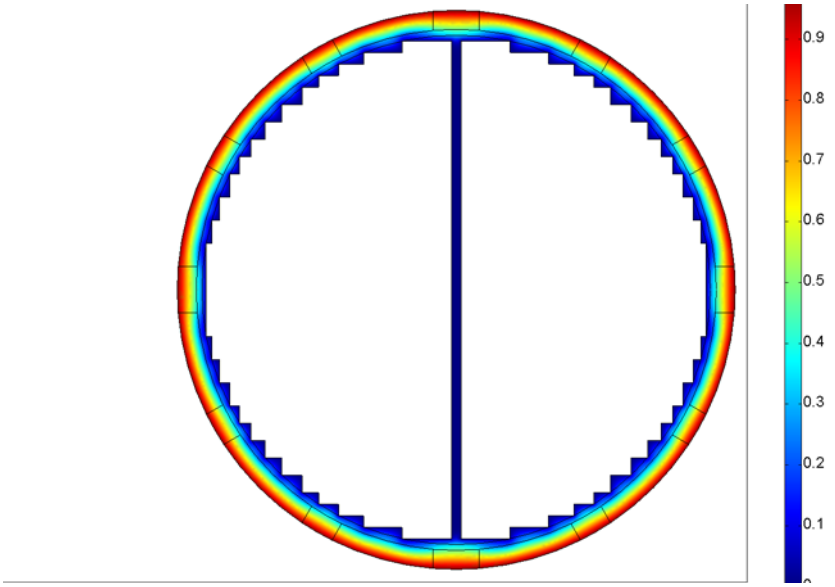

Figure 3.6: FEM-model showing normalized electric potential to investigate the error made when approximating the core surface to a circular screen with a radius equal to the circumscribed radius of the core

It is still questioned whether the steps will influence on the capacitance of a buckled winding since the “electrode” is much closer to the edges of the steps. For large transformers with a great number of different steps, the error of the circular simplification is minimal. When the inner winding has a high nominal voltage, the core is usually wrapped with a conducting screen, either metallic or semi-conducting rubber.

3.4 Winding losses

There are three components that determine the conductive losses in the windings:

- DC-losses
- Skin-effect losses
- Proximity-effect losses

The two latter ones are further elucidated in the following.

Eddy currents are induced in any conducting material subjected to time-varying magnetic fields, and therefore they occur in all types of electrical equipment. Whether eddy currents are beneficial (as in induction heating) or unfavourable (as in cores of electrical machines and transformers), a method of prediction is necessary at the design stage of such equipment.

When a magnetic field varying in time is applied to a conducting body, induced currents start to circulate perpendicular to the direction of the magnetic field according to the right-hand-rule as shown in fig. 3.7

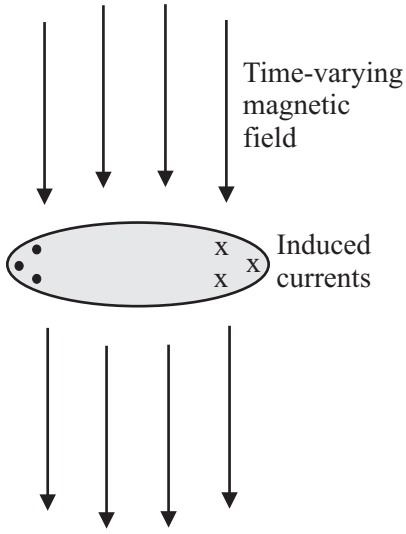

Figure 3.7: Induced currents in a conducting material when exposed to external magnetic field

The induced currents will provide a counter-induced magnetic field as shown in fig. 3.8

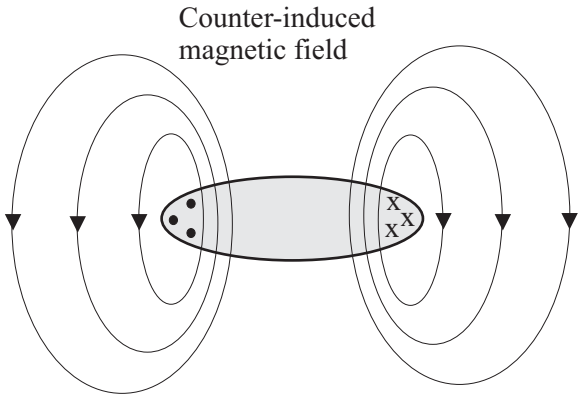

Figure 3.8: Counter-induced magnetic field due to induced currents

The resulting magnetic field surrounding the conducting body, will be displaced towards the boundaries of the body due to the induced currents. This effect will increase with frequency.

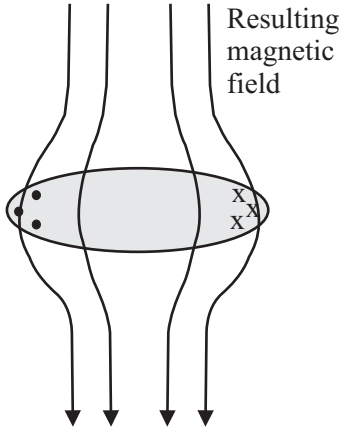

Figure 3.9: Resulting magnetic field

Induced eddy currents in the conducting material will generate a counter-induced magnetic field resulting in a displacement of the applied field (as shown in figure 3.9).

When modeling power transformers at high frequencies accurately, one has to consider the losses occurring in the winding, especially when simulating oscillating phenomena. One important damping-mechanism at higher frequencies

is the proximity-effect, which is eddy-current losses in a winding segment due to current in other segments (such a current establish a surrounding magnetic field, which induce eddy-currents in other conducting parts such as the windings, the core and other structural parts of the transformer).

Calculating the skin- and proximity-effects can be done analytically, assuming these effects are orthogonal.

To find maximum voltage-gradients within windings or to calculate accurate numerical values of resonance peaks in transfer functions, the losses have to be incorporated correctly into the model.

3.4.1 Skin-effect

The skin-effect redistributes the current in the conductor due to the magnetic field setup by the same current. The magnetic field setup by the current is dependent on the shape of the conductor. Different analytical formulations of skin-effect are compared to a FEM calculation on a typical strand in order to determine the best representation. The results of this comparison is shown in fig. 3.10.

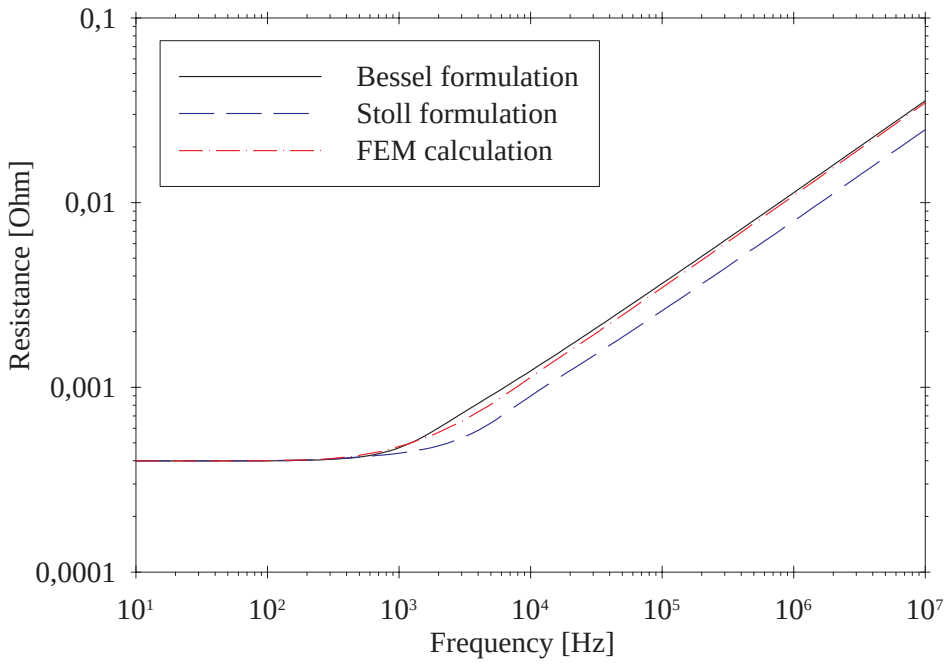

Figure 3.10: Comparison of different skin-effect formulations on a 12 mm^2 Cu-strand with rectangular (2 x 6 mm) and circular cross section

According to Moreau et al. [120] the Stoll [92] formulation is suitable for representing skin-effect in rectangular conductors. In this case the conductor has a large heigth/width-ratio and the Stoll-formulation underestimates the resulting

resistance. The skin-effect is best represented using an equivalent circular cross-section by utilizing the bessel-formulation given in [139]:

$$R_{skin} = Re\left\{\frac{\alpha}{2\pi a\sigma}\cdot\frac{I_0(\alpha a)}{I_1(\alpha a)}\right\} \tag{3.8}$$

where $\alpha = \sqrt{j\omega\mu\sigma}$, ω: angular frequency, σ: conductivity, μ: permeability, a: equivalent circular radius and I_n: bessel function of first kind and order n.

3.4.2 Proximity-effect

This loss-mechanism is a result of the current in one conductor creating eddy current losses in others. These mutual losses can be calculated if the magnetic field can be described analytically in every position due to a current in an energizing turn.

The magnetic field in an arbitrary position is then decomposed into radial and vertical components in order to calculate the induced eddy current loss in the conductor situated in this position as shown in fig. 3.11.

.

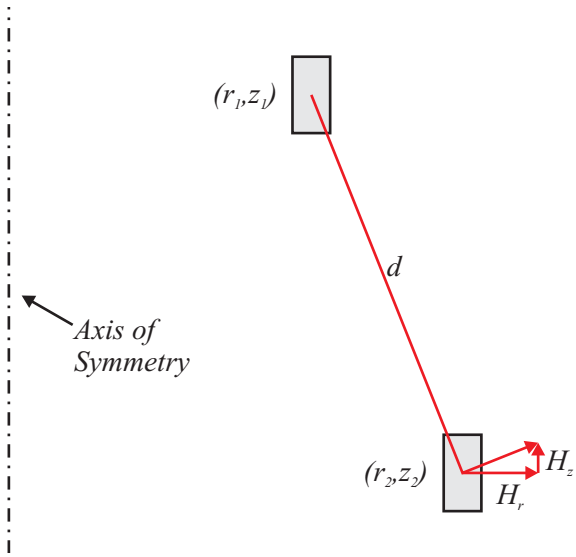

Figure 3.11: Magnetic field at conductor #2 due to current in conductor #1

The decomposed magnetic field is then used to calculate the induced eddy current losses in conductor 2, by using the formulas of Dietrich [96], [97]. The total loss supplied by conductor 1 represents the total proximity loss in other conducting parts and can be identified as one column/row in the resistance matrix of the system description. In this chapter, all mutual losses are added to the diagonal and appear as a sum of losses in the series resistance (R_i in fig. 3.1).

3.5 Conductance

All materials exhibit some form of dielectric losses. These losses depend upon geometry and material characteristics. As shown in table 3.1, a transformer has three main components in the dielectric structure (paper, oil and pressboard). These three have different characteristics and when combined the characteristics change. Little information is found on this topic in the literature, since these effects are usually neglected.

According to hypothesis number 4, these assumptions are valid but should be investigated if all losses are not identified. It is considered to be of minor importance since the winding losses seem to be more prominent.

3.6 Modified parameters due to deformation

When short-circuit forces result in deformed windings in a transformer, it is believed that the elementary parameters of the winding model are modified as the geometry is modified. In order to be able to model such changes, it is necessary also to know the change in the elementary parameters (mainly inductance and capacitance). Even if it is neglectable, it should be investigated, to confirm its relative influence on the transfer function and the validity of disregarding the influence.

Radial deformation (buckling) consists of two principal modes:

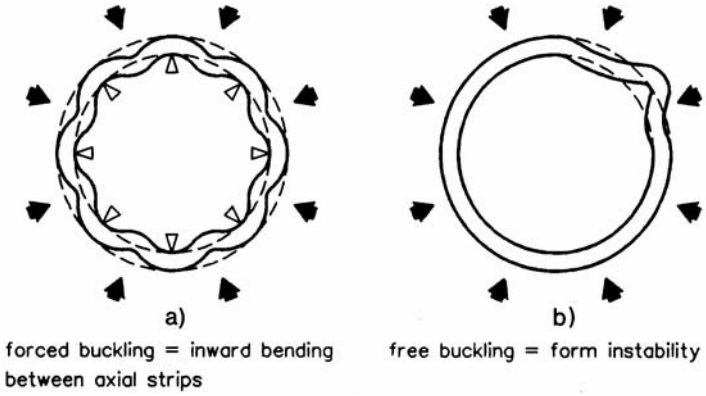

Figure 3.12: Failure-modes of compressive-stressed windings [121]

The forced buckling mode is depending on the strength of the conductor and the distance between the supporting strips, while the free mode buckling is not depending on the supports, but more on the instability of the winding itself. Radial forces are distributed unevenly around the circumference and may give rise to the kind of instability shown in figure 3.12b. This is the most common buckling mode for stacked core transformers [121].

It is assumed that the free buckling mode, given the form in figure 3.12b, is more difficult to detect than the forced mode (figure 3.12a), because the net change in both capacitance and inductance will be less at free buckling mode. The modelling of buckling is shown in the following.

An important finding in the work of Rahimpour [1] was that the change in inductance due to buckling is neglectable compared to the change in capacitance. Similarly, axial displacements mainly influence the inductance (change in capacitance can be neglected). Axial displacements may be modeled accurately in 2D and no simplifications must be applied. The validity of Rahimpour's investigations will be examined later.

3.6.1 Forced Buckling mode

The forced mode is modelled as:

$$r(\alpha) = \begin{cases} r_0 + \frac{b}{2}(\cos c\alpha) - 1), \alpha = [0 \ldots 2\pi / c] \\ r_0, otherwise \end{cases} \quad (3.9)$$

where b is defines the depth of deformation, c is the span width of the deformation, α is the angle and r_0 is the radius for non-deformed segments.

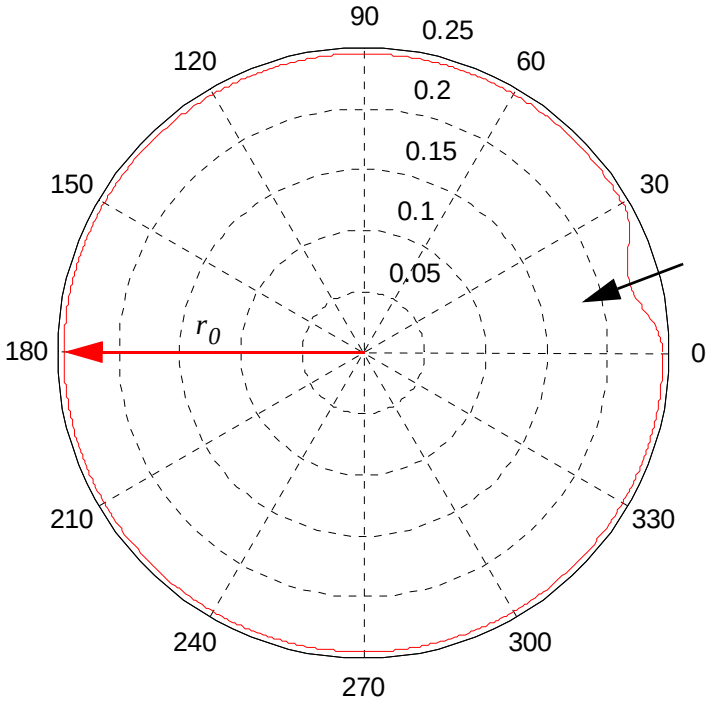

Figure 3.13: Modeling of forced buckling (radial dimension in [m])

A repeated pattern along the circumference is easy to obtain by changing the ranges for the function.

3.6.2 Free Buckling mode

This mode also have a movement in the angular direction in addition to the compression, since the stress is unevenly distributed around the circumference. As an example, the free mode can be modelled as shown in figure 3.14.

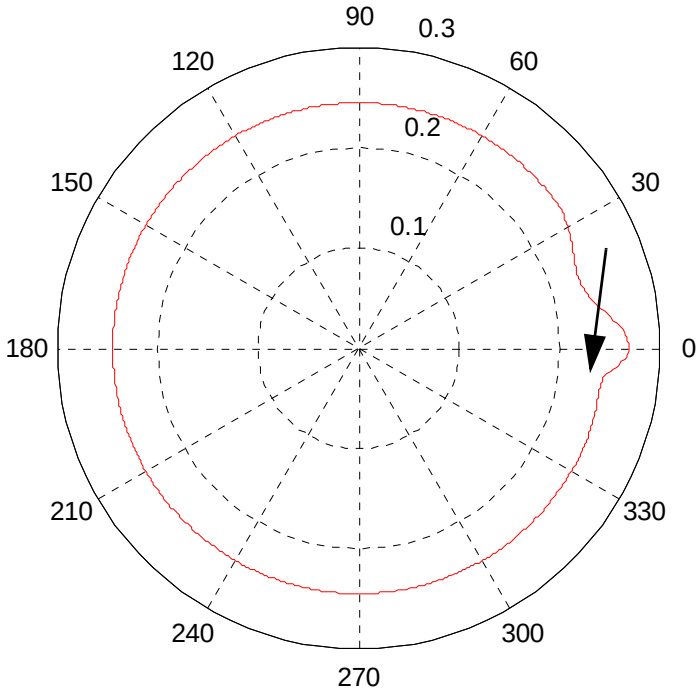

Figure 3.14: Free mode buckling (radial dimension in [m])

The equation for the shape found in fig. 3.14 is determined by:

$$r(\alpha) = \begin{cases} r_0 + \dfrac{b \cdot \mathbf{cos}(c\alpha)}{1 + 10c\alpha^{\sqrt{c}}} + \dots \\ \dots + \dfrac{b}{4} \cdot (\mathbf{cos}((1,2c\alpha) - 1)),\ \alpha = \left[0 \dots \dfrac{3\pi}{2c}\right] \\ r_0 + \dfrac{b \cdot \mathbf{cos}(1,5c\alpha)}{1 + 300c(2\pi - \alpha)^{\sqrt{1,5c}}},\ \alpha = \left[\dfrac{3\pi}{2c}(\dots 2\pi)\right] \\ r_0, otherwise \end{cases} \tag{3.10}$$

In this equation the parameters b and c do not describe the width and depth directly, so a trial and error method must be used to adjust these parameters to observed deformations.

In the following, a buckling is simulated on the low voltage winding of the main test object in this work (T3 Buran) in order to investigate influence of capacitive and inductive parameters. The depth of this buckling is equal to the available space for an inward radial deformation of the LV-winding, and this is approximately 2 cm (8,9% of the radius of the winding).

3.6.3 Inductance contributions of buckling

The double-integral for mutual inductance in eq. (F.9) is solved according to fig. 3.15.

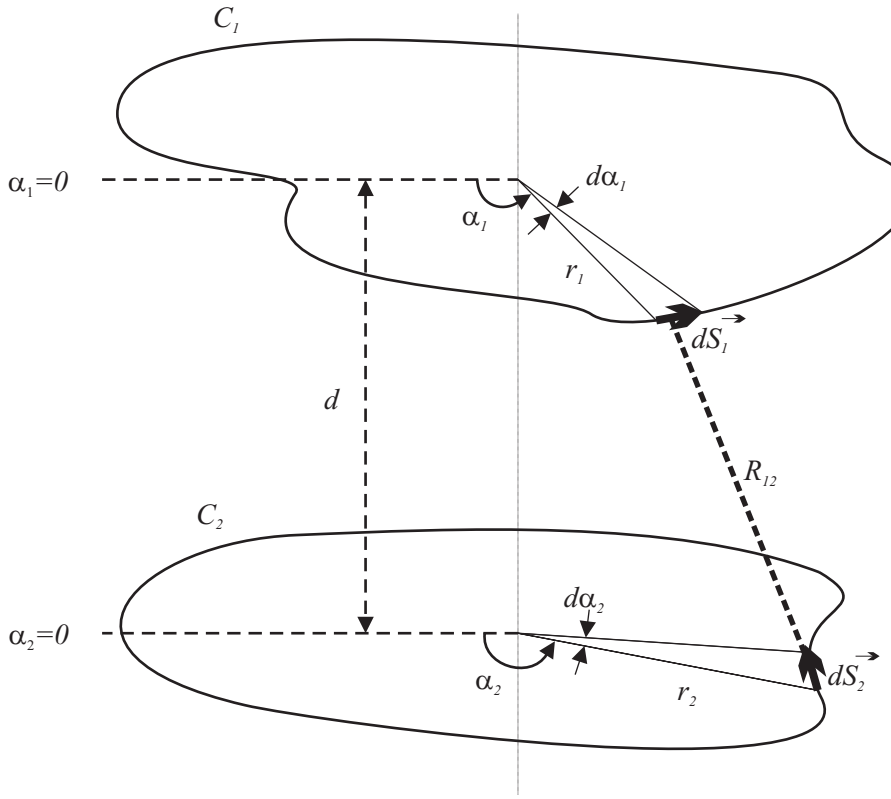

Figure 3.15: Parallel conducting filaments having an arbitrary path of circumference/radius.

It must be noted that the mutual inductance established using these relations are overestimated when the cross-sectional dimensions of the coils are considerable compared to the axial distance between them (due to internal leakage inductance). The distance between the two elementary filaments, is given by eq. (3.11):

$$R_{12} = \sqrt{r_1(\alpha_1)^2 + r_2(\alpha_2)^2 - 2 \cdot r_1(\alpha_1) \cdot r_2(\alpha_2) \cdot \mathbf{cos}(\alpha_1 - \alpha_2) + d^2} \tag{3.11}$$

As an initial approximation for modeling buckled windings, eq. (F.9) in appendix F is analysed numerically. It is implemented by means of a summation with a sufficiently small subdivision as shown in eq. (3.12):

$$M_{12} = \frac{\mu_0}{4\pi} \sum_{\alpha_1 = 0}^{2\pi} \sum_{\alpha_2 = 0}^{2\pi} \frac{r_1(\alpha_1) r_2(\alpha_2) \cos(\alpha_1 - \alpha_2)}{R_{12}(\alpha_1, \alpha_2)} \cdot \Delta\alpha_1 \Delta\alpha_2 \qquad (3.12)$$

The self inductance of buckled windings is calculated with the same equation as for mutual inductance, using the approach shown in appendix F (eq. (F.4) and fig. F.1).

The influence of buckling is also investigated by means of a 3D FEM-model with the transformer tank as boundaries. This leads to a smaller value for the inductance than the value computed using analytical formulas since they are based on an infinite space. But in this case the main prupose is to determine the change in inductance due to the buckling to see if it can be neglected compared to the capacitance. A visualization of the surrounding field from such a solution is shown in fig. 3.16

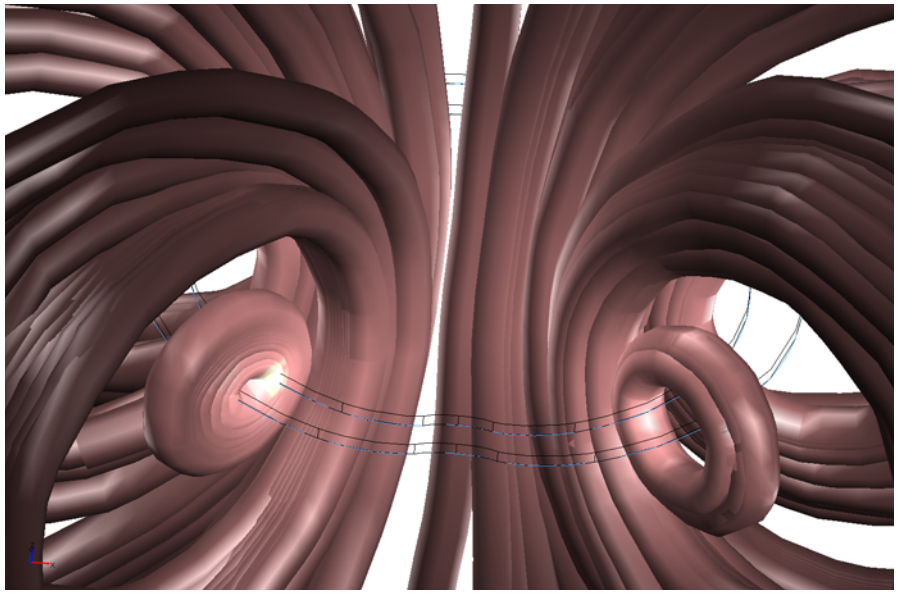

Figure 3.16: FEM-model for investigation of the 3D-influence of forced mode buckling on the inductance.

The FEM model with and without buckling shows a difference of less than 1%. This must be compared to the difference related to change in capacitance in order to utilize or reject this result for the investigation of buckling on the transfer function. Being able to neglect the influence of the inductance is desirable since it

reduces the complexity of the computation. This simplification can be applied if the change in capacitance is much larger than the change in inductance.

3.6.4 Influence of buckling on capacitance

The analytical calculation of capacitance is done by employing the classical analytical formula for capacitance between cylindrical electrodes as given in eq. (F.27) (in appendix F). The radius for the winding is obtained from the formulas given in eq. (3.9) or (3.10).

$$C_i = \sum_{\alpha = 0}^{2\pi} \left(\frac{2\pi\varepsilon_0\varepsilon_r}{\ln\left(\frac{r_o(\alpha)}{r_i(\alpha)}\right)} \right) \cdot \Delta\alpha \qquad (3.13)$$

The same formula is used for the calculation both inside and outside the buckled winding (from winding to ground and between windings). $\Delta\alpha$ is the fraction of the geometry under investigation.

The two different modes of buckling (free and forced) are assumed to have different influence on the capacitance. This is investigated to find correctional terms to use in the model. Buckling usually occur on the inner winding since it is this winding that experience the compression stresses.

- Forced mode buckling:

This mode results in an increase of the capacitance to ground and a decrease of the capacitance to the outer winding. One segment between two spacers are bent inwards towards the core at a radial depth equal to the available space for deformation (into the inner pressboard cylinder; equal to a depth of 2 cm).

- Free mode buckling:

The free mode results in a deformed shape related to an instability of the winding since the radial force is distributed unevenly around the circumference of the core. One part of the winding is moved towards the core and one part towards the outer winding, resulting in an increase of both capacitances.

A FEM simulation is established for a forced buckling in order to estimate the change in capacitance accurately, since details of the insulation structure can be included:

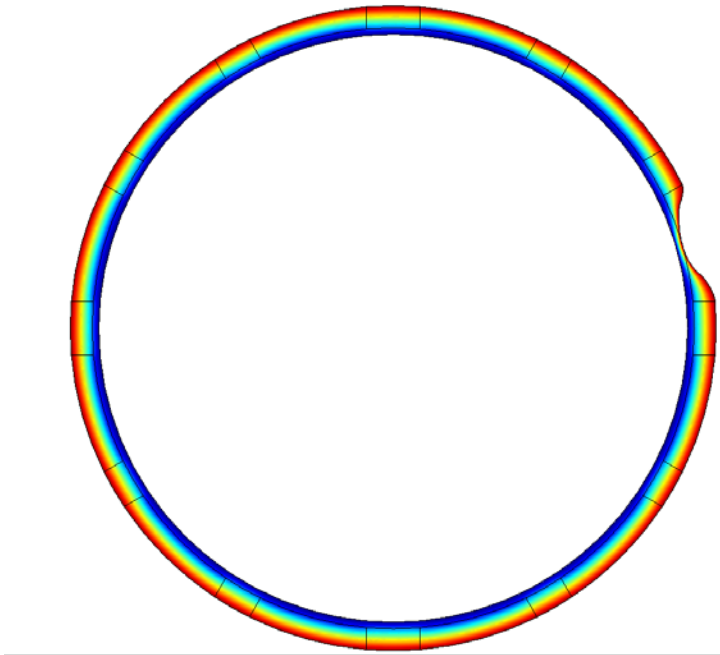

Figure 3.17: FEM-model of electric potential between core an LV-winding with forced buckling between two supports

When comparing to FEM, the difference in capacitance with/without buckling is over 10%. This is one decade more than the influence of the inductance, which enables the possibility to neglect the influence of the inductance.

3.6.5 Comparison of influence

The buckling influence on capacitance and inductance is computed using different techniques. The depth of the forced mode (inward) buckling is the maximum available space for deformation: Results are summarized in table 3.2 .

Table 3.2: Comparison of influence due to buckling deformations on the LV-winding (change in %)

Change in %	Inductance (Self/Mutual)		Capacitance (inner/outer)	
Method	3D FEM	Eq. (3.12)	2D FEM	Eq. (3.13)
Free mode	-0.37/-1.1	+1.2/-0.03	+4.5/+3.9	+2.95/+2.78
Forced mode	-0.99/-2	-0.92/-0.56	+10.6/-1.7	+9/-1.5

The series capacitance is assumed unchanged. What is shown here is the shunt capacitance from LV-winding to ground (inner) and between LV and HV (outer).

It can clearly be seen that the capacitance to ground is much more influenced by the buckling than the inductance, and this confirms the validity of neglecting the inductance for convenience when modeling buckling.

The difference between FEM and analytical calculation for the capacitance calculation, is due to additional details of the insulation included in the FEM-calculations.

Regarding the inductance, the differences between FEM- and analytical computations are mostly due to the difference in boundary conditions. The FEM-calculations in this case, are limited to the tank of T3 Buran, while the analytical formula assumes free space (no boundaries). There are also differences in the inductances for the free mode buckling since the exact geometry compared to the analytical formula could not be modelled.

Influence on losses due to buckling is not considered. Rahimpour [1] report a change in losses due to buckling. This is not consistent with the findings above. If change in self and mutual inductance is very small, it means that the flux is unchanged and then the proximity losses should also be unchanged. From his measurements, it can be observed that the amplitude of the resonant peaks is changed at radial deformations which indicate a change in damping/losses. In addition there seems to be a shift in frequency which indicate a change in capacitance (or inductance). A 3D FEM calculation revealed no change in proximity losses at forced mode buckling.

3.7 Results and discussion

Simulations and measurements are compared in order to assess the accuracy and errors made by employing analytical formulations for the elementary parameters.

3.7.1 Analytical model of a simplified geometry

The first attempt of analytical modeling was done by making use of the results of Rahimpour [1], [2]-[4] and his simplified geometries (uniform and coreless), since his work gains distinction compared to others for the high degree of resemblence between model results and measurements. His results of the admittance from the terminal to the neutral is shown in fig. 3.18 to emphasize the conformity between model and measurement.

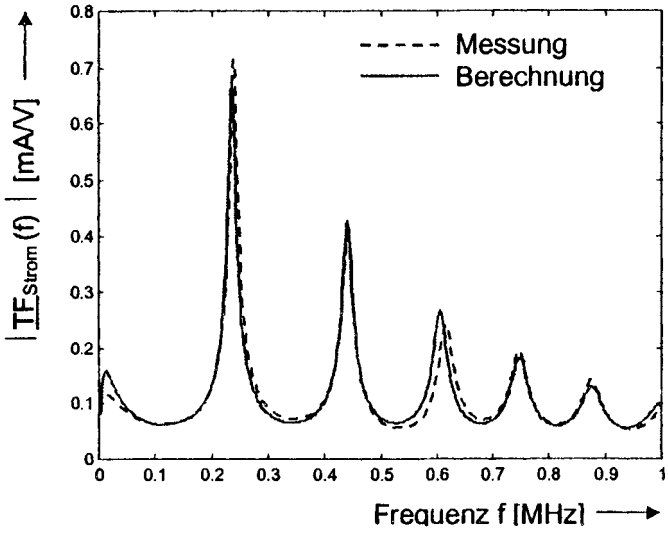

Figure 3.18: Measured and simulated transfer admittance from terminal to neutral for test-object #1 in the work of Rahimpour [1]

A fairly reasonable agreement was possible only after large adjustments of the series- and shunt losses (see fig. 3.19).

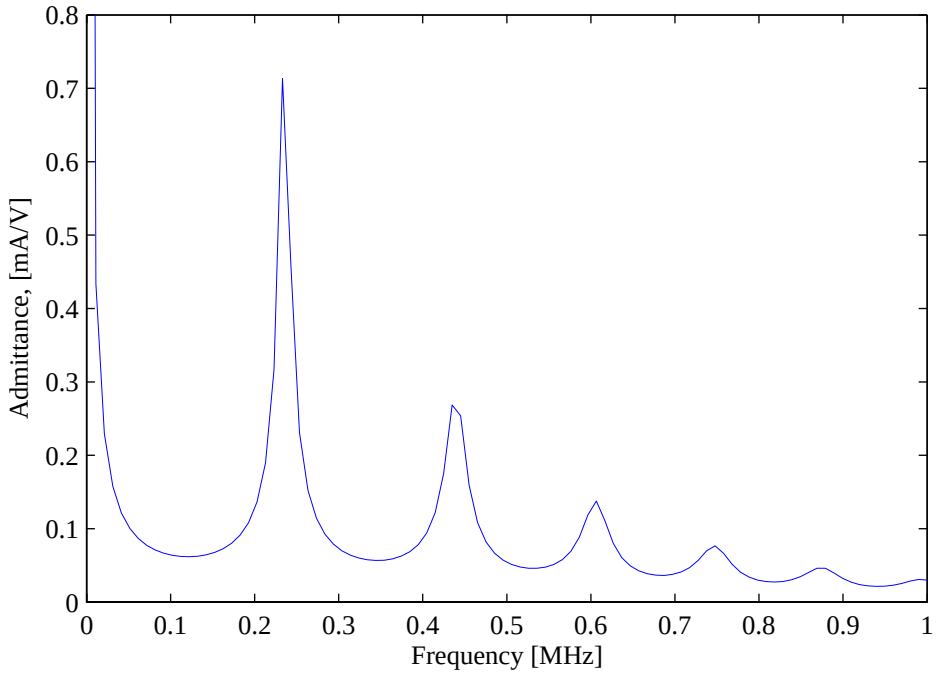

Figure 3.19: Simulation established in this work to compare with the results of Rahimpour [1] (fig. 3.18)

There is a significant difference at low frequencies due to the DC-resistance of the winding (and measurement-setup). The measurements performed by Rahimpour include a high pass filter since the LVI (Low Voltage Impulse)-method is employed. The establishing of transfer functions is based on the ratio between two fourier transformed time-series, and in order to cancel low-frequency problems, high pass-filters are usually used. They represent high impedance at frequencies below the filter cut-off frequency and the admittance approach zero.

Since agreement with measurements was not possible without adjusting the parameters (losses), the outlook for an analytical approach to a complex geometry is not the best. Still an attempt is proceeded since the necessary computer-code is already established.

3.7.2 Analytical model of T3 Buran

The next step was to use this method on the main test-object of this work. The geometry is more complex since it is non-uniform and it has a regulation-winding. Results and comparisons are shown in the following pages (measurements on the test-object are compared to simulations).

The first result of the analytical model is the input admittance of the low voltage winding:

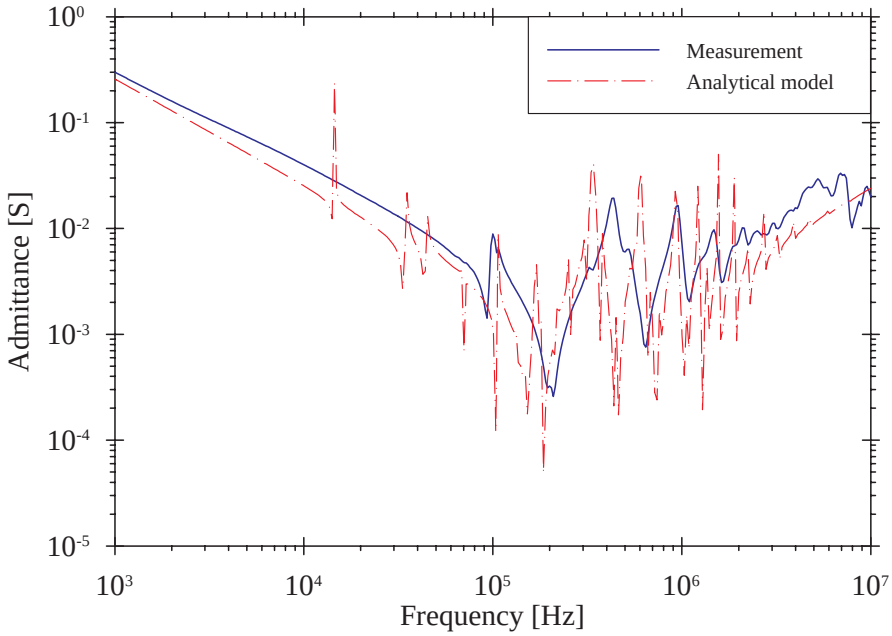

Figure 3.20: Comparison between analytical model and measurement of LV-winding input admittance

The immediate conclusion would be that the resemblence is quite poor. The general trends can be recognized, but the damping of the model is too low.

The low frequency response seems to be approximately the same. The difference here is attributed to the core influence at lower frequencies. Several resonances seem to occur where the measurement shows no sign of resonance. This indicates differences in the parameters of the modelled geometry compared to the real construction. The inductance representation will be different using analytical formulas compared to FEM-simulations where the tank wall can represent the boundary. This might improve the results.

Fig. 3.21 compares measured and calculated values of the input admittance of the high voltage winding:

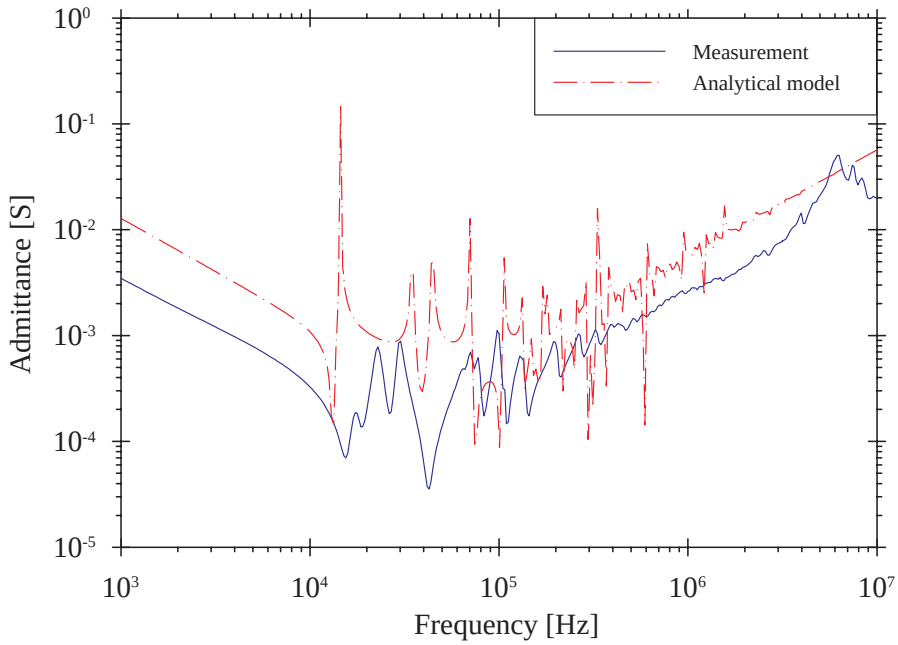

Figure 3.21: Measurement vs. analytical model of HV-winding input admittance

The resemblence for this result is even worse than for the LV-winding. The layout of the HV-winding is far more complex than for the LV-winding. It also incorporates the regulating-winding. There seems to be a constant deviation both at high and low frequencies, where the model overestimates the admittance. This means that the inductance is too low (almost a decade) at low frequencies, and the shunt admittance is also too high (possibly capacitance to surroundings; such as capacitance to ground and LV-winding). Stray capacitance from the tapchanger and the leads between the TC and the regulation winding is not included, but since these parts of the winding are close to the neutral (close to ground in this measurement), they will only have a minor influence.

The last result shown is the transfer function from HV- to LV-winding using the analytical model:

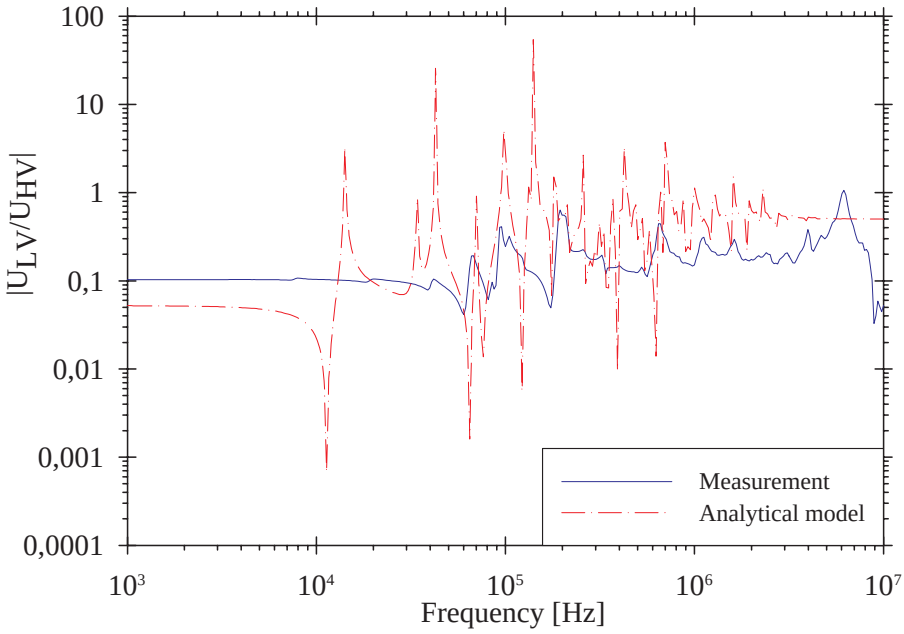

Figure 3.22: Transfer-function from HV to LV (analytical model)

As seen from the results and comparisons to measurements above, the accuracy of analytical modeling is not adequate in a real transformer geometry like the one utilized in this work. The difference from the first model (Rahimpour [2]-[4]), is that the geometry is complex and non-uniform. Neglecting the influence of the iron core is also questioned. The test-object has a regulating winding which complicates the modeling-process even further.

Proximity-losses were included an analytical approach [96], [97] where the magnetic field at all conductor surfaces were calculated by superposition as shown in chapter 3.4.2. This field strength was used to calculate the induced currents in each conductor/coil. The reflected resistance due to these eddy currents can then be calculated.

The large deviation at lower frequencies is caused by the lack of a proper low frequency core representation in the model. The leakage field at low frequency in a real transformer is mainly axial, while leakage field in an air-coil will be radial/ circular. This means that flux-linkage between distant elements, for instance discs in the upper and lower part of the winding will be much less in the model than for the real geometry (measurement). The transfer ratio for the air-core winding will thus be much lower.

3.8 Conclusions

Referring to hypothesis # 2, the utilization of a FEM-based software is expected to increase accuracy since geometry can be modelled more accurate. This would also make it possible to include other effects such as the proximity-effect directly on a more physical basis, since a proper representation of this effect is expected to create sufficient damping in the model.

Changes in inductance due to buckling can be neglected since influence is low (1 %) compared to the changes in capacitance (9-10 %). The change in capacitance is dependent on the relative change in distance between electrodes (winding to winding or winding to ground). The change in inductance due to buckling is dependent on the enclosed area of the winding segment, and therefore not as sensitive as the capacitance. Sensitivities to axial and radial deformations are not pursued further since coherence of model to measurements is low. Sensitivity analysis will be conducted when the obtained coherence is satisfactory.

The validity of neglecting capacitance when modeling axial displacement will be verified later.

Whether the core may be neglected or not, is also questioned.

4 FINITE ELEMENT METHOD

Hypothesis 2.: *Analytical methods are sufficient for simple/homogenous transformer geometries. A real transformer geometry complicates the analytical approach. Finite element methods would be an alternative for complex designs since details and variations may easily be included.*

The conclusion from chapter 3, indicate insufficiency of analytical methods for real transformer geometries. The move towards a FEM-based approach is expected to increase the resemblence between model and measurements.

4.1 Introduction

The finite element method is briefly described as a method where the problem is broken down to small pieces/elements, called a mesh. Once the mesh is obtained, approximations can be introduced for the dependent variables. As an example, the case of a single variable, u is given where the idea is to approximate u with a function that can be described with a finite number of parameters, the so-called degrees of freedom (DOF). The number of DOF's is depending on the order and number of mesh elements, and also the number of dependent variables. The upper limit for the number of DOF's will be given by the amount of memory and the time frame available for the calculation. The limiting step regarding the available memory is usually the LU-factorization/matrix-inversions.

The main challenge when modeling complex geometries is to keep the mesh-size on a reasonable level (so that the problem can be solved). These actions are described later. An accurate solution would require a 3D FEM-model, but this quickly leads to a non solvable problem. Therefore a 2D model using rotational/ axial symmetry is applied in order to be able to solve a complex geometry. Using axial symmetry in 2D results in only one dependent variable (the Vector Potential, A), while a 3D solution requires 3 dependent variables (the Magnetic Field in all directions: Hx, Hy, Hz).

The following shows basic formulas used when computing elementary magnetic and dielectric parameters (such as inductance and capacitance). A short introduction is also given to outline the computational demands when computing eddy currents in windings and laminations, but first a description of the software used is needed.

4.2 SUMER

SUMER is a specialized software developed by Electricite de France (EdF) [74], used to establish detailed high frequency power transformer models. It is based on the finite element method (FEM). It uses Flux2D [122] (as a pre-processor) for the construction of the geometry, and the generation of the mesh.

The software establishes a wide frequency range linear lumped model of the transformer, which can be used for lightning- and switching studies [123] as well as analysis of internal stresses or FRA sensitivity[124], [125].

A set of branch-matrices are calculated at a few discrete frequencies to incorporate the frequency-dependent features of the power transformer. A nodal model is then constructed and the eigenmodes and eigenfrequencies calculated by an iterative process (modal analysis). Once these data's are derived, a multipole equivalent is calculated. This equivalent is reduced to a terminal equivalent (a condensed admittance matrix). The reason for this is to make use of EMTP [126] as an interface for time-domain over-voltage studies in power networks. Once an EMTP-simulation is carried out at the terminals (transformer-network interaction), the internal voltages can be deduced from the full multipole equivalent (or the complete admittance matrix) by using a transfer matrix (between external and internal nodes) found in the modal analysis.

In order to have a reasonable mesh-size, the principle of an equivalent complex permeability [120] is applied to the complete winding geometry. The aim of this principle is to calculate the global flux through all electrical elements, without computing the eddy currents in the conductors. The conductor material is substituted with a non-conductive ferromagnetic material (featuring an elliptical hysteresis loop expressed by a complex permeability), which results in the same active and reactive power for a given geometry. This results in an accurate representation of the proximity effects within the winding structure, even with a coarse mesh compared to the skin depth in copper at high frequencies. The complex permeability approach is explained further in chapter 4.4.3, and the analytical basis for this principle is elucidated in chapter 5.2.

Detailed information regarding SUMER (features and limitations) can be found in Appendix B: “Modeling in SUMER” on page 208.

4.3 Alternative software

There are several alternatives to SUMER. The disadvantage is that these are general FEM-softwares with no automation specially made for giving transformer geometries.

FEMLAB [127] is a tool that is integrated with MATLAB [128] and this gives superiour possibilities of making “scripts” for the generation of transformer geometries, since all functions of Femlab can be controlled from matlab-code.

FEMLAB is used as a supporting tool throughout this work. A brief description is given in appendix H on page 213.

4.4 Parameter calculation

In SUMER separate models are established for the electrostatic and magnetostatic calculation. The electrostatic model incorporates more details and thus a denser mesh. Since the electrostatic model is solved at very few frequencies (1-3), and the magnetostatic model is solved at up to ten different frequencies, considerable time can be saved during parameter calculation by using two different models in spite of the extra time spent on modeling two geometries.

The two models can be combined (not in SUMER though) if the mesh size of the dielectric model can be reduced. This might be possible for EHV-transformers where the insulation thickness is large compared to transformers for lower voltages.

Complex frequency-dependent parameters are used in order to calculate simultaneously the inductance and losses for the magnetostatic model and capacitance and dielectric losses for the electrostatic model.

All matrices are symmetrical and only upper or lower part has to be computed in order to save time. Numerical inaccuracies could be reduced by computing the full matrix and then apply a symmetrization (by averaging), but since computation time is doubled it is not done here.

4.4.1 Inductance and resistance

When solving magnetic problems in FEM, the vector potential formulation is preferable, since this potential can easily be related to both flux and magnetic energy. Maxwell’s fourth equation states the fact that the flux density is divergence-free. The vector potential is chosen so that:

$$B = \nabla \times A \text{ which fulfils } \nabla \cdot (\nabla \times A) = 0 \tag{4.1}$$

By integrating the vector potential across the conductor's cross-section as in eq. (4.2), the average complex flux can be obtained, in order to find the mutual- or self-inductances/losses [120]. From this flux, it is possible to find the reflected

inductance and losses attributed to the windings (as seen from the terminals), and then represent these as series elements in a linear lumped model. These series elements will be frequency dependent due to skin- and proximity effect.

The average complex flux flowing through an element j, can be found by applying:

$$\varphi_j^* = \frac{1}{S_j}\int_{s_j}\int \vec{A} \cdot d\vec{S} \tag{4.2}$$

The mutual flux linkage between elements i carrying a current I_i and element j where $I_j = 0$ can be found as shown below:

$$\Phi_j^* = n_j\varphi_j^* = \left(-L_{ij} + j \cdot \frac{R_{ij}}{\omega}\right) \cdot I_i \tag{4.3}$$

The reflected inductance and resistance due to the core can according to [120] then be found by:

$$L_{ij} = -n_i n_j Re(\varphi_j^*)/I_i \tag{4.4}$$

$$R_{ij} = \omega n_i n_j Im(\varphi_j^*)/I_i \tag{4.5}$$

where n_i and n_j are the number of turns in element i and j respectively.

Using the approach in eq. (4.2) results in a low degree of accuracy when the mesh is coarse, due to the limited area/number of elements of the surface integral. In a transformer-model the mesh must be coarse to be kept at a reasonable/solvable size. Therefore the magnetic energy should be used instead. The advantage of considering the magnetic energy, is that the energy is stored in the complete geometry and errors due to a coarse mesh inside and around the conductor is averaged/minimised.

Self-inductance and resistance can be described as:

$$L_{ii} = 2 \cdot \frac{n_i^2 \cdot Re\{W_{mag,ii}\}}{I_{ii}^2} \tag{4.6}$$

$$R_{ii} = 2 \cdot \frac{n_i^2 \cdot \omega \cdot Im\{W_{mag,ii}\}}{I_{ii}^2} \tag{4.7}$$

Mutual inductance and resistance is calculated employing the parameters established in eq. (4.6) and (4.7), and an additional solution where current is applied to both elements.

$$M_{ij} = \frac{n_i \cdot n_j \cdot Re\{W_{mag,ij}\} - \frac{1}{2}L_{ii} \cdot I_i^2 - \frac{1}{2}L_{jj} \cdot I_j^2}{I_i \cdot I_j} \tag{4.8}$$

$$R_{ij} = \frac{n_i \cdot n_j \cdot \omega \cdot Im\{W_{mag,ij}\} - \frac{1}{2}R_{ii} \cdot I_i^2 - \frac{1}{2}R_{jj} \cdot I_j^2}{I_i \cdot I_j} \tag{4.9}$$

Where $W_{mag,ij}$ is the total magnetic energy when current is applied to both coil i and j. L_{ii} and L_{jj} is calculated using eq. (4.6). The disadvantage of using the magnetic energy instead of the vector-potential/flux is that it requires more computations, and the integrals are performed over the entire geometry rather than the conductor. This leads to a significantly higher time-consumption as discussed in chapter 4.4.4. In the same way as for the complex flux, resistance and inductance can be derived from the real and imaginary part of the complex energy.

4.4.2 Capacitance and conductance

To calculate capacitance using FEM one usually integrate some of the parameters solved for in the model. The two parameters normally used are surface charge and electrostatic energy.

The capacitance between two electrodes can be found by calculating the surface charges on the electrodes divided by the voltage between them.

$$C = \frac{Q}{V} \tag{4.10}$$

The total charge on a surface is found by integrating the charge density on the surface:

$$Q = \int_S \vec{D} d\vec{S} \tag{4.11}$$

When calculating a capacitance matrix between a set of electrodes, equation 4.10 can be used to calculate the coefficients of the matrix as shown below.

$$C_{ij} = \frac{Q_j}{V_i} \tag{4.12}$$

Since the calculation of the total surface charge is based on a boundary integral, the accuracy is dependent on the subdivision/mesh on these boundaries. Similar to inductance-calculation, the capacitance can be computed more accurately by using the electrostatic energy W_{el} since this involves integrating over a subdomain rather than a boundary (more elements involved averages the errors).

$$W_{el} = \frac{1}{2}CV^2 \text{ or } C = 2 \cdot \frac{W_{el}}{V^2} \tag{4.13}$$

The self and mutual capacitances are calculated from the real part of the energy as shown below:

$$C_{ij} = \frac{Re\{W_{el,ij}\} - \frac{1}{2}V_i^2 c_{ii} - \frac{1}{2}V_j^2 c_{jj}}{V_i \cdot V_j} \tag{4.14}$$

$$C_{ii} = 2\frac{Re\{W_{el,ii}\}}{V_i^2} \tag{4.15}$$

$W_{el,ij}$ is the total electrostatic energy when both electrode i and j is energized, while $W_{el,ii}$ represents the electrostatic energy when electrode i is energized and all others are grounded. The dielectric losses are computed similarly to the capacitance by applying the imaginary part of the electrostatic energy, since the permittivity is defined by its relative (real) part and the loss factor (imaginary part).

4.4.3 Eddy currents

As outlined in chapter 3.4, eddy currents appear as soon as time-varying magnetic fields surrounds and penetrate conducting parts such as conductors, core, supports, tank etc. The penetration is highly frequency-dependent and at high frequencies, penetration is very low. The depth of penetration is defined as the skin-depth:

$$\delta = \sqrt{\frac{2}{\omega\mu\sigma}} \tag{4.16}$$

This is where the penetrating field or current is reduced to 37% (e^{-1}) as illustrated in fig. 4.1.

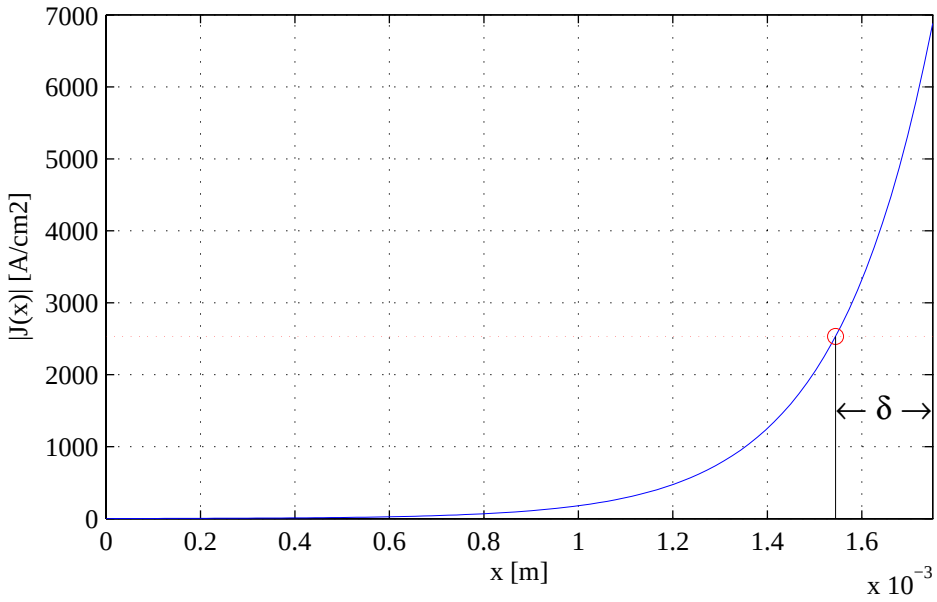

Figure 4.1: Current distribution and skin-depth at 100 kHz in a typical strand for power transformers

Fig 4.1 shows the current distribution due to the skin-effect in a single strand at 100 kHz. Only half of the strand is shown due to symmetry. The conductor surface is to the right in the figure and x=0 is in the middle of the strand.

In a real transformer, the geometry is complex. It usually incorporates several hundreds of geometrical groups/objects (such as discs). If modeling the geometry on a turn to turn basis, the number of geometrical objects will exceed several thousands. Considering this together with the fact that current flows close to the surface at high frequencies, requires a very dense mesh. This results in a mesh size in the complete model that will be impossible to handle, even for super-computers. Consequently, approximations are required in order to handle frequency-dependent effects accurately and efficiently. One approach is to use a frequency-dependent complex permeability as outlined in chapter 4.2 for handling of proximity effects. Skin-effect can be represented analytically, ref. eq. (3.8) assuming these two effects can be superimposed.

The above challenges are illustrated with a simple example where a single strand of a winding is modeled for skin-effect. In order to have an accurate model, the number of elements in the mesh across the skin-depth should be at least two (higher order elements). Since we are interested in the current distribution up to at least 1MHz, the discretisation/element-size on the boundary should be half of the skin-depth at this frequency. The skin-depth in copper at 1 MHz is $65\,\mu m$. With a single strand measuring 3,2x13,2mm, the boundary will be divided into over 1000

segments. A dense mesh is not needed in the internals of the strand so a growth-factor is specified for the mesh, resulting in 32.000 elements inside the strand.

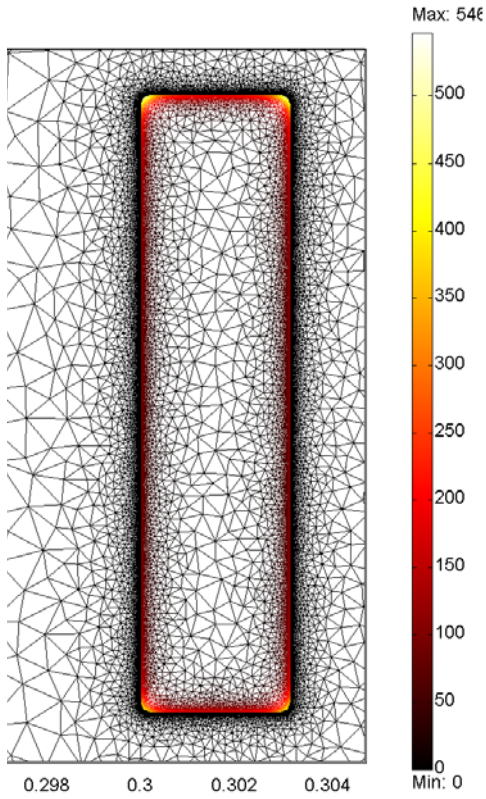

Figure 4.2: Current density in a Finite Element Model of single strand applied to skin-effect investigations at 100 kHz.

As seen from fig. 4.2, the mesh needs to be very dense in order to represent the current distribution/skin-effect correctly at higher frequencies. The total number of elements needed inside the strand is very high and since the upper practical limit for the complete model will be in the area of 200-400.000 elements, it is clearly stated that eddy current influence must be represented by approximations. These approximations must be accurate and at the same time solver-efficient (reducing the mesh size considerably). This is the main purpose of using the complex permeability representation of eddy currents.

As mentioned, the complex permeability approach substitutes the conductor material with an isotropic, non-conducting, ferromagnetic material having a complex permeability (equal to a material having hysteresis loss, ref. fig. 4.3).

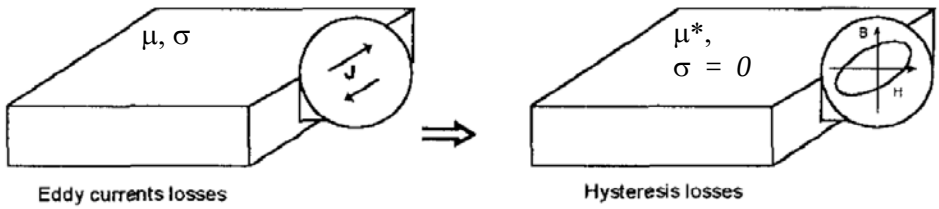

Figure 4.3: Principle of the complex permeability representation of eddy currents [120]

The complex permeability of this equivalent material is deduced from the analytical solution of the internal magnetic field (and thus the current distribution) as a function of frequency, given the external field. The external field is decomposed as shown in fig.4.4 and the two different components of induced currents are assumed independent.

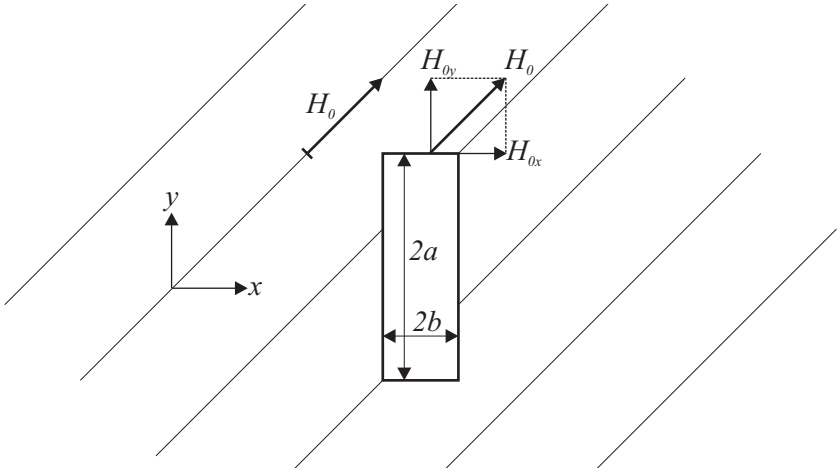

Figure 4.4: Decomposition of the external magnetic field (H_0), where $2a$ and $2b$ is the conductor height and width respectively

A complex permeability is derived for both x- and y-direction independently. The complex permeability represents both the displacement of the flux and the eddy-current losses in the material. A lumped element (several turns or discs) can be modeled as a solid isotropic material incorporating the eddy currents termed by the dimensions of the strands and the applied field, and of course the insulation thickness between strands, as shown by Moreau et al. [120]. The result is an accurate approximation identified by a coarse mesh, which is solvable even for a complete and complicated transformer geometry.

The internal magnetic field using this approach will not be identical to the original field, but losses and flux displacement observed externally will be approximately the same. The principle of complex permeability is explained in detail in chapter 5 since it is also used to implement the core into the model.

4.4.4 Time consumption

Establishing inductances by integrating the vector-potential across the conductors cross-section and capacitances by integrating the charge-density on the surfaces, is time efficient. Assuming a system of n branches, these methods establish one row including the diagonal element in each solution (requiring n integrals per solution). The total number of operations will then be: n FEM-solutions and $(n^2 + n)/2$ integrals.

When employing the electrostatic and magnetostatic energies into the parameter calculation, the number of operations increases severely. The number of solutions increase to the number of integrals; $(n^2 + n)/2$. And since the integral now is computed across the complete geometry, it will also be more time-consuming compared to the integral in the previous method. Establishing one matrix at one frequency may take from 20 min. up to several hours. This adds up to a time consumption for the whole model in the range of a few hours to a day. Still most of the time is spent interpreting constructional drawings and entering the geometry into the software.

The structure of this computation is well suited for parallel computation since up to ten solutions is computed on the same geometry at different frequencies. Utilizing a low-end cluster (one ordinary computer for each frequency to be calculated) would improve efficiency of the computations severely without increasing the cost significantly (only demand is memory). The cluster network does not need to be a high capacity LAN, since this is not a critical component in this application (as opposed to real cluster computers), but 64 bits computers are preferred for memory-reasons.

4.5 Results

Two different geometries were modeled in SUMER. The first one is a simplified reduced scale geometry, while the other one is the main test-object specified in chapter 1.4 (T3 Buran).

4.5.1 Simplified geometry

The first model established using SUMER is based on a geometry specified in a diploma project [129] at NTNU. This is a simplified and reduced scale model assembled to study influence of axial and radial displacements. Specifications for this geometry is given in appendix I. Since this geometry is homogenous and simplified it is well suited to establish an initial model in short time. The reduced scale model had a 4-layer outer winding and a 2-layer inner winding, each layer

counting 250 turns. In the model each electrical element represented 25 turns (each layer is divided into 10 equal parts). This coarse division might represents errors since one electrical element spreads out over a relatively large distance compared to the dimensions of the total geometry. When assembling the geometry, core effects are neglected in agreement with hypothesis number 3 and the core/tank is represented with a metallic tank in order to have a defined capacitance to ground.

Fig. 4.3 shows a comparison of the transfer function (voltage ratio from HV to LV-winding) between a measurement and the model established in SUMER:

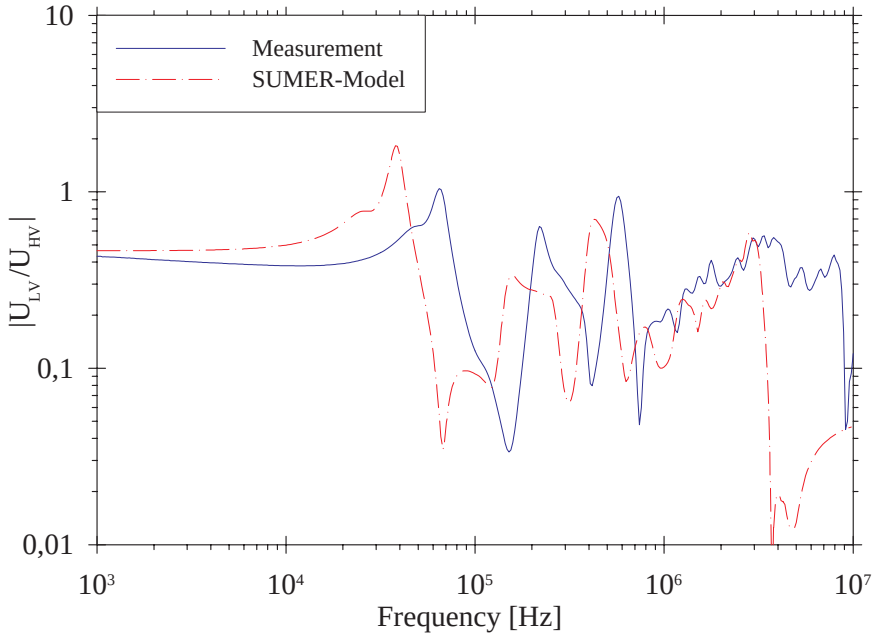

Figure 4.5: Comparison between SUMER-model and measurement

The differences between model and measurements are probably due to the coarse electrical mesh used (25 turns per lumped element) and possible eddy current effects in the tank- and core-equivalent. The general shape of the curves are similar but the model seems to have higher series capacitance since the curve is moved horizontally to the left. Since the layer windings are made by circular enamelled (thin insulation coating) conductors, the series capacitance has to be approximated. This approximation might lead to an inaccuracy. The representation of the losses seems to be ok. Next, measurements are compared to the model when applying axial displacement.

Fig. 4.6 show measurements when axial displacement of 1-10mm are applied to the inner winding:

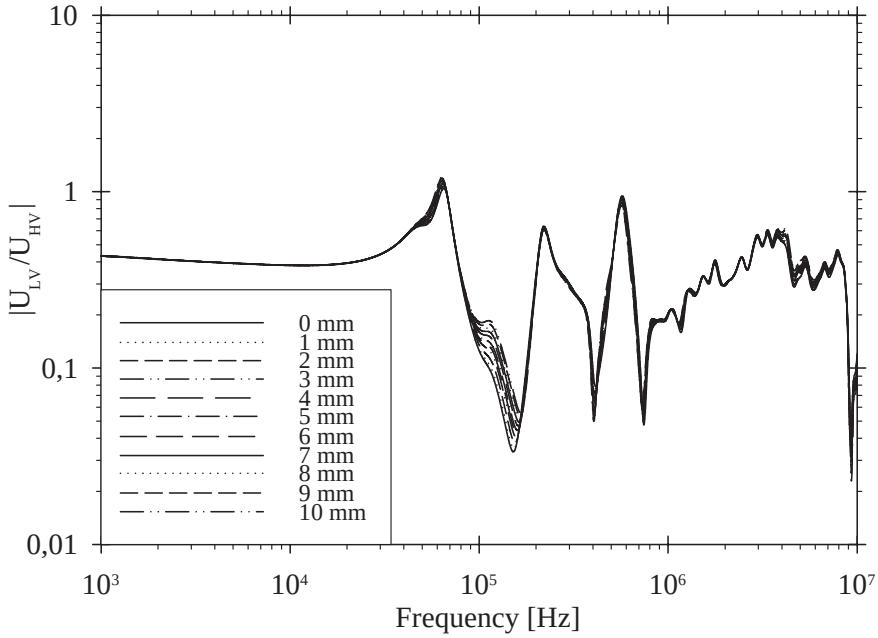

Figure 4.6: Measured transfer-function for simplified geometry at axial displ.

An interesting observation is the very localized change in transfer-function due to the displacement. The same effect can be seen in the SUMER-model in fig. 4.7:

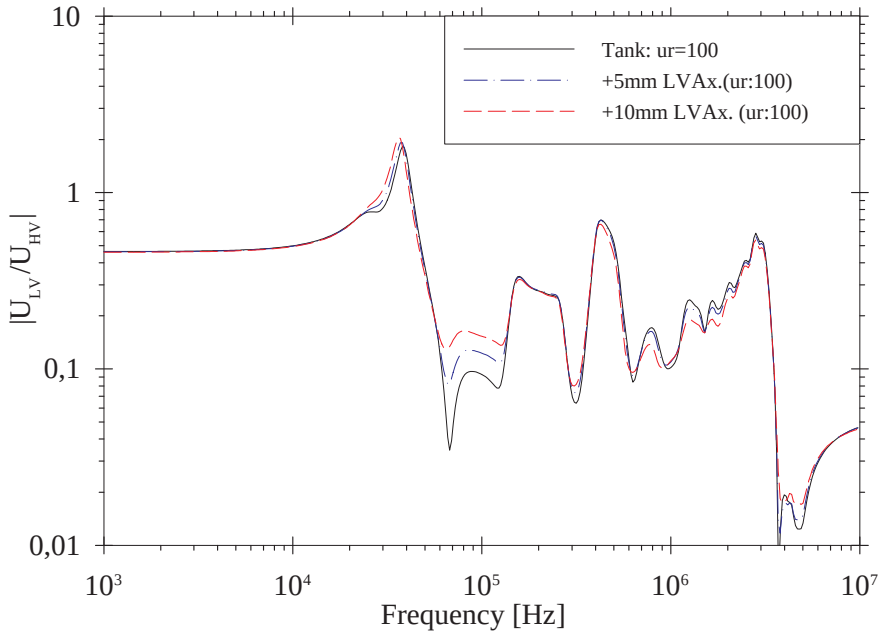

Figure 4.7: Calculated TF for simplified geometry at axial displ. of 5 and 10 mm and a tank permeability of 100

The changes due to the deformations occur in the same frequency-range as for the measurements.

Forced mode buckling are also investigated by measurements using this geometry without any change in FRA signature [129]. This is attributed to the unrealistic design of the winding compared to real designs, since available space for buckling deformation is very small compared to the radius of the winding. In addition the buckling is achieved by slitting the cardboard cylinder inside the winding. This reduces the capacitance to core and the net change in capacitance is very small.

4.5.2 Main test object

With fairly reasonable agreement for the simplified geometry, modeling of the main test object (T3 Buran) is proceeded.

The upper part of the dielectric model is shown in figure 4.8.

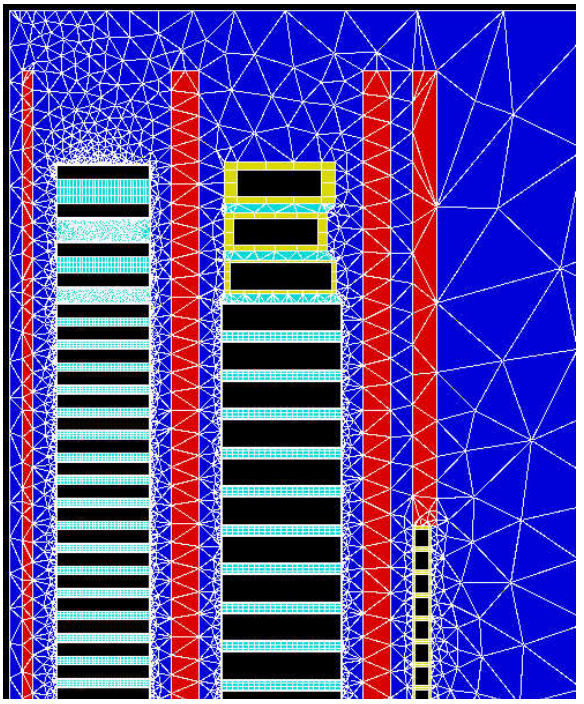

Figure 4.8: Dielectric model (upper part) in SUMER of T3 Buran

As seen from fig. 4.8 the mesh is very dense in the zones close to the winding. The reason for this is that the paper is also modeled and since this usually is quite thin, it is represented by very small elements. To improve efficiency of the simulations, the paper in thin zones can be neglected or included in composite structures (such as interdisc insulation). A new material is defined between the discs which represents the composition of combined materials. Pressboard cylinders and axial strips between windings are joined into cylinders. These cylinders are placed in the middle of each duct to be able to control the mesh.

The main idea of the magnetic model in SUMER is that the core displaces all flux above a certain frequency (1-10kHz) and that the core leg, yokes, and tank are used as boundaries of the problem formulation as shown in fig. 4.9:

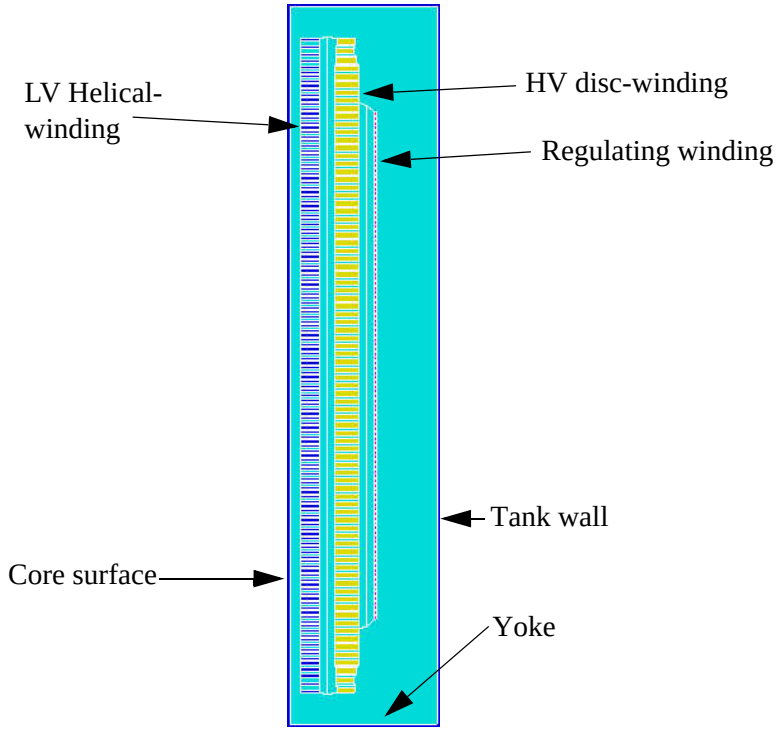

Figure 4.9: Complete magnetic model in SUMER of T3 Buran

The result of this first real transformer SUMER-model is shown in fig. 4.10. The large differences can clearly be seen, and the admittances are not presented since coherence did not increase significantly compared to the analytical approach used in chapter 3. The large difference at low frequencies must entirely be attributed to the common coupling in the core.

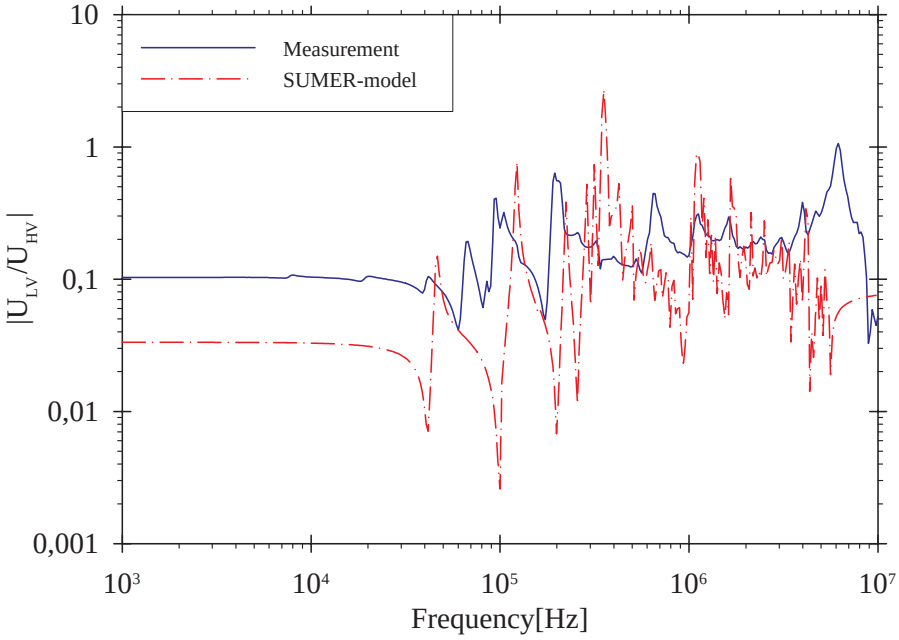

Figure 4.10: Initial SUMER-model of the main test object, T3 Buran

A large difference from the analytical result in fig. 3.22 is the location of the first resonance. In the analytical approach (fig. 3.22) the first resonance occurs at approximately 10-12 kHz, but in the SUMER-model in fig. 4.10 the first resonance is found at 35 kHz. The reason for this is probably the difference in the boundaries of the magnetic model. In the SUMER-model, the boundaries are defined by the tank wall and the core surface, but the analytical approach is based on an infinite domain definition. The available volume for the stored magnetic energy in a coil will be totally different in the two approaches. (The inductance is lower for the SUMER approach resulting in a higher frequency for the first resonance). In addition to this, the capacitances could be different in the two methods.

4.6 Discussion

When comparing analytical results to FEM-results, it is obvious that the resemblence is not increased significantly by the introduction of FEM, as stated in hypothesis 2.

The reduced scale model, shows reasonable resemblence between measured and simulated transfer function, but the main test object does not. The main difference between these geometries besides the complexity, is the lack of core in the reduced scale model. This emphasizes the need for detailed investigation of the core influence.

Originally, high frequency transformer models were based on a simplification that neglected the core. The reason for this partly being successful is that the calculated leakage inductance is fairly close to the actual value, and these models are applied to lightning impulse studies where the non-impulsed winding is grounded: This leads to a shielding of the flux from the core, with the result that coreless models could be used for modeling lightning impulse stresses during factory acceptance tests. At open terminals (for instance voltage ratio-measurements) this approach is questioned, and an iron core representation is probably needed. Still losses appear to be underestimated. Since skin and proximity losses seem to be accurately represented, the source of the missing losses must be either dielectric, core related or losses in the tank and auxiliary equipment surrounding the winding geometry.

The implementation of the winding geometry into the FEM software is very convenient and is therefore preferred.

4.7 Conclusions

The reduced scale model agrees well with the measurements, but the transfer function is shifted in frequency. This is probably due to a disagreement in the approximated series capacitance (circular conductors are represented with rectangular conductors). Losses seem to be properly represented. Further developments on this model were not proceeded, due to limitations in time spent at EdF's research department in Paris. Therefore the modeling was focused on the main test object (T3 Buran) in order to establish a more detailed model of this geometry.

As seen from the results in fig. 4.10, the losses (damping at resonance) of the model is insufficient compared to measurements. It can also be seen that the general coherence between measurement and model is still very low, but certain trends can be recognized.

It seems that the focus on the reduced scale model and the results of Rahimpour has concealed the importance of the core since both these designs are coreless based on the same assumption as hypothesis 3.

It is natural to investigate the influence of the core in the following, since the introduction of FEM did not increase coherence to measurements significantly.

The main conclusion at this point is to investigate the high frequency behaviour of the iron core and then implement these effects into the SUMER-model. Preferably by using a the same approximation as for winding proximity losses; A complex permeability representation of the core would keep mesh-size at a reasonable level and at the same time incorporate frequency-dependent iron losses. Transformer modeling using FEM is still desirable for reasons of conveniency, possible iron core representation and accuracy to winding details.

5 IRON CORE INFLUENCE

Hypothesis 3.: *Iron core can be neglected and considered to behave like a perfect conducting screen above 10 kHz.*

Using FEM to establish a detailed model did not increase coherence of models and measurements significantly. It is therefore natural to investigate prospective effects of the iron core at higher frequencies, both regarding losses and inductance.

It was originally assumed that the iron core could be neglected above a certain frequency since most literature supports this [109]-[111], [85]. Several methods include a core representation in time-domain in order to handle switching- and low frequency transients correctly, and a few methods, such as Fergestad/Henriksen [42] and Wilcox et al. [46], are reported to handle the iron core at high frequencies in the frequency-domain. Fergestad and Henriksen [42] proposed dealing with the common flux and the leakage flux separately. Measurements done by these authors showed that the leakage flux between single discs mounted on a core, is not very dependent on frequency in the limited range considered during impulse tests (50-200 kHz). The common flux however is highly frequency dependent, but this flux contributes to the same voltage induced in all turns and it is therefore the leakage inductance that is the determining factor for internal transients in transformer windings, at least when terminals are not floating/unloaded. The leakage field is however strongly dependent on the core leg (partial path in iron).

A complete, frequency-dependent (wide frequency-range) core-representation suitable for implementing into any FEM-based software is required. This chapter shows such an analytical description based on a physical implementation. Also a comparison to measurements on different iron cores is included in this chapter as well as an introduction of interlaminar effects. Interlaminar effects are not included in the complete model since it was discovered toward the end of this work, but considered as a possible explanation of different deviations in model and measurements.

5.1 Introduction

Iron losses have traditionally been the main focus for the constant development of electrical steel [130]. It has been estimated that some 5% of all electricity generated is dissipated as iron losses in electrical equipment [131]. Iron losses are generally made up of two main components at power frequency:

- Hysteresis loss
- Eddy current loss

Both these effects are strongly influenced by frequency and material parameters. In addition there are extra losses adding to the classical losses (calculated using classical theory on eddy-currents and hysteresis). One probable explanation is that these extra losses are eddy current losses due to domain wall movements during time-varying magnetization. These wall movements are not continuous, but rather step-wise (analogous to the relation between static and sliding friction). High frequency (impulse) eddy currents will be induced at every step movement [132], and this makes it more difficult to relate the losses to the applied field. This theory was initially suggested by Pry and Bean [133]. The time-constant of these step movements is unknown, but will be of importance if determining the upper frequency of contribution from these losses.

Only classical eddy currents are considered in this work. The high frequency model in this thesis use the initial permeability, referred to the slope of the initial part of the magnetization-curve. This excludes hysteretic losses from the model in the following. Lightning impulse tests done at full and reduced voltage indicate linearity [44] and thus no hysteresis and saturation at higher frequencies. Possible reasons are explained later.

Initial permeability of electrical steels is not included in standard material data, and must be estimated from measurements at low field strengths. It can be expressed as:

$$\mu_{ri} \cdot \mu_0 = \lim_{H \to 0} \left(\frac{B}{H} \right) \qquad (5.1)$$

An example of permeability dependency on field strength is shown in fig. 5.1
It is assumed that the iron behaves linearly rather than hysteretic in the initial part of the curve. The reason for this could be that a certain level of magnetization is needed to force non-reversible domain wall movements which is one of the main reasons for hysteretic behaviour of magnetic materials. Ferromagnetic materials are comprised of regions (known as magnetic domains), and within each of these regions the magnetic dipole moments are arranged in a common direction. When the material is not magnetized, it exhibits no net magnetic dipole moment, unless it possesses remanent flux.

Values between 50 [42], [43] and 800 [46] are used for the initial permeability for electrical steels, but this will be highly dependent on the type of material. Grain-oriented steel has highly increased permeability in the rolling direction and a lower permeability in the perpendicular direction. Measurements on non oriented SiFe alloys show an initial permeability between 150-500 [135], depending on the grain-size in the material.

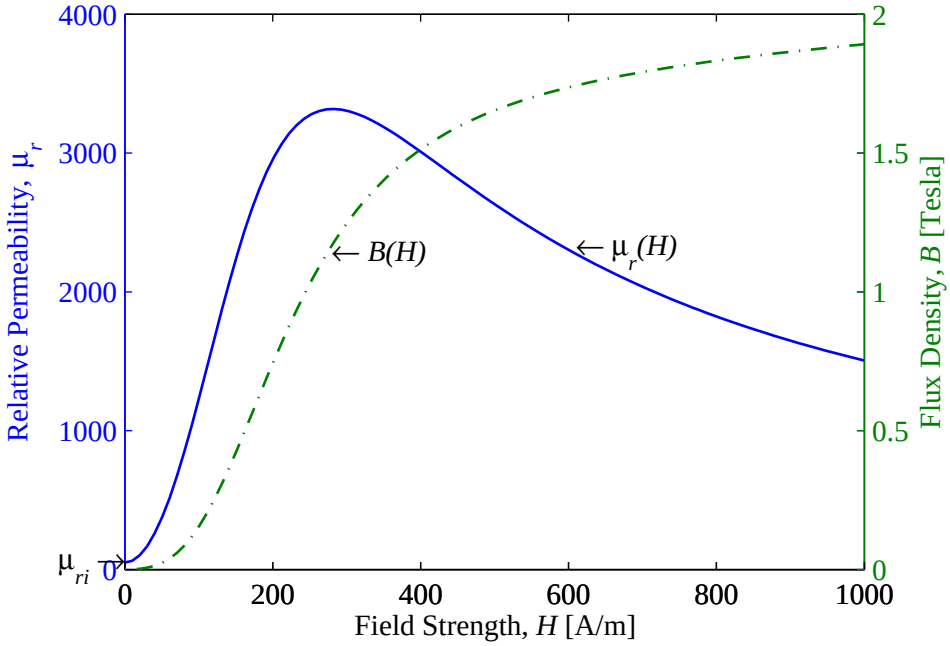

Figure 5.1: Example of initial magnetization-curve and field dependent permeability for iron

As shown in fig. 5.1, ferromagnetic materials have a highly nonlinear relation between the flux density *B*, and the field strength *H*. Fig. 5.1 shows the initial magnetization curve which excludes the influence of hysteresis. Ferromagnetic materials are also characterized by remanence and coercivity, where remanence describes the remanent flux density when the applied field is removed, and coercivity describes the field strength that needs to be applied to reduce (coerce) a remanent flux to zero.

There are usually 4 distinct regions in a magnetization curve like the H-B-curve in fig. 5.1. These can be explained in terms of changes to the materials magnetic domains:

1. A slow rise close to the origin due to “reversible growth” or stretching of the domains (initial permeability, μ_{ri}). No hysteresis in this zone.
2. A longer, fairly straight zone representing the “irreversible growth” or large domain wall movements which influence the hysteresis loss.

3. A slower rise representing “rotation” or the alignment of remaining non-aligned domains and dipoles.
4. An almost flat region corresponding to paramagnetic behaviour and then it approaches the slope of μ_0; The core can't handle any more flux growth and has saturated.

Neglecting the iron core will be valid at very high frequencies, where the flux is completely displaced from the core material, and only flows on the surface of the core, and in the cooling ducts. The main question is whether this can be assumed already at 10 kHz.

The iron losses are reported [136] to be the main damping mechanism for transients at some kHz. Above a few tens of kHz eddy current/proximity losses in the windings has been assumed to be the main source of loss [120]. For the high frequency model developed here, the only loss mechanism considered for the core is the eddy current loss due to flux penetration of the laminates. Additionally, influence of interlaminar effects are evaluated later in this chapter. Hysteresis is neglected since measurements indicate linearity and thus it is assumed that the iron is operated at its initial part of the magnetization-curve. Possible reasons are investigated in the following.

The frequency-range of interest for a high frequency transformer model is normally from the region around the first resonance and above. At the first resonance (half wave), the voltage to ground has its maximum amplitude in the middle of the winding. The total inductance of the winding oscillates with the shunt capacitance of the winding to the surroundings. The azimuthal/angular current (branch current) is largest at the terminals (assumed the neutral is grounded) and has a zero-point in the middle resulting in a magnetic field as shown in fig 5.2:

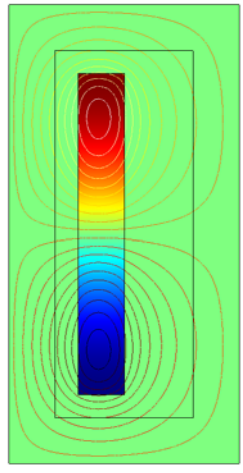

Figure 5.2: Pattern of leakage flux and current density in terms of color at first resonance. Common flux is not shown

Since effective permeability is now assumed to be much larger than in oil, the oil gap is determining for the total magnetic leakage field linking the iron. With the oil gap (core window), this field strength will be low. In addition to this, the high frequency transformer model will be compared with SFRA measurements, also facilitating the use of a linear low permeability representation of the core, since the SFRA-method uses a very low voltage for the applied signal.

Regarding the common flux, the most important reason for the low induction in the iron core at higher frequencies is explained by Faraday's induction law:

$$v \approx N \cdot \frac{d\phi}{dt} \tag{5.2}$$

where v is the voltage applied to the winding, N is the number of turns in the energizing winding and ϕ is the total flux per turn in the core. If assuming a sinusoidal flux, it will be expressed by:

$$\phi(t) = \hat{\phi} \cdot sin(\omega t) \; and \; \frac{d\phi}{dt} = \omega \cdot \hat{\phi} \cdot cos(\omega t) \tag{5.3}$$

giving the following relation for the total flux linkage:

$$\hat{\Phi} = N \cdot \hat{\phi} \sim \frac{v}{\omega} \tag{5.4}$$

This shows that the core flux is reduced at increasing frequencies. The core induction at 50 kHz will be 0.1% of the power frequency induction if the volts/turn is assumed constant along the winding. The same relation is used to avoid saturation during induced AC voltage withstand tests on transformers with grounded neutral (ACSD) [137] (by increasing the frequency of the applied voltage).

This altogether substantiate the use of a non-hysteretic low permeability for the iron core, because the induction of the core is very low and then the permeability will be in its initial zone (B-H-relation). Since hysteresis loss is attributed to the domain wall movements, it can be neglected at very low core induction. The time-constant of these movements is also important at higher frequencies. At sufficiently high frequency the movements will start lagging the magnetic field and finally no movements will occur.

Admittance measurements between outer legs/phases of different transformers, show inductive behaviour up to several tens of kHz. It is therefore believed that the core also has some influence well above 10-30 kHz in spite of the fact that published literature (for instance [109]-[111]) totally neglects the influence of the core above 10 kHz. This widespread assumption has probably arisen from the fact that non-impulsed windings are short-circuited and grounded during standard impulse tests, which reduces the core influence. Another reason might be the convenience of excluding the core from the model and turning to air-core-theory.

5.2 One dimensional approximation

The purpose of these analytical steps is to determine the equivalent complex permeability as a function of frequency, field intensity, material and dimensions, as outlined in chapter 4.4.3. This permeability is obtained by determining the average of the complex field penetration/core reaction (including eddy current losses). The conducting, laminated core is replaced by a non-conducting, solid core where core reaction and losses are represented by the equivalent complex permeability obtained analytically. This means that the eddy current losses in the laminated, conducting core is represented as linear hysteresis loss in a solid, ferromagnetic non-conducting core.

This enables the users of FEM-programs to take into account frequency dependent eddy current losses and core flux penetration (inductance variation) without using the vast number of elements normally needed at high frequencies in such calculations. A solid core representation is very convenient in order to make use of an axisymmetric model.

The first part is the description and limitation of the model as outlined below. This is a classical situation used in many textbooks on electromagnetic field-theory, see for instance: [138], [139]:

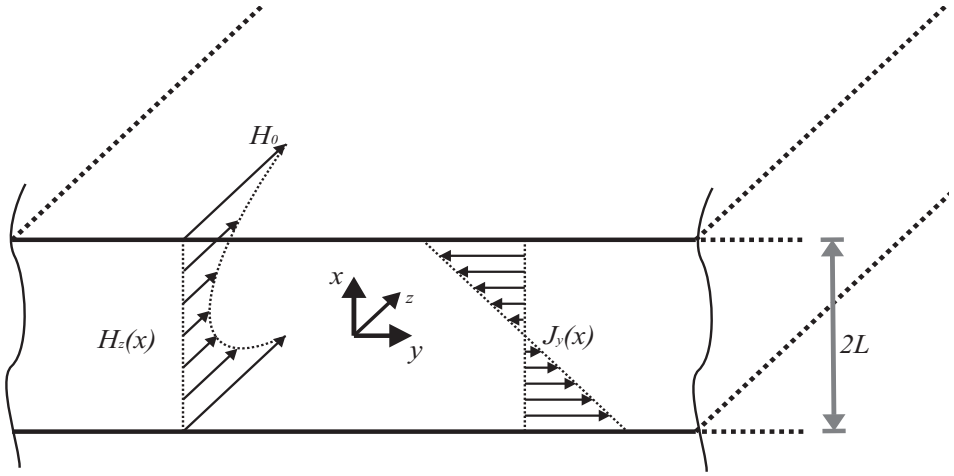

Figure 5.3: Infinite plate representation of a core lamination

The lamination has a thickness of $t = 2L$. The end effects are neglected (because the thickness << width) so the width is not important at first (it is important if considering interlaminar effects). Using Maxwell's equations in frequency domain:

$$\nabla \times \vec{E} = -j\omega\vec{B} \qquad (5.5)$$

$$\nabla \times \vec{H} = \vec{J} + j\omega\vec{D} \qquad (5.6)$$

together with the constitutive relations: $\vec{J} = \sigma\vec{E}$, $\vec{D} = \varepsilon\vec{E}$ and $\vec{B} = \mu\vec{H}$, the general wave equation is found by:

$$\nabla^2\vec{H} = k^2\vec{H} \text{ where } k^2 = j\omega\mu(\sigma + j\omega\varepsilon) \qquad (5.7)$$

The magnetic field is applied in the z-direction, hence the only component of the magnetic field is H_z. H_z varies only in the x-direction: $\vec{H} = H_z(x)$. The induced currents flow only in the y-direction, with its variation along the x-axis: $J = J_y(x)$ as shown in fig. 5.3. If $\sigma \gg \omega\varepsilon$, k is reduced to:

$$k^2 \approx j\omega\mu\sigma \qquad (5.8)$$

In one dimension, eq. (5.7) is reduced to:

$$\frac{\partial^2 H_z}{\partial x^2} = j\omega\mu\sigma H_z \qquad (5.9)$$

This differential equation has the standard solution of:

$$H_z(x) = H_1 e^{kx} + H_2 e^{-kx} \qquad (5.10)$$

where

$$k = \frac{1+j}{\delta} \qquad (5.11)$$

and

$$\delta = \sqrt{\frac{2}{\sigma\omega\mu}} \qquad (5.12)$$

The latter equation is usually termed as the skin depth of any conducting material with the material characteristics $\sigma[S/m]$ and $\mu[H/m]$ and with an angular frequency of $\omega[rad/s]$

To find the expression for the magnetic field $H_z(x)$, the boundary conditions is applied. The field strength on the surface of both sides of the laminate is assumed to be H_0 (and equal). This strictly means that the field strength on the surface of all laminates in the core has the same value. This will be discussed further in chapter 5.4. For reasons of symmetry, the following conditions are obtained:

$$H_z(L) = H_z(-L) = H_0 \qquad (5.13)$$

The final equation for the magnetic field can then be found:

$$H_z(x) = H_0 \cdot \frac{\cosh(kx)}{\cosh(kL)} \qquad (5.14)$$

Eq. (5.6) can be applied to find the current density:

$$J_y(x) = \frac{\partial}{\partial x} H_z(x) = kH_0 \frac{\sinh(kx)}{\cosh(kL)} \tag{5.15}$$

The amplitude is found by using the complex conjugate as shown below:

$$|H_z(x)| = \sqrt{H_z(x) \cdot \overline{H_z(x)}} = H_0 \sqrt{\frac{\cosh\left(\frac{2x}{\delta}\right) + \cos\left(\frac{2x}{\delta}\right)}{\cosh\left(\frac{2L}{\delta}\right) + \cos\left(\frac{2L}{\delta}\right)}} \tag{5.16}$$

The normalized magnetic field intensity is shown in figure 5.4

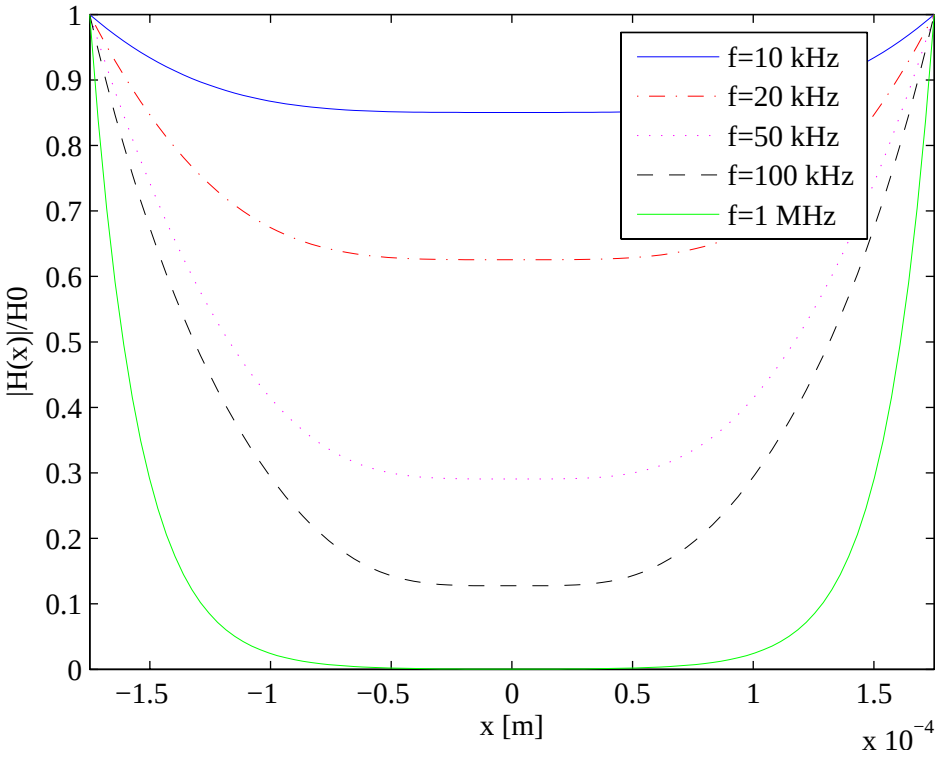

Figure 5.4: Normalized magnetic field intensity. Values: $\sigma = 2e6$, $\mu_{ri} = 300$ *and* $2L = 0,35mm$

As seen above, the change is largest from 10-100 kHz, while above 1MHz the field is completely displaced from the middle of the laminate and the penetration depth is much less than the thickness of the laminate. The change from DC to 10 kHz is moderate. This is the part where the skin depth is much larger than the thickness of the lamination, and the eddy currents are restricted by lack of space and the resistivity of the material. The eddy current distribution is said to be “resistance-limited”. For high frequencies, the current distribution is limited by the effect of

its own field, and the are said to be “inductance-limited” as per Stoll [92]. This can be further elucidated by studying the current distribution at the different frequencies, where the distribution is linear at low frequencies and parabolic at higher frequencies. The amplitude of the current density at the different frequencies used in fig. 5.4 is shown in figure 5.5:

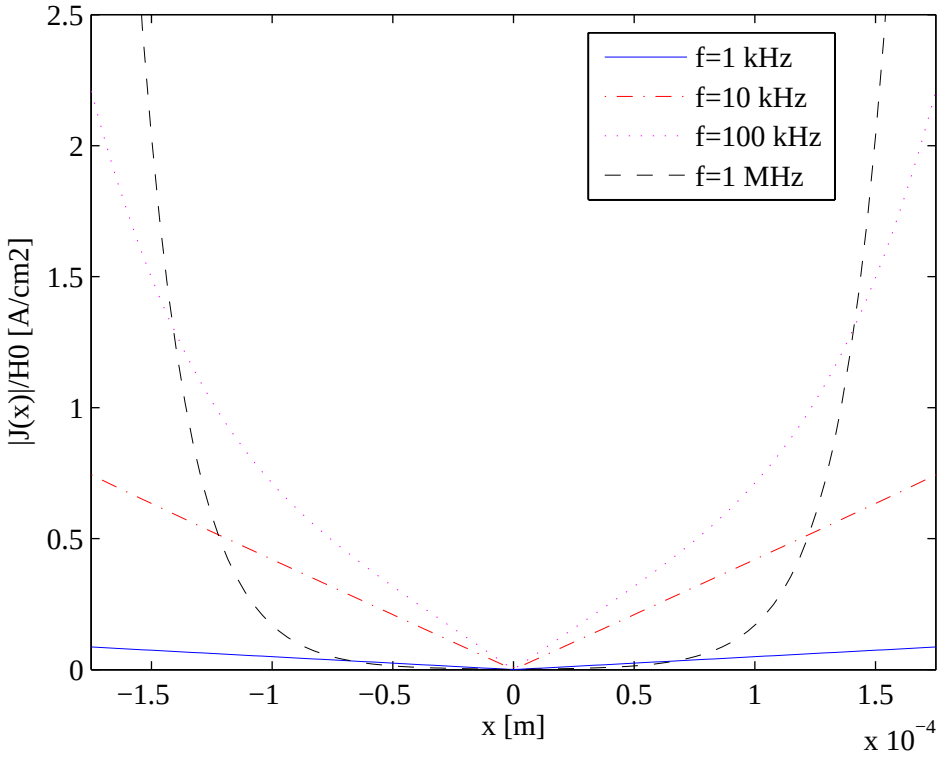

Figure 5.5: Normalized current density. Values: $\sigma = 2e6$, $\mu_{ri} = 300$ *and* $2L = 0,35mm$

As outlined initially, the goal is to establish an expression for the permeability based on the complex magnetic field distribution. Moreau et al. [120] used the complex power loss density distribution. A simpler approach is described in the following. The complex magnetic field distribution is averaged to be able to equalize the laminated iron core to an isotropic non-conducting material having a complex permeability. This permeability is then easily implemented into any FEM software.

The effective, complex permeability of a lamination is given as the average, magnetic flux-density in the laminate normalized to the surface magnetic field:

$$\mu^* = \frac{1}{H_0} \cdot \bar{B} = \frac{1}{H_0 2L} \cdot \int_{-L}^{L} (\mu H) dx \qquad (5.17)$$

Eq. (5.14) is inserted into (5.17) and the permeability is obtained by its solution:

$$\mu^* = \mu_r \mu_0 \cdot \frac{tanh(kL)}{kL} = \mu_0(\mu' - j\mu'') \qquad (5.18)$$

The equivalent complex permeability for the core material is obtained in terms of its real and imaginary parts by splitting the permeability as shown in eq. (5.18):

$$\mu' = Re(\mu^*)/\mu_0 = \frac{\mu_r \delta}{2L} \cdot \left(\frac{sinh\left(\frac{2L}{\delta}\right) + sin\left(\frac{2L}{\delta}\right)}{cosh\left(\frac{2L}{\delta}\right) + cos\left(\frac{2L}{\delta}\right)} \right) \qquad (5.19)$$

$$\mu'' = -Im(\mu^*)/\mu_0 = \frac{\mu_r \delta}{2L} \cdot \left(\frac{sinh\left(\frac{2L}{\delta}\right) - sin\left(\frac{2L}{\delta}\right)}{cosh\left(\frac{2L}{\delta}\right) - cos\left(\frac{2L}{\delta}\right)} \right) \qquad (5.20)$$

The reason for splitting up into real and imaginary parts is that some FEM-programs do not handle a complex permeability and thus must make two separate calculations for the inductance and resistance respectively.

The interlaminar zones are so far neglected. The permeability of these zones (equal to μ_0) should be represented as a parallel flux-path to the laminates. Its influence is determined by the stacking factor (usually around 0.96):

$$\gamma = \frac{L}{L + l} \qquad (5.21)$$

where L is the lamination thickness and l is the interlaminar/coating thickness.

If the cooling ducts are to be taken into account, the following total stacking factor is defined:

$$\gamma_{Total} = \gamma - \gamma_{Cooling} \qquad (5.22)$$

where $\gamma_{Cooling}$ is the percentage value of the cooling duct areas (for instance 5%) compared to the net iron area of the core. The final complex permeability for the homogenized core can then be expressed as:

$$\mu_{tot}^* = \frac{\mu^* \cdot L + \mu_0 \cdot L(1 - \gamma_{Total})}{L + L(1 - \gamma_{Total})} = \frac{\mu_0 \cdot (1 - \gamma_{Total}) + \mu^*}{2 - \gamma_{Total}} \qquad (5.23)$$

Resulting complex permeability for a M6 lamination is shown in fig. 5.6

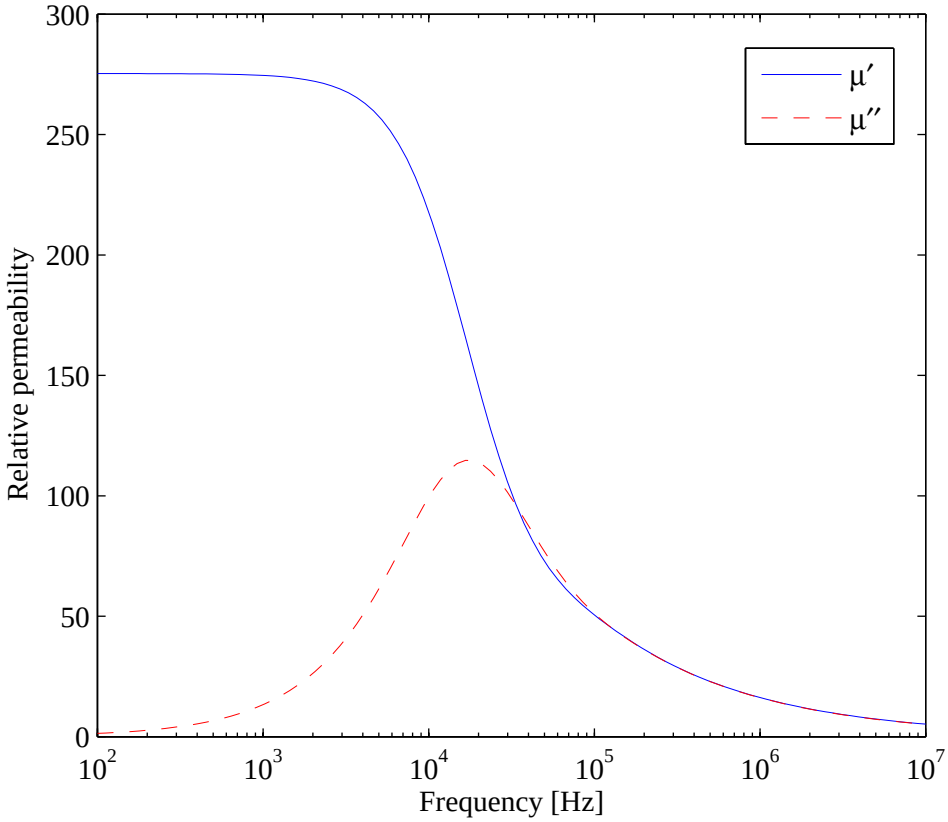

Figure 5.6: Resulting complex permeability for a M5 lamination with $\mu_{ri} = 300$, $\sigma = 2e6[S/m]$, $2L = 0,35mm$, $\gamma = 0,96$ *and* $\gamma_{cooling} = 5\%$

The material parameters to be used are in most cases not known and have to be estimated. Wilcox et al. [46] derived analytical formulations of frequency dependent inductances and losses due to the core with high degree of accuracy when compared to measurements. The material-parameters where calculated based on measurements on the respective cores.

In practice the material parameters are hard to obtain since the yoke and windings must be removed to make possible the fitting of test windings for measurements. Alternatively the permeability can be estimated from the slope of minor hysteresis loops of the core steel (if available). Due to limited data normally available during modelling, it is important to know the influence of each of these parameters. Measurements from [44] and [46] are used during the next chapter to validate the principle in a FEM-calculation.

5.3 FEM verification

In order to verify the theory developed regarding frequency-dependent iron core characteristics and the equivalent complex permeability representation, a few test cases are used for comparison. A small core from a distribution transformer [46] is employed as the first test object due to well-documented details and measurements. The second one is a large single phase core used by Fergestad [44]. Both these cases have measurements performed with only a test-winding attached to the core, simplifying comparison to FEM-simulation.

5.3.1 Wilcox 25 kVA core

The model below is implemented to quantify the influence of the core for the flux distribution, and to verify/calibrate the calculation according to measurements done by Wilcox et al. [46]. The geometry comprises a double disc with 12 turns and the core is a 3-legged stacked core. All measures are given in fig. 5.7:

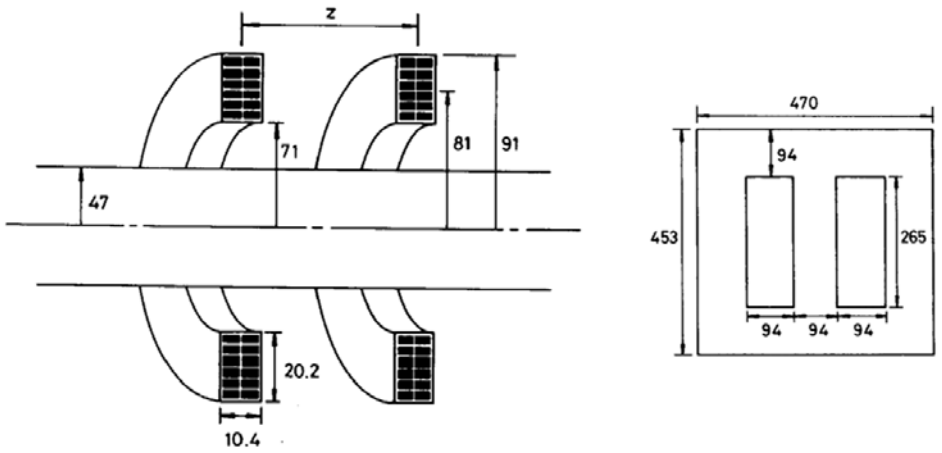

Figure 5.7: Dimensions in millimetres of the 25kVA test object used by Wilcox [46]. Double-disc dimensions to the left. Core dimensions to the right.

All measurements done by Wilcox in this experiment are performed at the outer leg. The FEM-model is developed in 2D-axisymmetric with a closed core surrounding the geometry. Core dimensions are adjusted in order to obtain the same reluctance for the two different geometries. The yoke of the axisymmetric model is shaped so that the cross-section is constant. Calculation of axisymmetric core dimensions is shown in appendix J.1. The axisymmetric FEM-model is shown in fig. 5.8.

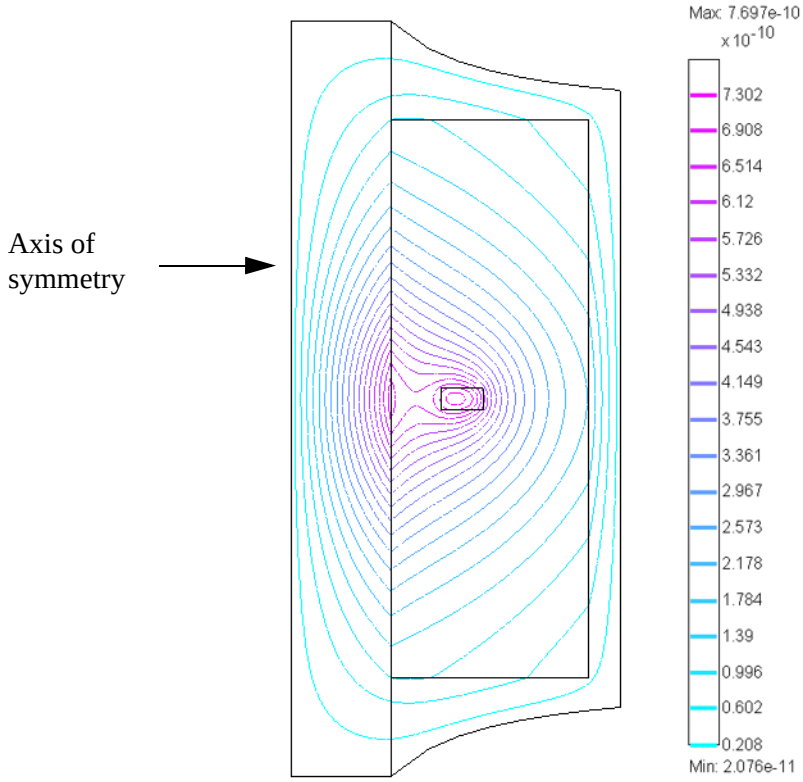

Figure 5.8: Axisymmetric FEM-representation of the geometry specified by Wilcox [46]. Field distribution (Vector Potential, A) solved at 1 MHz

The model includes the complex permeability found in eq. (5.23), and the self-inductance and losses are calculated as a function of frequency as shown in fig. 5.9

In [46], the equivalent permeability was found to be 843 by measurements. Wilcox et al. use a solid core approximation in his method, and calls for a frequency-dependent adjustment of the resistivity in order to obtain agreement with measurements. Neglecting leakage flux, the permeability can be determined by calculating the reluctance of the core from the dimensions given in fig. 5.7, and the low frequency measurement of the inductance (shown in fig. 5.9 and [46]). Using these results, the permeability is calculated to be 850. The deviation is attributed to the contribution of the leakage flux.

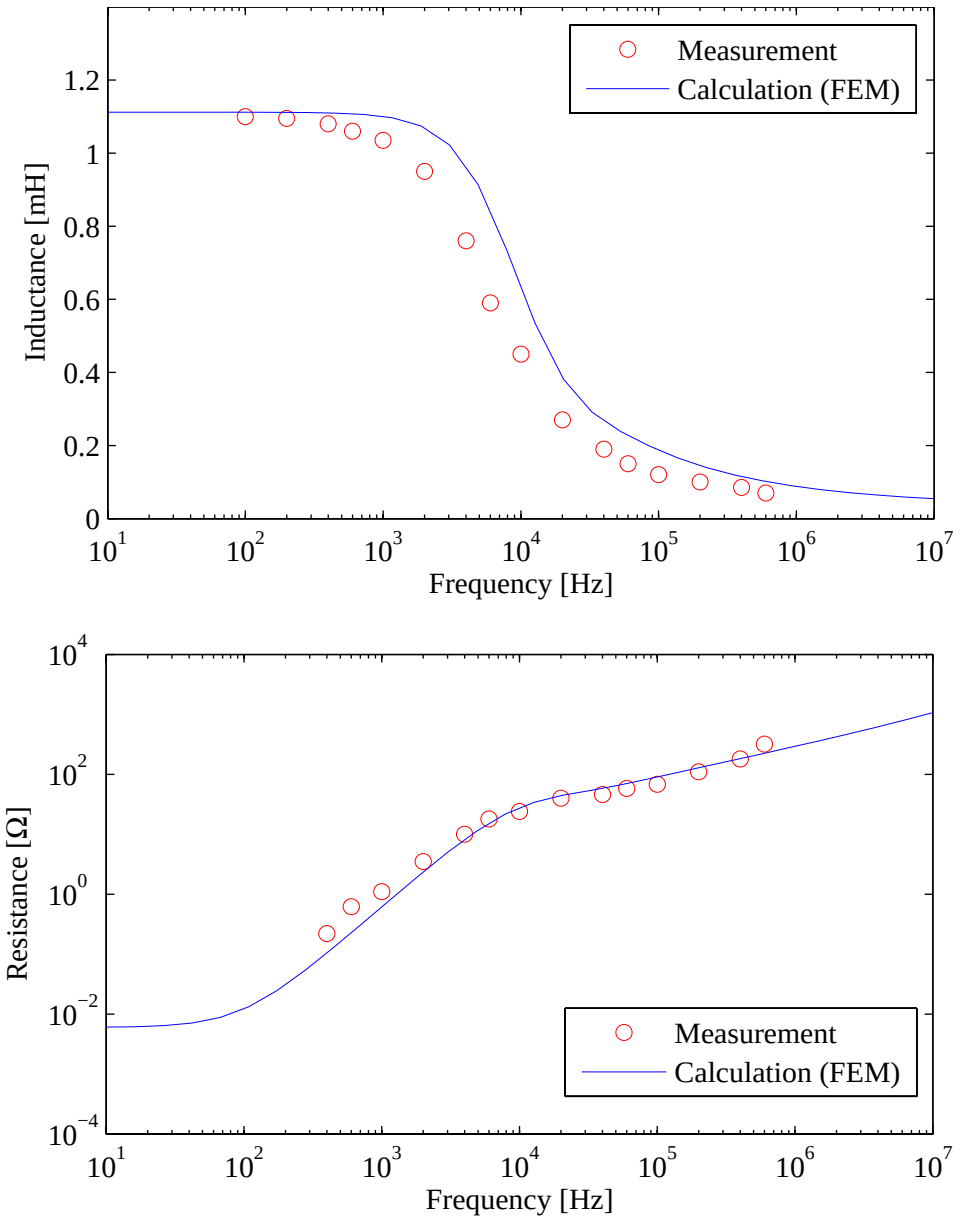

Figure 5.9: Self inductance (upper) and series resistance (lower) vs. frequency for a complex permeability-representation of the core compared to measurements by Wilcox [46]

The results of the calculation are shown in fig. 5.9. The proximity effect is incorporated using complex permeability representation similar to the core following [120]. The contribution from the proximity effect will then calculated

together with the iron losses. Skin effect in the conductors is implemented using an analytical approach initially introduced by Stoll [138].

In the loss calculation given above, a characteristic 'knee' can clearly be seen in the curve at 10 kHz. This 'knee' is typical in the area where the penetration depth, δ, approaches the thickness of the lamination, $2L$. This 'knee' occurs at the same frequency as where the imaginary part of the permeability reaches its maximum value.

The analytical approach by Wilcox assumes the total core length to be straightened out between two plates of infinite permeability, which means that a flux line leaving at one end, immediately enters the model at the other end (same position). This should also be possible in FEM using periodic boundary conditions. The advantage would be the inclusion of inductance between phases/legs.

As seen in fig. 5.9 there is a deviation between the measurement and the model. This can be due to a difference in the resistivity of the iron laminates. In the FEM-model, a resistivity of $\rho = 4,8 \cdot 10^{-7}$ which is considered to be a common value for iron laminates [140]. There will of course be differences between oriented and non-oriented laminations and also the different alloys to control the resistivity (Si-Fe). The method of Wilcox et al. seems to have a slightly better agreement with his measurements [46], but this is due to the adjustment done for the resistivity in order to utilize a solid core. Their model needs measurements on each specific core in order to calibrate the parameters of the model.

Another source for the deviation is interlaminar effects. Such effects will reduce the net flux carried by the core and hence reduce effective permeability.

Interlaminar effects are caused by interlaminar currents, either capacitive or resistive. This is investigated in chapter 5.4.

5.3.2 Fergestad 200 MVA core

Wilcox also compared his method [46] to one of the cores used in Fergestad's doctoral work [44]. This core is a single phase core rated at 200 MVA. Wilcox adapted the permeability $\mu_r = 343$. In lack of anything more accurate, the resistivity is assumed to be $\rho = 4,8 \cdot 10^{-7}$. Fergestad investigated the influence of the mutual coupling between single discs mounted on this core in order to be able to separate the common flux and leakage flux. Dimensions and the equivalent axisymmetric model is shown in fig. 5.10.

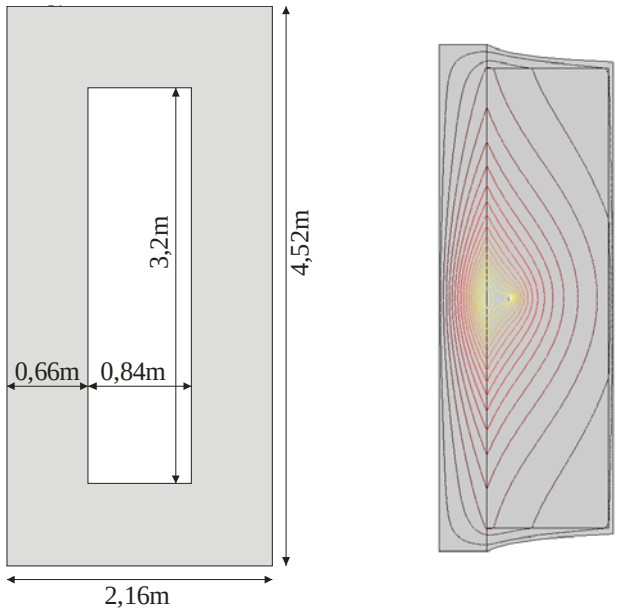

Figure 5.10: Dimensions and axial symmetrical model of the 200 MVA core investigated by Fergestad [44]

By making use of the many different measurements done by Fergestad, it is possible to investigate the validity of the complex permeability approach in 2D axial symmetry. This is important both in terms of possible difference in high frequency behaviour, and also the mutual coupling between discs depending on the distance.

The first comparison is shown in fig. 5.11, where calculated self-inductance at two different positions on the core is compared to the measured self-inductance.

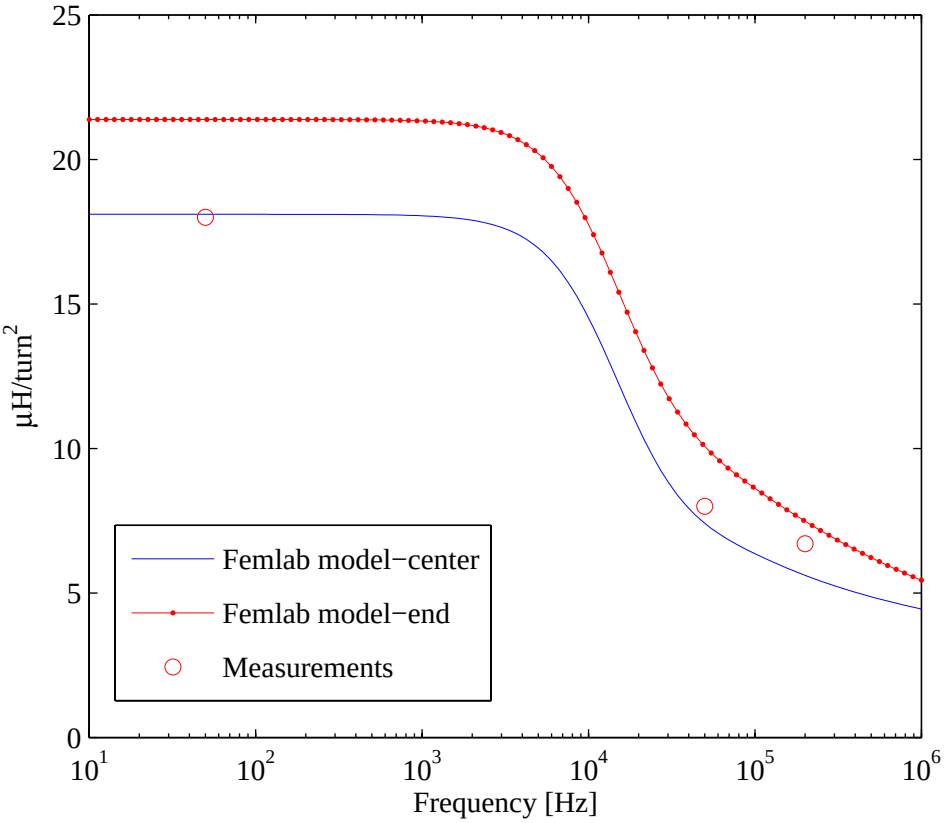

Figure 5.11: Comparison of calculated self-inductance to the measurements done by Fergestad [44]. Measurements obtained from fig. 5.12 ($M'_{12}(x = 0)$)

The self inductance in the Femlab-model is calculated at two different positions on the core. Centre means at the centre of the leg, while end means 10 cm from the yoke. This shows a clear difference for the self-inductance depending on the position along the leg, which is the contrary to what is reported in the measurements by Fergestad and Henriksen [42]-[44].

Fig. 5.11 shows that there is a possibility that the representation using axial symmetry and a core window equal to the window for the real core overestimates the inductance close to the yoke at all frequencies, while slightly underestimating the inductance at high frequencies at the centre of the leg. Since the leakage field in a real transformer is equal to the axisymmetric model only inside the core window, it is possible that the leakage field outside the core window is more important.

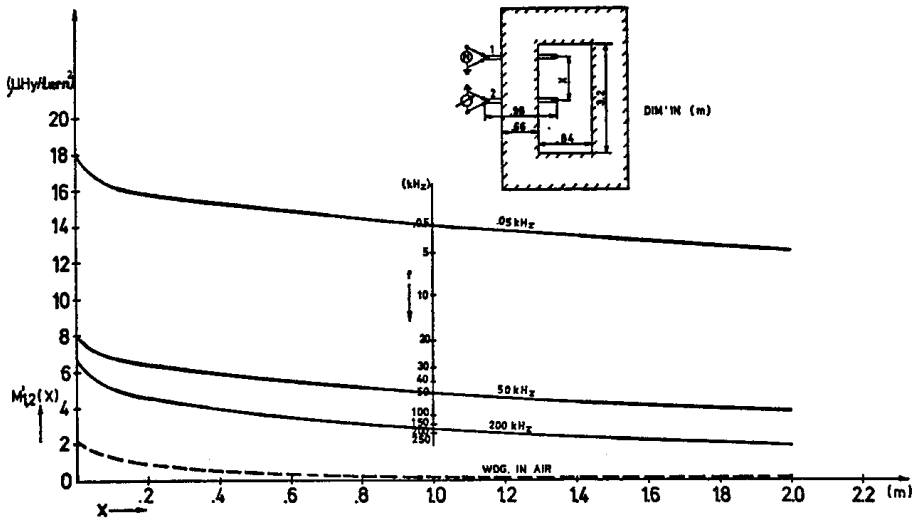

Figure 5.12: Mutual coupling between single discs due to distance and frequency as measured by Fergestad [44]

As seen from fig. 5.12, the inductance for the winding in air is quite different from the winding on core at 200 kHz. This demonstrate the importance of the core at higher frequencies.

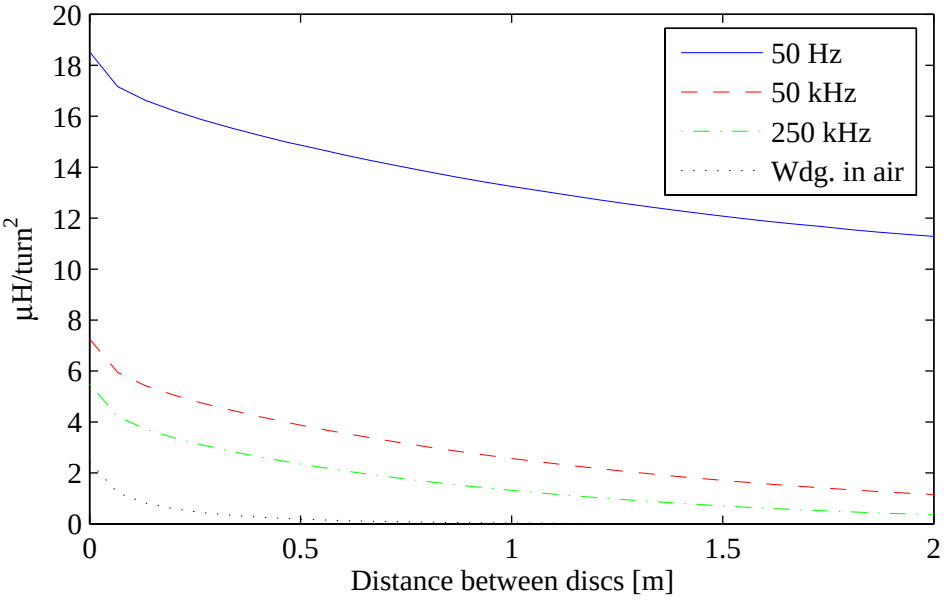

Figure 5.13: Mutual coupling (simulated) between single discs as a function of distance and frequency

The comparison shows a clear underestimation of the inductance by the FEM-model. Winding in air is simulated by setting permeability of core equivalent to 1.

Since it is unknown whether these measurements were performed un-tanked or in-tank, the use of this verification is rather limited, and calls for similar measurements to be done in the future. This is important when permeability is reduced at higher frequencies since the leakage field play a prominent part at increasing frequencies. From a practical point of view, it is reasonable to assume that these measurements were performed out of tank due to the many operations necessary if done in tank.

Using this assumption it is reasonable to assume that the leakage field will be different from the calculated field, since the boundaries are different. This is further confirmed by comparing calculation and measurement of the curves for “winding in air”. The measured mutual inductance is larger at all distances and this is probably due to the difference in available space for “storing” the magnetic energy of the leakage inductance.

If the core is un-tanked, it will introduce errors in the axisymmetric representation promoting alternative representations such as a straight core-equivalent with periodic boundary-conditions.

5.4 Interlaminar effects

5.4.1 Introduction

Since the one dimensional complex permeability approximation (CP1D) overestimates the self-inductance compared to the measurements done by Wilcox [46], an attempt to study interlaminar effects was initiated.

It may be assumed that there exist currents between the laminates in the core at high frequencies. Eddy-currents at very high frequencies appear as currents flowing at the core surface rather than at the surface of the laminates. This supports the possibility to represent the core with a thin cylinder at very high frequencies as assumed by Buckow [109].

With a sheet thickness of 0.35mm and a stacking factor of 0.96, the interlaminar capacitance at a sheet width of 440 mm will be in the order of 300 nF/m (assuming $\varepsilon = \varepsilon_0$). The reactance of this capacitance will be 5-6 Ohm/m at 100 kHz. Additionally, the resistance of the interlaminar coating will be important. Very little theoretical considerations on interlaminar effects are found in the literature.

The interlaminar resistive current is usually very low at power frequency due to the fact that the induced electrical field between laminates is low, and that an insulating coating is applied to restrict the eddy currents from flowing between laminations. The resistance is heavily dependent on the type of insulation and its thickness. For older designs, a paper insulation was usually used. For more recent designs the insulation is employed by a coating on the surface of the laminate [141], usually an organic resin coating. At power frequency the interlaminar losses are usually 0,5-2% of the no load losses, and this is mainly due to imperfect joints and cutting.

At higher frequencies, the induced interlaminar electrical field will most likely increase. At a certain point, the effective resistance in the laminates approaches the interlaminar impedance. Increasing the frequency further will make the interlaminar currents dominate the total eddy currents and a larger eddy current loop is formed. Attention must be paid regarding the cooling-ducts within the core, where the inter-laminar capacitance will be very small and resistive currents will be zero. This leads to a separation into a number of smaller loops for the resulting eddy currents.

Interlaminar effects might be important for high frequency transients in transformers and should be investigated further to find the frequency limit where it dominates the induced currents in the core. The problem at very high frequencies is that the quasi-static assumptions becomes less accurate (the magnetic influence of displacement currents can no longer be neglected at a certain frequency).

Interlaminar currents will add another dimension to the expressions of the magnetic field strength and the current density (variation along both the x- and y-axis). Interlaminar currents are flowing in the x-direction according to fig. 5.14.

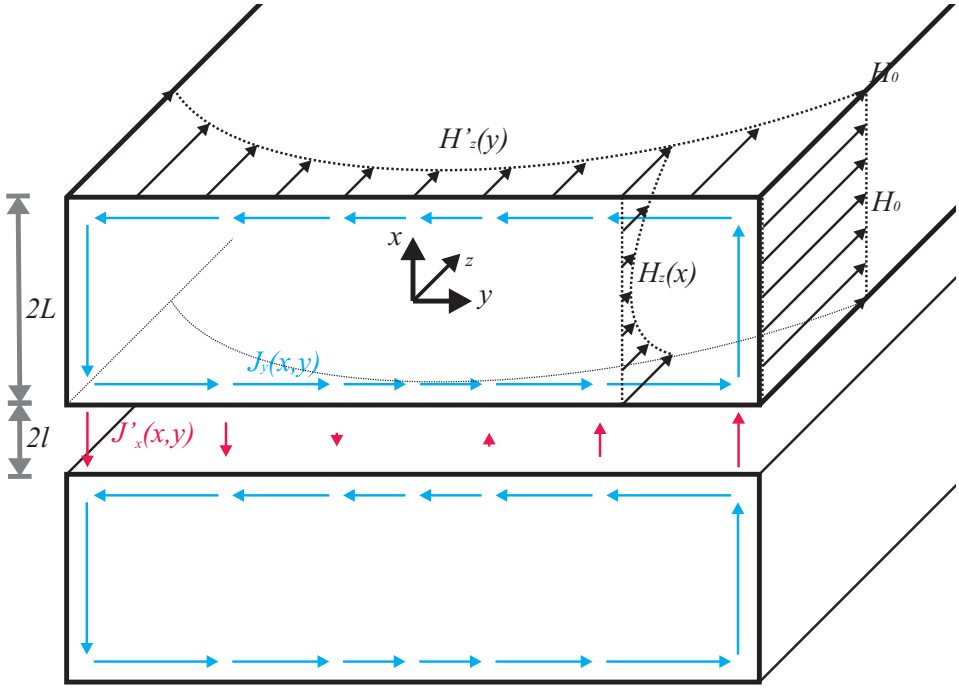

Figure 5.14: The interaction of currents within core laminates

The situation given in fig. 5.14 will be the case at an intermediate frequency where the interlaminar currents start making a difference. At even higher frequencies the magnetic field will be completely displaced from the middle of the laminates ($y = 0$) as indicated in figure 5.15. The current-distribution will in this case be characterised by the interlaminar penetration depth, Λ, as shown in fig. 5.15 and 5.19.

The effect of flux displaced from the centre of the core upon the leakage field distribution should also be investigated. This would be important for the complex permeability-representation, when interlaminar effects are included. Two very different ways of including these effects into the FEM-calculations are proposed:

- Keep homogeneous core description, but correct the initial formulas (eq. (5.19) and (5.20)) for complex permeability, by using the interlaminar penetration depth Λ as shown in figure 5.15.
- Make the complex permeability in the core leg dependent on r (position/ distance from the centre axis) and Λ, in order to realize a flux displacement from the inner parts of the core.

The best method will be dependent on whether the interlaminar penetration depth is constant to the last lamination in the stack (core surface) or if the end effects influence on this penetration depth across many laminations. If the former is the case, then this will be a 2D-description and the proposed descriptions will be coarse approximations.

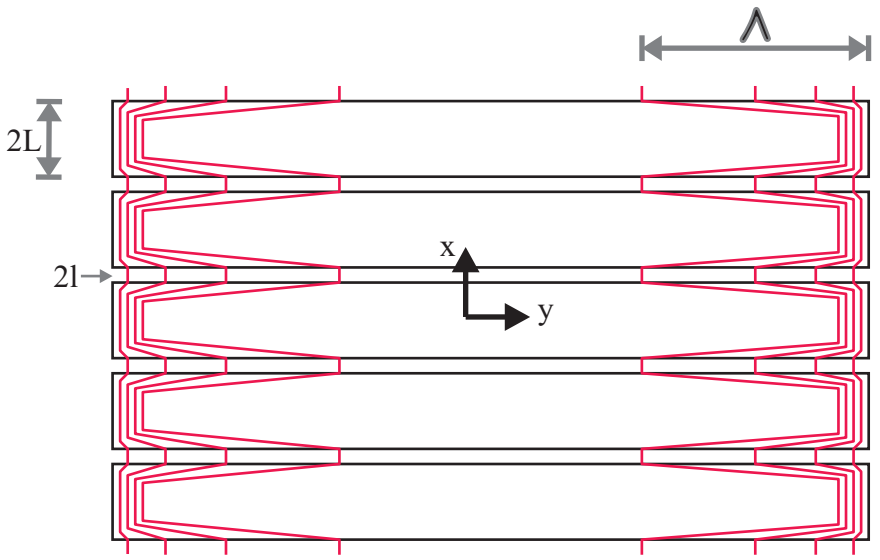

Figure 5.15: Interlaminar currents dominating the field distribution over the eddy currents.

Interlaminar conductive losses will also contribute to a certain extent, and will dominate interlaminar currents at low and intermediate frequencies. It is described by the Surface Insulation Resistance:

The resistance of a unit area of surface coating measured perpendicular to the surface usually expressed in $\Omega \cdot cm^2$ per lamination. Surface insulation resistance is considered adequate if the inter-laminar loss is restricted to less than 2% of total core loss at power frequency. In absolute values it should be greater than or equal to 10 $\Omega \cdot cm^2$ when measured by the Franklin test method [142]-[144]. With a surface resistance of 10 $\Omega \cdot cm^2$, a lamination thickness of 0,35 mm, and a stacking factor of 0,96, the interlaminar conductivity becomes:

$$\sigma = \frac{(1-0,96)\cdot 0,00035m}{0,001\Omega m^2} = 0,014[S/m] \qquad (5.24)$$

At a given magnetic field in the core, the quality of the interlaminar surface insulation is a function of lamination width. Increasing the width of the laminations, also increase the induced voltage per turn requiring an improved insulation coating [145].

Since the interlaminar induced voltage increases with frequency, the resistive currents and losses also increase with frequency. For distribution-transformers the interlaminar resistance can be lower than 10 $\Omega \cdot cm^2$. A typical value for distribution transformers according to AK Steel [146] is 3-15 $\Omega \cdot cm^2$ (using C3-grade coating; Gradings are defined in [147] and [148]). For large power transformers this number is given to be 5-50 $\Omega \cdot cm^2$ (C5-coating). Additionally there exists a C6-coating for very high interlaminar resistance: up to 1500 $\Omega \cdot cm^2$. To evaluate this effect, we make use of the complex conductivity in order to compare:

$$s = \sigma + j\omega\varepsilon \tag{5.25}$$

As seen from eq. (5.25) the conductive current dominates when $\sigma \gg \omega\varepsilon$. The transitional frequency is found from:

$$\omega_0 = \frac{\sigma}{\varepsilon} \tag{5.26}$$

When $\varepsilon = \varepsilon_0$ and $\sigma = 0,014[S/m]$, the transition where dielectric interlaminar currents start dominating the conductive currents, will occur at approx. 250 MHz. If maximum frequency of consideration is 10 MHz, it means that the dielectric currents can be neglected if the conductivity of the coating is well above $0,00056[\Omega m]^{-1}$. This equals a surface resistance of 200 $\Omega \cdot cm^2$.

Tavner and Jackson [149] solved the magnetic field due to interlaminar capacitive currents by means of eigenfunctions. They found interlaminar capacitive currents neglectable below 20 MHz for laminated cores in electrical machines. Resistive currents were neglected assuming a perfect insulation between laminates. Even though the application is different from a transformer core, the analysis is similar. A surface resistance corresponding to a transition from resistive to capacitive currents at 20 MHz is equal to 100 $\Omega \cdot cm^2$. It should be investigated whether this value cancel the effect of resistive interlaminar currents at lower frequencies or not. In other words the upper value for surface resistance should be determined in order to evaluate what coating-types that influence and not.

A FEM-simulation (fig. 5.16) for a package of 8 laminates where performed to study interlaminar effects at different frequencies (1 kHz - 10 MHz). The geometry is scaled (x- and y-axis not equal) in order to be able to illustrate the results.

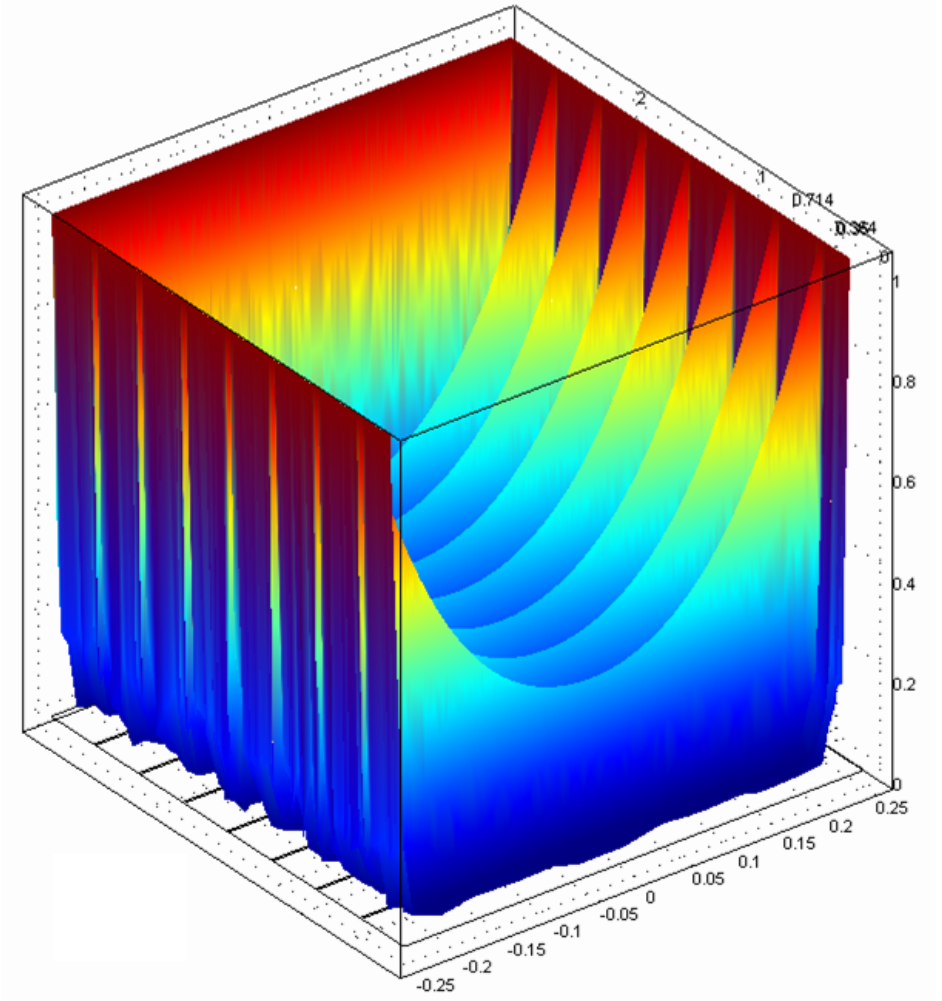

Figure 5.16: FEM-solution of the normalized internal and interlaminar magnetic field at 1MHz (color indicating field strength)

The outer lamination of the package is applied to a field strength, H_0 at one of its surfaces. The interlaminar field on the other side of this lamination is not very different from the field in the other interlaminar zones. This means that such end-effects can be neglected and that the analytical solution in the next chapter can be applied to the whole core as one unit. This also means that the penetration into the core is dependent on the direction of the field (perpendicular to the surface or the edge of the laminate). But since the width of the laminates is reduced towards the surface, the importance of this 2D-effect is assumed to be small.

A cross-section plot (fig. 5.17) is made from this simulation for the field strength in the gap between the laminates at different frequencies.

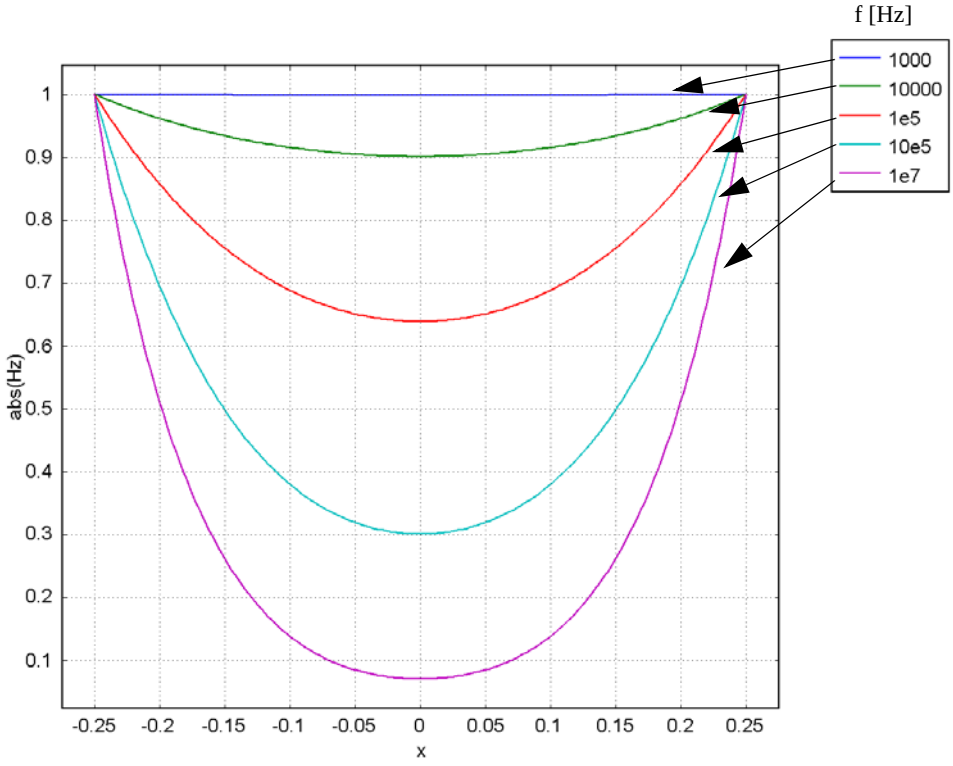

Figure 5.17: Normalized magnetic field $|H_z|/H_0$ between laminates at different frequencies (1kHz-10MHz)

Fig. 5.17 shows that the field is not completely displaced from the middle of the core (between the laminates) even at 10 MHz.

Since this effect is clearly important at low values for the surface resistance, usability of these results calls for an analytical solution of the magnetic field, in order to be able to utilize the results in a FEM-based transformer model.

5.4.2 Two-dimensional approximation

The formulation is extended compared to the one-dimensional approach (CP1D). The end-effects can no longer be neglected since the ends (edges) of the laminates incorporate the main boundary-condition (source) for the formulation. Both the thickness and width of the lamination is given according to the configuration shown in fig. 5.18. Lamination width is $2D$, and thickness is $2L$, while the interlaminar gap is $2l$.

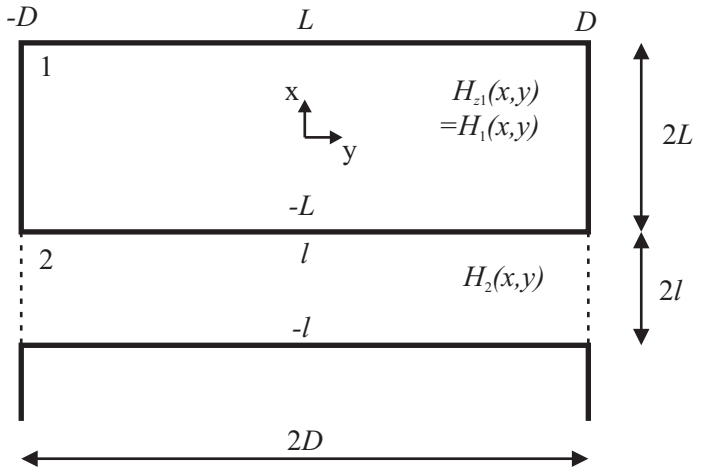

Figure 5.18: Configuration and dimensions of the CP2D formulation

The problem is now two dimensional and the general wave equation (5.7) is reduced to:

$$\frac{\partial^2 H_i(x,y)}{\partial x^2} + \frac{\partial^2 H_i(x,y)}{\partial y^2} = k_i \cdot H_i \qquad (5.27)$$

where H_i is the magnetic field in the z-direction in material i.

The magnetic field inside and between the steel laminates is solved analytically in appendix J.2, and the field inside the steel can be approximated as:

$$H_1 \approx H_0 \cdot \frac{\cosh(k_1 \cdot x)}{\cosh(k_1 \cdot L)} \cdot \frac{\cosh(\beta \cdot y/D)}{\cosh(\beta)} \qquad (5.28)$$

(5.29)

$$\text{where } \beta = k_2 \cdot D \cdot \sqrt{\frac{\gamma}{1-\gamma} \cdot \mu_r \cdot \frac{\tanh(k_1 \cdot L)}{k_1 \cdot L}} \qquad (5.30)$$

$$\text{and } k_i = \sqrt{j\omega\mu_i \cdot (\sigma_i + j\omega\varepsilon_i)} \qquad (5.31)$$

$i = 1$: magnetic steel, $i = 2$: non-magnetic interlaminar coating

The penetration depth, Λ of the field along the surface of the lamination is given by:

$$\Lambda = \frac{D}{\beta \cdot tanh(\beta) + k_2 \cdot D \cdot tanh(k_2 \cdot D)} \qquad (5.32)$$

The absolute value of the penetration depth Λ is plotted against frequency to show its frequency-dependency:

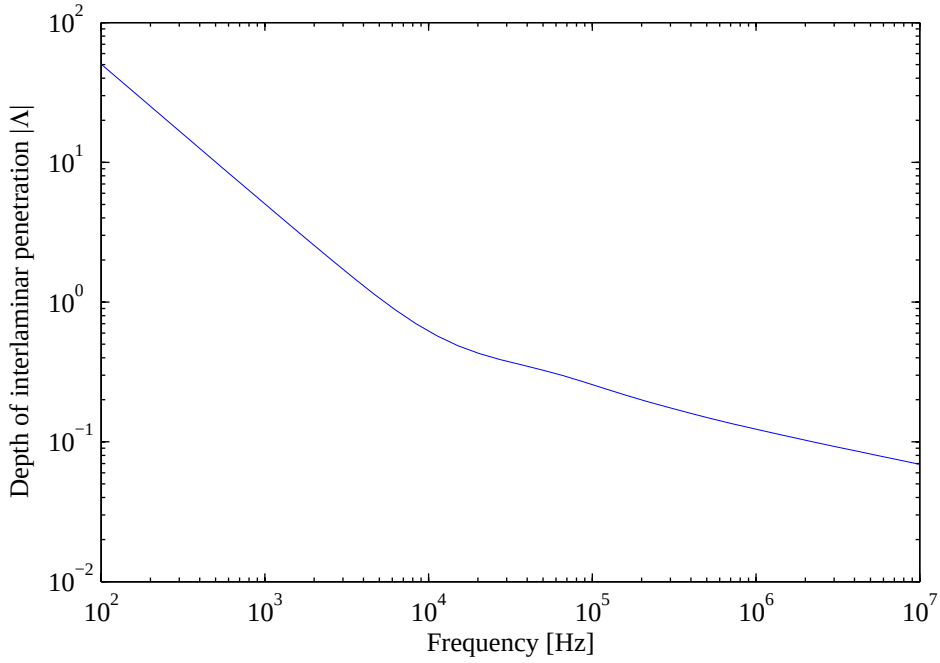

Figure 5.19: Interlaminar penetration depth $|\Lambda|$ in [m]. Values: $\mu_{r1} = 300$, σ_1 =2e6 S/m, σ_2 = 0,014, 2L=0.035mm, 2D=0,5m γ =0,96

Observing fig. 5.19, there is a change in slope of the curve at 10-20 kHz. This is investigated further in appendix J in fig. J.4.

The relative permeability of the core including interlaminar effects is obtained by averaging the magnetic flux density across the lamination and interlaminar zone, normalized to the applied field strength (at the edges) H_0:

$$\mu^* = \left(1 - \gamma + \mu_r \cdot \gamma \cdot \frac{tanh(k_1 \cdot L)}{k_1 \cdot L}\right) \cdot \frac{tanh(\beta)}{\beta} + \mu_r \cdot \gamma \cdot \frac{tanh(k_1 \cdot D)}{k_1 \cdot D} \qquad (5.33)$$

The real and imaginary part of the complex permeability is shown in fig. 5.20.

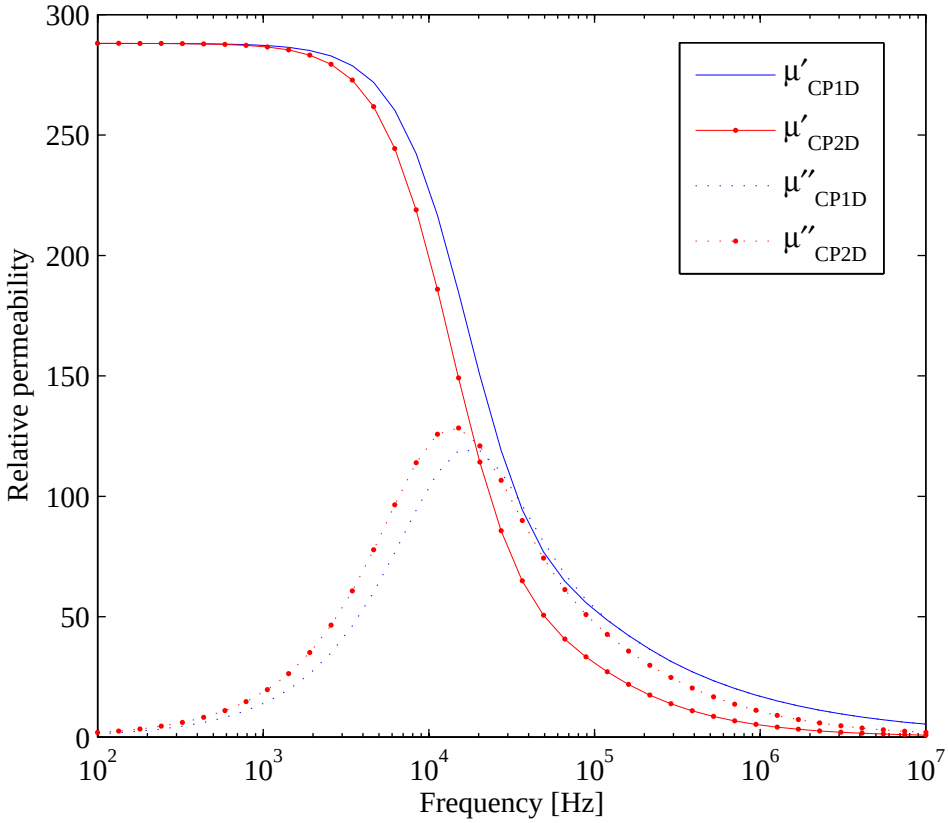

Figure 5.20: Relative permeability: Influence of interlaminar currents. Values: $\mu_{r1} = 300$, σ_1 *=2e6 S/m,* σ_2 *= 0,014, 2L=0.035mm, 2D=0,5m* γ *=0,96*

An interlaminar conductivity of $\sigma_2 = 0,0014[S/m]$ resulted in a very small difference and must be regarded as the limit where interlaminar effects may be neglected for practical frequencies. This conductivity equals a surface insulation resistance of approximately $100[\Omega m^2]$, and high quality coatings have surface insulation resistance above this value, resulting in an accurate representation using the one dimensional approach (CP1D).

In order to investigate permeability at the higher frequencies, it is better to make a logarithmic plot. This way it is possible to see the frequency where the core approaches a permeability equal to one, and also if it possibly can be approximated to a shielding cylinder.

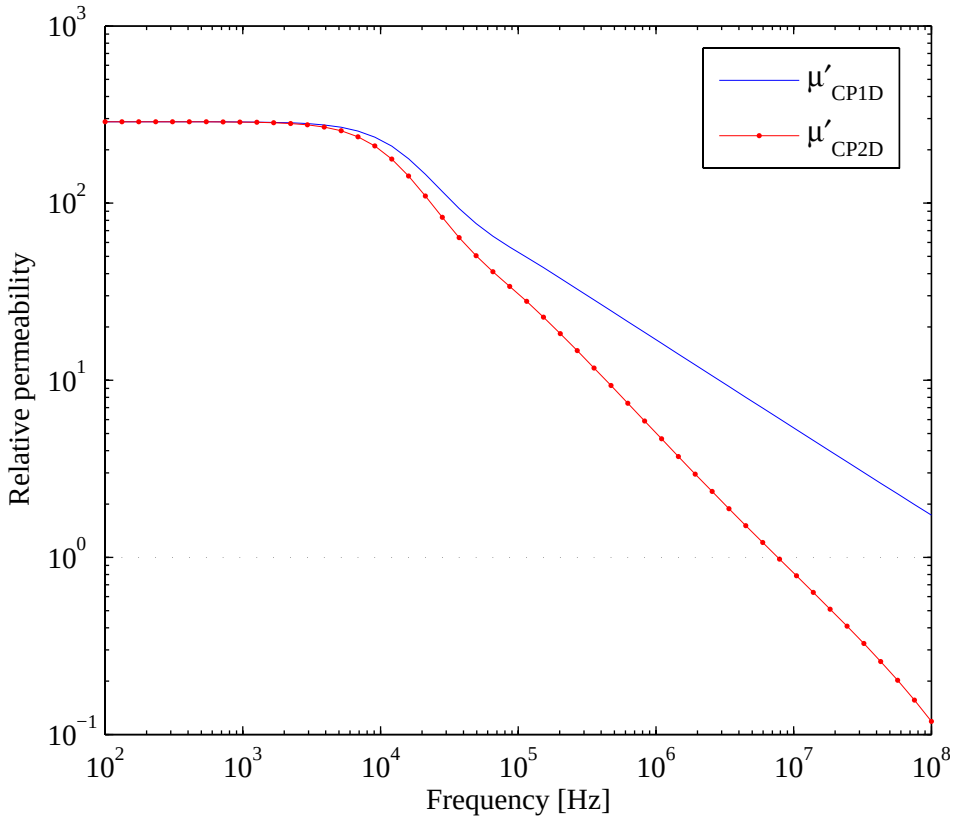

Figure 5.21: Relative permeability (logarithmic) equal to fig. 5.20

As seen from fig. 5.21 CP2D crosses μ_0 at approximately 10 MHz, while CP1D cross the same permeability above 100 MHz. This clearly shows that the iron core cannot be neglected for any of the frequencies considered in this work, if it is to be represented correctly in versatile high frequency power transformer models.

5.4.3 CP2D verification

As concluded in chapter 5.3.1, the FEM-based model for the core of Wilcox overestimated the inductance. CP2D is applied to the same model in order to verify the prospective improvements of including interlaminar effects.

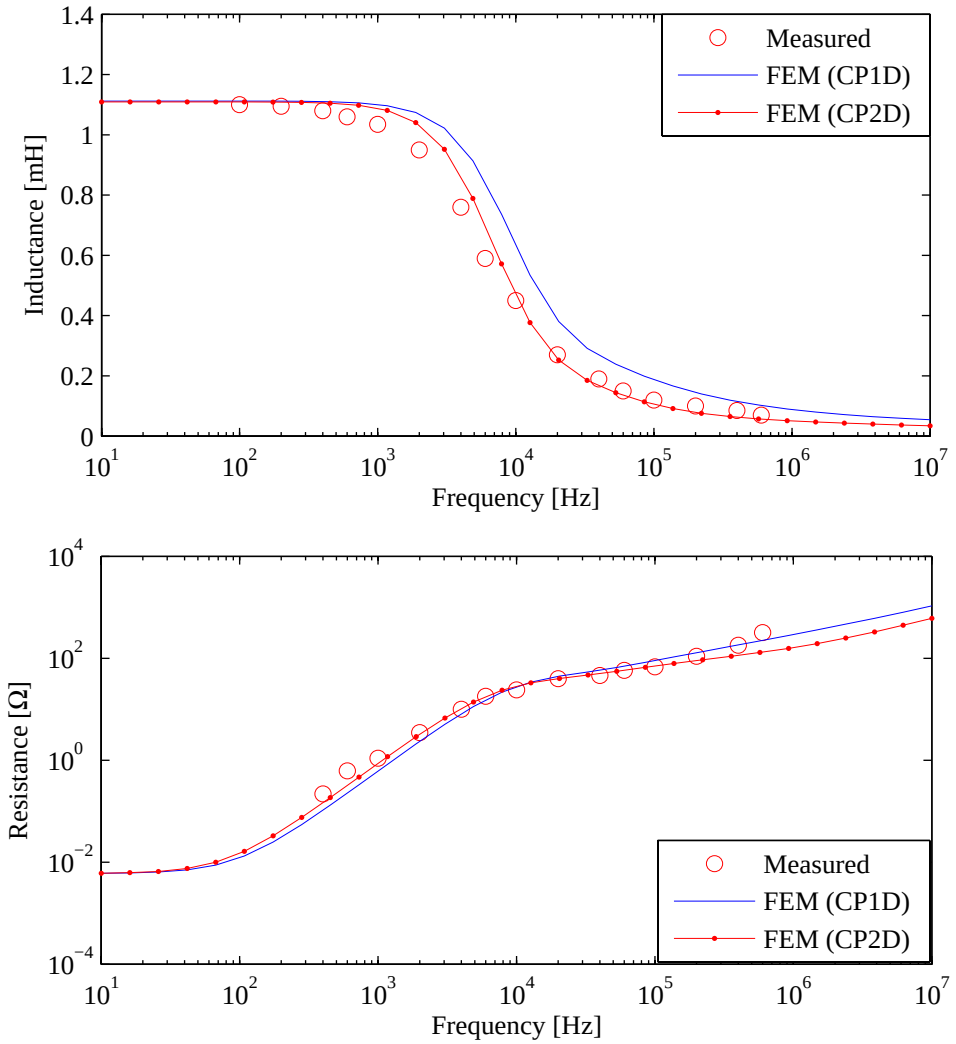

Figure 5.22: Comparison of the one- and two-dimensional approach applied to the geometry of Wilcox [46]

As observed in fig. 5.22, CP2D seem to improve accuracy for the inductance calculation, but still the inductance is overestimated around 1 kHz. A possible explanation for this might be a difference in the conductivity of the core steel.

5.5 Results - Core Influence

The importance of a proper iron core representation is emphasized in this chapter. When determining the inductance matrix in a transformer model, even at high frequencies, the iron core influences on the leakage flux. It is shown that the core cannot be neglected for any of the frequencies considered in this work. In the following different investigations are done to evaluate which parameters in an iron core representation that are important in a transformer model (voltage ratio/TF).

The different parameters investigated are: Core topology (Size, shape and parts), permeability and laminate thickness.

All measurements shown are done on phase B at OLTC-pos. +6 unless otherwise noticed.

All models established, are based on the one-dimensional frequency-dependent complex permeability-description (CP1D) given in chapter 5.2

5.5.1 Open core equivalent

The first attempt of core representation in SUMER is to model only the core leg (with no return-path) in order to try to correct the leakage field surrounding the core leg.

Since periodic boundary-conditions is not possible within SUMER, this result is merely of interest compared to the no-core representation presented in chapter 4. A periodic boundary-condition would be preferable since the core can be modeled as a core leg with length equal to the effective length of the core seen from either the outer or centre phase. This is utilized in the analytical/numerical approach suggested by Wilcox [46], and using this approach enables the inclusion of the other phases (coupled by the common flux).

In this work, with the core window approach, the coupling between phases cannot be directly included into the model. Fergestad [42] concluded that the interphase leakage field is of minor importance. This means that only the common flux might be of interest for interphase inductance. And these inductances might be calculated analytically by means of a reluctance consideration (using CP1D).

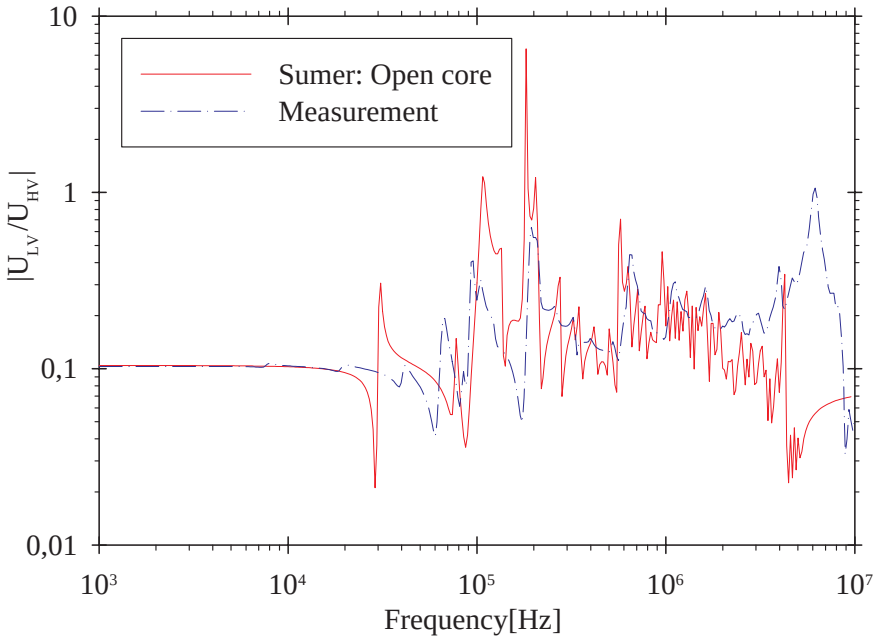

Figure 5.23: Comparison with open core model: Transfer function from HV to LV winding with both neutrals grounded.

As seen from figure 5.23, there are large improvements compared to the previous results neglecting the core (figure 4.10 on page 74). As mentioned SUMER does not support periodic boundary-conditions and all flux must travel through the core window. This makes the reluctance too large and naturally it influences on the transfer function at the first resonances, but general trends and low frequency behaviour has improved significantly.

The conspicuous peak of the model at 4 MHz is not physical but it is the upper resonance due to the bandwidth of the model. This peak occurs since the model is built up of lumped equivalent circuits, and this discretisation will limit the frequency range applicable to the model as the peak showing up at 4MHz. This distinct feature occurs in all the following models one way or the other and must be taken as a disability of the model rather than a physical characteristic of the model.

5.5.2 Closed core equivalent

The next step is to establish a closed core equivalent.

The shape of the yoke equivalent is modeled to obtain a constant reluctance. Since it is modeled in axial symmetry, the reluctance of the yoke will be depending upon its height and the distance from the centre-axis (the total cross-section increases with the distance from the centre-axis). Details on the translation into axisymmetric representation is found in Appendix J.1 on page 216.

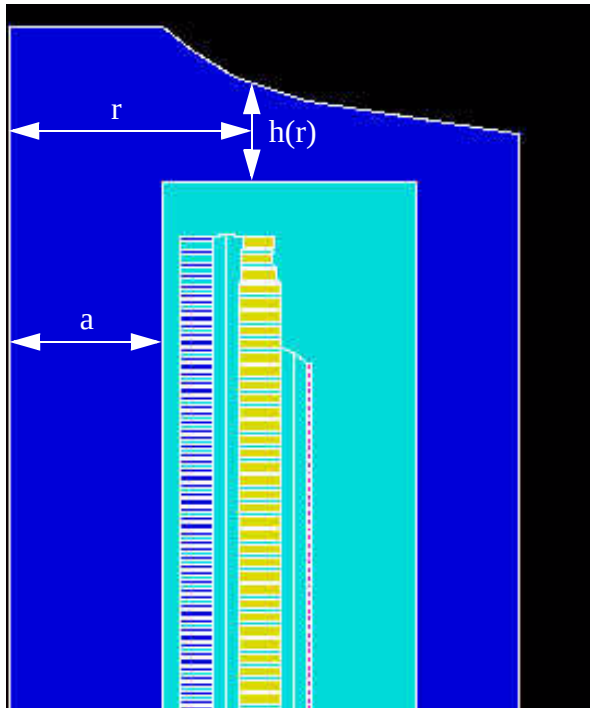

Figure 5.24: Closed core representation in SUMER

Depending on the type of transformer (two leg (single phase), three leg or five leg), the cross-section of the yoke will be equal to or larger than the cross-section of the leg. Assuming a three legged core with the same cross-section for the yoke and the leg, and that figure 5.24 shows the centre phase, the total cross-section for the yoke (two in parallel) will be twice the cross-section of the leg.

Two different topologies were tested regarding the width of the core window:

- Full window size: The full size of the window is used (leg to leg distance).
- Half window size: Half the size of the window is used in order to correct for the distance to the tank and other windings.

A comparison of the two different core shapes (half- and full window size) is shown in fig.5.25

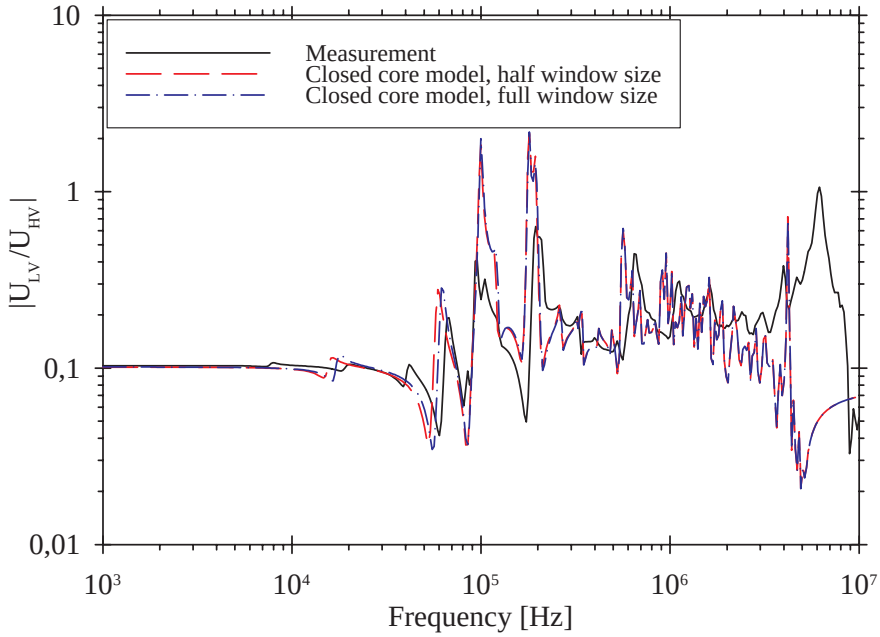

Figure 5.25: Closed core: Full- and half window size (width), $\mu_r = 100$

As can be seen from figure 5.25 the difference between the two is not very large. It seems like the full window size is a bit closer to the measurement. A possible reason is that this situation is closest to the available space between winding and tank since most of the leakage field is set up in this area, and not inside the window. The difference appears only around the lower resonances. Other parameters could also be influencing in the same region, such as the permeability.

5.5.3 Influence of permeability

To study the influence of different initial/nominal permeability for the iron, a set of different simulations led to the conclusion that permeability is not very important since the main part of the field strength will be applied across a large “air-gap” (the core window) at the resonances, and the permeability is at least one decade larger than for free space. The value that seem to agree best to measurements is found to be in the area of 50-100, which complies well with values found in literature (will actually depend on the core material used)

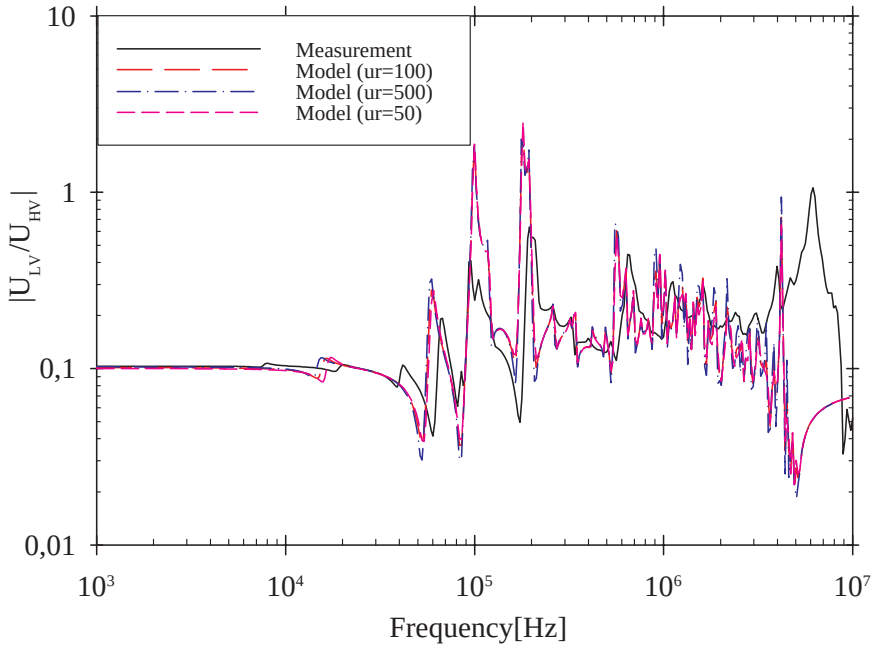

Figure 5.26: Influence of different initial permeability

As seen in fig. 5.26, the permeability is not very important for the accuracy of the model. This means that the values for the self- and mutual inductances in it self are not critical, but the leakage inductance defined by the difference between these two is important. It is obvious that the leakage inductances are determining for the internal resonances. The flux pattern of the leakage flux seems to be important and this is determined by the core leg and the oil volume outside the leg.

Fig. 5.27 illustrates the difference between low and high frequency permeability, where the difference at high frequencies is clearly lower (ratio: 1.4) than at low frequencies (ratio: 10). The reason for this is that the internal skin effect due to the eddy currents is also dependent on the initial permeability.

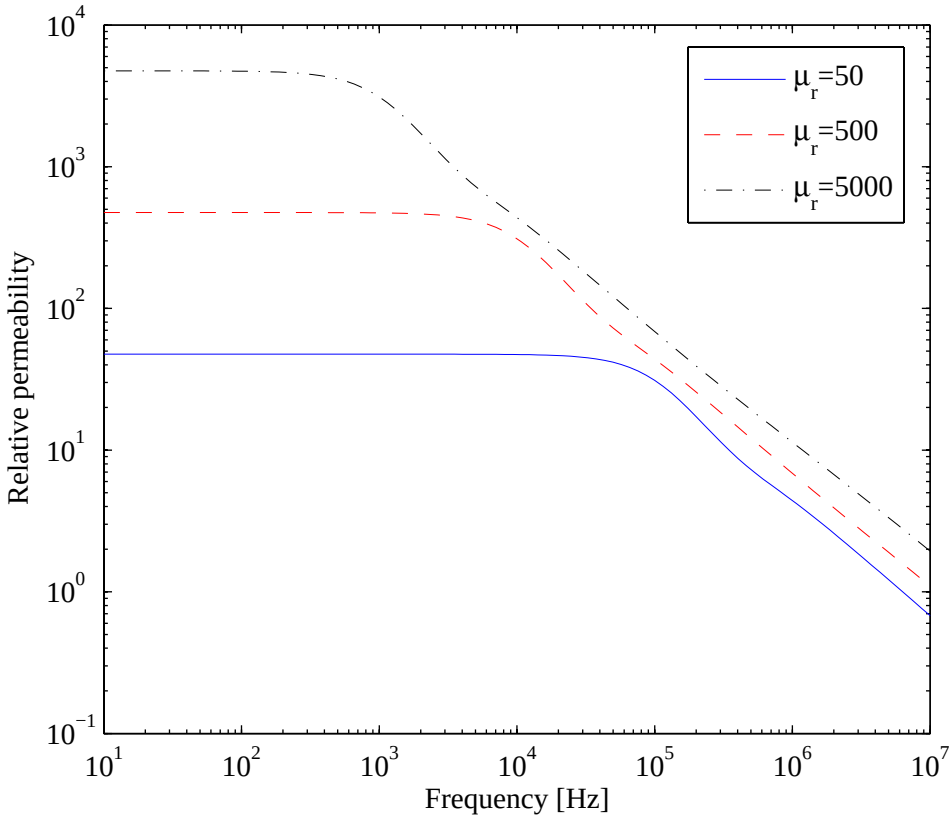

Figure 5.27: Comparison of different permeabilities (real part) as a function of frequency

5.5.4 Other influences

For parameter comparison (to previous chapters), a simulation on 2 different laminate thicknesses were performed, but led to only minor changes in damping. Since the changes are very small the result is not included here.

Another topic for discussion is whether different steels have different high frequency characteristics (non-oriented, domain-refined, laser-scribed etc.) This should be investigated, since additional losses compared to losses calculated using classical eddy current theory are very large at lower frequencies.

The yoke-representation is also questioned, since the inductance of coils close to the yoke seems to be overestimated.

5.6 Discussion and Conclusion

A one-dimensional approach for the complex permeability of the core seems to be fairly accurate. The initial permeability and the resistivity of the laminates is of great importance for an accurate inductance calculation, but are rarely known.

For the two-dimensional representation of the complex permeability including interlaminar effects, the coating resistivity is very important. The resistivity is assumed to be higher for large transformers than for small ones, such as distribution transformers). Coating properties is also assumed to have improved over the years so older transformer may incorporate a lower quality coating. A high coating resistivity reduces the influence of interlaminar effects.

Hypothesis 3 has been disproved in this chapter. The basic formulas developed for one-dimensional complex permeability can easily be implemented into any FEM-software. The one-dimensional approach is used in the following since the two-dimensional approach requires detailed knowledge on the materials used in the laminations, and that is usually not available.

The complex permeability can also be made anisotropic to account for any difference in the x- and y-direction inside the core (grain oriented materials). This has shown to have little effect on the overall losses.

A two-dimensional representation of the core using rotational symmetry will result in a different leakage field than for a real transformer since most of the winding is outside the window of the core rather than inside.

The core representation seem to increase the accuracy of the model since damping is underestimated in the earlier models.

Dielectric losses should also be evaluated since the model will be dominated by the dielectric characteristics at high frequencies. The limit of domination is not known but an assumption could be above 500 kHz. Ageing might also change some of these parameters.

The complex permeability representation does not take into account the fact that the leakage flux will enter the core in two principal directions to the laminates: Either at the edge of the laminate or at its surface. This might be a source of error for the assumption that all laminates carries the same flux or at least have the same field strength on both sides. The leakage-flux will also induce eddy currents in other directions than the flux confined to the core when entering or leaving the core. This is not taken into account. Leakage flux entering a surface will induce large-loop eddy currents.

The homogenized permeability is really anisotropic in 3 directions: The rolling direction of the laminate, the perpendicular direction to the rolling direction and

the perpendicular direction to the laminate surface. This means it is really a 3D problem. An evaluation of the limitations by of the 1D permeability-approximation should therefore be considered in the future (in 3D).

The permeability of the iron does not seem to have a large influence on the voltage ratio. This supports the idea of the leakage inductance being important for the resonances, while the common flux results in a constant voltage per turn. A reasonable value for the initial relative permeability should be between 50-1000, highly dependent on the material.

The size of the window does not seem to be important. It is therefore natural to choose tank radius as the inner radius of the outer leg (in the axisymmetric model).

6 DIELECTRIC PROPERTIES

Hypothesis 4.: *High frequency characteristics of insulating materials are independent of frequency, temperature, moisture, ageing etc. Ageing should therefore not change the FRA-signature.*

6.1 Introduction

As outlined in chapter 2.5, the dielectric characteristics of transformer insulation are normally regarded to be constant. Dielectric losses are usually neglected. Since improving performance of the transformer model is important, it would be natural to take a closer look at the dielectric properties of transformer insulation. If the insulation inhibits dependencies regarding the parameters mentioned in hypothesis 4, it would also be important to know the influence from these parameters onto the FRA-signatures. The reason for this is that it would increase FRA-sensitivity if such effects can be separated from different kinds of deformations.

This chapter review the data available in literature on the typical materials used in insulation systems on power transformers. Additionally some initial measurements are shown for impregnated pressboard (dry and moist), together with a paper sample from a service-aged transformer.

In high frequency models for power transformers, all dielectric properties are normally considered independent of frequency [44], [115], [117]. The reason being limited data on such materials, and the fact that magnetic properties such as inductances and eddy current losses depend more upon frequency than dielectric properties possibly do. This might be one of the reasons for the low priority in investigating prospective effects of dielectric materials for use in high frequency models of power transformers.

The complex characteristics of combined oil and paper insulation have long been recognized [151].

6.2 Definitions

In general, the behaviour of a dielectric in an electrical field is described by means of a complex frequency-dependent permittivity:

$$\varepsilon^* = \varepsilon_r{}^* \varepsilon_0 = \varepsilon_0(\varepsilon'(\omega) - j\varepsilon''(\omega)) \tag{6.1}$$

$$\varepsilon_r{}^* = \varepsilon'(\omega) - j\varepsilon''(\omega) = \varepsilon'(\omega)(1 - j\tan\delta) \tag{6.2}$$

The dissipation-factor ($\tan\delta$) is defined as the ratio between the real and imaginary part of the permittivity:

$$\tan\delta = \frac{\varepsilon''(\omega)}{\varepsilon'(\omega)} \tag{6.3}$$

6.3 Literature survey

Cellulose paper is used in many types of electrical insulation. In its purest form it has a low breakdown strength, it is chemically inert and of low inherent electrical conductivity [150]. Due to its mesh-like structure and fibrous character it normally contains much air and absorbed moisture, seriously lowering its insulating qualities, which is why both air and moisture must be removed and replaced with another material of proper insulating characteristics. With the aid of capillary forces (after drying and vacuum treatment), a replacement of air and moisture with an insulating liquid such as oil is effectively accomplished, resulting in a high breakdown strength.

One approach implementing frequency-dependent behaviour of dielectric materials are Buckow [109]. Buckow measured the dielectric response directly in a transformer geometry (Interturn, interdisc and interwinding measurements). At high frequencies such a measurement setup could lead to erroneous results and should therefore be used with care.

A linear approximation of one of Buckow's [109] experimental results utilized in transformer modeling by Rahimpour [1]:

$$\tan\delta = 1,082 \times 10^{-8} \cdot \omega + 5,0 \times 10^{-3} \tag{6.4}$$

Measurements/data from a more controlled environment such as a custom-built test-cell is highly desirable, in order to confirm or reject the possibility of a frequency dependency.

At high frequencies the dielectric properties in a transformer model becomes dominant, and the importance of possible frequency dependent dielectric effects may become significant.

It has not been possible to find relevant information in the literature on dielectric properties of pressboard regarding frequency, temperature, moisture, field strength and ageing processes (at least for higher frequencies). Published material is reviewed in the following for a comparison to the measurements performed.

6.3.1 Insulating oils

Insulating oils have been used in transformers since 1892 [152]. The first oils were paraffin-based, but due to the high pour-point they were replaced with naphtenic oils. Sludging soon occurred to be a problem with naphtenic oils, and reclaiming techniques were developed, but this also led to an extraction of the natural oxidation inhibitors which resulted in a higher rate of deterioration than new oils. In the late 1950s, the development of industrial anti-oxidants commenced, but such additives are consumed with time and monitoring/refilling is needed.

The many different mechanisms contributing to dielectric loss in insulating oils are thoroughly reviewed by Bartnikas [153]. Dipole orientation, space-charge polarization and ionic conduction was found to be the most dominant mechanisms. Losses related to dipole orientation and ionic conduction increased markedly with the aromatic content of the oil. Another finding was that the ionic conduction losses were found to depend on the viscosity of the oil. Space-charge or interface loss was ascribed to residual moisture since it did not appear to be a simple function of neither viscosity nor aromatic content. His $\tan\delta$-measurements show a distinct temperature-dependent peak, attributed to dipole-losses due to the aromatic content of the oil [153]. At normal, operational temperatures of a transformer, the dielectric losses of insulating oils will be very low in the frequency-range considered in this work (since the peak is well above this range for higher temperatures). It has not been possible to find data regarding losses of aged, polluted oils.

6.3.2 Insulating paper

The major reasons for the widespread use of paper as high voltage insulation are low cost, availability, good electrical and mechanical properties. Paper contain about 90% cellulose, 6-7% hemicellulose and 3-4% lignin [154]. Cellulose, which is a natural polymer of glucose, degrades slowly during service as the polymer-chains break down. This process releases degradation products into the oil.

Investigations done by Morgan [155], show that dielectric properties in a stack of dry multi layer paper is dependent on both frequency and temperature as well as compression and air pressure. His investigations shows that the permittivity increases with compression due to the increased density. As expected, the permittivity asymptotically approaches the permittivity of pure cellulose, when all fibres are compressed.

Race et.al. [156] investigated the dielectric properties of dry cable paper in 1940, where relative permittivity is reduced at high frequencies as the dielectric losses increase towards a peak. This peak is temperature-dependent and is attributed to the dynamics and movements of the main chains. If measurements are complemented using even higher frequencies, another relaxation/peak would occur, which is related to the movement and dynamics of side groups of the cellulose chains [157].

6.3.3 Oil-impregnated paper

Heat and vacuum are applied to the paper before impregnation to remove residual moisture from the paper. If kept in humid surroundings, the insulation will eventually obtain an equilibrium. Moisture degrade electrical properties and must be avoided. It also accelerates the processes of ageing. Ageing itself produces water and it is therefore not possible to avoid moisture in the paper. Nevertheless it is desirable to reduce the initial ageing-rate by lowering the water-content as much as possible. Due to the bonding-strength between H_2O dipoles and the hydroxyl groups of the cellulose molecules, vacuum-dried paper fibres retain between 0.5-1% [158] of bound water.

Race et al. [156] also measured the real and imaginary part of the permittivity for oil-impregnated cable-paper. Since cable-paper and kraft-paper might be slightly different, and the oil-quality is unknown, these measurements must be used with care within a transformer model, but may be used in lack of anything else. As a base for comparison to future measurements they might prove beneficial.

6.3.4 Ageing effects

Deterioration results in sludging, particles and ageing-products such as acids, moisture and others. These by-products will probably have some influence on the dielectric characteristics. At least for the dielectric losses. The big question is whether this influence will appear in the frequency-range of interest in this work, i.e. above a few hundred kHz.

The high frequency dielectric properties are traditionally considered to be insensitive to ageing. But Batruni et.al. [159] investigated the effect of thermally accelerated ageing of kraft-paper. The real part of the permittivity and the loss tangent were investigated by monitoring the changes in capacitance and conductance as a function of frequency and time of ageing. The initial DP-value were 717, and after 30 days of accelerated ageing, it measured 390. This means that the paper was not aged to near-end-of-life stage (at a DP of 150-200). Water was produced resulting in a 10% increase of the capacitance. Additionally the degradation of the cellulose structure contributes to an increase of 15% resulting in a total increase of 25%.

It must be noted that the conductance changed significantly at low frequency but only minor at high frequency. Service-aged paper might hold other deterioration products in addition to those found in this experiment, but high frequency influence is not known. A conclusion can therefore not be drawn from these results, but rather emphasise the importance of further measurements, both on new, aged (experimentally) and service-aged samples.

Since one of the by-products of deterioration is water, dielectric properties could be expected to change at high frequencies with ageing, as for low frequencies. Results presented in [159] show little or no change in the dielectric losses at higher frequencies.

While the influence of moisture upon dielectric properties seem to be minor for high frequencies, it is of great importance at lower frequencies when measuring dielectric response [161].

6.3.5 Discussion

It is important to notice the fact that equilibrium of water in oil-paper insulation is temperature-dependent. This equilibrium will not be important for prospective FRA measurements. But if the moisture influences on the dielectric properties, it will be important to notice the fact that there is a difference in temperature inside a winding structure, and that less moisture will be bound in the hottest areas of the insulation structure. It may be important to be aware of the time since the transformer was disconnected when applying FRA measurements (at least for low frequency dielectric response measurements as utilized by Gäfvert et al. [160]).

6.4 Measurements

Since published literature are not complete on the above subjects (specially for pressboard), measurements are needed in order to determine dielectric parameters to use in power transformer models. The main purpose of this is to accurately balance the influence of dielectric vs. the magnetic parameters at high frequencies in a transformer model and to identify the losses accurately.

6.4.1 Measurement-setup

A test setup using Novocontrol Alpha Analyser [162] was used to measure the dielectric properties (derived using the calculated geometric capacitance) of impregnated paper/pressboard. A custom-built test-cell is developed in order to benefit the sensitivity of the instrument (fig. 6.1). It is made of teflon (PTFE) with stainless steel electrodes. It is has seals to minimize moisture ingress, it has a spring loaded electrode to ensure contact between electrodes and sample, and it is built without guard since this involves problems at high frequencies.

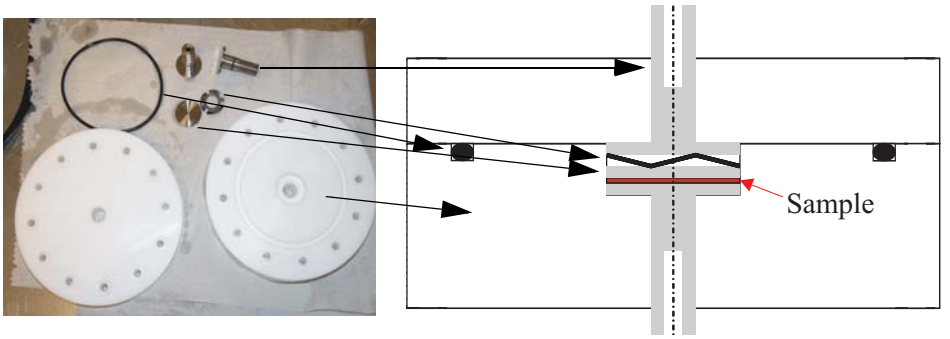

Figure 6.1: Custom-built dielectric test cell (Electrode diameter: 25 mm)

The test setup consists of a laptop for measurement automation. The laptop controls the temperature and starts a new measurement when desired stable temperature is reached. It also controls the Novocontrol dielectric measurement system and the principle of the setup can be seen in fig. 6.2:

Figure 6.2: Novocontrol Alpha analyser, ZG4 test interface, laptop and test cell

6.4.2 Service-aged paper

Experiments were performed using samples taken from a service-aged 6MVA transformer that was replaced after 50 years of operation (windings were replaced in 1969). The moisture content of this sample has been determined to be approximately 2% (weight), containing in addition high degree of ageing by-products such as acids, particles etc. The real part of the relative permittivity is shown in fig. 6.3:

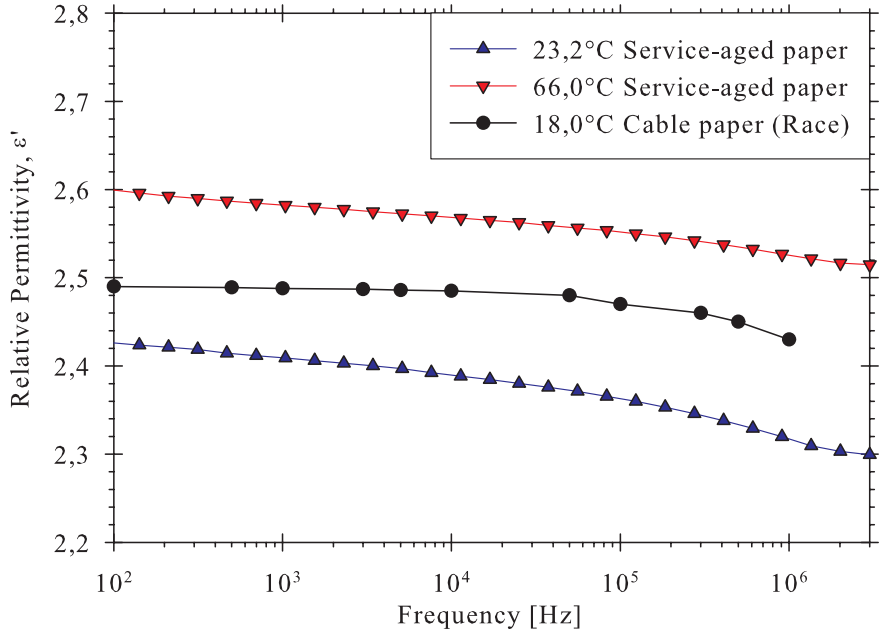

Figure 6.3: Relative permittivity ε′ of service-aged impregnated paper at two different temperatures compared to a measurement by Race [156] on cable paper

The measured relative permittivity values are compared to results presented by Race on oil-impregnated cable-paper (impregnant unknown).

Comparison of the dissipation factor ($\tan\delta$) is more interesting in terms of the transformer modeling. In fig. 6.4, the imaginary part of the permittivity (loss factor) is not shown since the variation in the real part is minor.

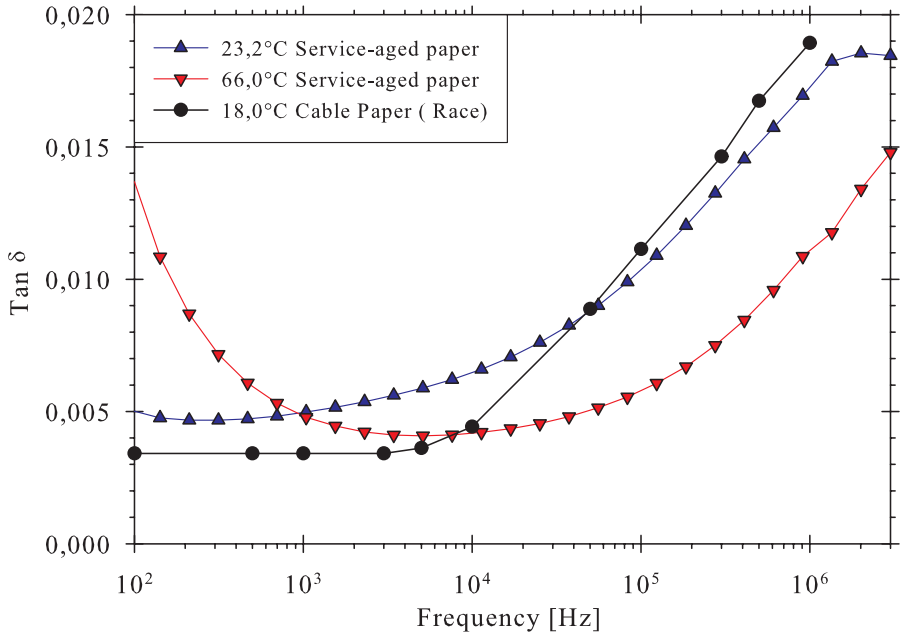

Figure 6.4: $\tan\delta$ *of service-aged impregnated paper at two different temperatures compared to a measurement by Race [156] on cable paper*

As seen from fig. 6.4, the high frequency dielectric losses does not increase with ageing compared to the cable-paper. Temperature shifts the curve to higher frequencies. At the highest temperature examined (66°C), the influence of moisture gain distinction at frequencies below 10^3 Hz, due to increased conductance.

6.4.3 Impregnated Pressboard

Fig. 6.5 shows measured relative permittivity for oil-impregnated pressboard at different temperatures and levels of moisture.

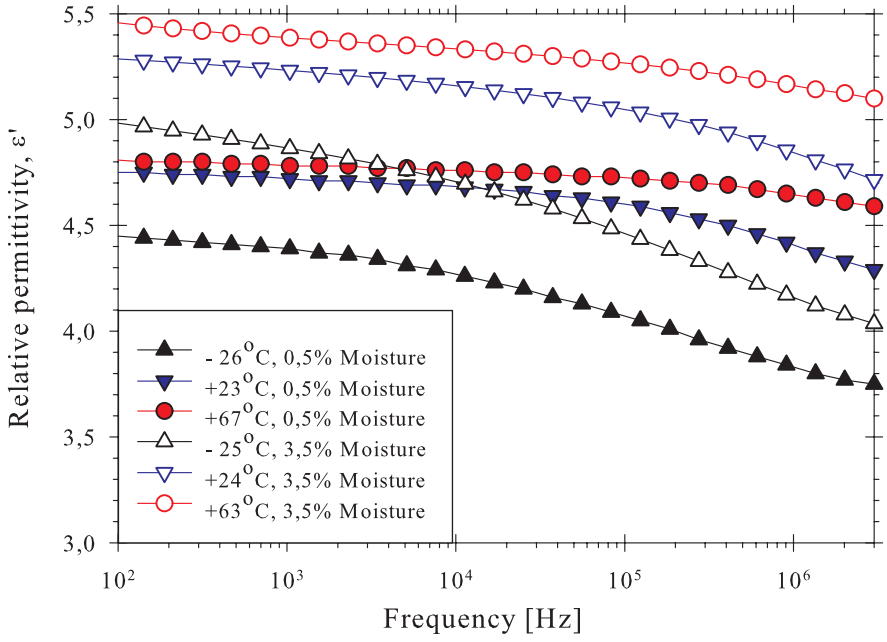

Figure 6.5: Relative permittivity ε′ of impregnated pressboard at three different temperatures and two moisture-levels (dry/wet)

By studying fig. 6.5, it can be seen that the influence of moisture decreases with increasing frequency as for kraft-paper. Temperature controls low frequency behaviour, and also the position (in frequency) of the β -relaxation around 1MHz as observed for the dielectric losses in fig. 6.6.

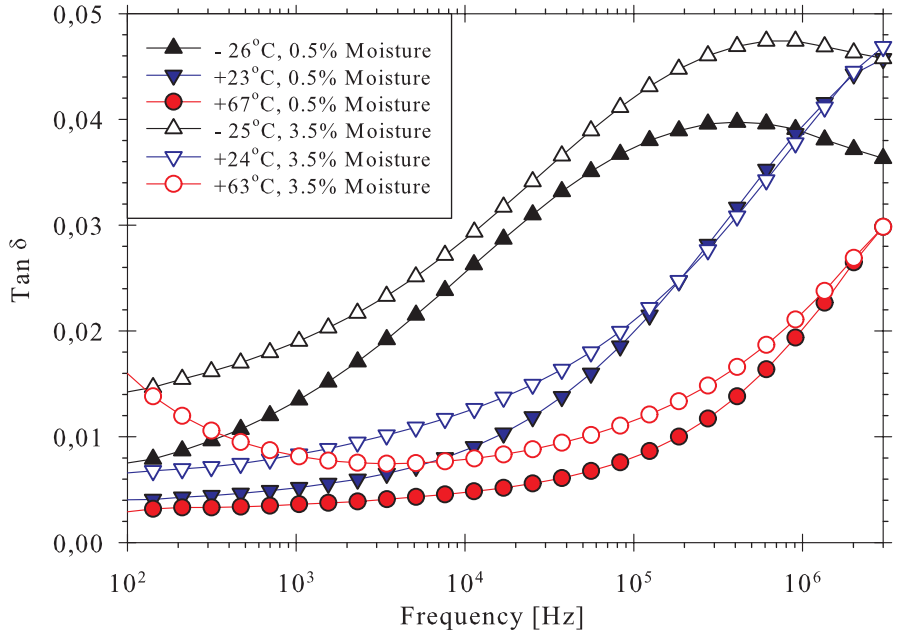

Figure 6.6: Tan δ of impregnated pressboard at three different temperatures and two moisture-levels (dry/wet)

The dielectric losses show a clear decreasing dependency of moisture to increasing frequencies. This is in agreement with the finding in ref. [159]. The dielectric loss of pressboard is twice the loss of cable paper. Substituting pressboard-data with data from cable paper into a transformer model, may result in too low damping in the transformer model at high frequencies. From the measurements at low temperature, it can be seen that high moisture content increases the amplitude of the β-relaxation, while temperature results in higher peak frequency.

6.4.4 Discussion

The slope of the measurements in fig. 6.3 seem to be different from the results of Race [156] (cable-paper). This might be due to the moisture-content of the service-aged paper sample.

The relative permittivity for impregnated pressboard is slightly over-estimated. The test-cell was initially built for measurements on paper, and by using pressboard, the pressure on the sample is increased (but density unknown) due to the limited space inside the test cell. The geometric capacitance of the test cell is used to calculate the real and imaginary part of the permittivity from the measured complex capacitance. The calculated geometric capacitance is based on nominal thickness and applied pressure is not known. Since the loss factor is equally overestimated, the dissipation factor, $\tan\delta$, which is the interesting part for this work, is assumed to be correct (see fig. 6.6).

The results in fig. 6.5 indicate that FRA-measurements are independent of variations (temperature and moisture) in the real part of the permittivity, since the difference between a moist, hot pressboard sample and a dry, cold one is only 10%. The reason being that the insulation structure mainly consists of oil-gaps. This means that the total influence is reduced since temperature dependency of permittivity is lower for oil than for cellulose. The same assumptions can be made for the dielectric losses, where influence of moisture is reduced at higher frequencies. On the other hand, increasing temperatures shift the curve upwards in frequency and the difference in dielectric loss at 23° C and 67° C is one decade at 1MHz. This difference might be sufficiently large to create differences in FRA-measurements, and should therefore be investigated further.

6.5 Implications for the transformer model

It is interesting to know the difference between changes due to ageing and mechanical deformations. Three different cases are studied in terms of ageing or frequency-dependent parameters.

6.5.1 Loss of clamping pressure

Losing clamping-pressure is a common problem of old transformers, especially when excessively dried after refurbishment. This is caused by the mechanical hysteresis in paper and pressboard. The pressure is reduced when drying, due to paper shrinkage.

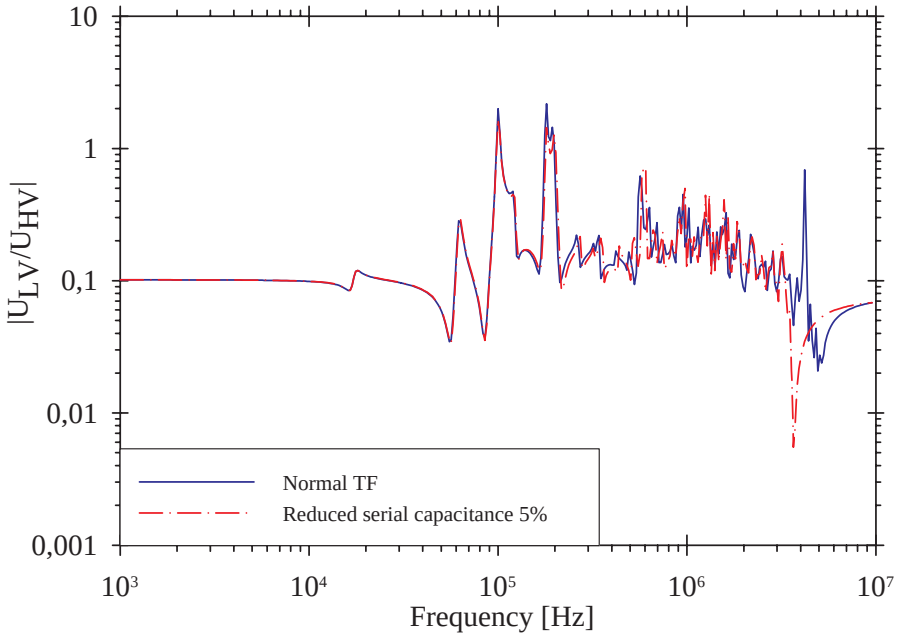

Figure 6.7: Simulation of decreased series capacitance due to loss of clamping pressure

As seen in fig. 6.7, the reduction of series capacitance creates a minor displacement of the transfer function upwards in frequency. A reduction of 5% is mainly assumed to arise from the reduction of permittivity in pressboard spacers since permittivity is dependent on the applied pressure (density) as shown by Morgan [155]. Time constants and hysteresis are also involved in the process of clamp-force reduction, and this must be kept in mind if reducing the clamping force in an experiment. A better approach for such an experiment would be to measure before and after re-clamping the windings.

6.5.2 Frequency-dependent dielectric losses

Deterioration-products severely changes the low-frequency characteristics of oil-paper insulation, the reason being ionic conduction and moisture. The high frequency characteristics are not equally influenced by moisture. Some influence is observed but not sufficient to cause severe changes in FRA-signature.

The importance of including the dielectric losses properly, is shown in fig. 6.8

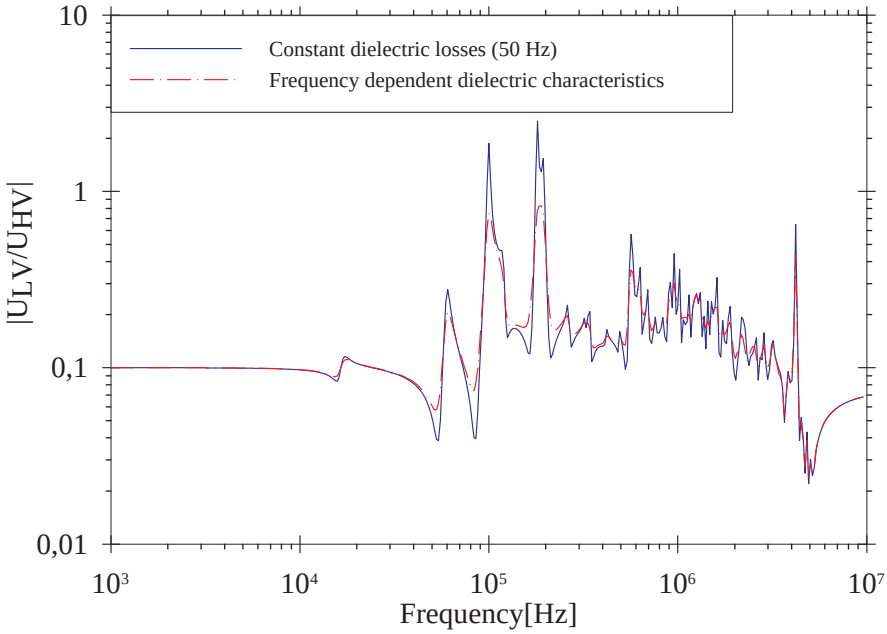

Figure 6.8: Simulation with/without frequency dependent dielectric losses included.

A two point linear interpolation is used in this case for determining the dielectric loss factor (from measurements at 50 Hz and 1MHz). Since the increase in dielectric losses is low below 100kHz and high above, the losses are overestimated up to 1 MHz in this case. A future improvement would be to use a 3-point interpolation. Losses in the area around 1MHz is accurately represented.

The same model is utilized to find the influence of temperature on FRA-signatures due to change in dielectric losses. A small difference is found when simulated FRA-signatures are compared at 23° C and 67° C degrees. This difference is expected to increase with increasing difference in temperature.

6.5.3 Ageing

Some change due to ageing should be expected in capacitance depending on degree of ageing and ageing by-products. Since there are large oil gaps in a winding structure, the overall change is small and the transfer function is not changed severely. Still it is important to know the difference between changes induced by deformations and changes as result of ageing etc.

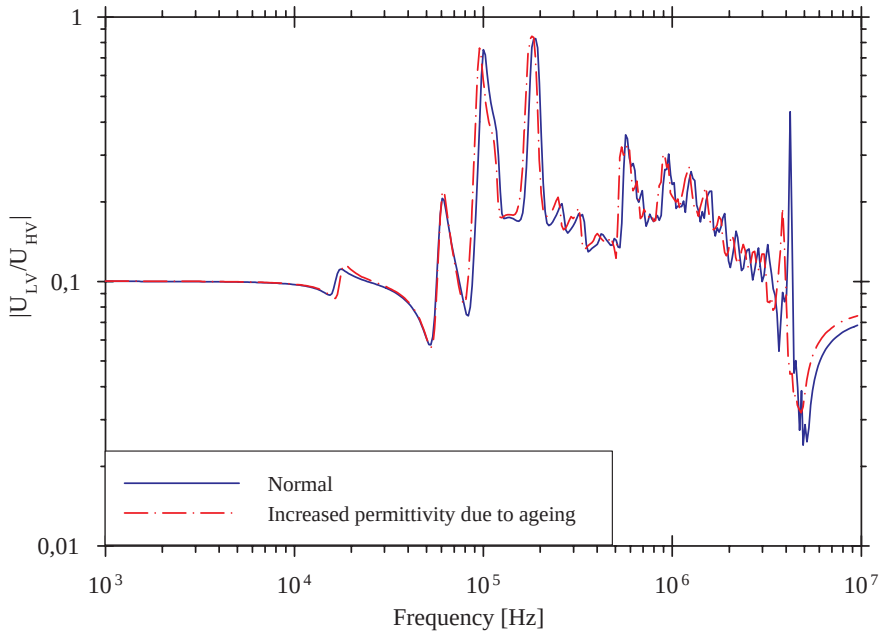

Figure 6.9: Simulation of increase in capacitance due to ageing as outlined by Batruni et al. [159]

The degree of ageing applied to the model is the maximum change in properties due to ageing found by Batruni et al. [159]. Their experiment showed an increase in relative permittivity of 15% due to the deterioration and 10% due to moisture. The samples were aged to a DP-value of 390. Equal to own experiments, these measurements also showed that influence of moisture is less at higher frequencies than for the lower frequencies, and that the change in dielectric losses at higher frequencies is very small.

Since the characteristics of the oil are kept constant (unaffected by the ageing) the resulting series capacitance is not severely changed in spite of the large change in the characteristics of paper (and pressboard). The dielectric losses were kept unchanged as explained above.

6.6 Conclusions

The survey of literature showed a dependency of dielectric characteristics to temperature, ageing (related to moisture), frequency, and density. This survey also revealed the lack of measurements on pressboard insulation. Pressboard is extensively used in power transformers and some initial measurements are performed. Additionally measurements on service-aged oil-impregnated paper are conducted since little information is found on service-aged samples.

From fig. 6.4 it is apparent that the high frequency characteristics of aged impregnated paper are not significantly increased compared to unaged paper, since it is comparable to measurements done by Race [156] at the same temperature on unaged cable paper. Using data from impregnated paper to describe dielectric losses for pressboard leads to deviations. As seen in fig. 6.6, the dielectric losses for pressboard is twice the losses for paper at 1 MHz. In addition to this, a strong influence from moisture can be observed in the real part of the permittivity for pressboard (ref. fig. 6.5)

Interfacial polarisation is believed not to influence on high frequency characteristics since this typically is a low frequency mechanism (the conductivity is very low in the materials considered). It is therefore assumed that interface polarization at higher frequencies can be neglected when different materials are combined in a transformer model.

Voltage-dependent loss-mechanisms are not included since all results will be compared to measurements done on very low voltages, but might be important for a model applied to impulse overvoltages etc.

Loss of clamping-pressure is investigated in chapter 6.5.1. This investigation does not show a severe change in spite of a 5% change in series capacitance. The FRA-signature is shifted slightly upwards in frequency due to the reduction in capacitance. The change is largest above 100 kHz.

Ageing-studies have identified an increase in capacitance (real part of permittivity) due to degradation of cellulose. An increase of 25% in cellulose results in a total increase of about 5% in the example investigated in this work. This increase results in a shift towards lower frequencies above 100 kHz. Since ageing and loss of clamping-pressure usually occur together, these changes may cancel each other.

The inclusion of frequency-dependent dielectric losses compared to constant values (based on 50Hz measurements), increased resemblence to measurements. The improvements will be further discussed in the beginning of next chapter.

Referring to hypothesis 4, it is shown that material characteristics are highly dependent on moisture, temperature and frequency (important for high frequency

transformer models). In addition, ageing may increase the real part of the permittivity by as much as 25%. On the other hand, these changes does not seem to influence severely on FRA-characteristics.

Hypothesis 4 is rejected. The high frequency characteristics of insulating materials are dependent on frequency, temperature, moisture and ageing. On the other hand, no significant change to the FRA-measurement was observed due to the ageing phenomena.

7 MODEL APPLICATIONS

Hypothesis 5.: *High frequency transformer models can be established with high degree of conformity to terminal measurements, provided constructional information is available.*

The introduction of the iron core representation and the inclusion of frequency-dependent dielectric losses have increased the agreement with model and measurements significantly. There are still some difference, but compared to the approaches in chapter 3 and 4, the improvements are substantial, and demonstrate the importance of a proper representation of the iron core and also the dielectric properties of the insulation structure.

The final model established in chapter 6.5.2 is here further investigated in order to identify the reasons for the differences between measurements and calculations.

Further some results are presented on overvoltage calculation using the final model, both internal stresses and terminal overvoltages/resonances to show the versatility and possible applications of the model.

At the end of this chapter some results from FRA investigations are presented. These are mainly simulations, but some measurements are also evaluated in order to identify natural variations when comparing signatures.

For some of the investigations (as indicated in each case), the inclusion of frequency-dependent dielectric losses led to numerical problems in SUMER. These investigations are performed with different terminal conditions, different tap-changer position or simply based on the initial approach for the dielectric parameters (dielectric losses included using constant values based on 50 Hz measurements).

7.1 Final model

By identifying the reasons for the differences between measurements and calculations, details for further research on this topic can be suggested. It seems to be possible to establish high frequency transformer models based on constructional information with high degree of accuracy compared to terminal measurements. Experimental verification should be done to assess the validity of the internal stresses calculated using this model.

Agreement with measurements have increased significantly with the inclusion of the iron core and additionally the implementation of frequency-dependent dielectric losses. Still there are deviations as seen in fig. 7.1:

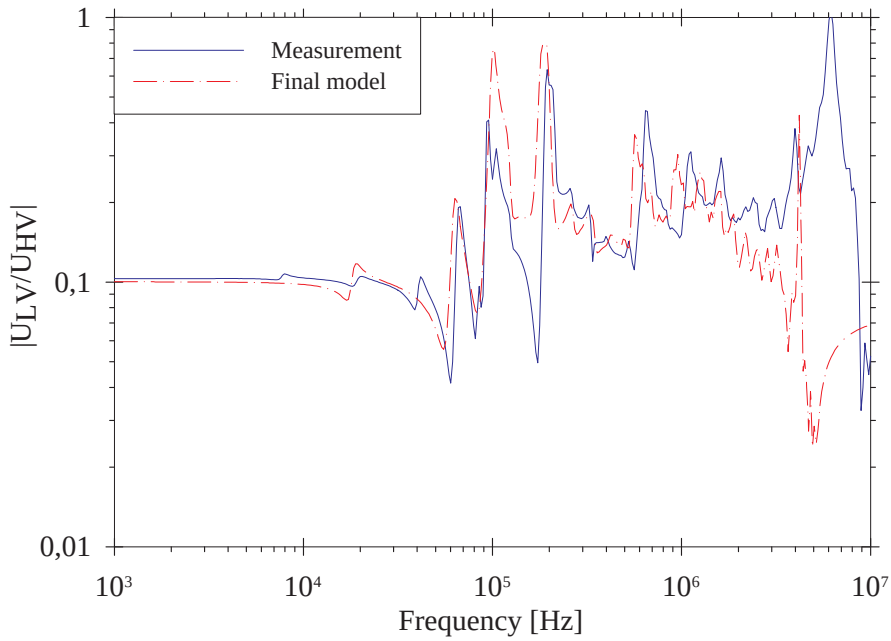

Figure 7.1: Comparison of final model to measurement (voltage ratio)

In order to study and identify the deviations, it is preferable to compare the calculated short circuit input admittances to measurements.

The reason for using the admittance rather than the voltage-ratio measurement, is that it simplifies the identification of differences between model and measurement. It is easier to relate the differences to certain parts of the transformer, since the voltage ratio/transfer function may be represented by a set of admittances between terminals and from terminals to ground (such as the representation in fig. 7.4). Each of these admittances have different characteristics that can be recognized either through comparison to measurements or simulations.

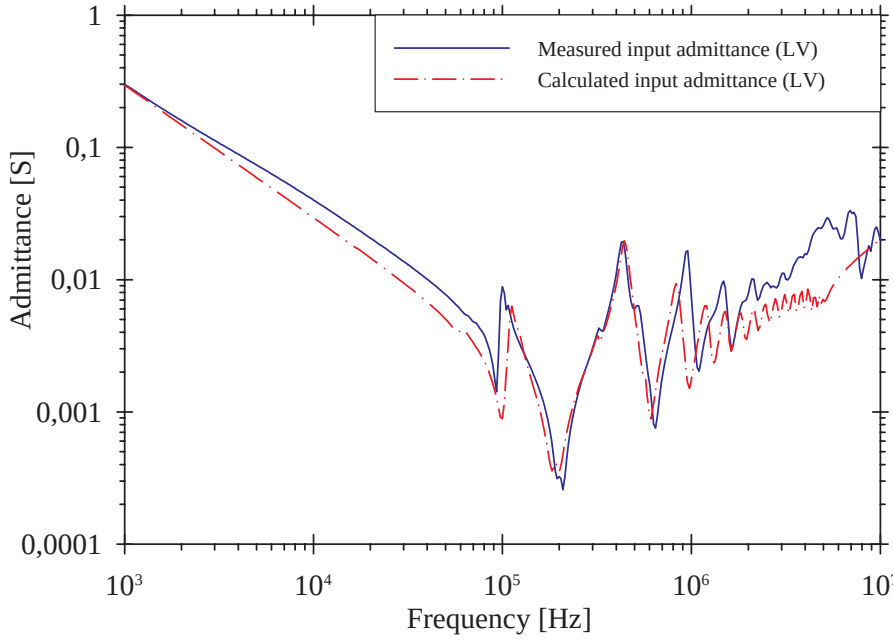

Figure 7.2: Comparison of measured and calculated input admittance for the LV-winding

Fig. 7.2 shows good agreement between measurement and model up to 1MHz. The LV-winding consists of a simple design and it is modeled with a discretisation of 4 turns per lumped element. Amplitude and damping of the resonance-frequencies are accurately represented up to the practical bandwidth of the model.

The next figure shows the corresponding input admittance for the HV-winding.

Comparing model to measurement for the HV-winding (see fig. 7.3) shows more disagreement than the LV-winding, since the design is more complex (a regulating winding is included), and the discretisation is not as refined as for the LV-winding

(7 turns per lumped element for the HV winding, and 9 turns per lumped element for the REG.-winding).

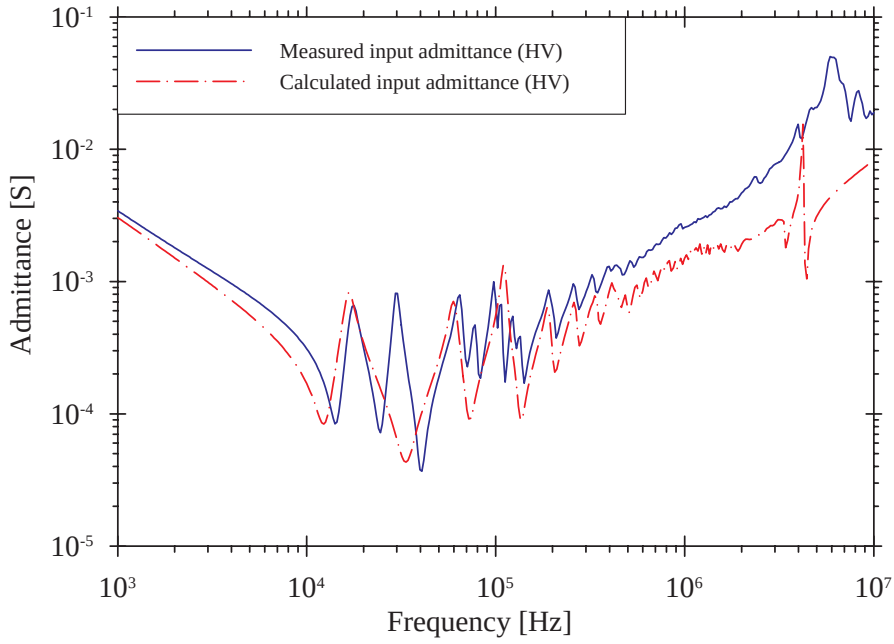

Figure 7.3: Comparison of measured and calculated input admittance for the HV-winding

A possible explanation for the deviations in the range from 10-50 kHz is the influence of the leakage field coupled to neighbouring phases since this is not modeled when applying the axisymmetric approach. These influences are discussed further in chapter 7.4.4.

The reason for the disagreement around 100 kHz is attributed to the representation of the tap-changer and the regulation-winding (explained in chapter 7.4.5). The cause of the vertical displacement at higher frequencies might be an incorrect representation of shunt admittance (possibly capacitance to ground). Some of these disagreements are also elucidated later.

7.2 Transferred overvoltages

In order to apply the model developed in network studies, a time-domain model must be established. The model in this work is established in the frequency domain. In order to perform time-domain simulations, ATP/EMTP is preferably used. This requires an equivalent, linear terminal-model consisting of frequency-independent elements to be established, representing the admittances illustrated in fig.7.4:

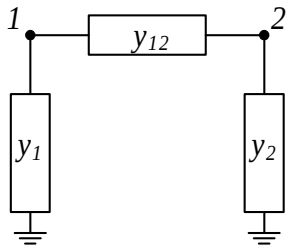

Figure 7.4: Terminal admittance model to be approximated

The input admittance of terminal 1 will be: $Y_{11} = y_1 + y_{12}$

A robust and versatile tool for approximating terminal equivalents is developed by Gustavsen and Semlyen [62], and is available in public domain. It is named Vectfit and applies vector fitting in order to find a linear equivalent to the terminal model of the transformer.

The first step is to reduce the system description as outlined in chapter 3.1 to the terminals or internal nodes of interest. Establishment and reduction of the system is described in detail in appendix E. The same technique can be applied for a study of internal stresses during impulse overvoltages, by defining internal nodes as terminals before reducing the system-description. An example is shown in chapter 7.3

The reduced terminal description, is processed by the vector-fitting routine, Vectfit. The output from Vectfit is a set of poles and residues that describes the system approximation. A set of starting poles is calculated from the system-description in order to have faster convergence. Vectfit approximates the frequency response (in this case an admittance) with rational functions, expressed in the form of a sum of partial fractions:

$$Y(s) \approx \sum_{i=1}^{N} \frac{c_i}{s - a_i} + d + s \cdot e \qquad (7.1)$$

c_i and a_i are the residues and poles, respectively. Terms d and e are optional.

The equivalent terminal admittance is built up of a set of real and complex conjugated poles together with the constant terms d and e as shown in fig. 7.5.

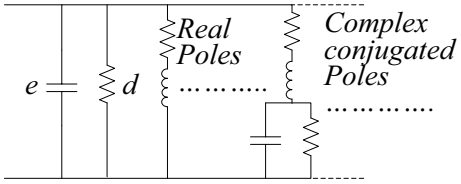

Figure 7.5: Terminal equivalent of approximated admittance

The approximated terminal admittances for T3 Buran are shown in fig. 7.6

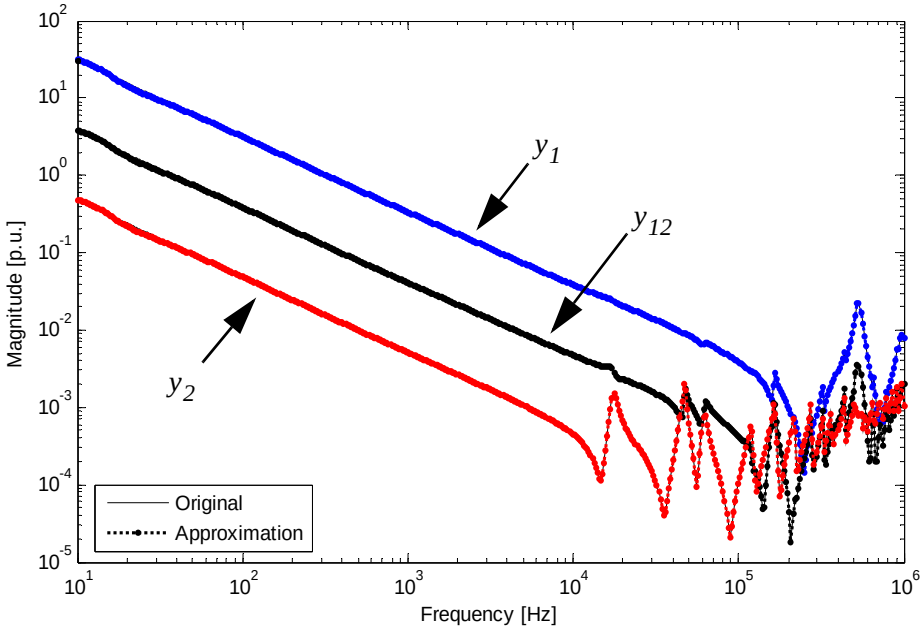

Figure 7.6: Results from Vector-fitting the terminal admittances of the T3 Buran model

After the fitting is completed, Vectift outputs a file describing the terminal equivalent. The format is a RLC-coupled branch file, compatible with ATP. Time-domain simulations can be applied to the model in order to investigate transformer-network interaction, transferred overvoltages or internal stresses.

The transfer function of T3 Buran model (minimum tapping position: -6) is investigated in order to determine the critical frequencies for terminal resonance overvoltages in fig. 7.7.

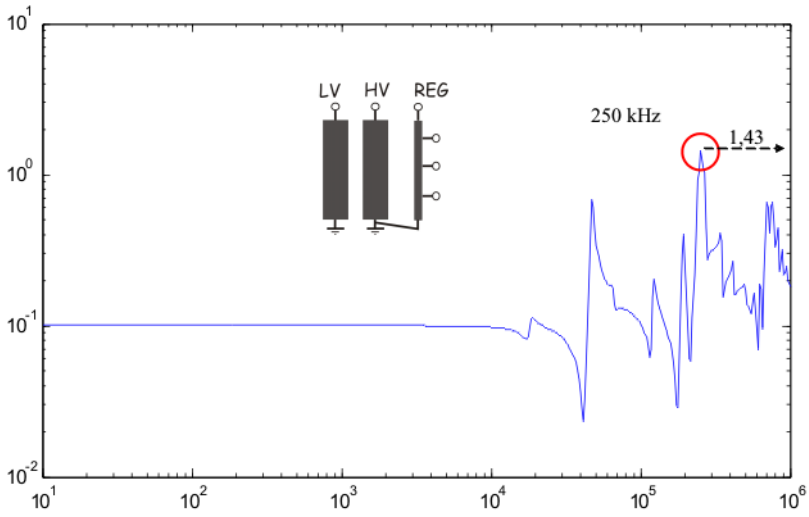

Figure 7.7: Transfer function from HV- to LV-side, showing critical frequency at 250 kHz (minimum tapping position).

A critical frequency can be found at 250 kHz, where the secondary terminal may reach 1,43 pu referred to the HV-side. When referring this to the secondary side it equals 14,3 pu. This voltage will likely result in a flashover, but in order to investigate the time-constant, the model established using Vectfit is evaluated in ATP by means of a constant excitation at 250 kHz as seen in fig. 7.8:

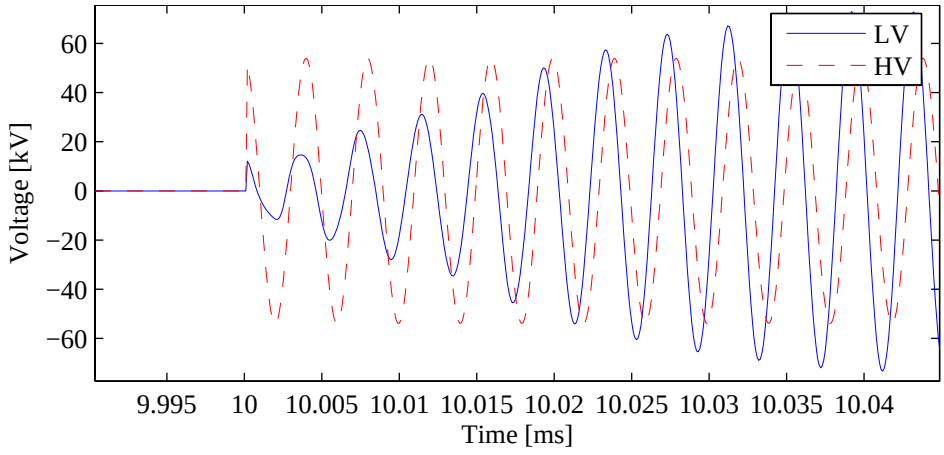

Figure 7.8: Constant excitation at 250 kHz in order to investigate the time constant of the model.

Fig. 7.8 shows the buildup of the overvoltage at the secondary side and the time constant involved (approximately 0,02 ms in this case). The primary side must be excited for a sufficiently long time in order to reach a critical voltage at the secondary side. Whether this will occur or not in a real network depend on the damping in the transformer and in the network.

A simple example is given in the following in order to investigate the phenomena in a more realistic case. The layout is shown fig. 7.9 where an unloaded transformer is fed by a short cable, and an earth fault occurs at the feeding end of the cable initiating travelling waves between primary terminal of the transformer and the fault-site:

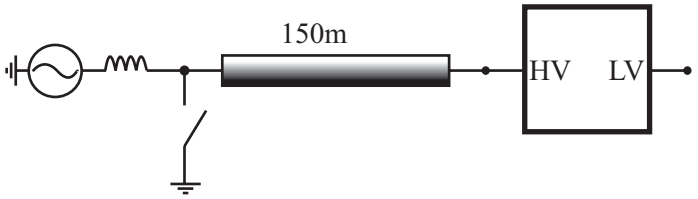

Figure 7.9: Network-transformer resonance example

For illustrative purposes, the cable in fig. 7.9 is assumed to be loss less, which for this short cable length is a reasonable approximation.

As seen in fig. 7.10, the overvoltage on the secondary side reaches 12 pu, which most likely will result in a flashover.

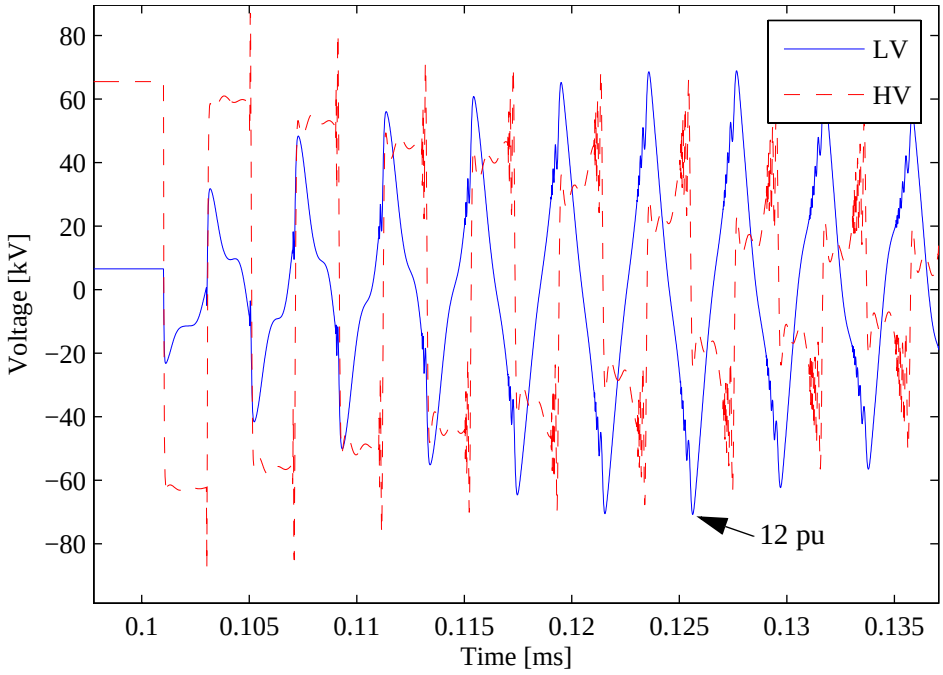

Figure 7.10: Resonant overvoltage at secondary side reaching 12 pu

7.2.1 Neutral connection

The approach used in this work has been to study a single phase of a three phase transformer. This simplification is made in order to be able to identify influencing parameters and to reduce the complexity of the model. In all investigations the neutral have been directly grounded. In real cases, the neutral can be isolated, grounded through an impedance or directly grounded. The topology used for grounding will have a large influence on the terminal and internal behaviour of the transformer.

7.2.2 Secondary loading

Most of the investigations done in this work on overvoltages, include an open/ unloaded secondary terminal and thus they represent a worst case scenario. If the secondary terminal is connected to the grid, the proper high frequency representation would probably be the characteristic wave impedance of the connected cable or line. This will in most cases result in sufficient damping and limit the switching overvoltages. The FRA investigations done in this work are compared to measurements using probes, and since these have a high input impedance, it is correct to compare with an unloaded model of the transformer.

7.3 Internal stresses

Abnormal incidents in the network such as switching operations, faults and lightning strokes cause internal stresses in a transformer winding. Basic considerations are normally conducted by the manufacturer at an early stage in the design phase in order to predict possible problems. Additional calculations may be necessary in close cooperation with the customer, if special problems related to either fast GIS-transients or switching oscillations, are anticipated.

The first step in an analysis of internal stresses may be an investigation of the resonant modes inside the winding. For a given set of terminal conditions, the internal voltages can be derived as a function of frequency and position, ref. fig. 7.11:

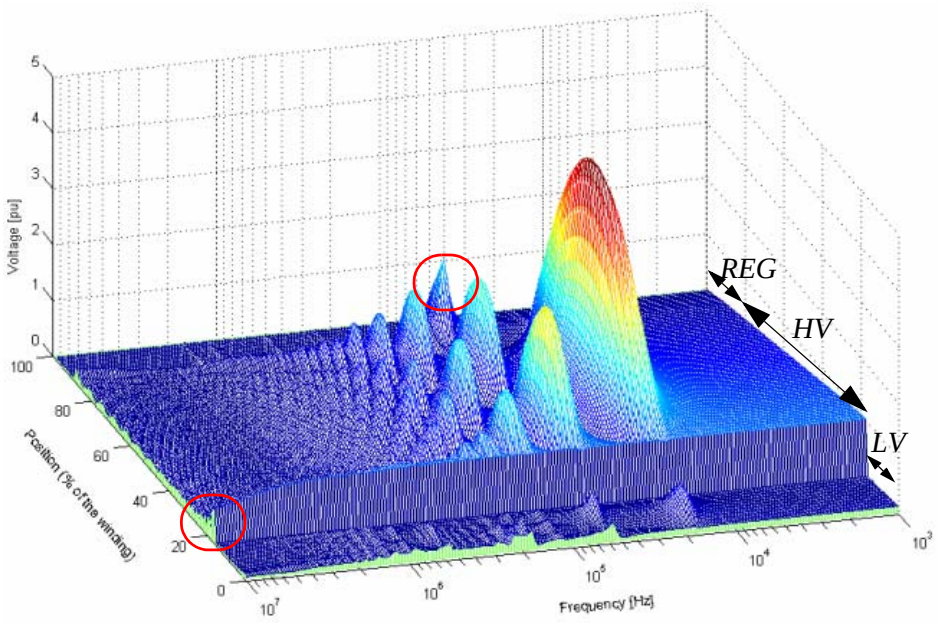

Figure 7.11: Internal voltage distribution plotted against frequency and position along the winding (LV:0-18%, HV:18-90% and REG:90-100%)

This type of visualization gives a detailed overview of the different potential problems within the winding. The main resonant modes of the HV-winding can clearly be observed (Fergestad [44] designated this as space harmonic currents). The second mode coincide with a resonance in the regulation-winding. This will be dependent on the tapping-position. The capacitive behaviour of the HV-winding can be seen at high frequencies (a steep gradient at the first discs in the HV-winding). The resonant modes must be considered together with the different line- and cable-lengths connected to the transformer. Capacitor-bank-switching is one of the topics that must be considered seriously. In general, any switching- or

fault-situation leading to a resonant excitation at any of the frequencies showing up in figure 7.11, must be evaluated in particular since the time-constants cannot be directly derived from the admittance matrix of the transformer.

7.3.1 Interdisc stresses

Stresses between discs are normally evaluated for standard lightning impulse amplitudes according to [137]. The test object in this thesis was designed to withstand a BIL-amplitude of 300kV. Constructional measures have been taken in this design in order to withstand impulse stresses: The number of turns in the 3 first discs are reduced, in order to make room for extra pressboard insulation is surrounding these discs. Such details of the geometry can be seen in fig. 7.16.

The discretisation in these calculations are 2 discs per element. This means that the voltage between node 1 and 2 is the voltage across the two first discs. The reason for this was to be able to compare with similar results from another software. Node 1 is the winding terminal.

Fig. 7.12 shows the nodal voltages to ground during a standard lightning impulse having an amplitude of approximately 300 kV. Nodes 1-6 cover the first 10 discs within the HV-winding.

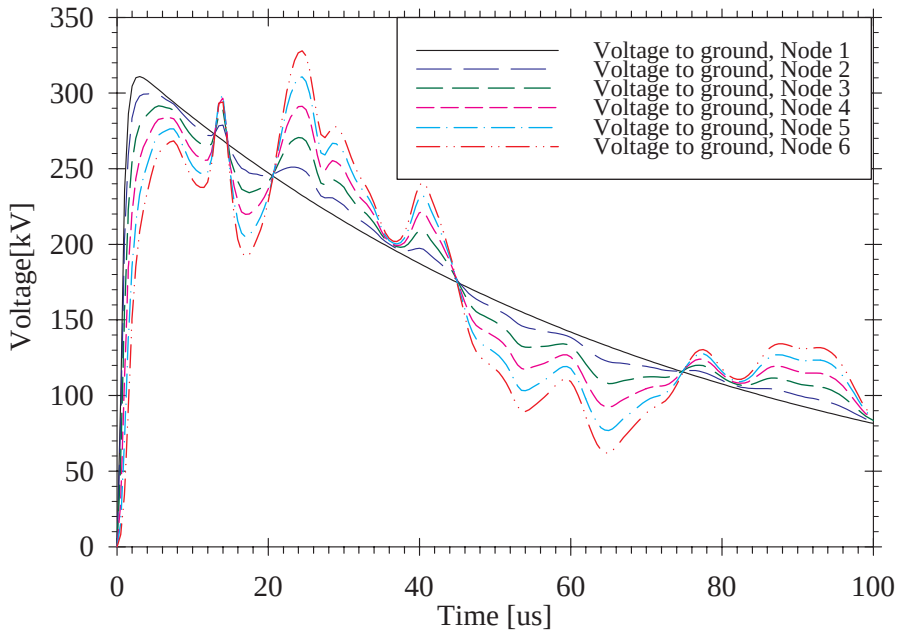

Figure 7.12: Nodal voltages to ground at full lightning impulse

As seen from fig. 7.12, some of the internal resonances are exited.
In order to study internal stresses, the interdisc voltages must be evaluated.
Fig. 7.13 shows the interdisc voltages (2 discs).

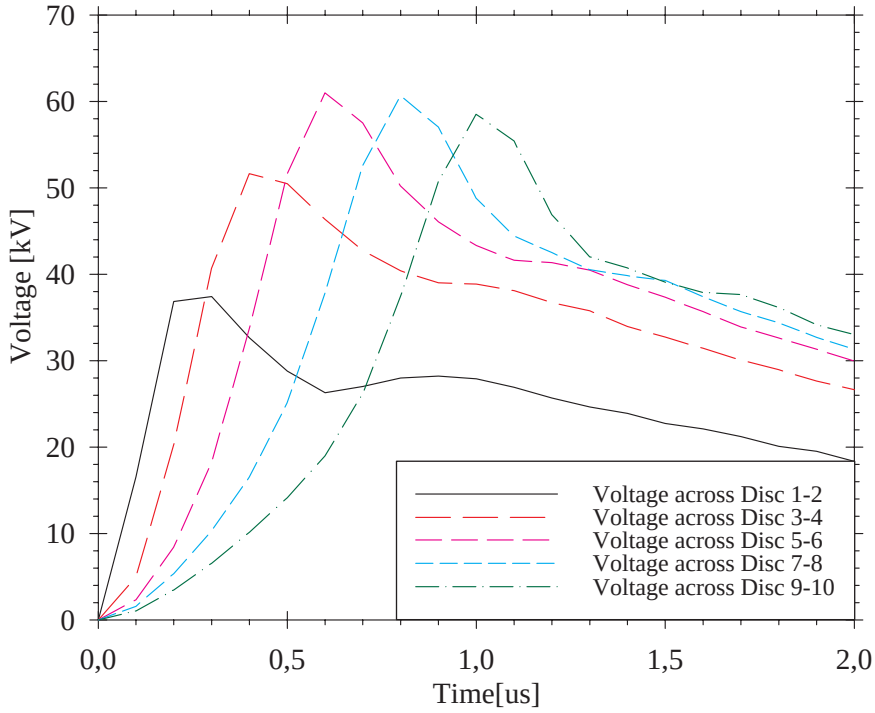

Figure 7.13: Interdisc voltages at full lightning impulse

As seen from fig. 7.13, the maximum voltage across discs 1&2 is less than for the four subsequent groups within the winding. Normally the voltage will be highest across the first disc within the winding at impulse stresses [131].

The reason for the increase in voltage across subsequent discs are the reduced number of turns in the first discs. This shows that the frequency is not high enough to use only the capacitance to evaluate stresses within the first discs during the fast rise-period of the impulse.

The voltages obtained between disc 5 & 6 are still not large enough to cause a flashover.

The next situation evaluated is a special test: Tailchopped Lightning Impulse. The rapid voltage change in this test is believed to cause a larger gradient within the first part of the winding than the previous test.

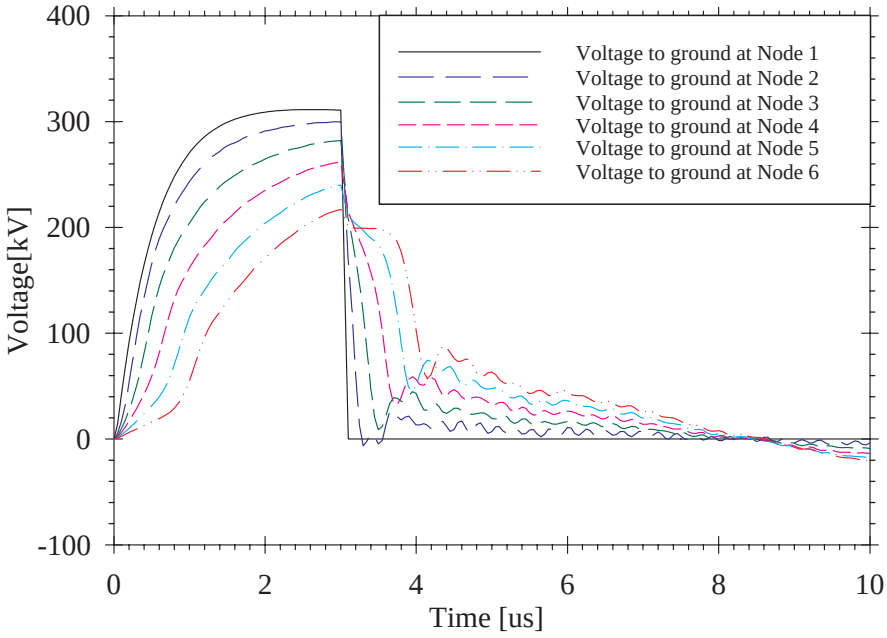

Figure 7.14: Nodal voltages at tailchopped lightning impulse

As seen from fig. 7.14 the voltage at the terminal collapses within a very short time. This can for instance be caused by a flashover. The instantaneous voltage-difference to adjacent discs will in this case be dependent on the capacitive voltage distribution and the fall-off time for the chopping circuit. In this case the time-step of the simulation is used as the fall-off time: $\Delta t = 0,05 \mu s$

Such a small time to collapse is not very probable for a flashover, but in GIS-installations such fast changes might occur (or even faster).

The steepness of the imposed impulse represents very high frequencies (several MHz), and is therefore close to the bandwidth of the model. This means that the accuracy of the calculated responses may be low. In order to study very fast transients, the discretisation should be increased for the first discs in order to increase bandwidth for the region under investigation. A possible solution would be to implement a turn-to-turn model for the 10 first discs, and keep the rest of the model unchanged, but this was not proceeded due to lack of time. The rest of the investigation is therefore given as an example of the versatility of the method.

The interdisc voltages are shown in fig. 7.15.

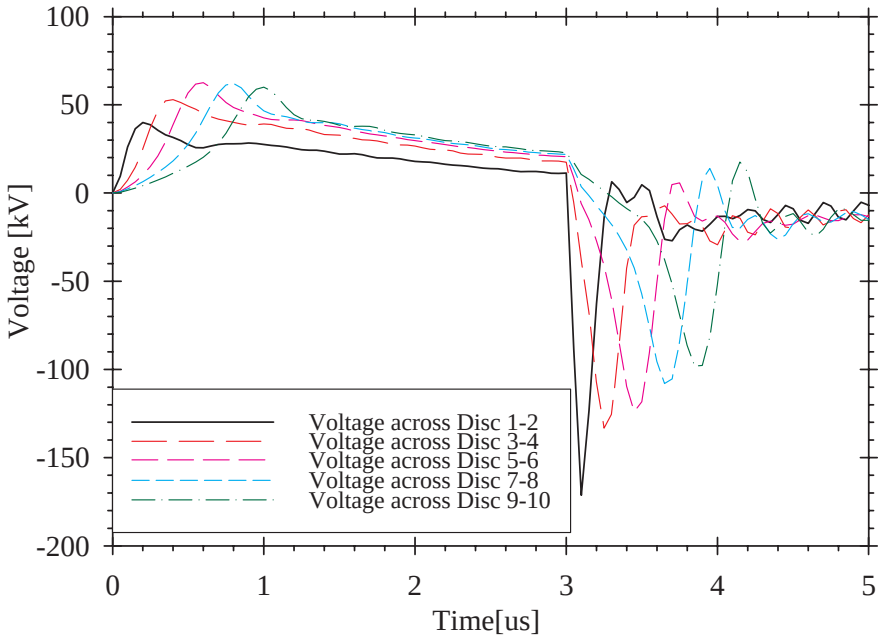

Figure 7.15: Interdisc voltages at tailchopped lightning impulse

The voltage across disc 1 & 2 reaches 171kV at $t = 3,05\mu s$. Whether this voltage is realistic or not is hard to tell. It mainly depends on the fall-off time for the chopping circuit and the accuracy of the estimated capacitances. It is therefore only considered as an example in this case.

When estimating the stresses for the first discs, it is assumed that internal voltage distribution in the discs are linear. This is usually applicable at intermediate frequencies, but if the frequency approaches the bandwidth of the model, this would be wrong since there is an internal capacitive voltage distribution equal to the major distribution in the winding. This leads to higher stresses between the first turns. If assuming linear voltage distribution, interturn stress will then be 17,1kV for the first two discs.

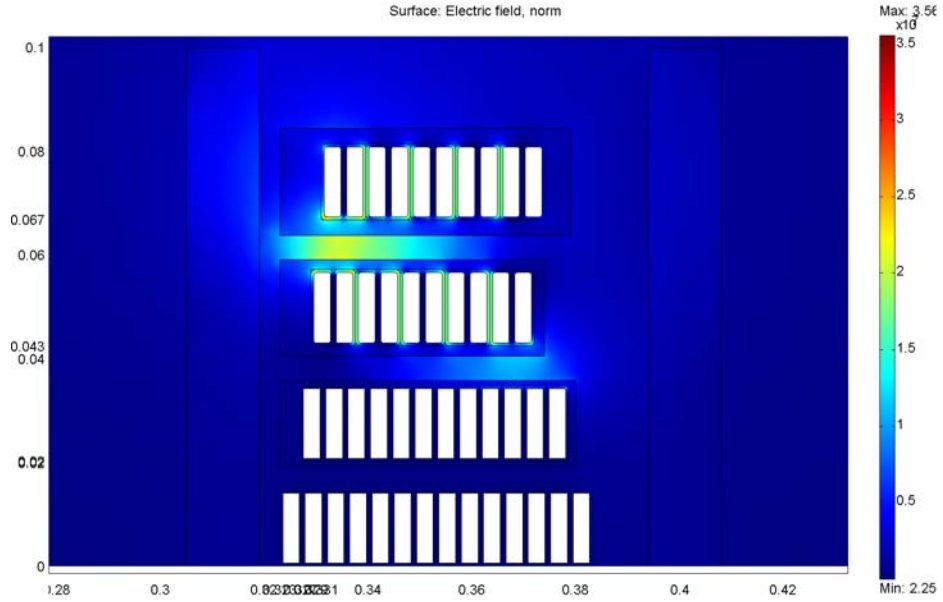

Figure 7.16: Electric field strength at tailchopped LI

The critical field strengths can be read directly from the graphical solution in FEMLAB, by pointing and clicking in the area with the highest intensity.

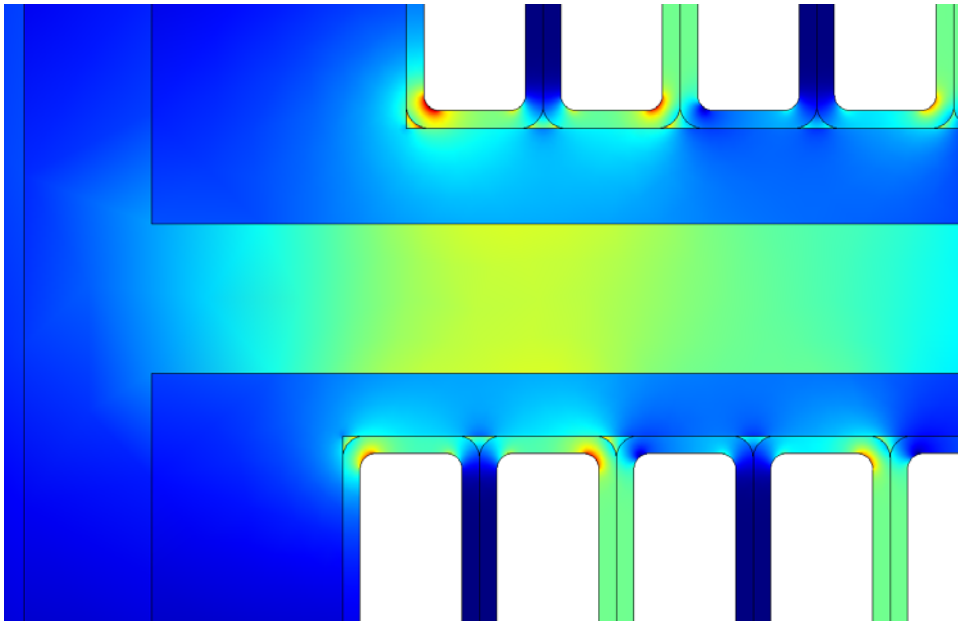

Figure 7.17: Electrical stress in the oil gap

The maximum field strength is found to be 29 kV/mm at the strand corners and the maximum field strength in the oil gap between the discs is 19 kV/mm. Since pressboard and paper barriers are present between electrodes (discs), the breakdown voltage is increased [163]. During a type-test for a new transformer with this design, the transformer is likely to withstand this stress. But after severe ageing, a breakdown is possible.

7.3.2 Internal resonance

If the HV-winding is energized by an oscillating transient with a frequency coinciding with any of the resonance frequencies (see fig. 7.11) for the windings, a severe internal voltage buildup will occur. For the first resonance, this buildup will occur in the middle of the HV-winding. The build-up will be very dependent on the damping in both the transformer and the impedance of the exiting source (for instance a cable or capacitor switching incident). If the damping is sufficiently low, a breakdown may occur, since the resonant overvoltage is built up over several periods.

Problems related to internal resonances are not discovered by type-tests during manufacturing and have gained interest during the last two decades closely connected to switching operations of lines/cables [106], faults, capacitor banks [164]. Travelling waves depend on the travelling time of the transmission medium.

Breakdowns in regulation-windings may arise from oscillating overvoltages comparable to those discussed in the previous chapter, but the difference is the open end of the regulating winding (semi quarter-wave resonance). Such overvoltages depend upon the design of the transformer. Interleaved layer windings are commonly used. The advantage of these windings are the distribution of the ampere turns along the height independent of the tapping-postition. Resonances can be investigated using the same approach as in chapter 7.2.

As mentioned earlier, transformers withstand type-tests, but the influence of ageing is not accounted for. A study by Sokolov [165] shows no reduction in breakdown voltage due to moisture/ageing for lightning impulse. Particles decreased the breakdown voltage by 12%. For switching surges the breakdown voltage was decreased by 15% after ageing. Particles decreased breakdown voltage additionally by 10%. This reduction might be sufficient for lowering safety limits to a critical level. The decreasing influence of moisture at increasing frequencies is consistent with the findings in chapter 6.

7.4 FRA - Range of application

A set of different aspects are assessed regarding the applicability of FRA as a diagnostic method. Some of the most common fault-modes are simulated in order to establish initial sensitivity guidelines for FRA interpretation. Since this work is focused on one particular transformer rather than several different designs, the guidelines established here should not be generalized. It is therefore pointed out that future investigations on other designs and types are important.

There are mainly 3 types of faults considered in this thesis:

- Axial displacement
- Radial deformation (Buckling)
- Disc-to-disc short-circuit

The first are mechanical faults and the last being an electrical fault.

7.4.1 Axial displacement

For axial displacement the LV-winding is displaced 20 mm downwards.
This is approximately 1,2% of the winding height and the TF comparison can be seen below:

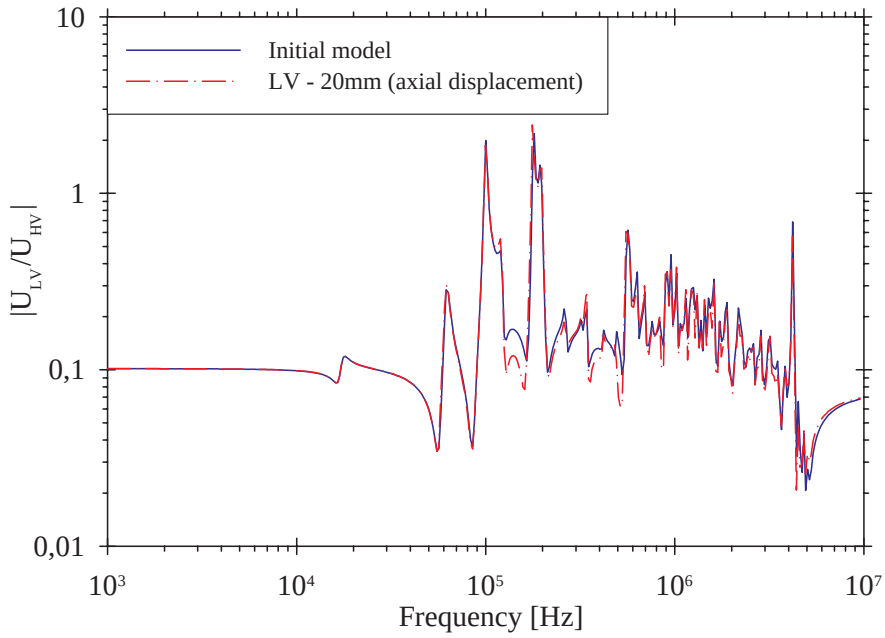

Figure 7.18: Model comparison: 20mm axial displacement of LV-winding

By investigating fig.7.18, some vertical change of the TF can be seen in the area above 100 kHz, but no shifts in resonance frequencies are observed. The change seen in fig. 7.18 is rather small, but a larger displacement is improbable since the

height of the core window does not allow a larger displacement. This leads to the result that the possibility to detect this kind of deformation is depending mainly on available space if end-supports collapse. The available space is depending on the voltage level of the transformer. Less than 20 mm axial displacement were investigated without significant visual differences. More than 20 mm of displacement are not likely to occur (for constructional reasons) and are therefore not investigated.

The transfer function in fig. 7.18, has been established both with and without change in capacitance due to the axial displacement. These two curves are identical, and this indicates that the capacitance can be kept constant during simulations of axial displacement.

Calculated short circuit admittances were also compared to measurement with less sensitivity to the deformations. This is consistent with the results reported by Christian [24].

Initial experiments regarding axial displacement on one of the windings from the T3Buran transformer has also been performed. This is done with the winding inside a special tank for electrostatic representation of the core and tank. But since the core has proved to be very important, simulations have been given priority. Thorough experimental work on coreless designs has already been performed by Christian [24], for axial displacements, radial deformations and internal short-circuits, making further investigations on coreless designs redundant.

Results and illustrations from the experiments in this work can be examined in appendix K.

7.4.2 Radial deformation

For buckling, the low voltage winding is deformed by a forced pattern similar to fig. 3.12a, using four different degrees.

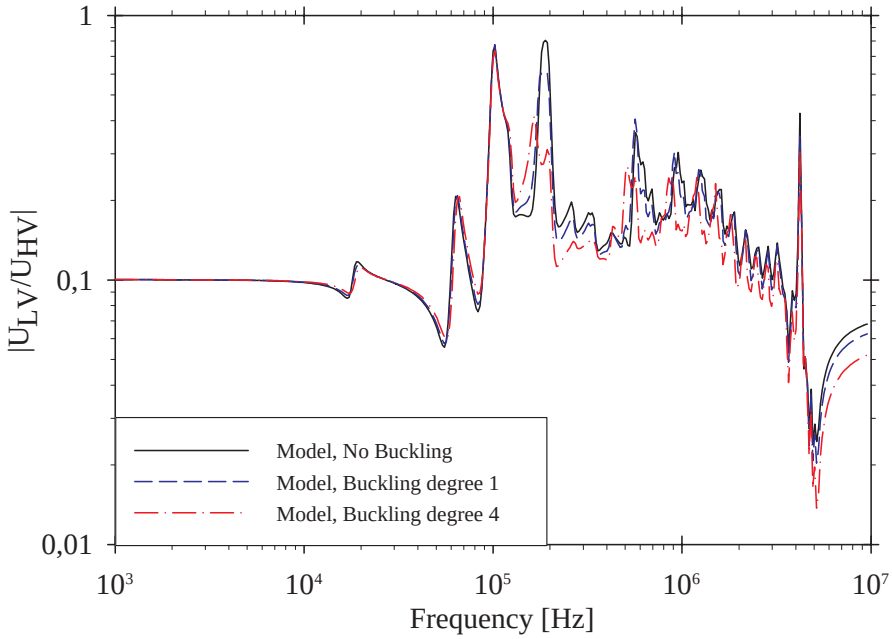

Figure 7.19: Model comparison: Radial deformation of LV-winding with different degree of forced-mode buckling

Fig. 7.19 show model results comparing forced buckling of degree 1 & 4. It is evident that degree 4 is detectable. Degree 1 also result in visual changes, but when taking measurement accuracies into account this degree will be close to the sensitivity limits of FRA. The degree 1 incorporates an increase in capacitance of 9% which compares to a buckling depth of 2cm. This equals 9% of the radial dimension of the LV-winding. Change in degree 4 is 4 times degree 1:

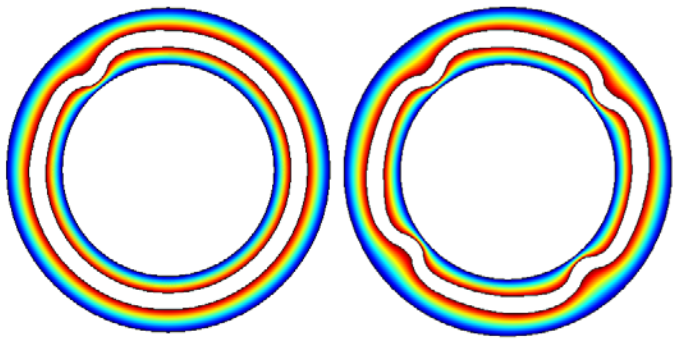

Figure 7.20: Radial (forced mode) buckling: Degree 1(left) and 4(right)

7.4.3 Disc to disc short circuit

For disc to disc short circuit, the fault is applied in the system description by adding a large admittance (low impedance) between the nodes representing adjacent ends of two discs. This has been done in several different positions along the winding in order to observe differences.

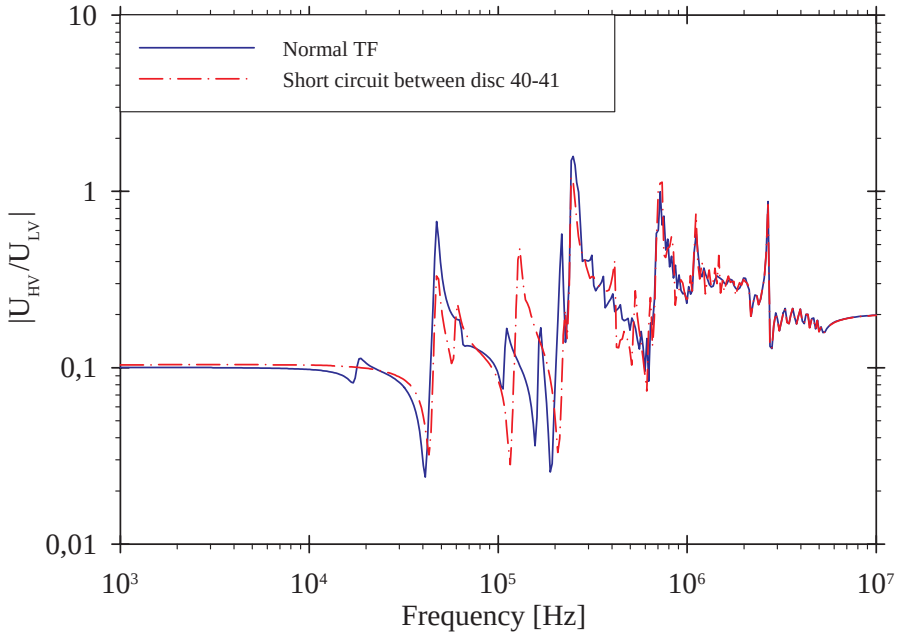

Figure 7.21: Calculated transfer function at disc-to-disc short-circuit in the middle of the HV-winding at OLTC-pos. -6

This fault type is clearly detectable independent of where the fault is applied, but becomes more distinct the closer to the terminal the fault is applied. It seems to affect the transfer function at all frequencies, even the low frequency response since conditions for the magnetic circuit is changed (leakage field and losses). Since there exist simpler methods to detect such faults, this fault type is not emphasized.

Turn to turn faults where also investigated, but since this model is established by means of a discretisation at disc-level, the turn to turn short circuit will not be properly represented. The only possibility without changing the geometry of the model is to reduce the number of turns in the faulty disc, but this will not represent the leakage field created by the circulating currents in the faulted turn, neither will the additional losses supplied by this current be. The only way to model such a fault using this method, is to establish a turn-to-turn model, at least for the disc involved.

7.4.4 Influence of non-symmetrical 3D effects

When applying an inter-phase comparison of FRA-measurements, a difference is usually observed between the centre- and outer phases. For a 3-legged core with Yy-connected windings, this usually occurs as two peaks at the first resonance for the outer phases while the centre phase has one distinct peak. There are two different explanations for this behaviour:

- If the first resonance is attributed to a resonance between the total inductance and shunt capacitance, this effect relates to the reluctance paths of the core. The centre-phase “see” two equal reluctance-paths in parallel, while the outer phases “see” two different reluctances. This explanation demands a flux confined to the core, but since the measurements are admittances it is uncertain whether the short-circuited windings screen the core from conducting flux and this brings up the other explanation:
- The leakage field surrounding the centre phase will be different in the way that it links two equal windings, while the outer phases links mainly the centre-phase. The number of resonance-peaks depend upon this linkage and how the leakage field links with the different resonant modes of the other phases. This effect is only visible at the first resonances / winding harmonics, since leakage-field at higher harmonics of the winding will not “spread out” as much as for the lower harmonics, with the result that the leakage flux does not link other windings at higher frequencies. This is illustrated in fig. 7.22:

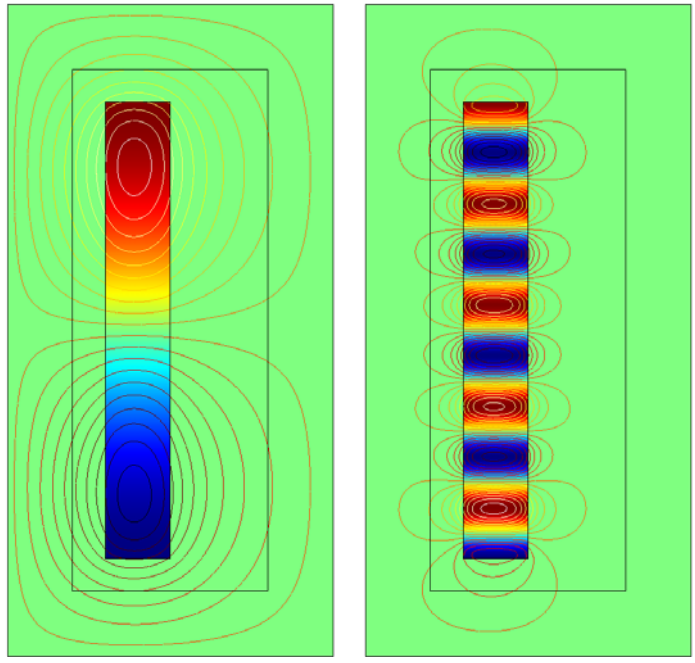

Figure 7.22: 1st(left) and 9th(right) space harmonic current distribution due to resonance

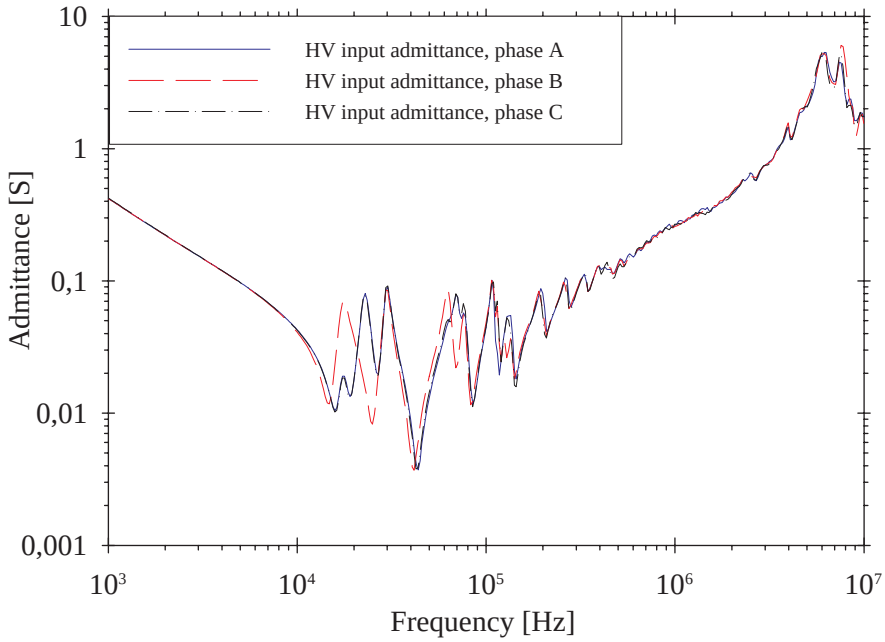

Figure 7.23: Interphase comparison of measured HV-winding input admittance showing normal deviations in a 3-legged transformer due to non-symmetry.

Fig. 7.23 shows an inter-phase comparison with deviations in a very localised frequency range (10-100 kHz). The difference at 15kHz is very interesting: The outer phases have quite identical traces with two small peaks, while the centre phase has only one distinct peak. There also seem to be some disagreement just above 100kHz. This can probably be attributed to the influence of the tapchanger as described in fig.7.24.

It is also interesting to note the consistency of the measurements up to 7 MHz, which indicates that inter-phase comparison of admittances can be used for admittance up to this frequency for this transformer size. The resemblance between the phases is very high from 200 kHz to 7MHz. Since mechanical damages usually influence on the FRA signature in this frequency-range, an inter-phase comparison will supply a sufficient sensitivity.

7.4.5 Influence of tapchanger position

The tapchanger influences the FRA measurements and its position must be known in order to compare with fingerprint measurements. Even the history (direction of control) is important for some designs. Measurements of HV-admittance (phase B) at different tapchanger positions are shown in fig. 7.24 in order to identify possible frequency-ranges where the tap-changer influences the response.

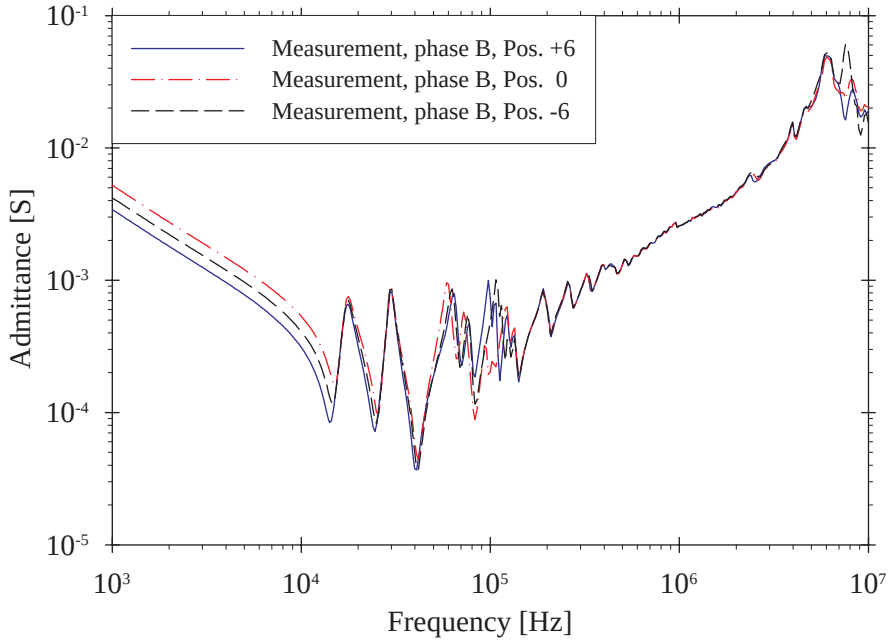

Figure 7.24: Influence of different OLTC tapping positions on the HV input admittance (measurements on T3 Buran)

The change at low frequency behaviour is evident, and a major area of difference can be seen around 100 kHz (see fig. 7.24). Above 120 kHz the OLTC does not seem to influence on the measured admittance. There are some deviations above 6 MHz, but this is attributed to the measurement setup and difference in leads and internal connections of the transformer.

The observations made above are important knowledge when performing FRA interphase comparisons, since the tap-changer seem to influence the FRA-signature below the frequency range of interest for mechanical deformations. In other words, the tap-changer seems not to be a problem for FRA interpretation.

7.4.6 Influence of bulk oil

In rare cases the transformer will only be available for measurements after draining or before filling oil. This will of course influence the capacitances internally in the windings, since permittivity is reduced. Short circuit admittance- and voltage ratio-measurements were taken for T3 Buran before and after draining the oil in order to investigate this influence. Fig. 7.25 shows the input admittance of the HV-winding (phase A) at the principal tapping-position (pos. 0):

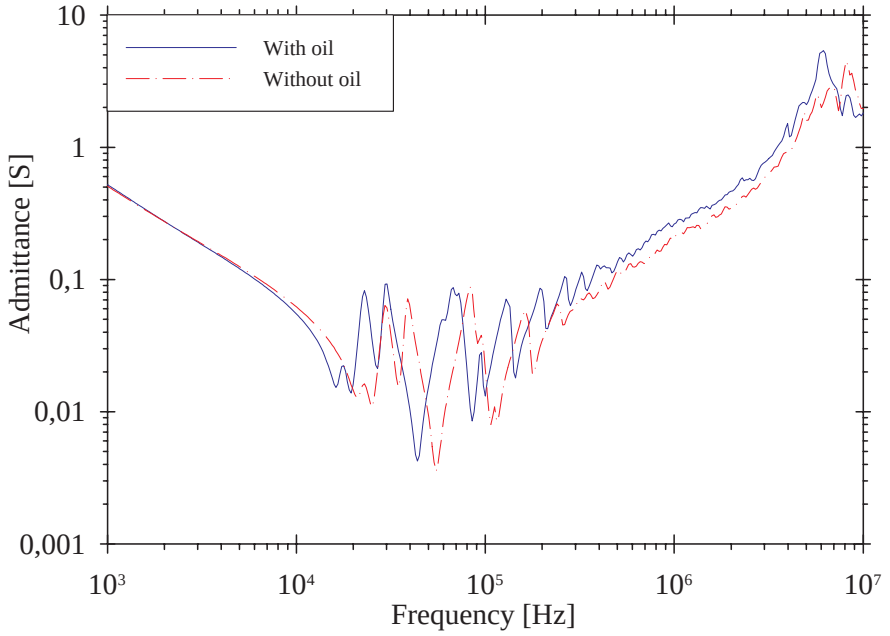

Figure 7.25: Input admittance of HV-winding (phase B) at OLTC-pos.0, with/ without oil present in the tank.

As seen in fig. 7.25 the admittance is displaced upwards in frequency when oil is drained due to the decrease in permittivity of the series and shunt capacitances. The first resonance is a series resonance between the series inductance and parallel capacitance (to ground/LV-winding). The change at higher frequencies will be different due to the growing influence with frequency of the series capacitance.

From constructional information the change in capacitance between LV- and HV-winding when draining the oil is found to be 27,7%, while the increase in frequency for the first resonance frequency is 25,8%. One would expect the frequency to change with the square-root of the change in permittivity [20], but the reality is a bit more complex since the capacitance is distributed both as series and shunt capacitance. An additional uncertainty of this measurement is the replacement of oil with air (humidity unknown), since the transformer was drained for approximately a week and moisture could have entered the insulation structure, increasing permittivity slightly.

7.4.7 Influence of measurement-setup

In order to investigate the degree of influence from the measurement-setup, two different measurements are tested. The first one applies the measurement at the bushing flange. A short grounding-lead to the flange is used while a longer lead connects the top of the bushing to the measurement-cable/probe. This is the usual setup.

The other setup tested was to measure the voltage at the top of the bushing, having a longer grounding lead along the body of the bushing down to the flange. The last method will add capacitance to the terminal due to the grounding-lead running along the body of the bushing. Additional inductance is added to the grounding lead so that there will be an additional impedance in the grounding-lead instead of the measurement-lead. This impedance will be important at high frequencies as seen below:

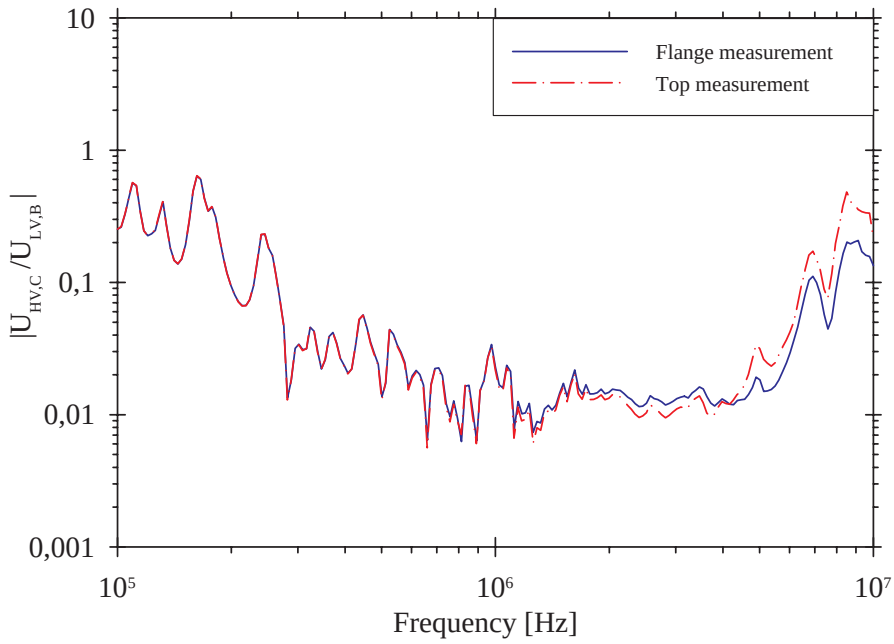

Figure 7.26: Influence of the measurement-setup onto the measured transfer function (HV phase C to LV phase b, pos. 0)

In spite of a severe change in the measurement setup, the difference is not significant below 4 MHz (see fig. 7.26). At increasingly larger transformers (higher voltage-levels), this effect will become more prominent as dimensions of the bushings increase and longer leads must be used. The comparison in fig. 7.26 is done between HV phase C and LV phase b, in order to have high impedance conditions on the terminal measured, but this did not influence the degree of deviation compared to normal voltage ratio measurements.

The series inductance contribution to the impedance of the measurement leads is important. The difference introduced by this inductance depends on the current in the measurement leads. Less current gives less influence from the series impedance (inductance). This gives preference to the use of high impedance probes rather than a low impedance termination (for instance 50 Ohm).

7.5 Discussion

7.5.1 Model accuracy

As identified in chapter 7.1, there are still differences between measurements and the final model. The introduction of the iron core representation used in this work increase conformity to terminal measurement significantly by representing the inductances and losses in a physical way. Additionally the introduction of frequency-dependent dielectric losses seem to add sufficient damping to the model. Still there are deviations, related to elements of uncertainty such as 3D leakage field with coupling to other phases, influence of tap-changer, leads, constructional details such as supports, shields, static plates, interlaminar effects etc. In addition, the measurements might be influenced by the measurement-setup (in particular test-leads and grounding points).

Clearly there is room for further research and improvements on the approach presented in this thesis, but the general coherence to measurements supports hypothesis 5 assuming that the remaining minor differences can be identified and investigated in the future.

When it comes to the application of the model for investigation of overvoltages, it is reasonable to assume that internal behaviour is related to terminal behaviour of the model since the terminal model is solely established based on the internal construction of the winding. This must of course be verified experimentally, but the physical implementation of all losses give preference to this method for resonance investigations, since the losses are important for the time-constants of the resonant voltage buildup.

7.5.2 FRA sensitivities

As mentioned in chapter 2.2.2, quantified sensitivities of FRA are rarely published. Most of the publications that report successful detection using FRA do not include sensitivity-investigations since these are tests on service-damaged windings. It is therefore necessary to involve laboratory experiments or detailed modeling in order to establish guidelines for sensitivity. This work has led to some preliminary guidelines regarding the sensitivity to radial deformations and axial displacement.

For the test-object used in this work, the sensitivity limit for axial displacement is about the same as the available space for displacement if the end-support collapses. In other cases the available space might be too small. This space depend on the voltage level used (insulating level needed from winding to yoke). Modern transformers are not likely to experience such faults since end-support are constructed in a way that does not allow a collapse. Earlier designs may experience such collapses. The sensitivity limit is found to be 1,2% of the axial height. This is consistent to the experimental findings of Christian [24] (1-2%).

A quite common type of axial displacement is telescoping, which means that a part of for instance a regulating winding is subjected to huge forces and become stretched. This may lead to a situation were the stretched part passes the healthy part and overlaps. This might be a reason for failure in this kind of designs (interleaved regulating windings). Telescoping is not considered in this work but should be investigated in the future.

For radial deformation (forced mode buckling), the sensitivity limit is established at an increase in capacitance from LV-winding to ground of: $\Delta C = 9\,\%$, which corresponds to a buckling depth of 2 cm along the whole height of the winding. The depth equals 9% of the radial dimension for the LV-winding. Comparing this to the results of Christian [24], identifies a large difference. Christian found the sensitivity-limit of buckling to be 3% of radial dimension along 10% of the winding heigth. Even though the designs are quite different, this large difference is difficult to explain.

7.5.3 Limitations in FRA application

There are several limitations of using FRA to detect minor damages. Interstrand short circuits create additional losses in the winding since it results in circulating currents. Detection of such faults are reported in literature, but in practice the changes are smaller than inaccuracies of the measurements. FRSL [34] could be an alternative since interpretation is much easier.

Axial bending is a minor deformation but very common when deformations start to occur. This deformation is a result of excessive axial short-circuit forces and occur usually at the ends of the winding. In order to detect such local deformations, the increase in series capacitance must be large. Since most windings have reinforced insulation at the winding ends, the available space for deformation is less than what is required to detect it.

As stated earlier in this work, the free buckling mode results in less changes than the forced mode, and this results in a lower sensitivity to the free mode buckling.

When fingerprint measurements are not available, interphase comparison is necessary. This is straight forward for Y-connected windings, but for delta- and zig-zag-windings the symmetry is broken if the windings cannot be opened (which is rarely the case).

7.5.4 Measurement accuracy and errors

The accuracy of the FRA method is confined to the accuracy of the measurement setup. Since the method usually will be applied to transformers in the field (during revisions), noise must be expected since large currents, high voltages and partial discharges are usually present to a certain extent in substations. This limits the dynamic range (increases noise floor) of the method.

In addition the measurement setup influences the measurements. If the setup is made completely equal each time, a good sensitivity can be expected. The smaller the deformations to be detected are, the higher frequencies need to be applied in order to detect them. The upper usable frequency depends on the voltage level for the transformer, since the length of the measurement leads will depend on the length of the bushings.

7.6 Conclusions

The final model shows a reasonable agreement to terminal measurements. Some of the remaining differences are identified. Further the versatility of the modeling method established in this work is shown by means of different examples and applications.

Internal stresses can be investigated either in time- or frequency domain. Assuming the losses are accurately represented resonances can be evaluated in time domain. Time constants of resonant voltage build-up are important and must therefore be investigated in the time-domain.

The detailed model can easily be reduced to an equivalent terminal model in order to implement it into any network simulations.

The model is also applicable for FRA simulation to investigate the sensitivity limits of different fault types for the specific transformer design utilized in this work. The sensitivity limit for axial displacement is 1.2% of total winding height, and for radial deformation it is 9% buckling depth related to the radius of the winding when the buckling extends along the whole height of the transformer. Axial bending is not detectable. Disc to disc short circuits are clearly detectable. Turn to turn and interstrand short-circuits are not investigated due to the structure of the model. The sensitivity limits are also dependent on the accuracy of the measurement equipment and setup. Additionally there are differences to be aware of when applying a symmetric comparison (interphase comparison). The differences around the first resonances seem to be related to the leakage field. In addition the tap-changer/regulating winding seem to have some influence around 100 kHz. Since most of the deformations change the signature above 100kHz, these natural deviations does not degrade the FRA sensitivities for the specific transformer used in this work.

8 DISCUSSION

The following hypotheses have been investigated in this work:

1. *"Deviations observed in FRA measurements can be related to actual winding deformations by means of a detailed high frequency model of the transformer."*

This work presents an approach for modeling power transformers based on the physical/internal layout of the winding (constructional information) and the material parameters. Effects of deformations, modeled as geometrical corrections, appear in calculated FRA-signatures. These are not verified with experiments, but are compared to the experimental work done by Christian [24]. One of the goals on FRA is to establish preliminary interpretational guidelines. This seems to be possible from the results reported by Rahimpour [1], which has based his simulations on the experimental results of Christian [24].

The investigations done in this work found the sensitivity limit to forced mode buckling at an increase in capacitance from LV-winding to ground of 9% along the whole winding heigth. This equals a depth of buckling of 9% of the radial dimension of the LV-winding. On the contrary, Christian [24] reported a sensitivity-limit for forced mode buckling of 3% buckling depth (of the radial dimension) along 10% of the winding height. Such a small deformation would not be detectable by the model used in this work. Investigations show that only changes in the dielectric model need to be taken into account in the case of buckling.

A 20 mm axial displacement has been simulated on the LV-winding, and some vertical change of the transfer function can be observed in the frequency-range of 100 kHz-1MHz. The degree of the displacement correspond to available height for displacement for this particular transformer. The change in the transfer function is small and may be regarded as the sensitivity limit for this deformation mode. The axial displacement equals 1.2% of the total winding height and this agrees well to the results reported by Christian [24] (1-2%). The axial displacement is simulated

both with and without change in capacitance, with the conclusion that the dielectric model need no modification at axial displacements.
The model developed in this work is based on constructional information only (in addition to its material parameters). The constructional information describes the internal construction of the transformer winding, and since the model agrees well to terminal measurements, the internal representation is assumed to be properly defined. This means that deformations in a winding can be detected by terminal measurements (FRA), and thus hypothesis 1 is verified.

2. *"Analytical methods are sufficient for simple/homogenous transformer geometries. A real transformer geometry complicates the analytical approach. Finite element methods would be an alternative for complex designs since details and variations may easily be included."*

The analytical methods tested in this work show some coherence with the work of Rahimpour [1], but since he worked with simplified coreless designs, it is not representative for real transformers. When applying these analytical steps on a real transformer geometry (T3 Buran), it results in a poor resemblence lacking sufficient losses and distribution of the resonant frequencies.

Advancing to a FEM-based software (SUMER) was expected to increase accuracy since the windings could be modeled with a higher accuracy. This software also includes the proximity losses of the windings in a physical way based on the geometry and materials, but the results were only slightly improved compared to the analytical approach. Still at this point the iron core is neglected and equalized with a conducting screen.

3. *"Iron core can be neglected and considered to behave like a perfect conducting screen above 10 kHz."*

By representing the iron core eddy currents utilizing a frequency-dependent complex permeability, the coherence to measurements increased significantly. This is obviously the most important factor in transformer models. Eddy currents in the laminates are important also at higher frequencies. This work identify the iron losses to be the most important loss-mechanism up to several hundred kHz.

The permeability is shown to have little influence as long as it is much larger than μ_0. The reason for this is the fact that it is the leakage inductance that is involved in the internal resonances and the accuracy of determining these resonances is then related to an accurate calculation of the leakage field. Since the leakage inductance is represented by the difference between self- and mutual inductances, the values of these are not important but rather the difference. The difference (leakage inductance) seem to be constant when varying the permeability but the self- and mutual inductances are not. The proper representation of the core leg is however

very important in order to obtain an accurate solution for the leakage field in the core window.

The accuracy of the calculated self- and mutual inductances are compared to measurements utilizing single coils on cores. The accuracy of the complex permeability approach together with the shape of the core equivalent is also assessed. The two comparisons made in this work, are based on measurements found in literature and must be used with precautions since not all material-parameters and boundary-conditions are known.

At relatively large distances between coils, the mutual inductance vary linearly with the distance. The common flux is highly frequency-dependent while the leakage-flux is less dependent (assumed constant in the work of Fergestad [44]).

Inclusion of interlaminar eddy currents increases the accuracy of the core representation. The coating conductivity used in this work is set to the limit of what is allowed by standard tests. This narrow the effect down to smaller or older transformers since modern transformers usually use a double, high quality coating on the laminations.

For iron core representation, FEM show to be suitable in terms of implementing the equivalent complex permeability approach examined in chapter 5. Even though the introduction of FEM in chapter 4, did not increase coherence to measurements, it introduced the principle of using an equivalent description to incorporate frequency dependent losses and inductances into the model on a physical basis. This led to the iron core representation using the same approach. Hypothesis 3 is disproved.

4. *"High frequency characteristics of insulating materials are independent of frequency, temperature, moisture, ageing etc. Ageing should therefore not change the FRA-signature."*

The dielectric losses showed to be highly frequency-dependent and also dependent on temperature and moisture. Regarding the high frequency characteristics of the materials considered, the effect of moisture/ageing is not pronounced at high frequencies. The influence of temperature is clearly identified, and the so-called β-relaxation around 1MHz is attributed to the motion of the main cellulose chain. Moisture adds an additional β-relaxation where water is bound to the main molecular chain, but this is at a much lower frequency and is not of concern in this work.

The inclusion of frequency-dependent dielectric losses showed an influence onto the transfer function, adding damping to the resonances. Using constant values based on $\tan\delta$-measurements at 50 Hz, results in too low damping.

The dielectric losses start to influence on the transfer function around 100 kHz. It will become the dominating loss-mechanism in the upper frequency range of the model. When frequency approach 1MHz, the current mainly flows in the insulation structure and winding resonances fades out. Part one of hypothesis 4 is disproved. Part two is verified for other reasons than part one.

5. *"High frequency transformer models can be established with high degree of conformity to terminal measurements, provided constructional information is available."*

As mentioned, the method utilized in this work is based on constructional information to establish the model. Quite reasonable results are obtained when comparing terminal measurements to model results, especially for the input admittances.

Whether the model correctly represents the internal voltages and ratios, is not known, but since the model is based on internal constructional information, and all losses are calculated from the geometrical layout, it is assumed that the model also represents internal behaviour with a reasonable accuracy. This will of course have to be validated to measurements on a real transformer with a core.

It must also be mentioned that the tap-changer is not modeled due to its complexity. It will add capacitance between turns in the regulating winding, in addition to capacitance to ground. Its influence is seen in the measurements on T3 Buran in a narrow frequency range around 100 kHz. Influence from leads, bushings, measurement setup, and connections is minimal. Terminal loading (terminations in setup) is minimized since active probes are used for the voltage measurements. This means that no corrections need to be made in order to compare measurements and model. The influence from the setup is less in this work than in published literature. This is most likely due to the active probes, since influence of the inductance of measurement leads are minimized (small current results in a minimized voltage drop in the test leads). Use of high impedance, differential, active probes is therefore highly recommended to increase repeatability of the measurements.

Hypothesis 1 and 5 are verified, while 2 and 3 are rejected. Hypothesis 4 is partially rejected.

9 CONCLUSIONS

The main purpose of this work is to find the most suitable method for high frequency modeling of power transformers in order to calculate internal stresses and effect of winding deformations. FRA is a fairly new diagnostic method for detection of mechanical damages to transformer windings. This method can be applied without opening the transformer and this makes costly inspections redundant (damages to inner winding is normally not visible without disassembling the unit).

One of the demands for the method of modeling is that it should support real transformer geometries based on constructional information from the manufacturer. The model should also be versatile in terms of being applicable to computation of internal and external overvoltages and resonances.

A set of hypotheses has been established based on an initial study of the literature. The importance of the iron core in transformer models is emphasized in this work since it represents the most complex part in a model and at the same time the most important factor in such models.

The main conclusions for this work are outlined below:

- Simple, analytical methods cannot be used to establish a versatile high frequency power transformer model. In terms of low coherence to measurements using analytical modeling, the transition to a numerical FEM-description (SUMER) was expected to increase coherence since a more accurate implementation of design details could be included. FEM (SUMER) did not increase coherence considerably, but the techniques for calculating proximity effects are adopted in the description of the iron core.

- A proper and accurate representation of the iron-core is essential in terms of computing the magnetic parameters accurately. In this work an analytical solution of the complex magnetic field inside laminations is used to establish an equivalent, frequency-dependent, complex permeability that describes the frequency-dependent behaviour of the core accurately over a wide frequency

range. This enables a simple and accurate implementation of the core behaviour into any FEM software. Iron losses dominate the total losses up to several hundred kHz. The computation of self- and mutual inductances rely on a precise description of the frequency-dependent behaviour of the core. The internal resonances is determined by the leakage inductances (difference between self- and mutual inductance), and thus the permeability is not important. Interlaminar effects are shown to have influence on the inductance if the coating resistivity is sufficiently low. An analytical correction is developed in order implement these effects into the initial complex permeability description. The topology of the model must correlate to the real transformer design. Since the model is established in axial symmetry (2D), with the core leg and window as the determining dimensions, there are room for future improvements of the model.

- The permittivity of dielectric materials is strongly influenced by frequency, moisture, and temperature. Ageing does not seem to influence high frequency characteristics of oil-impregnated paper significantly. Since data on impregnated pressboard apparently is missing in literature, measurements are performed and presented in chapter 6. Main reason for this investigation is to determine possible influence important for FRA. A proper representation of the dielectric losses is shown to be important in a high frequency transformer model above 100 kHz. Ageing does not seem to influence on FRA-signatures. Temperature has only minor influence on the FRA-signatures provided that the difference in temperature is sufficiently large.

- FRA sensitivities are established for buckling (radial deformations) and axial displacement. Forced mode buckling is detectable for a change in capacitance to ground above 9%, while the sensitivity limit for the free mode buckling is very dependent on the shape of the deformation (Preliminary simulations insinuate a sensitivity limit of 15% change in LV to ground capacitance, but this is very dependent on the shape of the deformation). Both modes require deformation along the entire height of winding in order to be detectable. Sensitivity to axial bending is determined to be 1,2%. In many cases this is close to the available space for deformation if end-support collapses. So axial displacement is on the limit of being detectable.
  Disc-to-disc short circuits are clearly detectable independent of the position within the winding since the magnetic behaviour is changed. Axial bending is not detectable.

- Since terminal behaviour seems to be close to the model behaviour, and the description is based only on the internal geometry and material parameters, it is assumed that the internal behaviour is properly described by the model. Examples are shown were internal (and external) stresses are calculated both in terms of impulse overvoltages and resonances. The validity of the internal

model must be verified to measurements on a real winding geometry mounted on its core.

10 FURTHER WORK

10.1 Iron Core representation

Since the iron core representation showed up to be the most important subject in the transformer model, it should be given more attention also in future in order to improve the representation even further. Domain-refined/laser-treated steel is used extensively today. The high frequency properties of these materials are not known. Can these materials also be represented using the classical representation presented in chapter 5? Or are there large differences?

An universal transformer model is frequently called for in the literature. The model developed here could also be extended to lower frequencies by adding terminal equivalents for representing hysteresis and saturation. Saturation at frequencies above power frequency, will appear in the surface of each lamination and this increases the penetration depth since permeability is lowered in the outer zone. This will in turn affect eddy current losses in the laminations, but since very high voltages are needed in order to saturate the iron at high frequencies, this may be important only for intermediate frequencies (during switching- and power frequency transients).

Since the inductance seems to be slightly overestimated close to the yoke, this must be verified through measurements, and if confirmed, another core shape has to be found in order to avoid this overestimation (In real transformer designs with a stacked core, most of the winding is outside the core window, but in the 2D-axi all the winding is inside). A representation where the equivalent length of the core seen from the winding is “stretched” out and placed between two periodic boundary-conditions would probably increase accuracy and at the same time simplify the implementation of the core representation. The tank wall can still be represented as a boundary in the geometry for proper calculation of losses employing its material. The tank wall can be assumed to have an infinite thickness compared to the penetration depth of the leakage field.

10.2 Overvoltages

The most important factors when starting to use this method for calculation of internal and external overvoltages, is that the model must be verified to measurements on real transformers. Since the core was removed from the testobject in this thesis, it was not possible to accomplish such a verification since the importance of the core was realized at a later stage.

Another important topic is the handling of interleaved windings and in wound shields. This should be possible to handle analytically in order to obtain the correct series-capacitance.

10.3 Interlaminar effects

Since it seems like some core materials could have sufficiently low interlaminar resistance to set up currents between laminations, different types of coatings should be investigated. It is also of great importance to identify the range of applications for the different coatings. Since interlaminar currents displaces the flux from the inner parts of the core, this creates a three-dimensional problem. A representation in axial symmetry will necessitate an approximation. Whether the losses can be averaged the same way as for the one-dimensional permeability deduced in chapter 5.2, or implemented in other ways such as an implementation dependent on the radius; $\mu(r)$ is questioned.

10.4 3D effects

As outlined from the measurements in fig. 7.23, there are differences when comparing outer phases to the centre phase. There are two possible solutions for these difference, where both are related to non-symmetric phenomena (3D-effects):

- Since the number of resonances seems to be lower for the centre phase (around the first resonances), it seems like the reluctance plays a role. The reluctance seen from the centre leg, is a parallel connection of two equal paths, while reluctance seen from one of the outer legs is a parallel connection of two different reluctances. The inductance resulting from these reluctances will resonate with the shunt capacitance of the winding, creating two different resonances for an outer winding and one for the winding on the centre leg.
- The other possible explanation of the interphase difference is that the leakage field is different for the centre winding compared to the outer windings. This leakage field will be linked to other phases and the linkage for the centre phase will be twice the linkage from the outer phases, which explains the different behaviour of the winding.

Investigating these effects will be important in order to find approximations to use in 2D axi-symmetric models. 3D models with the required level of details are not realistic at the moment, due to the computational demands.

10.5 Ageing effects

The influence of temperature, frequency and moisture on the dielectric properties of insulation materials was studied on a preliminary basis in this thesis. A more complete study would be preferable, using a combined insulation structure. It would then be possible to invalidate or approve the influence of these parameters in real transformer designs. Some test can be performed on real transformers regarding the temperature but such test would be rather macroscopic regarding the material characteristics since several insulation structures influence the result.

10.6 FRA

One of the goals in this work was to increase the understanding on how FRA-signatures are changed due to deformations. A more detailed study would probably lead to further increase in understanding FRA. This could be obtained by applying variational analysis of FRA in order to investigate which faults influence on which part of the winding structure, and at which frequency.

10.6.1 Modeling

The simplification in modeling buckling neglected the change in inductance. The influence from a buckled zone with the core present should be investigated. The core might increase influence from the buckled zone, as indicated from some initial 3D FEM-simulations which were not included in this thesis, since the simplifications necessary was rather extensive. A very coarse mesh is necessary in order to be able to solve the FEM-problem.

10.6.2 Fault location

The faulted phase and winding can normally be located, but no clear indications are reported on how to locate the point of fault within the winding. By using the information from the different resonance-frequencies in a voltage-ratio measurement or an admittance measurement, it could be possible to determine the location also within the winding. Since some of the resonances change less than others at certain types of faults, it gives an indication of the influence of each resonance. Since the current (and voltage) has a space-harmonic distribution with a wavelength according to the resonance frequency, parts of the winding has no angular current (magnetizing current), and thus no losses are created at this particular part of the winding. If the voltage is zero for a particular part, then a change in capacitance would not be detected at this resonance, but will be detectable at other resonance frequencies.

10.6.3 Interpretation and presentation

Hässig and Bräunlich [166] reports a better sensitivity to small changes in transfer function using a locus plot in the complex plane than the conventional frequency spectrum. The disadvantage is that the frequency must be labelled inside the plot

which might create confusion, but their conclusion was that the locus plot was favourable for the comparison of different measurements.

Some work has been done to automate the interpretation of data, but the problem is the amount of data. If some important features were extracted, it could be possible to automate this process to a certain degree. For instance if the poles and zeros of the transfer function is extracted, it could be used as an input to an artificial neural network (ANN). Such network needs training, and a transformer model such as the model developed in this work is perfect for training ANN-networks for different fault types. Noisy measurements must be accounted for.

Statistical indicators is an interesting tool as a support during interpretation of FRA measurements. Such measures are not evaluated in this work, but the influence from a computer model would be interesting to study since different effects can be isolated with reasonable effort.

11 APPENDICES

Complementary reviews, deductions and explanations are put into appendix in order to try to increase readability of the main part.

Appendix A. Constructional information, T3 Buran

As outlined in chapter 1.4, the main test object of this thesis is a 2-winding step-down, power transformer with a regulating winding connecting the HV-winding to the neutral. The following name-plate information is given:

HV: 60kV +/-6 x 1.46% (Reg.winding), 20 MVA, 195 A, YN
LV: 6,6 kV, 20 MVA, 1724 A, yn0

ek: 7,51% (Ek: 4506 V)
er: 0.478%
I0: 0,306%
P0: 18.84 kW
Pc: 84.1 kW

The local utility (Trondheim E-verk) was upgrading the voltage level in the secondary network from 6,6kV to 12kV. Since this transformer was quite old, an upgrade of the windings was not recommended and it was scrapped. The transformer was disconnected and FRA measurements were performed in all combinations (voltage ratios and admittances) for 3 different tapping-position: Max/min and principal position (middle). Then the oil was drained and measurements performed again. The initial plan was to untank the transformer in order to apply deformations to the winding. But since the OLTC was placed in a separate tank requiring a disassembly inside the main tank before the active part could be lifted out, these experiments were cancelled. Instead the windings were separated from the core (to save space) and brought the laboratory for future experiments.

A.1. The windings

The high voltage (HV) winding consists of a double-stranded continuously wound disc winding with 82 discs and 564 turns. The insulation is reinforced at the ends in order to cope with impulse stresses. To enable the addition of extra insulation, the number of turns are reduced for the 3 discs closest to the winding ends. A “normal” disc has 7 turns while the end discs have 5 and 6. Strand dimension is 3,2 x 13,5 mm. Inner and outer diameter is 646 mm and 747 mm respectively. Axial height is 1576 mm, and insulation thickness is 0,55 mm.

The regulation winding is connected in series with the HV-winding, between HV and neutral, and consists of an interleaved single layer-winding with 9 turns per tapping (12 tappings). Conductor dimension is 9 x 7 mm. Inner diameter is 837 mm, and axial height is 1374 mm. Insulation thickness is 1,225 mm.

The low voltage (LV) winding is a double start, 24-stranded single layer helical winding with 69 turns. Interturn distance is increased at the winding ends to have local balance of the ampere turns (equal length of the two windings). The strand dimension is 2 x 7 mm. Inner and outer diameter is 483 mm and 576 mm respectively. Thickness of insulation is 0,325 mm.

A.2. The core

The core is three-legged and has a nominal diameter of 460 mm for the legs. This diameter includes pressboard strips and steel-ties. This equals an outer iron core diameter of approx. 450 mm. The core is built up of M6-gl. standard steel (thickness: 0,35 mm) with 13 different widths/steps as shown in fig. 3.6. The effective diameter is approx. 440 mm (due to the stepped width of the laminations), and the net area of the main legs is 1406 cm2. (The space-factor due to insulation and cooling ducts within the core is not included in the net area)

The area of the top/bottom yokes are: 1,13 x 1406 = 1589 cm2.(These sections have elliptic cross-section with a height of 480 mm).

The window height and width are 1750 mm and 450 mm respectively. Other dimensions are shown in fig. A.1

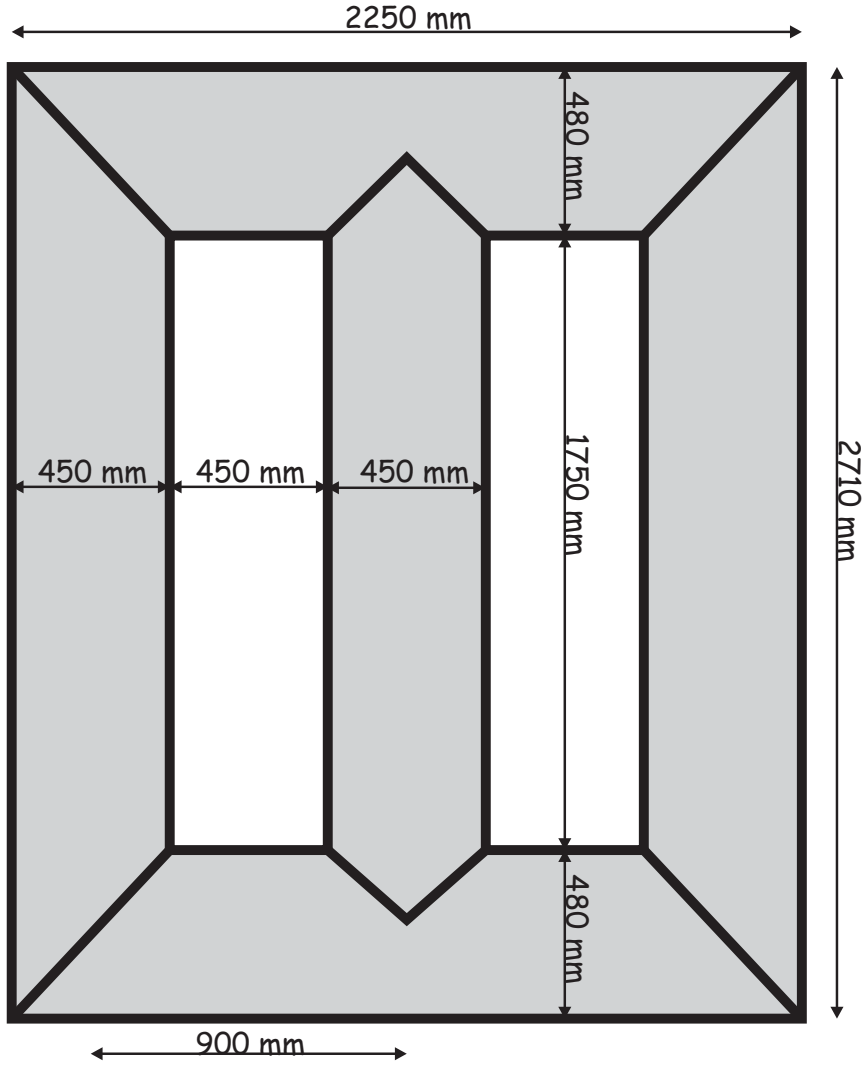

Figure A.1: Core dimensions of T3 Buran

The end-support, steel-ties and core cooling-duct is shown in fig. A.2

Figure A.2: Core details: End support, cooling duct and steel-ties

A.3. The tank

The internal tank dimensions in millimetres are as follows:

-Width: 1150
- Total length: 2850
- Rect. length: 1700
- Heigth: 3350

The ends of the tank are rounded (oval) and the tapchanger is placed in a separate tank added to the end of the main tank. Cooling-scheme is ONAF.

Appendix B. Short circuit forces

A power transformer's ability to withstand short-circuits is recognized as an essential parameter for such an important component. International standards (for instance [11]) as well as national standards specifies a necessity for power transformers to be short-circuit-proof and the way to verify such performance.

The effect of short-circuit currents in transformer windings can be grouped in two categories:

- Thermal effects
- Mechanical effects

It is shown [131] that the thermal effects normally will not affect the insulation life-time of a transformer due to sufficiently infrequent occurrence and fairly low temperature rise.

A power transformer in a normal network would probably have to deal with few or none short-circuit faults through its lifetime, but should be designed to withstand such faults if they occur. Transformers can be designed to cope with several such faults a day, for instance at short-circuit test station of arc furnace transformers. Building ordinary power transformers suitable for such purposes would be expensive. In other words, economy is one of the main factors when choosing the level of specification for a new transformer. The designer should anyhow make some considerations to be able to calculate the strength of the transformer and its components. The following procedure is given in [167]:

- Study system faults and their characteristics.
- Evaluate possible over-currents occurring in the network.
- Calculate the electromagnetic forces due to these over-currents.
- Determine the strength of the windings needed to resist these forces.

Usually faults in a power network have currents far below the maximum short-circuit current. In rear cases a transformer will be subjected to the highest possible currents. The forces produced are proportional to the square of the current, so a small reduction in the current makes a substantial decrease in short-circuit stresses and therefore the effect of asymmetry is very important. At maximum asymmetry (a factor of 1,8), forces at the crest of the first loop of the fault current are 3,24 times higher ($1,8^2=3,24$), than at a symmetrical fault. The situation of maximum asymmetry is shown in figure B.1 and B.2:

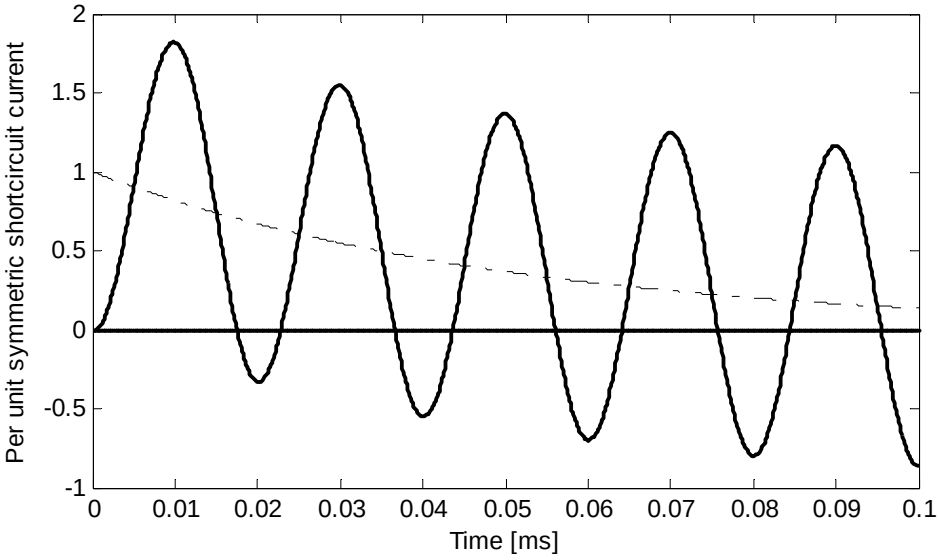

Figure B.1: Fully asymmetric short-circuit current

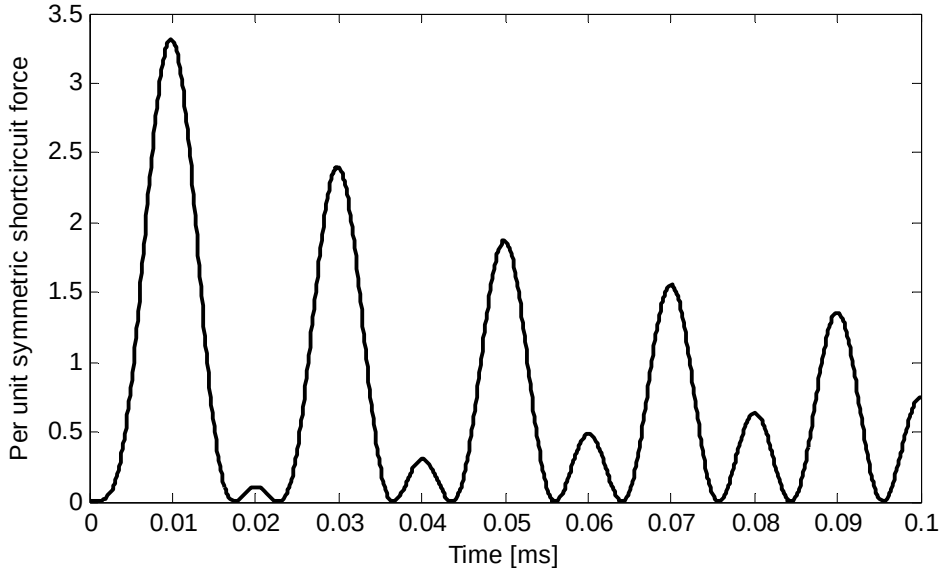

Figure B.2: Force variation vs time during short circuit for an asymmetric fault [167]

The asymmetrical factor can be derived from the network and transformer parameters.

Another important factor for the designer is, as mentioned earlier, the frequency and duration of faults, the methods of protection, temperature-limits for the equipment. According to [167] the manufacturers usually use the maximum asymmetry for designs.

The next step is to determine level of fault current, and by considering a fully asymmetrical fault, the current for a transformer connected to an infinite system is:

$$\hat{I}_{SC} = \frac{1,8 \cdot S_n \cdot 10^3}{\sqrt{3} \cdot E \cdot e_z} \qquad \text{B.1}$$

Where $\hat{I}_{SC}$ = peak value of short-circuit current [A]
S_n = rated output of transformer in MVA.
E = rated line-to-line voltage [kV].
e_z = per unit impedance of the transformer [%].

If the transformer has a tapping winding, this has to be considered because it influences both the impedance and the maximum forces occurring during short-circuit events.

The IEC publication 60076 part 5 [11] states that the maximum duration for a short circuit is 2 seconds for impedances less than 5% and 3 seconds for impedances of 5% and above. The publication also give the maximum permissible winding temperatures, which for copper is 250° C. The asymmetrical value given by the publication is initially 1,8 but allowance may be made for system impedances by agreements between manufacturer and purchaser. For instance, this can be allowed if interconnecting buses or cables are to be made short-circuit-proof.

The temperature limit permitted by the standard is usually not reached due to shorter fault clearing times and lower short-circuit currents (lower current density applied). The yield strength or hardness grade of copper increases by cold working the metal. In the “as cast”-stage or after a complete annealing, copper is an isotropic material. By cold working/wire drawing, the crystals are reoriented and deformed, which leads to an increasing hardness grade. Usually the yield strength is given as the stress value causing a permanent strain equal to 0,1 or 0,2%

Standard grades cover values ranging from 90 to 280 N/mm2 yield strength at 0,2% offset. These standard grades are usually called semi-hard copper, and when exposed to temperatures between 200-250 C, some annealing start to occur [168]. This leads to a substantial reduction in the yield strength, and the winding will be less able to withstand the electrodynamic stresses at the next occurring short-circuit if exposed to such temperatures.

Additional considerations must be made for multiwindig transformers, autotransformers and tertiary stabilizing windings (depending on the connection mode).

The possibility of resonance must be clarified for the different modes of electromagnetic forces, because the windings and the supporting system constitute a mechanical system having a mass and elasticity. This must be accounted for when studying displacements and stresses during short-circuits [167].

Radial forces produce a hoop-stress in the outer winding, where elasticity is high and mass is small. This results in a high natural frequency (>> 50Hz). For this reason there is little chance of displacements being increased by resonance effects. In this case the forces may be considered applied slowly, producing a stress corresponding to the peak of the first half-cycle of fault current.

When forces in the axial direction act upon paper and pressboard, which is easily compressible, the natural frequency may be close to the frequency components of the forces (1^{st} and 2^{nd} harmonic). The designer must aim for a construction not amplifying the stresses by resonance effects.

The methods of force calculation are quite different for shell type and core type transformers. In this thesis only core type transformers are considered due to the fact that it is by far the most common design for power transformers (at least in Europe), as it has emerged as the most economical and useful alternative for power systems.

The reason why forces occur is the fact that a major leakage field is produced in the transformer during a short-circuit when the windings oppose each others ampere-turns. The field produced in the transformer window creates both axial and radial forces on all parts of the windings.

The field is spreading out at the ends, producing axial forces, while the vertical field produces radial forces. This is due to the relation given in the formula below:

$$\vec{F} = \vec{B} \times \vec{I} \qquad \text{B.2}$$

which give the force per length perpendicular to the magnetic field and the flow direction of the current (right-hand-rule). An example of a leakage field calculation inside the core window is shown in figure B.3.

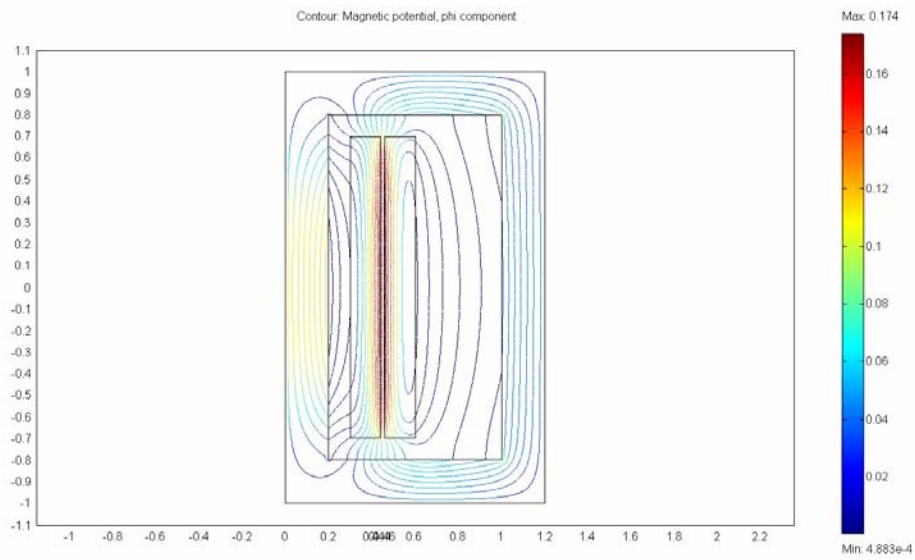

Figure B.3: Leakage field at short circuit for a simplified geometry

Displacements can in certain cases cause further displacements due to imbalance/ increased forces in one direction. The disposition of the windings is an important factor when the designer estimates the short-circuit strength of the design.

B.1. Radial Forces

The result of equation (B.2) yields that an axial field and a current perpendicular to the field and paper plane as in figure B.4 produce radial forces.

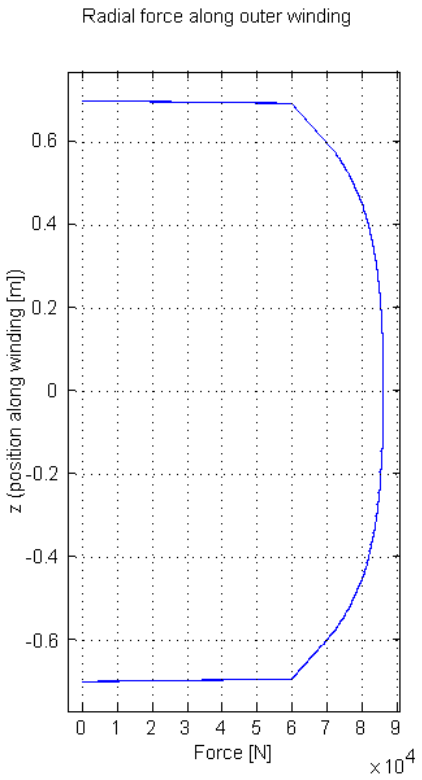

Figure B.4: Radial forces in concentric windings [167]

Since it is the maximum force which is important, it is convenient to ignore the curvature of the field at the winding ends. The approximated maximum flux density in the leakage channel can be found by:

$$B_A = \frac{\mu_0 \sqrt{2} NI}{H_w} \qquad \text{B.3}$$

where H_w is the average winding height and
NI is the total number of ampereturns in one winding

The conductors being closest to the leakage channel are subjected to the highest forces, since the radial force distribution depends on the axial flux density. Normally, provided that the conductors are wound tightly, the force pattern is such that some of the force is transferred to less loaded conductors, and a load sharing is achieved. Because of this, it is possible to assume that all conductors are subjected to an average force (per unit length):

$$F_{AV} = \frac{1}{2} \cdot B_A \cdot I_C \cdot \left[\frac{N}{m}\right] \quad \text{B.4}$$

where I_C is the peak conductor current in amperes. For layer-type windings there is no load sharing, so the layers next to the leakage duct face the biggest forces. For tightly wound windings such as disc windings, the total radial force exerted on the whole winding is given by:

$$F_{rad} = F_{Av} \cdot \pi \cdot D_m \cdot N \quad [N] \quad \text{B.5}$$

The tensile stress σ in the outer winding can be determined from the following formula:

$$\sigma = \frac{F_{rad}}{2 \cdot \pi \cdot A \cdot N} \quad \text{B.6}$$

In case of layer-type windings (no load sharing) the tensile stress of the conductors adjacent to the leakage channel will be twice as high. The outer winding withstands these forces if the tensile stress is below the level causing permanent deformation. With some margin of safety (due to unequal force-distribution around the circumference), the tensile stress obtained should not exceed 80 N/ mm^2 [168] (depending on the grade of hardness used).

B.2. Failure modes caused by radial forces

The failure modes due to radial forces are quite different depending whether it is the outer or inner winding, since the outer winding will experience outward forces creating a tensile stress, and the inner winding will be exposed to inward forces resulting in a compressive stress.

Tensile stress may result in conductor stretching if the yield strength is exceeded. This can also lead to destruction of conductor insulation or axial instability of the coil. If joints are not made properly, rupture of conductors may occur.

Compressive stress may result in a winding collapse according to two patterns:

- Forced buckling
- Free buckling

Forced buckling mode occurs when the supporting structure on the inner side has significant stiffness compared to the stiffness of the winding conductors. The conductors are bent in each span or in alternate spans between the axial supporting strips. This results in the typical shape of a many-pointed star or a flower. The stress has to exceed the elastic limit of the conductor.

Free buckling is a much more common collapse-pattern. This buckling mode cause the conductors to bulge outwards as well as inwards at one or a few specific points along the circumference and is not dependent on the supporting structure.

B.3. Axial Forces

The leakage field at the ends of the windings tend to spread out and a radial component of the leakage field is formed. This radial field give rise to an axial force along the winding. As long as the ampere-turns are balanced, the net force will be zero and the only force occurring is a compressive force. When the ampere-turns are not balanced axially, the total force will try to increase this imbalance (separating the windings and exerting a mechanical stress on the clamping structure).

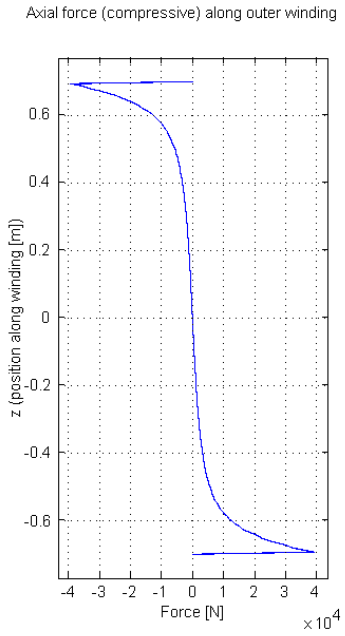

Figure B.5: Axial force-distribution on concentric winding

B.4. Failure modes caused by axial forces

Substantial axial forces may result in different failure modes and combinations of these. Several different mechanisms may be present during a short circuit event:

- Tilting of conductors: The axial stability of the winding is degraded severely due to tilting of conductors/group of conductors. Every other group axially (e.g. a disc) are tilted the same way resulting in a zig-zag pattern. This may result in broken conductor insulation, internal short circuits and even increased forces due to displacement of conductors
- Telescoping: stretched conductors cause radial looseness. This can lead to a displacement where some turns pass outside adjacent turns axially. This failure mode is typical for layer-type windings. Telescoping usually results in destroyed conductor insulation and turn-turn faults and at worst conductor rupture with the possibility of severe breakdown.
- Axial bending: The conductors are bent axially between the supporting spacers. This may lead to broken conductor insulation.
- Axial displacement/End support collapse: An axial deformation/displacement of the windings due to either overstressed materials or instability within the support structure.

Minor degrees of these mechanisms can lead to interstrand short circuits. Such faults are difficult to detect, but appear as a slight increase in the I^2R-losses and may show up, according to [169], as a thermal fault (T2) with a hot spot temperature above 300° C. A potential evolution could be that the fault develops into a major insulation breakdown if the hotspot temperature is sufficient, but this normally take some time.

Appendix C. FRA Measurement Setup

The setup used so far in Norway [20] is the SFRA-method using a network analyser (HP4195A) with active probes (HP41800A) and double-screened coax-cables. A network analyser has a very large signal-to-noise ratio, when used correctly.

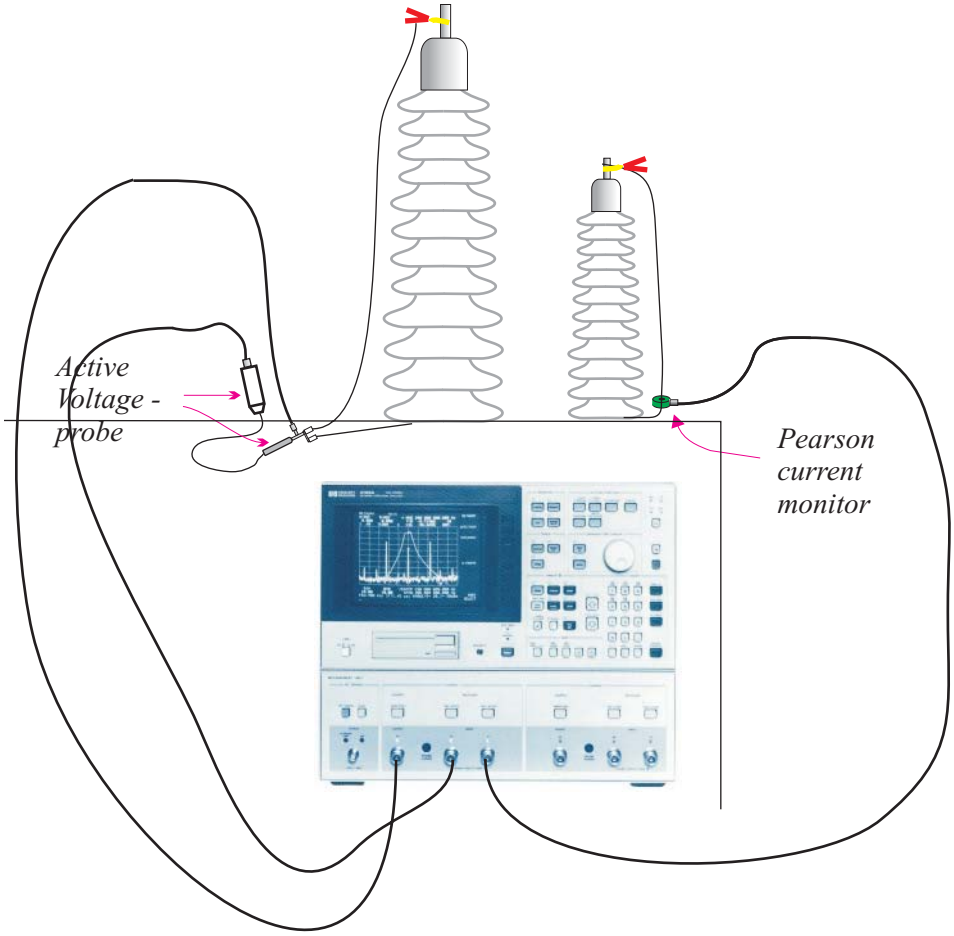

Figure C.1: FRA measurement setup with network analyser, active voltage probe and current monitor (compensated current transformer)

Using active probes eliminate the influence of terminations and the coax-cables running from the point of measurement to the network analyser. If these cables are equal of length (applied voltage is measured at the bushing), phase-related problems at high frequencies will be minimized (if active probes are properly calibrated).

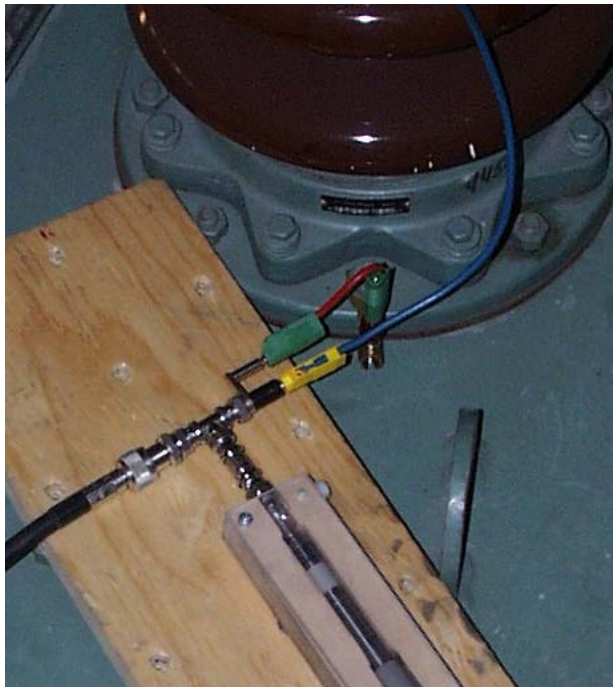

Figure C.2: Setup using active probe to measure applied voltage

The input impedance of the probes is very high (1 MOhm+1pF), and does not influence on the measured response. The disadvantage of using active probes, is that they need calibration. When measuring admittance/impedance, a pearson current monitor [21] is used for current measurements (see fig. C.3). The insertion impedance is usually very low for such units (typically a few milliΩ).

Figure C.3: Current measurement using a Pearson Current monitor

Proper grounding must be established at all flanges/bushings that are to be measured. This is to insure a low-impedance grounding to the tank and a short grounding lead. Both the connection to ground, and the stranded wire connecting the top of the bushing to the probe must be as short as possible. The wire from top of the bushing must also be as close to the body of the bushing as possible (preferably stretched) to minimize loop inductance and maximize reproducibility.

By using this measurement-setup, the influence of the coax-cables, instrument terminations and cable-layout is reduced to a minimum. This also makes it easier to perform comparisons when different equipment is used for the measurements. With long leads, the lead admittance becomes dominant somewhere above 500 kHz depending on the size of the bushing. This means that using long leads at a large transformer, reduces the sensitivity of FRA. In order to make a measurement independent of the coax cables when active probes are not used, it could be possible to compensate for the capacitance of the cables [63] (assuming the length is electrically short). As long as the cables are shorter than 1/4 of the shortest wavelength (upper frequency), no phasing-effects will occur.

As mentioned in chapter 2.2.1.4, the effect of the series inductance of the test leads may be reduced by using active, high impedance probes since the current in the measurement leads is reduced.

Appendix D. Historical Review - Transformer modeling

Transformer models have a variety of applications, and different requirements make use of different principles due to various demands regarding frequency range, needed degree of accuracy, application and so on. The history of transformer modeling is reviewed from the “early beginning” until today describing the main lines and principles used. The different challenges attended with transformer modeling are elucidated.

D.1. Introduction

The two first transformers were built and patented in 1885 and one of them was the Ganz transformer [170] incorporating a wound core.

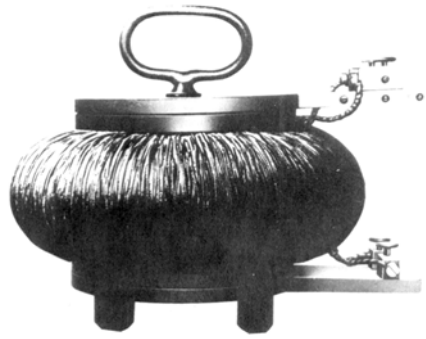

Figure D.1: The Ganz Transformer

The commercial breakthrough of power transformers was achieved by Westinghouse [171]. The development of the transformer during the first decades was based mainly on experience rather than science and research. At the beginning of the last century it was revealed that the response of transformers to lightning and switching surges was entirely different from the normal performance at operational frequencies, and the need for more detailed modeling and knowledge arose. The transformer is still a very complex component to model and there are details that are not fully understood even today.

During the last 50 years the need for detailed transformer models have been one of the driving forces of transformer research. The manufacturers need a reliable tool to design cost efficient and reliable transformers. Utilities need transformer models to simulate transformer interaction and backfeed during faults in their networks, and also as a tool for insulation coordination. Lately transformer models have found new applications such as in this work: Sensitivity analysis of FRA as a diagnostic method.

D.2. The early ages

The first era of transformer modeling is well described by Abetti's bibliographies [172], [173], [174] and historical survey [175]. The second era, from the early fifties until today, is mainly influenced by the use of computers. Abetti's bibliography is ranging from 1902 to the publication date of the last supplement [174] in 1964. His bibliographies contain 1265 references regarding transformer/ machine modeling and he collected them over a period of 10 years. Because of its importance and lack of credits from recent publications, a very brief summary is given. Abetti also contributed [176], [177] to the topics of surge response and transformer modeling and his work represents a milestone in these topics.

In 1902, Thomas [178] discovered that the voltage distribution in transformer windings exposed to surges with steep fronts is far from linear, resulting in very large voltage gradients in limited parts of the winding. Some years later Steinmetz, when discussing a paper by Jackson [7], indicated that a winding resembles more like a capacitance than an inductance at high frequencies. This led to the discussion of reinforced end-turn insulation, and many years later: shielding and “inter-leaving” to control the electrostatic voltage distribution. The initial (electrostatic) voltage distribution was recognized to follow a certain hyperbolic pattern. For the subsequent oscillations, the solution was attempted in many ways, which at the time where classified according to the following three methods:

- Treating the winding as a transmission line, was first done by Rudenberg [179], [180].
- Representing the winding by means of a ladder network (mesh) of concentrated parameters was first done by Weed [40]. He neglected all mutual inductances. (Included by Wagner [181], [182] but only between adjacent elements).
- An equivalent circuit of distributed inductive and capacitive parameters were suggested by Wagner [59], still with mutual inductances only between adjacent elements. He solved the differential equations for the oscillations by applying as boundary conditions the initial and final distribution as boundary conditions.

These 3 representations have subsequently been widely used and further developed.

During the 1920's attempts were made to get more precise solutions by including all self- and mutual inductances. This attempt led to highly mathematical and unsatisfactory results, and found no practical applications until 30-40 years later (using computers).

D.3. Introduction to principles of modern modeling

In 1919 Blume and Boyajian [50] introduced the concept of leakage inductance of the winding and methods for determining leakage inductances, which describes the difference between the self- and mutual inductance of two filaments directly. Rosa [183] made important contributions in calculation of self-inductances in 1906 and his work was later extended by Roth [184] and Grover [185]. Another approach of transformer modeling is the principle of duality, which was introduced by Cherry [55]. Duality means representing magnetic circuits with electrical equivalents. In the 50's and 60's manufacturers used reduced scale models [176] to improve their designs, but because it is a time-consuming and expensive way of modeling, they searched for new methods. Measurements can also be used to identify high frequency terminal characteristics of transformers [62], but this is not a method of modeling other than deriving the model from the measurements. Electromagnetic field computations have developed through the last 40 years due to the development of computers, and can be used to implement most methods mentioned above.

D.4. The age of computers

The introduction of computers enabled transformer engineers to solve their theoretical problems with higher accuracy and less simplifications than earlier. Today all methods of transformer modeling is based on computers, some demanding severe resources, others not. The main problem in the beginning of this era was the computation of the inductances. Most of the capacitances could be calculated analytically, but both the inductances and losses are frequency dependent to some extent and need numerical techniques to be calculated with high accuracy. The finite element method (FEM) is the most advancing one novadays.

Appendix E. Nodal System Description

The goal is to establish a system description on a nodal admittance form, but first all relations between branch and nodal elements must be described:

$$\mathbf{Z} = \mathbf{R}(\omega) + j\omega \cdot \mathbf{L}(\omega) \qquad \text{E.1}$$

$$\mathbf{Y} = \mathbf{G}(\omega) + j\omega \cdot \mathbf{C}(\omega) \qquad \text{E.2}$$

The established branch-matrix (number of branches: m) consists of the R and L-elements at each frequency-point as shown in eq. E.3

$$[Z_B] = \begin{bmatrix} R_{11}+j\omega L_{11} & R_{12}+j\omega L_{12} & \dots & R_{1m}+j\omega L_{1m} \\ R_{21}+j\omega L_{21} & R_{22}+j\omega L_{22} & \dots & R_{2m}+j\omega L_{2m} \\ \dots & \dots & \dots & \dots \\ R_{m1}+j\omega L_{m1} & R_{m2}+j\omega L_{m2} & \dots & R_{mm}+j\omega L_{mm} \end{bmatrix} \qquad \text{E.3}$$

while the C- and G-elements form the nodal admittance matrix shown in eq.E.4 (number of nodes: n):

$$[Y_N] = \begin{bmatrix} G_{11}+j\omega C_{11} & G_{12}+j\omega C_{12} & \dots & G_{1n}+j\omega C_{1n} \\ G_{21}+j\omega C_{21} & G_{22}+j\omega C_{22} & \dots & G_{2n}+j\omega C_{2n} \\ \dots & \dots & \dots & \dots \\ G_{n1}+j\omega C_{n1} & G_{n2}+j\omega C_{n2} & \dots & G_{nn}+j\omega C_{nn} \end{bmatrix} \qquad \text{E.4}$$

The branch matrix must be converted to its inverse nodal form (admittance) as shown in the example below:

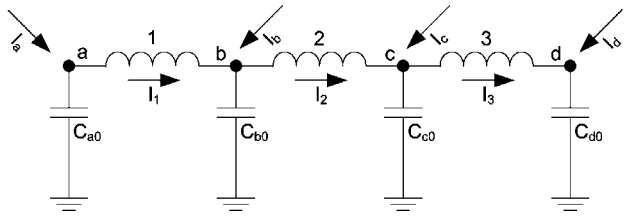

Figure E.1: Relations between nodal and branch currents

Since the inductance-matrix have mutual elements (off-diagonal elements), the matrix cannot just be inverted directly to its admittance description. The relations between the nodal currents and the branch currents has to be described. In the example of fig. E.1 we have two types of nodal currents:

$$\mathbf{I_N} = \mathbf{I_C} + \mathbf{I_L} \tag{E.5}$$

$\mathbf{I_L}$ is the inductive part of the nodal currents.
What we want to achieve is a nodal description as given below:

$$\mathbf{I_L} = \frac{\mathbf{1}}{\mathbf{s}} \cdot \Gamma_\mathbf{N} \cdot \mathbf{U_N} \tag{E.6}$$

The starting point is the branch description below:

$$\mathbf{U_B} = \mathbf{sL_B} \cdot \mathbf{I_B} \Rightarrow \mathbf{L_B^{-1}} = \Gamma_\mathbf{B} \Rightarrow \mathbf{I_B} = \frac{\mathbf{1}}{\mathbf{s}}\Gamma_\mathbf{B} \cdot \mathbf{U_B} \tag{E.7}$$

Then the relation between each inductive nodal current and the branch currents are described:

$$\begin{aligned} I_{La} &= I_1 \\ I_{Lb} &= -I_1 + I_2 \\ I_{Lc} &= -I_2 + I_3 \\ I_{Ld} &= -I_3 \\ \mathbf{I_L} &= \mathbf{A} \cdot \mathbf{I_B} \end{aligned} \quad \text{where} \quad \mathbf{A} = \begin{bmatrix} 1 & 0 & 0 \\ -1 & 1 & 0 \\ 0 & -1 & 1 \\ 0 & 0 & -1 \end{bmatrix} \tag{E.8}$$

The equivalent relation is then found for the branch and nodal voltages:

$$\begin{aligned} \mathbf{U_1} &= \mathbf{U_a} - \mathbf{U_b} \\ \mathbf{U_2} &= \mathbf{U_b} - \mathbf{U_c} \\ \mathbf{U_3} &= \mathbf{U_c} - \mathbf{U_d} \\ \mathbf{U_B} &= \mathbf{B} \cdot \mathbf{U_N} \end{aligned} \quad \text{where} \quad \mathbf{B} = \begin{bmatrix} 1 & -1 & 0 & 0 \\ 0 & 1 & -1 & 0 \\ 0 & 0 & 1 & -1 \end{bmatrix} \tag{E.9}$$

Observing the fact that $\mathbf{B} = \mathbf{A^T}$ gives:

$$\mathbf{U_B} = \mathbf{A^T} \cdot \mathbf{U_N} \tag{E.10}$$

Eq. (E.10) is inserted into eq. (E.7) giving:

$$\mathbf{I_B} = \frac{\mathbf{1}}{\mathbf{s}}\Gamma_\mathbf{B} \cdot \mathbf{A^T} \cdot \mathbf{U_N} \tag{E.11}$$

Eq. (E.8) is rewritten to $\mathbf{I_B} = \mathbf{A^{-1}} \cdot \mathbf{I_L}$ and inserted into eq. (E.11):

$$\begin{aligned} \mathbf{A^{-1}} \cdot \mathbf{I_L} &= \frac{\mathbf{1}}{\mathbf{s}}\Gamma_\mathbf{B} \cdot \mathbf{A^T} \cdot \mathbf{U_N} \\ \mathbf{I_L} &= \frac{\mathbf{1}}{\mathbf{s}} \cdot \mathbf{A} \cdot \Gamma_\mathbf{B} \cdot \mathbf{A^T} \cdot \mathbf{U_N} \end{aligned} \tag{E.12}$$

When comparing eq. (E.12) to eq. (E.6) we see that $\Gamma_\mathbf{N} = \mathbf{A} \cdot \Gamma_\mathbf{B} \cdot \mathbf{A^T}$
Using the above result, the nodal transformation of the branch matrix in eq. (E.3) can be transformed to its admittance description:

$$\mathbf{Y_B} = \mathbf{A} \cdot \mathbf{Z_B}^{-1} \cdot \mathbf{A}^{\mathbf{T}} \tag{E.13}$$

Equalizing $s = j\omega$ results in a Laplace-description of the system:

$$\mathbf{Y_{sys}}(s) = \mathbf{Y_N}(s) + \mathbf{Y_B}(s) \tag{E.14}$$

The system description (admittance matrix) builds the relation between nodal voltages and currents as shown below:

$$\mathbf{Y_{sys}} \cdot \mathbf{V_N} = \mathbf{I_N} \rightarrow \begin{bmatrix} Y_{11} & Y_{12} & \cdots & Y_{1N} \\ Y_{21} & Y_{22} & \cdots & \cdots \\ \cdots & \cdots & \cdots & \cdots \\ Y_{N1} & \cdots & \cdots & Y_{NN} \end{bmatrix} \cdot \begin{bmatrix} V_1 \\ V_2 \\ \cdots \\ V_N \end{bmatrix} = \begin{bmatrix} I_1 \\ I_2 \\ \cdots \\ I_N \end{bmatrix} \tag{E.15}$$

Depending on the type of analysis, the system description is then reduced to the nodes of interest (terminal/internal). Terminals/nodes of interest are hereby called external nodes.

The matrices are restacked so that the external nodes are situated at the left upper part of the admittance-matrix as shown in eq.(E.16). Current into internal nodes are 0 ($\mathbf{I_i} = \begin{bmatrix} 0 & 0 & \cdots & 0 \end{bmatrix}^T$).

$$\begin{bmatrix} \mathbf{Y_{ee}} & \mathbf{Y_{ei}} \\ \mathbf{Y_{ie}} & \mathbf{Y_{ii}} \end{bmatrix} \cdot \begin{bmatrix} \mathbf{V_e} \\ \mathbf{V_i} \end{bmatrix} = \begin{bmatrix} \mathbf{I_e} \\ 0 \\ \cdots \\ 0 \end{bmatrix} \tag{E.16}$$

In general we could say that with N number of nodes in total, there are P external nodes. The above matrices then have the following dimensions:

$$\begin{aligned} &\mathbf{Y_{ee}}(P, P) \\ &\mathbf{Y_{ei}}(P, N-P) \\ &\mathbf{Y_{ie}}(N-P, P) \\ &\mathbf{Y_{ii}}(N-P, N-P) \\ &\mathbf{V_e}(P, 1) \\ &\mathbf{V_i}(N-P, 1) \\ &\mathbf{I_e}(P, 1) \end{aligned} \tag{E.17}$$

Multiplying the matrices in eq. (E.16) results in the following equations:

$$\mathbf{Y_{ee}} \cdot \mathbf{V_e} + \mathbf{Y_{ei}} \cdot \mathbf{V_i} = \mathbf{I_e} \tag{E.18}$$

$$\mathbf{Y_{ie}} \cdot \mathbf{V_e} + \mathbf{Y_{ii}} \cdot \mathbf{V_i} = 0 \tag{E.19}$$

Eq. (E.19) is then rewritten to:

$$\mathbf{V_i} = -\frac{\mathbf{Y_{ie}} + \mathbf{V_e}}{\mathbf{Y_{ii}}} = -\mathbf{Y_{ii}^{-1}} \cdot \mathbf{Y_{ie}} \cdot \mathbf{V_e} \qquad \text{E.20}$$

and then inserted into eq. (E.18):

$$\mathbf{Y_{ee}} \cdot \mathbf{V_e} + \mathbf{Y_{ei}} \cdot (-\mathbf{Y_{ii}^{-1}} \cdot \mathbf{Y_{ie}} \cdot \mathbf{V_e}) = \mathbf{I_e} \qquad \text{E.21}$$

This reduces to the following condensed or reduced description of the system:

$$\tilde{\mathbf{Y}} \cdot \mathbf{V_e} = \mathbf{I_e} \qquad \text{E.22}$$

$$\text{where } \tilde{\mathbf{Y}} = \mathbf{Y_{ee}} - (\mathbf{Y_{ei}} \cdot \mathbf{Y_{ii}^{-1}} \cdot \mathbf{Y_{ie}}) \qquad \text{E.23}$$

Since these steps require several inversions, it is a possibility that the resulting matrices will be badly conditioned (large errors due to the inversions). It is therefore preferable to also have the opportunity to use a an approach with a modal analysis according to the approach of SUMER (for future implementation into a possible Femlab-substitute to SUMER)

Appendix F. Analytical formulations

Equations regarding inductance are based on air-core theory.

Equations for capacitance are based on geometrical and energetic considerations. If not otherwise referenced, equations for the capacitances are mainly based on [44].

F.1. Self Inductance

From Maxwell's first equation (on integral form) we may obtain the magnetic contribution along a circular loop carrying current (due to the applied electrical field):

$$\oint \vec{E} \cdot \vec{ds} = -\frac{\partial \phi}{\partial t} = -\frac{\partial}{\partial t}\iint (\vec{B} \cdot \vec{n}) dA = -\frac{\partial}{\partial t}\oint (\vec{A} \cdot \vec{ds}) \qquad \text{F.1}$$

Assuming $\vec{B}$ is proportional to $\vec{H}$ (only linear materials) the flux through the loop is proportional to the total current carried by the loop. The proportionality is described by the self inductance of this loop. Assuming the loop is placed in vacuum (no ferromagnetic materials included), the inductance of the loop is depending on its geometry only.

The total flux through the loop is expressed as:

$$\phi = \iint (\vec{B} \cdot \vec{n}) dA = \oint (\vec{A} \cdot \vec{ds}) = L \cdot I \qquad \text{F.2}$$

In the latter only the external inductance is considered, due to the fact that the internal inductance is depending on the current distribution within the conductor (which in turn is determined by the skin-effect/frequency).

For a circular conductor the flux through the loop is determined by:

$$\phi = \phi_{outer} = \oint_{C_2} \left[\frac{\mu_0 \cdot I}{4\pi} \oint_{C_1} \frac{\vec{ds_1}}{r} \right] \cdot \vec{ds_2} = \frac{\mu_0 \cdot I}{4\pi} \oint_{C_1} \oint_{C_2} \frac{\vec{ds_1} \cdot \vec{ds_2}}{r} \qquad \text{F.3}$$

and then:

$$L = L_{outer} = \frac{\mu_0}{4\pi} \oint_1 \oint_2 \frac{\vec{ds_1} \cdot \vec{ds_2}}{r} \qquad \text{F.4}$$

The two paths of integration to find the inductance is shown in figure F.1, where $\vec{ds_1}$ is the unity vector quantity along the centre-line of the loop, and $\vec{ds_2}$ is the unity vector along a closed curve on the surface of the conductor. r is the distance between the two elements $\vec{ds_1}$ and $\vec{ds_2}$

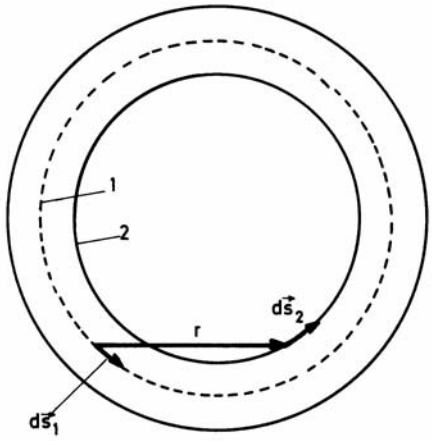

Figure F.1: Integration paths to find self inductance

For a circular coil with a rectangular cross-section, the following first approximation is used (employing a mean geometric radius) to find the inductance:

$$L_i = \mu_0 R\left(\ln\frac{8R}{R_s} - 2\right) \qquad \text{F.5}$$

where R is the mean radius. R_s represents the mean geometric radius expressed by (given by Grover [185]):

$$\ln\frac{R_s}{\sqrt{a^2+b^2}} = \frac{2b}{3a}\tan\left(\frac{a}{b}\right)^{-1} + \frac{2a}{3b}\tan\left(\frac{b}{a}\right)^{-1} - \frac{b^2}{12a^2}\ln\left(1+\frac{a^2}{b^2}\right) \qquad \text{F.6}$$
$$-\frac{a^2}{12b^2}\ln\left(1+\frac{b^2}{a^2}\right) - \frac{25}{12}$$

The parameters *R*, *a* and *b* are the average radius, coil height and coil width respectively as given in figure F.2:

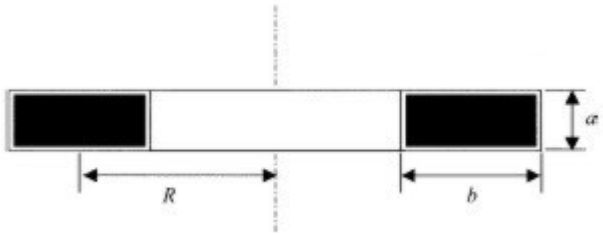

Figure F.2: Dimensions for a rectangular cross-section coil

This is the usual design of disc winding, which comprises rectangular conductors with wound insulation. The validity of this method is confirmed by FEM-analysis.

The insulation space is considerable and requires some form of correction. One way of correcting for insulation space and partial flux linkage due to dimensions, is to apply a method given by Kirchoff [186], where the equivalent self inductance of a section is equal to the sum of self inductances of the turns plus the sum of all mutual inductances between all turn combinations:

$$L_{eq} = \sum_{i=1}^{n} \sum_{j=1}^{n} M_{ij} \qquad \text{F.7}$$

The computational load can be decreased by making use of the symmetrical property of the mutual inductances. The eq.(F.7) then becomes:

$$L_{eq} = \sum_{i=1}^{n} L_{ii} + 2 \sum_{i=1}^{n} \sum_{j=i+1}^{n} M_{ij} \qquad \text{F.8}$$

The mutual inductances can be calculated by using Lyle's method [187] as shown by Wirgau [107]. This method will be discussed in the following.

F.2. Mutual inductance

Mutual inductance is calculated using the same approach as the initial considerations for self inductance, where the mutual inductance between two parallel conducting filaments is calculated using eq. (F.4).

This integral can be expressed as:

$$M_{12} = \frac{\mu_0}{4\pi} \int_0^{2\pi} \int_0^{2\pi} \frac{r_1(\alpha_1) \cdot r_2(\alpha_2) \cdot \cos(\alpha_1 - \alpha_2)}{R_{12}(\alpha_1, \alpha_2)} d\alpha_1 d\alpha_2 \qquad \text{F.9}$$

The integral is also used for calculating the inductances of deformed/buckled windings.

The approach, by assuming filaments of negligible cross-section, is rather coarse if the dimensions of the cross-section are appreciable compared to the distance *d*, between the filaments. If so, the mutual inductance is over-estimated.

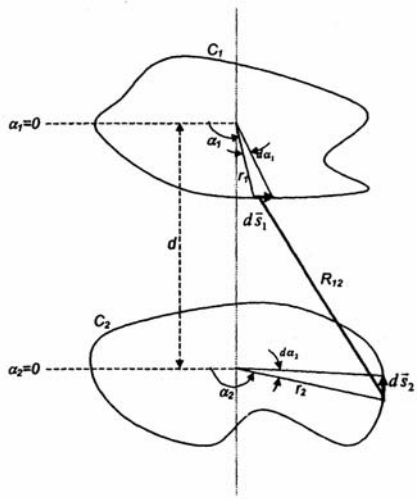

Figure F.3: Two paralell conducting filaments

Maxwell [188] derived an exact formula for mutual inductance of two coaxial circular filaments from the general integral above using elliptic integrals [189] to represent solution of the double integral.

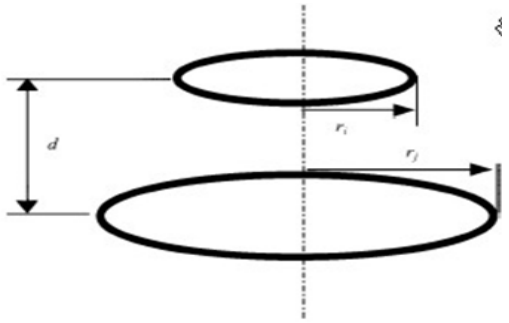

Figure F.4: Mutual coupling between two circular filaments

The mutual coupling from loop i to j, is given by:

$$M_{ij} = \frac{2\mu_0\sqrt{r_i r_j}}{\sqrt{k'}}[K(k') - E(k')] \qquad \text{F.10}$$

where r_i and r_j are the radii of the two circular loops and d is the separation between them. The argument for the elliptic integrals, k', is given by eq. (F.11) and (F.12):

$$k' = \frac{1 - \sqrt{1 - k^2}}{1 + \sqrt{1 - k^2}} \qquad \text{F.11}$$

$$k = \sqrt{\frac{4 r_i r_j}{(r_i + r_j)^2 + d^2}} \qquad \text{F.12}$$

As mentioned earlier, the mutual inductances are over-estimated when neglecting the dimensions of the winding cross-section. This can be seen from fig. F.1, when the dimensions of the conductor become very small, the inductance approaches infinity.

The use of Lyle's method [187] makes the results more accurate by replacing each coil with a certain number of filaments as shown below, and then calculating the total mutual inductance as the averaged sum all the partial mutual inductances.

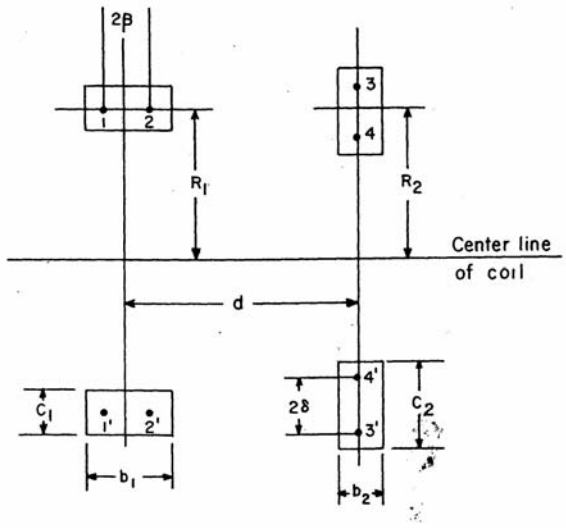

Figure F.5: Lyle's representation [187]

If the subdivision of the coils matches the turn division of the coil, then the mutual inductance is found simply by adding up all the mutual inductances between all combinations.

If even higher accuracy is needed the turns can be further subdivided (into strands or more), following the same principle.

F.3. Series capacitance

There are several types of windings but some of the main types of windings are listed here:

- Helical winding (single- or multi-layer)
- Disc winding (conventional, interleaved or in-wound shields)
- Layer winding (conventional or interleaved)

These have different ways of calculating the series capacitance. Equations on series and shunt capacitances are taken from [44],unless otherwise referenced.

Helical winding (inter-turn capacitance).

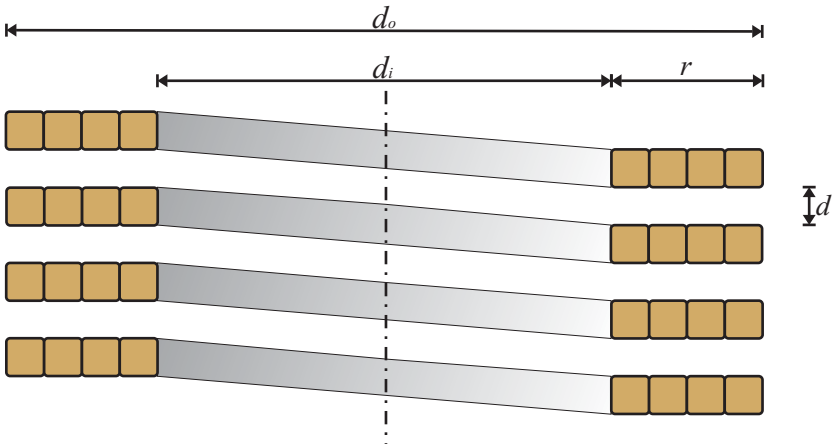

Figure F.6: Helical winding (single layer, single-start)

$$C'_S = \varepsilon_r \varepsilon 0 \pi \cdot \frac{{d'_0}^2 - {d'_i}^2}{4d} \qquad \text{F.13}$$

d: distance between turns.
$do' = do + d$: outer diameter + interturn distance (accounting for fringing)
di': inner diameter - distance between turns.

The series capacitance for the whole winding is:

$$C_S = \frac{1}{n_t - 1} \cdot C'_S \qquad \text{F.14}$$

n_t : number of turns

It is assumed that there is no voltage difference between parallell strands, and that the voltage distribution is linear along each turn. Multistart helical windings can be handled by the same equations.

Disc winding.

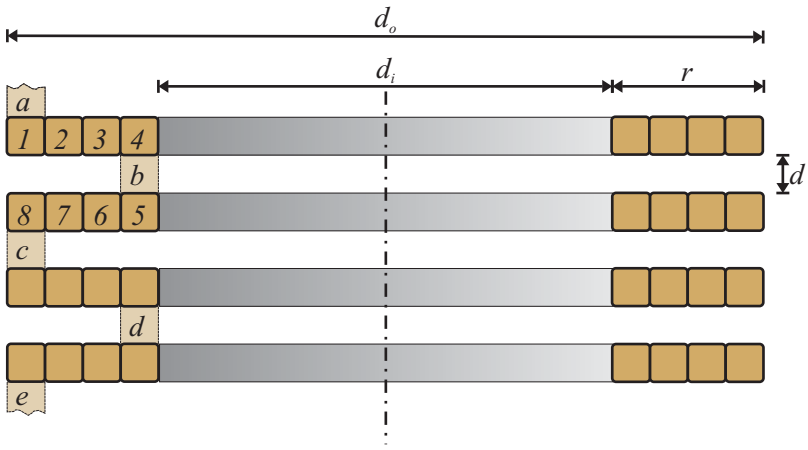

Figure F.7: Ordinary (continously wound) disc winding

For conventional disc windings, the method of Stein [79] is adopted. He treats the internal field in a disc in the same way as for a complete winding:

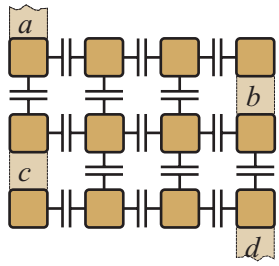

Figure F.8: Equivalent circuit for disc winding

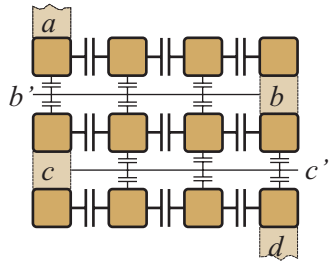

Figure F.9: Equipotential lines: b-b' and c-c'

The voltage distribution for the whole winding is determined by the external distribution constant:

$$\alpha_e = \sqrt{\frac{c_g}{c_s}} \qquad \text{F.15}$$

The voltage distribution inside a disc is determined by the internal distribution constant:

$$\alpha_i = \sqrt{\frac{4c_g}{c_t}} \qquad \text{F.16}$$

c_g = capacitance between disconnected discs.
c_t = capacitance between turns.

Stein showed that:

$$\frac{c'_s}{c_d + c_t} = \frac{1}{1 + \left(\frac{1}{\alpha'_i}\right)^2} \cdot \left(1 + \frac{1}{\alpha'_i} \cdot \coth(\alpha'_i)\right) \qquad \text{F.17}$$

where:

$$\alpha'_i = \frac{1}{2} \cdot \alpha_i = \sqrt{\frac{c_d}{c_t}} \qquad \text{F.18}$$

$$c_d = \varepsilon_r \varepsilon_0 \pi \cdot \frac{d'^2_o - d'^2_i}{4 \cdot d} \qquad \text{F.19}$$

$$c_s = \frac{1}{n_d} \cdot c'_s = c_d \cdot \frac{1}{n_d} \cdot \left(1 + \frac{1}{\alpha'_i} \cdot \coth(\alpha'_i)\right) \qquad \text{F.20}$$

where n_d = number of discs.

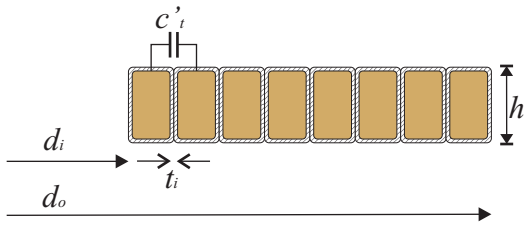

Figure F.10: Dimensions of a single disc

$$c'_t = \varepsilon_r \varepsilon_0 \pi \cdot \frac{d_o - d_i}{2} \cdot \frac{h}{t_i} \qquad \text{F.21}$$

$$c_t = \frac{1}{m_t - 1} \cdot c'_t \qquad \text{F.22}$$

h = axial height of insulated conductor (to compensate for fringing)
t_i = insulation thickness between turns
m_t = number of turns per disc

Interleaved Disc Winding.

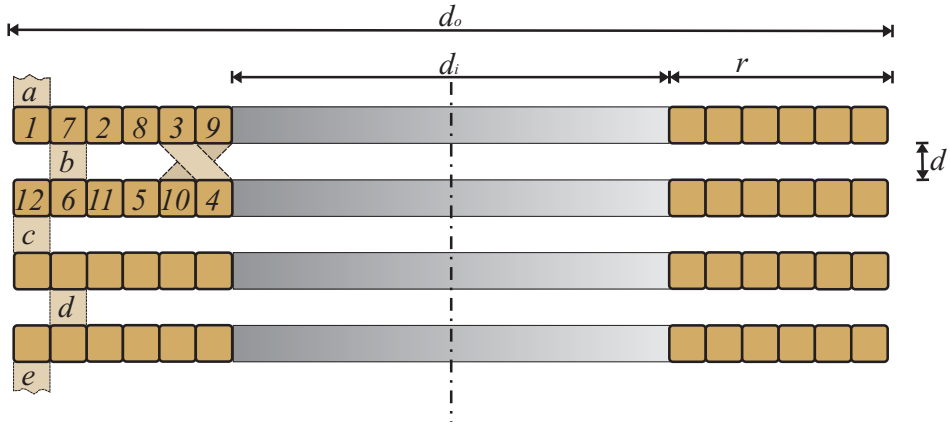

Figure F.11: Interleaved disc winding

In fig. F.11 an interleaved disc winding is shown. There are also other possibilities of interleaving, such as a 4 disc interleaving, but then the voltage between strands will be higher.

Pedersen [84] treated the interleaved winding based on surge impedance representation rather than traditional capacitance representation. His paper contributes to the understanding of internal voltages in interleaved windings during the charging period for the inter-turn capacitances.

As a starting point the phenomenas inside the discs are not evaluated and first the capacitance representation is reviewed. The equivalent capacitance between a and b in figure F.11 is given by:

$$\frac{1}{2} \cdot c'_s \cdot u^2 = w \qquad \text{F.23}$$

w = energy stored in the inter-turn and inter-disc capacitances (per disc)
u = voltage across one disc

It is then assumed that the voltage distribution inside each disc is linear. Based on this assumption, the following expressions for the stored energy can be considered:

Inter-turn capacitances:

$$w_t \approx \frac{1}{2} \cdot u^2 \cdot c'_t \cdot (m_t - 1) \qquad \text{F.24}$$

where c'_t is the capacitance between adjacent turns, and m_t is the number of turns per disc.

Inter-disc capacitances:

$$w_d = \frac{1}{2} \cdot u^2 \cdot \left(\frac{4}{3} \cdot c_d\right) \qquad \text{F.25}$$

Combining (F.23)-(F.25) gives the following expression for the series capacitance of the whole winding-segment considered:

$$c_s = \frac{1}{n_d} \cdot c'_s = [(m_t - 1) \cdot c'_t + 1,33 \cdot c_d] \cdot \frac{1}{n_d} \qquad \text{F.26}$$

where c'_t and c_d can be calculated using (F.21) and (F.19) respectively.

Series capacitance of windings with in-wound shields can be determined using the approach of Del Vecchio et al. [190].

Cylindrical windings may be treated equal to helical windings.

F.4. Shunt capacitance

These are capacitances between windings and between winding and ground. Some of these values are calculated with simplified geometrical formulas, and some are calculated on a semi-empirical basis.

Capacitance between windings. The windings are concentrically arranged around the core and can be treated as cylindrical capacitors given by:

$$C_g = \frac{2\pi\varepsilon_r\varepsilon_0 h'}{\ln\left(\frac{d_i}{d_o}\right)} \qquad \text{F.27}$$

where $h' = h + d$ to compensate for fringing of the field at the ends, d_i is the inner diameter of the outer winding and d_o is the outer diameter of the inner winding, d is the distance between them.

Capacitance between phases. The following formula applies for capacitance between windings on adjacent legs:

$$C_p = \frac{\varepsilon_r \varepsilon_0 \pi h'}{\ln\left(\frac{b}{d_0} + \sqrt{\left(\frac{b}{d_0}\right)^2 - 1}\right)} \qquad \text{F.28}$$

where b is the distance between adjacent windings (centre-centre) and d_0 is the diameter of the windings. ($h' = h + b - d_0$)

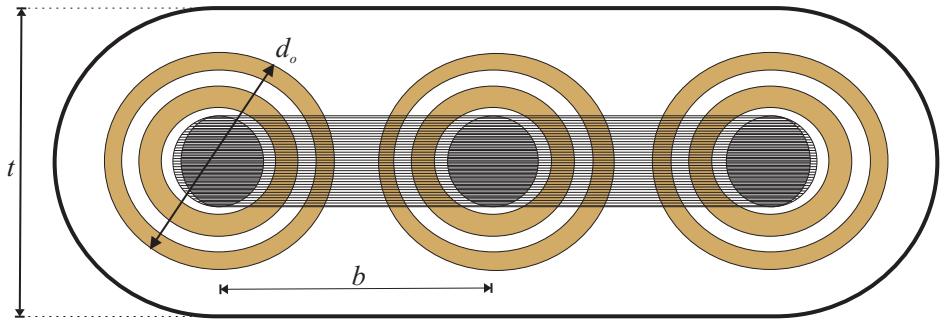

Figure F.12: Dimensions between adjacent windings and between windings and tank

Capacitance to the tank. For rough estimations, equations (F.27) and (F.28) can be applied for calculating the capacitance from the windings to the tank (Ct).

For the center phase, Eq.(F.27) is used and b is replaced by t, which is the internal width of the tank. A reduction factor of 0.25 is used compared to a cylinder over plane configuration:

$$C_t = 0,25 \cdot \frac{\varepsilon_r \varepsilon_0 \pi h'}{\ln\left(\frac{t}{d_0} + \sqrt{\left(\frac{t}{d_0}\right)^2 - 1}\right)} \qquad \text{F.29}$$

The capacitance between an end phase and the tank, C_q, is calculated from Eq.(F.27) with a reduction factor of 0.75 (due to the fact that the tank is not a complete circle) and where d_i is replaced by t.

$$C_q = 0,75 \cdot \frac{2\pi \varepsilon_r \varepsilon_0 h'}{\ln\left(\frac{t}{d_0}\right)} [F] \qquad \text{F.30}$$

Appendix G. Modeling in SUMER

SUMER is a specialized software developed by Electricite de France (EdF) [74], used to establish detailed high frequency power transformer models. It is based on the finite element method (FEM). It uses Flux2D [122] (as a pre-processor) for the construction of the geometry, and the mesh generation. The solver is implemented in SUMER and features a direct method based on SuperLU [191].

The software establishes a wide frequency range lumped linear model of the transformer, which can be used for lightning- and switching studies [123] as well as FRA sensitivity analysis [124], [125].

A set of branch-matrices are calculated at a few discrete frequencies to incorporate the frequency-dependent features of a power transformer. A nodal model is then constructed and the eigenmodes and eigenfrequencies calculated by an iterative process (modal analysis). Once these data's are derived, a multipole equivalent is calculated. This equivalent is reduced to a terminal equivalent (a condensed admittance matrix). The reason for this is to make use of EMTP [126] as an interface for time-domain over-voltage studies in power networks. Once an EMTP-simulation is carried out at the terminals (transformer-network interaction), the internal voltages can be deduced from the full multipole equivalent (or the complete admittance matrix) by using a transfer matrix (between external and internal nodes) found in the modal analysis.

The idea of the software itself is really clever, due to the fact that all frequency dependent characteristics can be included by for instance, using complex permeability [120] representation of eddy current effects in the winding (proximity effect). The level of discretisation (number of lumped elements in the model) is decided by the user according to the frequency range of interest. Frequency-dependent effects such as skin- and proximity-effect in the windings are incorporated. Frequency-dependencies for the insulating materials can also be included, if measurement data is made available. Effects due to changes in capacitance and dielectric losses can then be studied.

During a stay at EdF in Paris, a frequency dependent representation of the iron core was implemented by the author. The leakage field surrounded by the core proved to have an important effect on the characteristics. The importance of the iron losses at high frequencies were also demonstrated. (See Chapter 5)

This software is being developed continuously by adding both technical improvements and user friendliness. Still this software remains scientific and mainly for internal use. Due to limited resources compared to commercial software, the technical improvements remain the important ones. Still there are some parts related to the interface that ought to be improved to speed up the generation of new models, especially if the developers want to increase the number of users for their software.

The menus of SUMER are in French, as well as the documentation.
Flux2D has the ability to switch between different languages for the menu-system, but due to the scripting-tool used for transformer modeling, one is confined to use the same language (French) also for this one.
As a first step towards international users, there should at least be an English user-guide. Also a FAQ is highly recommended. The use of English menus would also attract foreign users.

G.1. Modeling procedure

The process of modeling is summarized: Details, features, and comments are given in the following.

G.2. Geometry

As mentioned earlier, the geometry is established using Flux2D. This is, and has for several years been a leading tool for industrial FEM analysis. It is able to handle complex problems, and it can be controlled by script-like command sequences making it ideal for transformer geometries because of symmetry and repeated geometrical input. The subdivision of the winding into smaller electrical elements (electrical mesh, for instance one disc) is done already at the stage of geometrical input. Each electrical element is given a unique name so that SUMER can recognize them.

G.3. Mesh

To solve a problem using FEM (Finite Element Method), the problem must be broken down to have a linear formulation in several small subdomains/elements. This subdivision is called meshing, and to obtain accurate results the mesh must be dense where the field (electric or magnetic) is expected to have a high degree of curvature. To optimize the mesh for CPU-consumption during calculation, areas with less curvature should have a coarser mesh.

The mesh-generator of Flux2D lacks possibility to automate the mesh-generation. All edges must be manually discretizised (this is done in the script), and to optimize the mesh, additional lines have to be added to “relax” the mesh (make the mesh grow). Modern mesh-generators have both adaptive features and also the ability to be controlled by directional growth-factors eliminating the need for additional lines. In SUMER/Flux2D these lines must be added at a certain stage in the modeling. Otherwise several time-consuming steps must be redone. Flux2D is able to produce mapped mesh (rectangular mesh) for rectangular domains with no gradient in the field. This is an efficient method to reduce the mesh size. The upper size of the configuration used by the author seems to be somewhere between 200-250.000 degrees of freedom (DOF) for the dielectric model, which in most cases is sufficient to produce accurate results for the capacitances and conductances. A short explanation regarding degrees of freedom in a FE-problem is given below:

Once the mesh is obtained, approximations can be introduced for the dependent variables. As an example, the case of a single variable, u is given. The idea is to approximate u with a function that can be described with a finite number of parameters, the so-called degrees of freedom (DOF). The number of DOF's is depending on the order and number of mesh elements, and also the number of dependent variables. The upper limit for the number of DOF's will be given by the amount of memory available for the calculation.

G.4. Physical properties

After the mesh and the geometry are imported to SUMER, the physical properties are applied to the model. Material-properties are chosen from a user-generated database. Frequency-dependencies can be included by defining several materials and then applying these in different frequencies/calculations. Afterwards a complete set of matrices can be obtained by joining the different calculations together. At the time this way of applying frequency-dependency for dielectric materials is rather cumbersome, and may also give rise to problems during the modal analysis. Boundary-conditions are then reapplied.

G.5. Frequency Distribution

Initially a set of 5-8 frequencies were given; One at low frequency (2Hz), one at power frequency, and one at the upper end of the frequency-range. The frequencies within the distribution should be carefully chosen, based on knowledge from the frequency-dependencies occurring in the model. When introducing a frequency dependent core representation, the inductance and iron-losses became the parameters changing the most. The largest change occurs at the frequency where the skin-depth of the iron laminates is equal to their thickness. A few frequencies are needed to cover such a change. Additional points are needed (at least 2 per decade). The rest of the frequencies are put in the higher region, due to the fact that most complex modes of the winding are located at higher frequencies (usually above 1MHz). Number of frequencies must be kept as low as possible; due to the fact that additional points add computational time (one extra frequency adds 0,5-2 hours of computation depending on the load of the host computer and the complexity of the model).

G.6. Solving the FE model

As mentioned, SUMER is based on a direct FEM-solver (SuperLU) which leads to a fast computation compared to an iterative solver (iterative solvers are less memory demanding).
All self- and mutual effects are calculated between all electrical elements.
One major drawback for SUMER is that solutions cannot be visually inspected.
Another limitation regarding portability of SUMER to for instance Linux, is that the solver establishes the FE-matrices by using a Flux2D-library written only for Unix.

G.7. Connections and configuration

The branches (frequency dependent RLCG-matrices) from the FEM-calculation, is connected together in a nodal admittance description. In the current version of SUMER there is a serious limitation regarding interconnection of discs within a disc-winding. The only possible way of interconnection is that the output of the first disc is connected to the start/input of the next disc. This is not the usual way of connecting a continuously wound disc-winding (which usually have a zig-zag-pattern). This limitation causes a large error to the series-capacitance of the disc-winding. Since one does not have access to the nodal capacitance matrix, changes cannot be made manually.

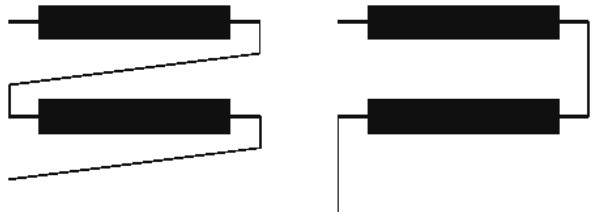

Figure G.1: Left: Sumer's connection mode.
Right: Desired connection mode

G.8. Calculating a terminal equivalent

The nodal admittance matrix is then reduced to a terminal description (frequency dependent). This is further approximated using rational functions by iterative eigenfrequency analysis to create a passive RLCG model compatible with EMTP. Some problems may occur when calculating the spectre (due to convergence problems). This may occur on models containing a high degree of damping. Increased dielectric losses and inclusion of the core yield such problems. At the time, the only solution here is to add another calculation at the frequency where the convergence-problem occurred. This seems to lower the residual in the eigenvalue-calculation, and the problem might be the linear interpolation between the calculations/frequency-points. Instead a spline interpolation is suggested to keep the derived of the curve continuous across all points in the frequency distribution.

G.9. Performing internal analysis

Results from EMTP-simulations at the transformer terminals can be transferred back to the detailed model by using a special transfer matrix determined during the modal analysis. This matrix describes the transfer functions from the terminals to the inner nodes. Inter-disc voltages can easily be obtained. Dielectric stress analysis would be preferable to add as a future option.
FRA signatures can easily be obtained by running a frequency-scan on the terminal equivalent.

G.10. Alternatives

There are some disadvantages of using SUMER. These are listed below:

- Establishing geometry in Flux2D is a bit complicated. Flux2D must be run with the French menu-system to be compatible with the scripting tool. This tool is completely necessary to save time during the input of the geometry. The tool is written in Scilab [192], which is a freeware-alternative to Matlab [128]. A better solution would be to have a windows-based PC-program to generate the scripts.
- Controlling the mesh is rather manual and time-consuming; no growth-factors can be specified in the domains. The result is a need for additional lines between windings in order to “relax” or control the mesh-growth.
- Frequency-dependent material parameters cannot be taken into account directly. Frequency-dependent dielectric losses must be included by manually adjusting material parameters for each frequency of calculation.
- SUMER is scientific software. It lacks English documentation and at the time there are minor bugs in the software which need to be fixed.
- No visualization of results to verify whether a solution seems correct or not.
- Connection of disc-windings lacks flexibility resulting in a wrong representation of the series capacitance (important at frequencies above 2-500 kHz).
- Convergence problems in the eigenvalue calculation when the circuit incorporates a high degree of damping. This might have something to do with the method of interpolation (linear rather than spline) used in SUMER.
- EMTP is a necessity for postprocessing results (except for investigation of the admittances).
- Maintenance is difficult because of the platform used (Unix/ SUN Sparcstation), but parts of the software are evolving towards Linux.

Another FEM-based software have been pushing lately, which would be a good alternative. It is described in the following.

Appendix H. Modeling in Femlab

Femlab [127] is a quite new FEM-based software, well suited for multiphysics and multidisciplinary analysis of complex problems. Since the software is fairly new compared to some of their competitors, it involves some minor flaws which probably will be fixed in the upcoming releases. Its advantages are not few: Direct interaction with Matlab for parameter-studies, advanced postprocessing, and also total control of internal details.

Femlab 3.1 has shown alot of great developments in its release. It is fast and memory-efficient, which makes it interesting for complex, industrial problems, and not only simplified academic problems.

The geometry is constructed either by making use of Femlabs built-in drawing-tools or by importing a geometry from the most common CAD-tools. Geometry can also be given in an m-file (Matlab-code), but the difficulty of keeping track of the coordinates makes it more practical to use the graphical interface for interpreting the geometry. For transformer modeling this is even more pronounced, due to the symmetries within transformer windings. Certain functions can be applied to make an array of similar elements. In time of writing, Comsol (the owner of Femlab) is working on an integration with Solidworks. Solidworks is an upcoming 3D CAD-software which are very userfriendly.

Expressions and constants are entered easily to express frequency-dependent characteristics. Boundary conditions and subdomain settings can also be given either in the GUI (graphical user interface) or in matlab-code. The terrific part here is that all settings can be given from matlab-routines making parameter-studies very easy to perform even with complex material-characteristics.

At the moment (version 3.1) there is no way of identifying the different geometrical elements other than the subdomain number. The boundaries are subjected to the same problem. In future versions it would be preferrable to be able to group all boundaries belonging to one subdomain. Specifying names onto the subdomains would also ease the handling of a large structure.

Femlab was initially running under Matlab resulting in a poor speed and low memory efficiency. All such matters are fixed in the new version (3.1). Femlab has a great variety of features suitable for power transformer modeling equal to the SUMER:

- Simple geometrical input.
- Application of boundary- and subdomain conditions is easy.
- The mesh-generator is able to control mesh growth etc.
- All steps in modeling can be controlled by a script in Matlab.

Parameters can be calculated in m-files. Matlab toolboxes can also be utilized.

- Anisotropic material-characteristics can be given. Curve fitting can be used to apply measured frequency dependent material characteristics.
- Incorporates both direct and iterative solvers. Version 3.1 is quite memory-efficient:

300.000 DOF can easily be solved (upper limit not known). The direct solver used for non-symmetric problems are known as UMFPACK [193]. This solver is found to be just as efficient [194] as the SuperLU-solver utilized in SUMER. If memory-consumption is a problem, another direct solver is available: SPOOLES [195]. This one is less efficient but use less memory. Iterative solvers are also available when the direct solvers fail.

- Postprocessing is easy and versatile both in Femlab and Matlab.
- Direct solution of nodal description to FRA-representation on terminals (by using Matlab). No need to use EMTP. Generation of terminal equivalent for EMTP/ATP is still possible.

Appendix I. Reduced Scale Model

Constructional details are shown for the reduced scale model used in a diplomawork at the Norwegian University of Science and Technology [129].

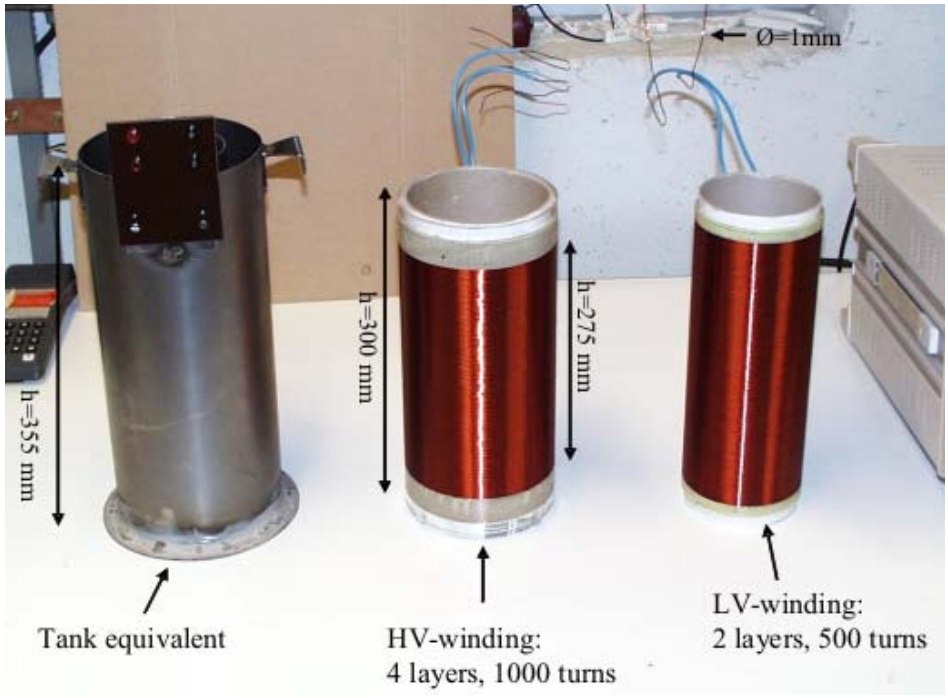

Figure I.1: Dimensions of the reduced scale model

As seen from fig. I.1 the HV-winding has four layers of 250 turns each. The LV-winding has 2 layers of 250 turns. Both windings use the same circular enameled conductor (diameter: 1 mm). Two different tanks were tested (magnetic and non-magnetic), which had some effect at lower frequencies and the overall losses.

This model was assembled in order to study axial and radial deformations. Axial deformations could clearly be detected in a localised frequency-range (at 100 kHz) for transfer-function measurements. Radial deformations was not detectable. The radial deformations were applied by cutting away a slice of the cardboard cylinder and pushing the winding into this slice. When comparing this geometry to a real transformer geometry it is obvious that the space available for radial deformation in this case is much less than for a real winding. Additionally the removal of the cardboard slice reduces the permittivity and the net increase of the buckling might be minimal.

Appendix J. Iron core representation

J.1. Axial symmetrical core representation

A full three dimensional core can be approximated with a two dimensional (2D) axial symmetrical model. This is done by modifying the cross sections of the yoke and outer leg and keeping the core window fixed. Consider a core with dimensions as shown in fig. J.1

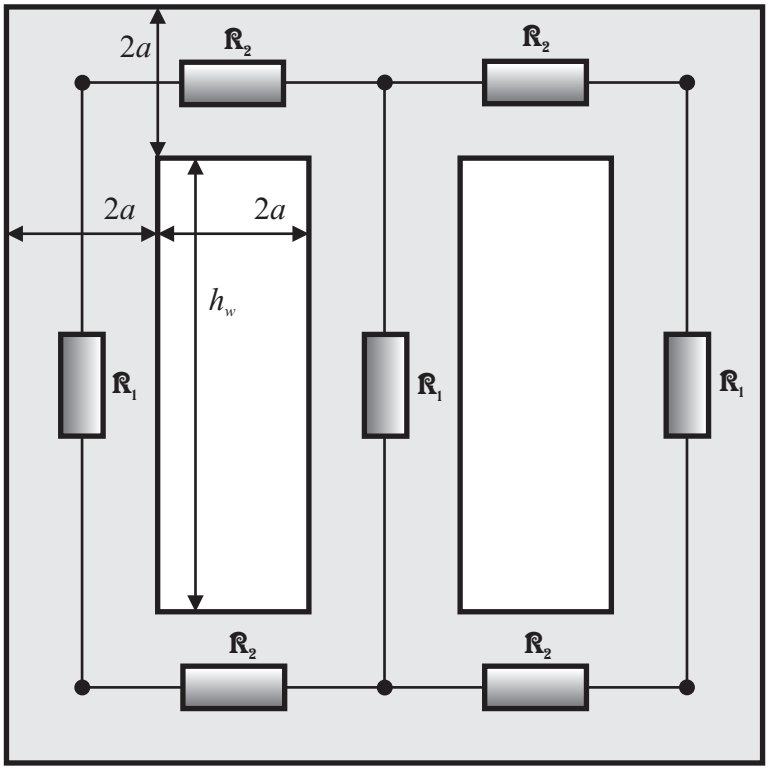

Figure J.1: Reluctance-network of 3 legged core

In this case, the core dimensions are simplified: Cross-section of the legs A_{leg} are assumed equal to the cross-section of the yokes A_{yoke}, and the width of the core window is the same as the diameter for the legs: $2a$.

The average lengths of the different parts are given as:

$$l_{leg} = h_w + 2a \qquad \text{J.1}$$

$$l_{yoke} = 4a \qquad \text{J.2}$$

The total reluctance seen from one of the outer legs will then be:

$$\Re_{tot} = \Re_{leg} + 2 \cdot \Re_{yoke} + \frac{\Re_{leg} \cdot (\Re_{leg} + 2 \cdot \Re_{yoke})}{\Re_{leg} + \Re_{leg} + 2 \cdot \Re_{yoke}} \qquad \text{J.3}$$

$$= \frac{h_w + 10a + \dfrac{h_w^2 + 12ah_w + 20a^2}{2h_w + 12a}}{\mu \cdot A_{leg}} = \frac{l_{eq}}{\mu \cdot A_{leg}}$$

where l_{eq} is the equivalent length of the core at a constant cross-section equal to A_{leg} seen from the outer leg. The same considerations are then carried out for the 2D axisymmetric model in order to have the same total reluctance as the 3-legged core:

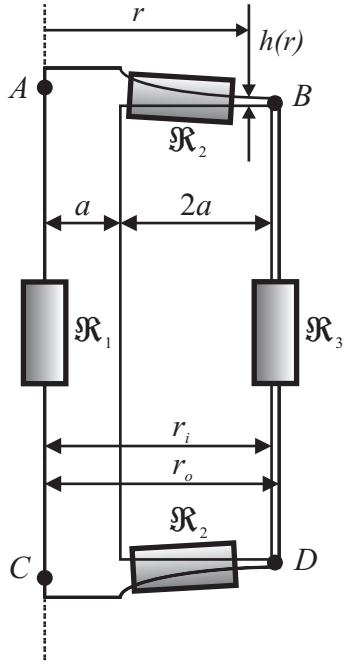

Figure J.2: Reluctance network for axisymmetric core model

The height of the yokes are made dependent on the radius so that the cross-section is kept constant. In this case the cross-section is equal to A_{leg} and then the height of the yoke at $r = a$ will be:

$$h(a) = \frac{a}{2} \qquad \text{J.4}$$

If modeling the center leg, this size will be different: $h(a) = a$

The average length of the leg (from point A-C), when modeling the outer leg will then be:

$$l_{leg} = h_w + h(a) = h_w + \frac{a}{2} \qquad \text{J.5}$$

The average length of the yokes (A-B & C-D) will be:

$$l_{yoke} = 3a + \frac{r_o - r_i}{2} \approx 3a \qquad \text{J.6}$$

The length of the yoke is approximated since r_o is unknown.

The leg and yokes have the same cross-section, and the total length will be:

$$l_a = l_{leg} + 2l_{yoke} = h_w + 3,5a \qquad \text{J.7}$$

The rest of the reluctance will have to be represented by the outer leg. In order to find its cross-section, it is feasable to use the remaining length:

$$l_{rem} = l_{eq} - l_a = 6,5a + \frac{h_w^2 + 12ah_w + 20a^2}{2h_w + 12a} \qquad \text{J.8}$$

Since the cross-section of the yoke is kept constant (equal to the leg), the height is expressed as:

$$h(r) = \frac{\pi a^2}{2\pi r} = \frac{a^2}{2r} \qquad \text{J.9}$$

The average length of the outer leg can be expressed as:

$$l_{outer} = h_w + h\left(\frac{r_o + r_i}{2}\right) \approx h_w + h(r_i) = h_w + \frac{a}{6} \qquad \text{J.10}$$

The cross-section of the outer leg can be found by:

$$A_{outer} = \frac{l_{outer}}{l_{rem}} \cdot A_{leg} \qquad \text{J.11}$$

The outer radius for the outer leg can then be found by:

$$r_o = \sqrt{\frac{A_{outer}}{\pi} + (3a)^2} \qquad \text{J.12}$$

Since r_o is unknown in equations (J.6) and (J.10), these calculations can be iterated with the updated dimensions until the change per iteration in r_o is adequately small. It usually converges after 2-3 iterations.

J.2. Interlaminar effects

The field equations for the two-dimensional problem considered in chapter 5.4 are solved, involving interlaminar effects and their impact on the magnetic field and resulting permeability.

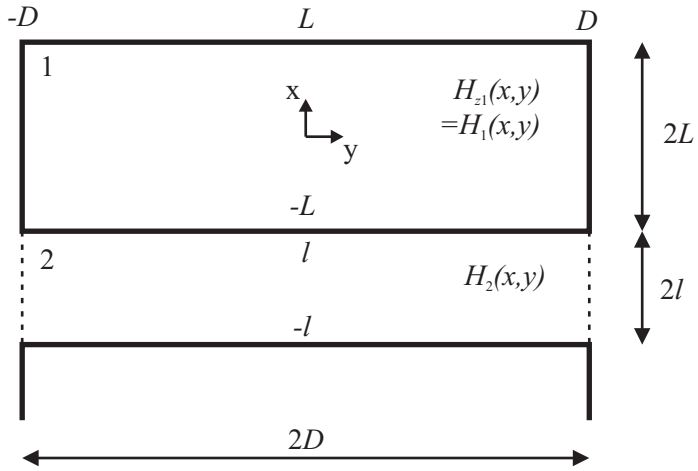

Figure J.3: Dimensions of 2D interlaminar problem

The problem is divided into two zones:

- The iron laminate (zone 1)
- The interlaminar insulation (zone 2)

Both zones will have the same type of formulation, and the magnetic field can be expressed by the wave-equation (5.7), in this case reduced to:

$$\frac{\partial^2 H_i}{\partial x^2} + \frac{\partial^2 H_i}{\partial y^2} = k_i^2 \cdot H_i \text{ where } k_i^2 = j\omega\mu_i(\sigma_i + j\omega\varepsilon_i) \qquad \text{J.13}$$

H_i is the magnetic field in z-direction inside the material i.
Symmetry in x- and y-directions is assumed:

$$H(x, y) = H(x, -y) \wedge H(x, y) = H(-x, y) \qquad \text{J.14}$$

and the boundary conditions are as follows:

$$H_1(L, y) = H_2(-l, y) \wedge E_{1y}(L, y) = E_{2y}(-l, y) \wedge H(x, D) = H_0 \qquad \text{J.15}$$

Applying separation of variables results in the following general solution:

$$H(x, y) = A \cdot \cosh(\lambda x) \cdot \cos(\nu y) \qquad \text{J.16}$$

This is a singular problem and another suitable solution is therefore suggested:

$$H_i(x,y) = A_i \cdot \cosh(\lambda_i \cdot x) \cdot \cos(\nu \cdot y) + H_0 \cdot \frac{\cosh(k_i \cdot y)}{\cosh(k_i \cdot D)} \qquad \text{J.17}$$

The second term in (J.17) avoids singularity when applying the boundary condition. The magnetic field at the external boundary ($y = \pm D$), is assumed to be constant (H_0): $H(x, D) = H_0$ which gives

$$\cos(\nu \cdot D) = 0 \Rightarrow \nu_m = \frac{2m-1}{2D}\pi \text{ with } m = 1, 2, 3\ldots \qquad \text{J.18}$$

This means that there are several solutions depending on m:

$$H(x,y) = \sum_{m=1}^{\infty} A_{im} \cdot \cosh(\lambda_{im} x) \cdot \cos(\nu_m y) + H_0 \cdot \frac{\cosh(k_i \cdot y)}{\cosh(k_i \cdot D)} \qquad \text{J.19}$$

$$\text{where } \lambda_{im}^2 = \nu_m^2 + k^2 \qquad \text{J.20}$$

The boundary conditions on the interface between the two materials gives the constants A_{im}. The first boundary condition is the continuity of the magnetic field across the inferface $H_1(-L, y) = H_2(l, y)$, which implies:

$$\sum_{m=1}^{\infty} A_{1m} \cdot \cosh(\lambda_{1m} \cdot L) \cdot \cos(\nu_m \cdot y) + H_0 \cdot \frac{\cosh(k_1 \cdot y)}{\cosh(k_1 \cdot D)} = \qquad \text{J.21}$$
$$\sum_{m=1}^{\infty} A_{2m} \cdot \cosh(\lambda_{2m} \cdot L) \cdot \cos(\nu_m \cdot y) + H_0 \cdot \frac{\cosh(k_2 \cdot y)}{\cosh(k_2 \cdot D)}$$

The other boundary condition applied, is the continuity of the tangential electric field: $E_{y1}(-L, y) = E_{y2}(l, y)$, which result in:

$$\frac{1}{s_1} \cdot \frac{\partial}{\partial x} H_1(-L, y) = \frac{1}{s_2} \cdot \frac{\partial}{\partial x} H_2(l, y) \qquad \text{J.22}$$

where s_i is the complex conductivity of material i. (J.22) results in:

$$\frac{1}{s_1} \cdot A_{1m} \cdot \lambda_{1m} \sinh(\lambda_{1m} \cdot L) \cdot \cos(\nu_m \cdot y) = \qquad \text{J.23}$$
$$\frac{1}{s_2} \cdot A_{2m} \cdot \lambda_{2m} \sinh(\lambda_{2m} \cdot L) \cdot \cos(\nu_m \cdot y)$$

The resulting equation is obtained when inserting (J.21) into (J.23):

$$\sum_{m=1}^{\infty} A_{1m} \cdot \cosh(\lambda_{1m} \cdot L) \cdot \cos(\nu_m \cdot y) \cdot \left[1 + \frac{\lambda_{1m}}{\lambda_{2m}} \cdot \frac{s_2}{s_1} \cdot \frac{\tanh(\lambda_{1m} \cdot L)}{\tanh(\lambda_{2m} \cdot l)} \right] \qquad \text{J.24}$$

$$= H_0 \cdot \left[\frac{\cosh(k_2 \cdot y)}{\cosh(k_2 \cdot D)} - \frac{\cosh(k_1 \cdot y)}{\cosh(k_1 \cdot D)} \right] = f(y)$$

Substituting

$$B_{1m} = A_{1m} \cdot \cosh(\lambda_{1m} \cdot L) \cdot \left[1 + \frac{\lambda_{1m}}{\lambda_{2m}} \cdot \frac{s_2}{s_1} \cdot \frac{\tanh(\lambda_{1m} \cdot L)}{\tanh(\lambda_{2m} \cdot l)} \right] \qquad \text{J.25}$$

gives the simplified relation:

$$\sum_{m=1}^{\infty} B_{1m} \cdot \cos(\nu_m \cdot y) = f(y) \qquad \text{J.26}$$

By noticing that (J.26) is a Fourier series of the symmetrical function $f(y)$ with a period of $2D$, B_{1m} is found by:

$$B_{1m} = \frac{1}{D} \cdot \int_{-D}^{D} f(y) \cdot \cos(\nu_m \cdot y) = H_0 \cdot \frac{2 \cdot \nu_m \cdot (-1)^{m+1}}{D} \cdot \frac{k_1^2 - k_2^2}{\lambda_{1m}^2 \cdot \lambda_{2m}^2} \qquad \text{J.27}$$

The constants A_{1m} and A_{2m} are obtained by inserting (J.27) into (J.25) and (J.23), and the resulting magnetic fields are obtained:

Magnetic field in the laminations:

$$H_1(x,y) = H_0 \cdot \left(\frac{\cosh(k_1 \cdot y)}{\cosh(k_1 \cdot D)} + \right. \qquad \text{J.28}$$

$$\left. \sum_{m=1}^{\infty} \frac{\frac{2\nu_m}{D} \cdot (-1)^{m+1} \cdot (k_1^2 - k_2^2) \cdot \frac{\cosh(\lambda_{1m} \cdot x)}{\cosh(\lambda_{1m} \cdot L)} \cdot \cos(\nu_m \cdot y)}{\lambda_{1m}^2 \cdot \lambda_{2m}^2 \cdot \left[1 + \frac{\lambda_{1m}}{\lambda_{2m}} \cdot \frac{s_2}{s_1} \cdot \frac{\tanh(\lambda_{1m} \cdot L)}{\tanh(\lambda_{2m} \cdot l)} \right]} \right)$$

Magnetic field in the coating/interlaminar zone:

$$H_2(x,y) = H_0 \cdot \left(\frac{\cosh(k_2 \cdot y)}{\cosh(k_2 \cdot D)} + \sum_{m=1}^{\infty} \frac{\frac{2\nu_m}{D} \cdot (-1)^{m+1} \cdot (k_1^2 - k_2^2) \cdot \frac{\cosh(\lambda_{2m} \cdot x)}{\cosh(\lambda_{2m} \cdot l)} \cdot \cos(\nu_m \cdot y)}{\lambda_{1m}^2 \cdot \lambda_{2m}^2 \cdot \left[1 + \frac{\lambda_{2m}}{\lambda_{1m}} \cdot \frac{s_1}{s_2} \cdot \frac{\tanh(\lambda_{2m} \cdot l)}{\tanh(\lambda_{1m} \cdot L)} \right]} \right) \qquad \text{J.29}$$

The penetration depth of the magnetic field along the the interface/surface of the two materials can be defined by the derivative of the magnetic field at the external boundary:

$$\Lambda = \frac{H_0}{\frac{\partial H_2(l,D)}{\partial y}} = \left(\sum_{m=1}^{\infty} \frac{2}{D} \cdot \frac{\nu_m \cdot \frac{k_1^2 - k_2^2}{\lambda_{1m}^2 \cdot \lambda_{2m}^2}}{1 + \frac{\lambda_{2m}}{\lambda_{1m}} \cdot \frac{s_1}{s_2} \cdot \frac{\tanh(\lambda_{2m} \cdot l)}{\tanh(\lambda_{1m} \cdot L)}} + k_2 \cdot \tanh(k_2 \cdot D) \right)^{-1} \qquad \text{J.30}$$

The permeability is found from integrating the magnetic field over both domains in order to find the ability core to carry flux. In other words the permeability is defined from the average, normalized magnetic field in the core:

$$\overline{\mu_{er}} = \frac{1/H_0}{4(L+l)D} \cdot \int_{-D}^{D} \left\{ \int_{-L}^{L} (\mu_r \cdot H_1) dx + \int_{-l}^{l} (H_2) dx \right\} dy = \qquad \text{J.31}$$

$$\frac{2}{(L+l)\cdot D} \cdot \sum_{m=1}^{\infty} \frac{(k_1^2 - k_2^2) \cdot \frac{\tanh(\lambda_{2m} \cdot l)}{\lambda_{2m}} \cdot \left(\frac{\mu_{r1} \cdot \lambda_{2m}^2 \cdot s_1}{\lambda_{1m}^2 \cdot s_2} - 1 \right)}{\lambda_{1m}^2 \cdot \lambda_{2m}^2 \cdot \left[1 + \frac{\lambda_{1m}}{\lambda_{2m}} \cdot \frac{s_2}{s_1} \cdot \frac{\tanh(\lambda_{1m} \cdot L)}{\tanh(\lambda_{2m} \cdot l)} \right]}$$

$$+ \frac{1}{D \cdot (L+l)} \cdot \left[\frac{L \cdot \mu_{r1}}{k_1} \cdot \tanh(k_1 \cdot D) + \frac{l}{k_2} \cdot \tanh(k_2 \cdot D) \right]$$

In spite of the validity of (J.28)-(J.31) to all types of materials, the expressions are not convenient to use in practice, and some approximations are introduced to simplify the expressions: The conductivity and permeability of the steel laminates are assumed to be much larger than for the coating. Additionally the expressions converges relatively fast. The fact that the width of the laminates are much larger than the thickness is also utilized. This results in

$$\lambda_{1m}^2 \approx k_1^2 \wedge \lambda_{2m}^2 \approx v_m^2 \wedge k_1 \gg k_2 \wedge \tanh(\lambda_{2m} \cdot l) \approx \lambda_{2m} \cdot l \qquad \text{J.32}$$

Then the magnetic field in the laminations can be approximated as:

$$H_1(x,y) \approx H_0 \cdot \left(\frac{\cosh(k_1 \cdot y)}{\cosh(k_1 \cdot D)} + \right. \qquad \text{J.33}$$

$$\left. \sum_{m=1}^{\infty} \frac{\frac{2\nu_m}{D} \cdot (-1)^{m+1} \cdot \frac{\cosh(k_1 \cdot x)}{\cosh(k_1 \cdot L)} \cdot \cos(\nu_m \cdot y)}{\nu_m \cdot \left[1 + \frac{k_1}{\nu_m^2} \cdot \frac{s_2}{s_1 \cdot l} \cdot \tanh(\lambda_{1m} \cdot L) \right]} \right)$$

$$= H_0 \cdot \left(\frac{\cosh(k_1 \cdot y)}{\cosh(k_1 \cdot D)} + \frac{\cosh(k_1 \cdot x)}{\cosh(k_1 \cdot L)} \cdot \frac{2}{D} \cdot \right.$$

$$\left. \sum_{m=1}^{\infty} \frac{\nu_m \cdot (-1)^{m+1} \cdot \cos(\nu_m \cdot y)}{\nu_m^2 + (\beta / D)^2} \right)$$

$$\text{where } \beta = k_2 \cdot D \cdot \sqrt{\frac{\gamma}{1-\gamma} \cdot \mu_r \cdot \frac{\tanh(k_1 \cdot L)}{k_1 \cdot L}} \qquad \text{J.34}$$

Using the Fourier series approach in (J.27) it can be shown that magnetic field inside the laminates can be approximated as

$$H_1(x,y) \approx H_0 \cdot \frac{\cosh(k_1 \cdot x)}{\cosh(k_1 \cdot L)} \cdot \frac{\cosh(\beta \cdot y / D)}{\cosh(\beta)} \qquad \text{J.35}$$

The penetration depth Λ and equivalent permeability $\overline{\mu_r}$ can be similarly approximated as:

$$\Lambda \approx \left[\frac{2}{D} \cdot \sum_{m=1}^{\infty} \frac{1}{1 + (\nu_m \cdot D / \beta)^2} + k_2 \cdot \tanh(k_2 \cdot D) \right]^{-1} \qquad \text{J.36}$$

J.37

The sums in (J.36) and (J.37) have analytical solutions on the form:

$$\overline{\mu_{er}} \approx \left[\frac{2}{(L+l)\cdot D^2} \cdot \sum_{m=1}^{\infty} \frac{l \cdot \left(\frac{\mu_{r1} \cdot s_1 \cdot v_m^2}{k_1 \cdot s_2} - 1 \right)}{v_m^2 \cdot (1 + (v_m \cdot D/\beta)^2)} \right]$$

$$+ \frac{1}{D \cdot (L+l)} \cdot \left[\frac{L \cdot \mu_{r1}}{k_1} \cdot \tanh(k_1 \cdot D) + \frac{l}{k_2} \cdot \tanh(k_2 \cdot D) \right]$$

$$\sum_{m=1}^{\infty} \frac{1}{1 + (v_m \cdot D/\beta)^2} = \frac{\beta}{2} \cdot \tanh\beta \wedge \qquad \text{J.38}$$

$$\sum_{m=1}^{\infty} \frac{1}{v_m^2 \cdot D^2 \cdot (1 + (v_m \cdot D/\beta)^2)} = \frac{1}{2} \cdot \left(1 - \frac{\tanh\beta}{\beta}\right)$$

After some algebraic manipulation, this ends up with:

$$\Lambda = \frac{D}{\beta \cdot \tanh\beta + k_2 \cdot D \cdot \tanh(k_2 \cdot D)} \approx \frac{D}{\beta \cdot \tanh\beta} \qquad \text{J.39}$$

and

$$\overline{\mu_{er}} = \left(1 - \gamma + \mu_r \gamma \frac{\tanh(k_1 \cdot L)}{k_1 \cdot L}\right) \frac{\tanh\beta}{\beta} + \gamma \mu_r \frac{\tanh(k_1 D)}{k_1 D} \qquad \text{J.40}$$

where the stacking factor γ is introduced (γ was defined in eq. (5.21)).

In order to investigate the change in slope for the interlaminar penetration depth, the terms A and B of β are plotted against β and Λ in fig. J.4

$$\beta = A \cdot B \wedge A = k_2 \cdot D \wedge B = \sqrt{\frac{\gamma}{1-\gamma} \cdot \mu_r \cdot \frac{\tanh(k_1 \cdot L)}{k_1 \cdot L}} \qquad \text{J.41}$$

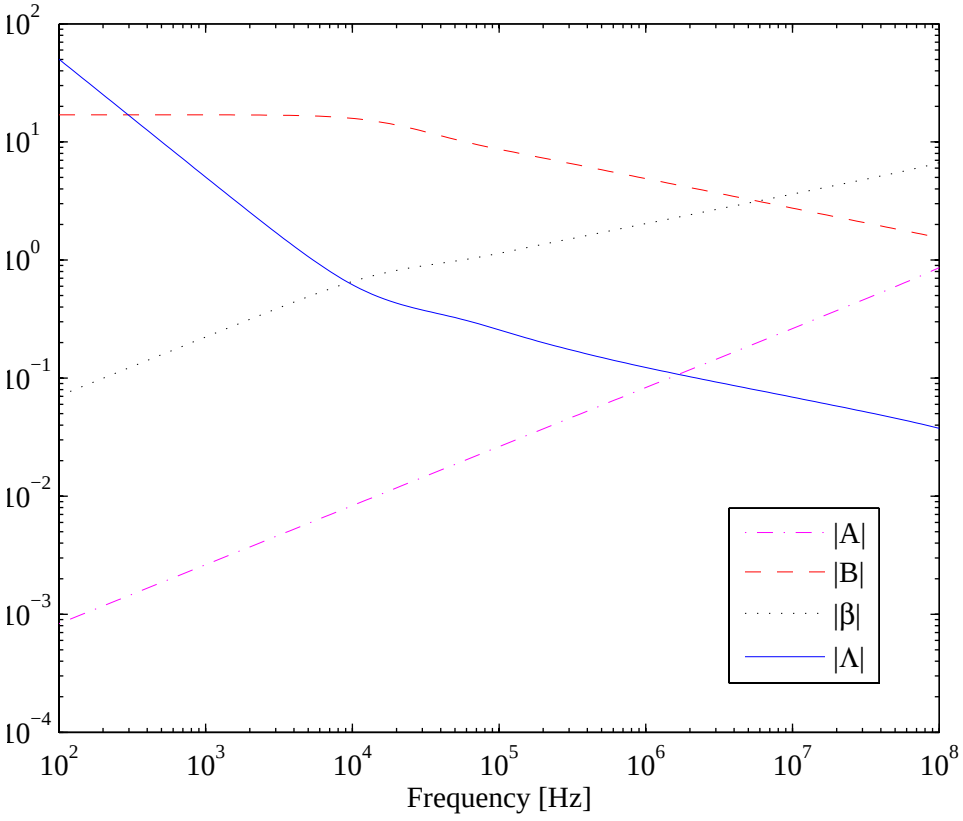

Figure J.4: Slope investigation of $|\Lambda|$ referred to fig. 5.19

As seen above, the term B depends on the skin-depth in the laminate and is reduced above 10 kHz. This changes the slope of β and thus Λ.

Appendix K. Axial displacement of winding from T3Buran

The measurement setup is equal to the setup outlined in appendix C, using two voltage probes for voltage ratio-measurement. Both neutrals are grounded. The result is given in fig. K.1

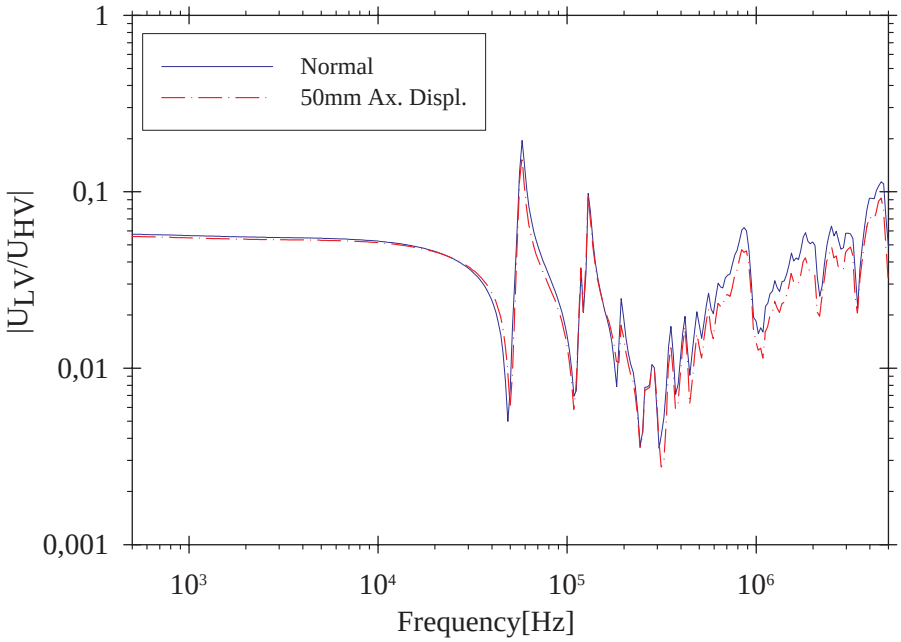

Figure K.1: FRA-measurement: 50 mm axial displacement of LV-winding (T3Buran). Core is replaced with an electrostatic representation of the core and tank.

Compared to the simulations shown in chapter 7.4.1, the deviations are much higher up in frequency. A similarity can be observed for the type of change; the transfer function is mainly shifted vertically and not with frequency. This is consistent to the simulations including the core. The main difference is the frequencies at where the changes occur. This is atributted the difference in inductance for the simulation (incorporating the core) and this experiment (which is without core).

Fig. K.2 shows the actual application of the displacement using a special lifting tool. The bottom and core equivalent can be seen. The tank equivalent is removed.

Figure K.2: Axial displacement on T3Buran winding

The regulation winding is connected equal to the original connection. Measurements are performed with the neutral in the principal position of the “tap-changer”.

12 REFERENCES

[1] Rahimpour, Ebrahim, “Hochfrequente Modellierung von Transformatoren zur Berechnung der Übertragungsfunktion”, Dissertation, ISBN 3-8265-9227-1, University of Stuttgart, 2001

[2] Rahimpour, E., Christian, J., Feser. K., Mohseni, H., “Modeling of a transformer winding for calculation of its transmission function”, *Elektrie*, Vol.54, no.1-2, 2000, pp.18-30

[3] Rahimpour, E., Christian, J., Feser. K., Mohseni, H., “Ability of detailed model to diagnose axial displacement of transformer windings”, *Electrical-Engineering*, Vol.83, no.1-2, Feb. 2001, pp.55-61

[4] Rahimpour, E., Christian, J., Feser. K., Mohseni, H., “Ability of Transfer Function Method to Diagnose Axial Displacement of Transformer Windings”, *ETEP*, Vol.12, no.3, May/June 2002, pp.225-232

[5] Rahimpour, E., Christian, J., Feser, K., Mohseni, H., “Transfer Function Method to Diagnose Axial Displacement and Radial Deformation of Transformer Windings”, *IEEE Trans. on PD*, Vol.18, No.2, April 2003, pp. 493-505

[6] CIGRE WG 12-05, “An international survey on failures in large power transformers”, Electra No.88, May 1983, pp. 21-48

[7] Jackson, R.P., “Recent Investigation of Lightning Protective Apparatus”, *AIEE Trans.*, Vol.25, 1906, pp.881-926

[8] CEA Report 485T1049, “On-line Condition Monitoring of Substation Power Equipment - Utility Needs”, Report for the Canadian Electricity association, B.C. Hydro, Ontario Hydro, Transalta Utilities Corporation, December 1996

[9] Sokolov, V., Berler, Z., Rashkes, V., “Effective Methods of Assessment of Insulation System Conditions in Power Transformers: A view based on practical experience”, *Proceeding from Electrical Insulation Conference and Electrical Manufacturing & Coil Winding Conference*, Oct. 1999, pp. 659-667

[10] Minhas, M.S.A., Reynders, J.P., De Klerk, P.J., “Failures in power system transformers and appropriate monitoring techniques”, *Eleventh International Symposium on High Voltage Engineering, 1999*. (Conf. Publ. No. 467) ,Vol. 1 , 23-27 Aug. 1999 pp.94-97

[11] IEC Standard 60076-5 “Power transformers – Part 5: Ability to withstand short circuit”.

[12] Hagenguth, J.H., “Progress in Impulse testing of Transformers”, *AIEE Transactions*, Vol. 63, 1944, pp. 999-1005

[13] Beldi, F., “The Impulse Testing of Transformers”, *The Brown Boveri Review*, Vol. 37, 1950, pp. 179-193

[14] Stenkvist, E., “Study of Fault Detection and Failure Location During Surge Testing of Transformers”, CIGRE, Supplement to paper No. 12-125, 1952.

[15] Lech, W., Tyminski, L., “Detecting transformer winding damage - The low voltage impulse method”, *Electrical Review*, No. 21, Vol. 179, November 1966, pp. 768-772

[16] Dick, E., P., Erven, C., C., “Transformer diagnostic testing by frequency response analysis”, I*EEE Transactions on Power Apparatus and Systems*, Vol. 97, No. 6, December 1978, pp. 2144-2153

[17] Malewski, R., Poulin, B., “Impulse Testing of Power Transformers Using the Transfer Function Method”, *IEEE Trans. on Power Delivery*, Vol. 3, Issue 2, April 1988, pp. 476-490

[18] Tenbohlen, S., Ryder, S.A., “Making Frequency Response Analysis Measurements: A Comparison of the Swept Frequency and Low Voltage Impulse Methods”, *Proc. of the 13th Int. Symp. on High-Voltage Engineering (ISH2003)*, Netherlands 2003.

[19] Kreβ, K., König, D., “Comparison of measured resonance frequencies of coils at sinusoidal and impulse voltage excitation”, *Proc. of the 7th Int. Symp. on High Voltage Engineering (ISH 1991)*, Technische universität Dresden, August 26-30, 1991.

[20] Høidalen, H.K., Brede, A.P., Lundgaard, L., “Transformer winding diagnosis using the transfer function approach”, *Nordic Symposium on Electrical Insulation 2001*, Stockholm, Sweden

[21] Pearson Electronics Inc., “Standard Current Monitors,” Online: http:// www.pearsonelectronics.com

[22] Leibfried, Thomas, “Die Analyse der Übertragungsfunktion als Methode zur Überwachung des Isolationszustandes von Groβ transformatoren”, Dissertation, University of Stuttgart, 1996

[23] Leibfried, T., Feser, K., “Monitoring of Power Transformers using the Transfer Function Method”, *IEEE Trans. on PD.*, Vol.14, No.4, October 199, pp.1333-1341

[24] Christian, Jochen, “Erkennung mechanischer Wicklungsschäden in Transformatoren mit der Übertragungsfunktion”, Dissertation, ISBN 3-8322-0480-6, University of Stuttgart, 2001

[25] Christian, J., Feser, K., “Procedures for Detecting Winding Displacements in Power Transformers by the Transfer Function Method”, *IEEE Trans. on PD*, Vol.19, No.1, January 2004, pp.214-220

[26] Pykälä, M.J., “Transfer Function as a Diagnostic Tool in Testing of Power and Distribution Transformers”, Report TKK-SJT-68, ISBN 951-22-6905-8, Helsinki University of Technology, High Voltage Institute, Espoo, Finland, December 2003.

[27] Vandermaar, A.J., Wang, M., “Transformer Condition Monitoring by Frequency Response Analysis”, *Proc. of the 10th Int. Symp. on High Voltage Eng. (ISH1997)*, August 25-29, 1997, Montreal, Canada, pp. 119-122

[28] Wang, M., Vandermaar, A.J., Srivastava, K.D., “Condition Monitoring of Transformers in Service by the Low Voltage Impulse Test Method”, *Proc. of the 11th Int. Symp. on High Voltage Eng. (ISH1999)*, paper 1.45.S3, London, England, 1999.

[29] Wang, M., Vandermaar, A.J., Srivastava, K.D., “Transformer Winding Movement Monitoring in Service - Key Factors Affecting FRA Measurements”, *IEEE El. Ins. Mag.*, Vol. 20, No. 5, September/October 2004, pp. 5-12

[30] McDowell, G., “Condition Monitoring of Power Transformers to Assess Residual Life and Fault Damage”, ERA Report 88-0566R, June 1989, 44 p.

[31] “M5100 SFRA Instrument User’s Guide”, Doble Engineering Company, Watertown, Massachusetts, USA, 72A-1849-01 Rev.B 06/02

[32] Coffeen, L., Britton, J., Rickmann, J., “A New Technique to Detect Winding Displacements in Power Transformers Using Frequency Response Analysis”, *Proc. Conf. Power Tech*, 2003 IEEE Bologna, Vol. 2, 23-26 June 2003, 7 pages

[33] Coffeen, L. T., Britton, J. A., Rickmann, J., Gockenbach, E., “ A New Objective Technique to Detect Winding Displacements in Power Transformers Using Frequency Response Analysis, Without the Need for Historical Data”, *Proc. of the 13th Int. Symp. on High-Voltage Engineering (ISH2003)*, Netherlands 2003.

[34] Bolduc, L., Picher ,P., Pare, G., Demers, R.J., Belanger, J., “Detection of Transformer Winding Displacement by the Frequency Response of Stray Losses (FRSL)”, Cigre 12/33-02, 2000

[35] Weiser, B., Pfutzner, H., "Relevance of magnetostriction and forces for the generation of audible noise of transformer cores". *IEEE trans. on magnetic*, Vol.36, No.5, 2000, pp. 3759-3777

[36] Bartoletti, C., Desiderio, M., Di Carlo, D., Fazio, G., Muzi, F., Sacerdoti, G., Salvatori, F., “Vibro-acoustic techniques to diagnose power transformers“ *IEEE Trans. on PD*, Vol.19 , Iss.1 , Jan. 2004 pp. 221-229

[37] de Klerk, P.J., Reynders, J.P., “Winding slackness monitoring as a diagnostic for insulation ageing in oil-paper insulated power transformers” *Eleventh International Symposium on High Voltage Engineering, 1999*. (Conf. Publ. No. 467) ,Vol.1 , 23-27 Aug. 1999, pp. 185-188

[38] Naiqiu, S., Can, Z., Fang, H., Qisheng, L., Lingwei, Z., “Study on ultrasonic measurement device for transformer winding deformation”, *Int. Conf. on Power System Technology*, 2002. Proceedings. PowerCon 2002. , Vol. 3 , 13-17 Oct. 2002, pp.1401-1404

[39] De Leon, G, “Transformer model for the study of Electromagnetic Transients”, Dissertation, University of Toronto, dept. of El. Eng., 1992

[40] Weed, J.M., “Abnormal Voltages in Transformers”, *AIEE Trans.*, Vol. 34, pt.II, 1915, pp. 2197-2236

[41] Rabins, L., “Transformer reactance calculations with digital computers”, *AIEE trans*., Vol.75, pt.1, 1956, pp.261-67

[42] Fergestad, P.I., Henriksen, T., “Inductances for the calculation of transient oscillations in transformer windings”, *IEEE Trans.*, 1974, PAS-93, (3), pp. 510-517

[43] Fergestad, P.I., Henriksen, T., “Transient oscillations in multiwinding transformers”, *IEEE Trans. on PAS*., Vol.93, Nr. 3, 1974, pp. 500-509

[44] Fergestad, P.I., “Transient oscillations in transformer windings”, dissertation, NTH, Norway, 1971

[45] Olaussen, E.M., “Magnetiske felter og felt-avhengige størrelser i spoler og transformatorer”, lic.thesis., NTH, 1971

[46] Wilcox, D.J, Hurley, W.G, Conion, M., “Calculation of self and mutual impedances between sections of transformer windings”, *IEE proc*. Vol.136, Pt.C, No.5, Sept. 1989

[47] Wilcox, D.J, Hurley, W.G, Conion, M., “Calculation of self and mutual impedances for coils on ferromagnetic cores”, *IEE proc.* Vol.135, Pt.A, No.7, Sept. 1988

[48] Mombello, E.E., “Modeling of a coil system considering frequency-dependent inductances and losses; I. Analysis of the impedance matrix characteristics”, *El. Eng.* Springer Verlag, Vol. 84, 2002, pp. 3-10

[49] Mombello, E.E., “Modeling of a coil system considering frequency-dependent inductances and losses; II. Equivalent circuit synthesis”, *El. Eng.* Springer Verlag, Vol. 84, 2002, pp. 11-19

[50] Blume, L.F., Boyajian, A., “Abnormal Voltages Within Transformers”, *AIEE Trans.*, Vol.38, pt.I, 1919, pp. 577-620

[51] McWhirter, J.H., Fahrnkopf, C.D., Steele, J.H., “Determination of Impulse Stresses within Transformer Windings by Computers”, *AIEE Trans. on PAS*, Feb. 1957, Vol.75, pp.1267-1274

[52] Shipley, R.B., Coleman, D., Watts, C.F., “Transformer Circuits for Digital Studies”, *AIEE Trans*., Feb. 1963, Vol.81, pp.1028-1031

[53] Brandwajn, V., Dommel, H.W., Dommel, I.I., “Matrix Representation of Three-Phase N-Winding Transformers for Steady-state and Transient Studies”, *IEEE Trans*., June 1982, Vol. PAS-101, No.6, pp.1369-1378

[54] Dugan, R.C., Gabrick, R., Wright, J.C., Patten, K.W., “Validated Techniques for Modeling Shell Form EHV Transformers”, *IEEE Trans. on PD*, April 1989, Vol.4, No.2, pp.1070-1078

[55] Cherry, E.C., “The duality between Interlinked Electric and Magnetic Circuits and the Formation of Transformer Equivalent Circuits”, *Proc. Phys. Soc.*, Feb. 1949, Section B, Vol.62, pp.101-111

[56] Edelmann, H., “Anschauliche Ermittlung von Transformator-Ersatzschaltbildern”, Archiv für elektrische Übertragung, 1959, Band 13, Heft 6, s.253-261

[57] Krähenbühl, L., Kulicke, B., Webs, A., “Simulationsmodell eines Mehrwicklungstransformators zur Untersuchung von Sättigungsvorgängen, Siemens Forschungs- und Entwicklungsberichte”, 198, Band 12, Heft 4, s. 232-235

[58] Arturi, C.M., “Transient Simulation and Analysis of a Three-Phase Five-Limb Step-Up Transformer Following an Out-of-Phase Synchronization”, *IEEE Trans. on PD*, Jan. 1991, Vol.6, No.1, pp.196-207

[59] Wagner, K.W., “The Progress of an Electromagnetic Wave in a Coil with Capacity between Turns”, Elektrotechnik und Maschinenbau, Vol.33, 1915, pp. 89-92 & pp.105-108.

[60] Al-Khayat, N., Haydock, L., “Analytical and new Transmission Line Equivalent circuit modeling methods for swept frequency of Power Transformers”, *Proc. on El. Ins. and El. Manufacturing & Coil Winding Conf.*, 18-21 September 1995, pp. 45 - 47

[61] M., Popov, L., van der Sluis, G.. C., Paap, H., De Herdt, “Computation of Very Fast Transient Overvoltages in Transformer Windings”, *IEEE Trans. on Power Delivery*, Vol. 18, No. 4, October 2003, pp. 1268-1274

[62] Gustavsen, B.; Semlyen, A. “Application of vector fitting to state equation representation of transformers for simulation of electromagnetic transients”, *IEEE Trans. on PD.* , Vol. 13 Issue 3 , Jul 1998 pp. 834 -842

[63] Gustavsen, B., “Wide Band Modeling of Power Transformers”, *IEEE Trans. on PD*, Vol.19, No.1, Jan. 2004, pp.414-422

[64] Degeneff, R.C., “A general method for determining resonances in transformer windings”, *IEEE Trans. on PAS*., Vol. PAS-96, No.2, March/April 1977

[65] Liu, Y., Sebo, S.A., Caldecott, R., Kasten, D.G., Wright, S.E., “Power Transformer Resonance - Measurements and Prediction”, IEEE/PES Winter meeting, February 3-7, 1991, paper No.91 WM 048-9 PWRD

[66] Wilcox, D.J., “Theory of transformer modeling using modal analysis”, *IEE Proc.-C*, Vol.138, No.2, March 1991, pp. 121-128

[67] Wilcox, D.J., McHale, T.P., “Modified theory of modal analysis for the modeling of mulitwinding transformers”, *IEE Proc.-C*, Vol.139, No.6, November 1992,pp. 505-512

[68] Wilcox, D.J., Hurley, W.G., McHale, T.P., Conlon, M., “Application of modified modal theory in the modeling of practical transformers”,*IEE Proc.-C*, Vol.139, No.6, November 1992,pp. 513-520

[69] Glaninger, P., “Modale Parameter der elektrischen Eigenschwingung von Transformatoren”, *Etz-Archiv*, Vol. 6, No. 12, 1984, pp. 399-405

[70] Glaninger, P., “Ersatzschaltbilder zur Berechnung der elektrischen Eigenschwingungen von Transformatoren mit Beürcksichtigung der modalen Dämpfung”, E&I, Vol. 109, 1992, pp. 6-13

[71] Soysal, A.O., Semlyen, A., “Practical transfer function estimation and its application to wide frequency range representation of transformers”, *IEEE Trans. on PD*., Vol.8, No. 1993, pp. 1627-1637

[72] Chari, M.V.K., D'Angelo, J., Palmo, M.A., Sharma, D.K., “Application of Three-Dimesional Electromagnetic Analysis Methods to Electrical Machines and Devices”, *IEEE Trans. on Energy Convension*, Vol. EC-1, No. 2, June 1986, pp. 145-157

[73] Lian, G., Ruopin, Y., Pizhang, C., “An Equivalent Magnetization Surface Current Approach of Calculation 3-Dimensional Leakage Fields of a Transformer”, *IEEE Trans. on PD*., Vol. PWRD-2, No.3, July 1987, pp. 817-822

[74] Moreau, O., Guillot, Y., “SUMER: A Software For Overvoltage Surges Computation Inside Transformers”, *Int. Conf. On Electrical Machines*, 1998, pp. 965-970

[75] De Leon, F., Semlyen, A., “Efficient calculation of Elementary Parameters of Transformers”, *IEEE Trans. on PD*, January 1992, Vol.7, No.1, pp. 361-369

[76] De Leon, F., Semlyen, A., “Complete Transformer Model for Electromagnetic Transients”, *IEEE Trans. on PD*, January 1994, Vol.9, No.1, pp. 231-239

[77] Gharehpetian, G.B., Mohseni, H., Möller, K., “Hybrid Modeling of Inhomogeneous Transformer Windings for Very Fast Transient Overvoltage Studies”, *IEEE Trans. on PD*., Vol. 13, No. 1, January 1998, pp. 157-163

[78] Frimpong, G., Gäfvert, U., Fuhr, J., “Measurement and Modeling of Dielectric Response of Composite Oil/Paper Insulation”, *Proc. 5th Int. Conf. On Prop.&App. Of Diel. Mat.*, Seoul ,Korea, May 25-30, 1997, pp.86-94

[79] Stein, G.M., “A Study of the Initial Surge Distribution in Concentric Transformer Windings”, *IEEE Trans.*, vol. PAS-83, Sept.1964, pp. 877-93

[80] Okuyama, K., “Effect of series capacitance on impulse voltage distribution in transformer windings”, *Electrical Engineering in Japan*, Vol. 87, No. 1, 1967, pp. 27-34

[81] Ambrozie, C., “Teilkapazitäten und grundlegende Kapazitäten in Scheibenspulentransformatorwicklungen”, *E und M*, Vol. 89, No. 9, 1972, pp. 370-377

[82] Ambrozie, C., “Berechnung der Ersatzkapazität einer Scheibenspule von einer Normalscheibenspule-transformatorwicklung”, *Etz-A*, Vol. 93, No. 8, 1972, pp. 446-450

[83] Ambrozie, C., “Berechnung der Ersatzkapazität der verschaltelten Scheibenspulentransformatorwicklungen”, *E und M*, Vol. 92, No. 1, 1975, pp. 23-35

[84] Pedersen, A., “On the Response of Interleaved Transformer Windings to Surge Voltages”, *AIEE Trans*., Vol. 82, June 1963, pp. 349-356

[85] De, A., Chatterjee, N., “Part winding resonance: Demerit of interleaved high-voltage transformer winding”, *IEE Proc.-Electr. Power Appl.*, Vol. 147, No. 3, May 2000, pp. 167-174

[86] Moreau, O., Guuinic, P., Dorr, R., Su, Q., "Comparison Between the High Frequency Characteristics of Transformer Interleaved and Ordinary Disk Windings", *IEEE Trans.*, 2000, pp. 2187-2192

[87] Del Vecchio, R.M., Poulin, B., Ahuja, R., "Calculation and Measurement of Winding Disk Capacitances with Wound-in-shields", *IEEE Trans. on PD*., Vol. 13, No.2, April 1998, pp. 503-509

[88] Seitlinger, W.V., "Wirkungsmechanismus der Verschachtelung einer Wicklung", *E & I*, Vol. 108, 1991, pp. 214-220

[89] Mombello, E. E., "New Power Transformer Model for the Calculation of Electromagnetic Resonant Transient Phenomena Including Frequency-Dependent Losses", *IEEE Trans. on PD.*, Vol. 15, No. 1, January 2000, pp. 167-174

[90] De Leon, F., Semlyen, A., "Time Domain Modeling of Eddy Current Effects for Transformer Transients", *IEEE Trans. on PD*, January 1993, Vol.8, No.1, pp. 271-280

[91] De Leon, F., Semlyen, A., "Detailed Modeling of Eddy Current Effects for Transformer Transients", *IEEE Trans. on PD*, April 1994, Vol.9, No.2, pp. 1143-1150

[92] Stoll., R., "The Analysis of Eddy Currents", Clarendon Press, Oxford, 1974

[93] Lammeraner, J., Stafl, M., "Eddy Currents", The Chemical Rubber Co. Press, Cleveland, 1966

[94] Dowell, P.L., "Effects of eddy currents in transformer windings", *IEE Proc*., Vol. 113, No. 8, 1966, pp. 1387-1394

[95] Urling, A.M., Niemela, V.A., Skutt, G.R., Wilson, T.G., "Characterizing high-frequency effects in transformer windings - A guide to significant articles", *IEEE Trans*., 1989, pp. 373-385

[96] Dietrich, W., "Berechnung der Wirbelstromverluste von transformatorwicklungen unter Berücksichtigung des tatsächlichen Streufeldverlafes", *ETZ-A*, Vol. 46, No. 4, 1961, pp. 209-222

[97] Dietrich, W., "Berechnung der Wirbelstromverluste in den Wicklungen von Mehrwicklungstransformatoren", *ETZ-A*, Vol. 10, No. 10, 1988, pp. 309-317

[98] Ferreira, J.A., "Appropriate modeling of conductive losses in the design of magnetic components", *IEEE Trans*., 1990, pp. 780-785

[99] Ferreira, J.A., "Improved Analytical Modeling of Conductive Losses in Magnetic Components", *IEEE Trans. on Power Electronics*, Vol. 9, No. 1, January 1994, pp. 127-131

[100] Dent, B.M., Harthill, E.R., Miles, J.G., "A Method of analysis of transformer impulse voltage distribution using a digital computer", *Proc.of the IEE*, Vol. 105, No. 23, 1958, pp.445-59

[101] Okuyama, K., "A numerical analysis of impulse voltage distribution in transformer windings", *Elec. Eng. In Japan*, Vol. 87, 1967, Nr.1, pp. 80-88

[102] Waldvogel, P., Rouxel, R., "Predetermination by calculation of electric stresses in a winding subjected to a surge voltage", in Proc. CIGRE, 1956, Paper No. 126

[103] Dong. X., Zhu, D., Wang, C., Tan, K., Liu, Y., “Simulation of Transformer PD Pulse Propagation and Monitoring for a 500 kV Substation”, *IEEE Trans. on Diel. Ins*., Vol. 6, No. 6, December 1999, pp. 803-813

[104] Akbari, A., Werle, P., Borsi, H., Gockenbach, E., “Transfer function-based partial discharge localization in power transformers: a feasability study”, *El.Ins.Mag.*, IEEE, Vol. 18, Iss. 5, July-August 2002, pp. 5-16

[105] Miki, A., Hosoya, T., Okuyama, K., “A calculation method for impulse voltage distribution and transferred voltage in transformer windings”, *IEEE Trans*., Vol. PAS-97, No. 3, May/June 1978, pp. 930-939

[106] Degeneff, R.C., McNutt, W.J., Neugebauer, W., Panek, J., McCallum, M.E., Honey, C.C., “Transformer Response to System Switching Voltages”, *IEEE Trans. on PAS*., Vol. PAS-101, No. 6, June 1982, pp. 1457-1470

[107] Wirgau, K.A., “Inductance calculation of an air-core disc winding”, *IEEE Trans. on PAS*., Vol.95, 1976, pp. 394-400

[108] Ram, B.S., “Inductance and winding eddy loss of air-cored reactors” ,*IEE Proc.-Gen. Transm. Distrib.*, Vol.146, No.5, September 1999, pp. 416-420

[109] Buckow, E., "Berechnung des verhaltens von leistungs-transformatoren bei resonanzanregung und möglichkeiten des abbaus innerer spannungsberhöhungen", Dissertation der Technischen Hochschule Darmstadt, 1986

[110] Nothaft, M., “Untersuchung der Resonanzvorgänge in Wicklungen von Hochspannungsleistungstransformatoren mittels eines detaillierten Modells”, Dissertation, Technische Hochschule Karlsruhe, 1994

[111] Gharehpetian, G.B., “Modellierung von Transformatorwicklungen zur Untersuchung schnellveränderlicher transienter Vorgänge”, Dissertation, RTWH Achen und Universität Teheran, 1996

[112] Rüdenberg, R., “Electrical shock waves in power systems”, Harvard University Press, 1968, 157-158

[113] Wright, M.T., Yang, S.J., McLeay, K., “General theory of fast-fronted interturn voltage distribution in electrical machine windings”, *IEE Proc*. *B*, 1983, 130, (4), pp. 245-256

[114] McLaren, P.G., Oraee, H., “Multiconductor transmission-line model for the line-end coil of large AC machines”, *IEE Proc. B*, 1985, 132, (3), pp. 149-156

[115] de León, F., “Transformer Model for the Study of Electromagnetic Transients”, Dissertation, University of Toronto, 1992

[116] Chimklay, S., “High-Frequency Transformer Model for Switching Transient Studies”, Doctoral Dissertation, University of British Columbia, 1995

[117] Vakilian, M., “A Nonlinear Lumped Parameter Model for Transient Studies of Single Phase Core Form Transformers”, Doctoral Dissertation Rensselaer Polytechnic Institute, Troy, New York, June 1993.

[118] Neves, W. L. A., “Transformer Modeling for Transient Studies”, Doctoral Dissertation, University of British Columbia, 1994

[119] Gafvërt, U., Frimpong, G., Fuhr, J., “Modeling of Dielectric Measurements on Power Transformers”, CIGRE, 15-103, 1998.

[120] Moreau, O., Popiel, L., Pages, L. "Proximity Losses Computation with a 2D Complex Permeability Modeling", *IEEE Trans. On Magn.*, Vol. 34, No. 5, September 1998

[121] Bertagnolli, G, “Short circuit duty of power transformers - The ABB approach”, 2nd ed., 1998, Golinelli Editore

[122] Sabonnadiere, J.C.M., Meunier, G., Morel, B., "Flux : a general interactive finite elements package for 2D electromagnetic fields", *IEEE Trans. on Mag.*, Vol. 18, No.2, March 1982

[123] O. Moreau, R. Michel and Y. Guillot, "Overvoltages Computation in a Power Transformer Connected to the Power System", *Electrimacs* 1996-Vol 1 p. 47-52

[124] O. Moreau, Y. Guillot, B. Barre, "FRA Diagnostic Method: Simulation Applied to Feasibility Study and Efficiency Improvement", Power Eng. Soc. 1999 Winter Meeting, IEEE ,Vol. 2 , 31 Jan-4 Feb 1999 pp. 1059 - 1064

[125] Y. Guillot, O. Moreau, D. Vo-quoc, " FRA Diagnostic Method: Simulation Applied To Sensitivity Analysis And Criteria Derivation For Mechanical Shiftings", *Proc. of the 12th Int. Symp. on High-Voltage Eng. (ISH2001)*, 20-24 August 2001, Bangalore, India.

[126] H. W. Dommel, W. S. Meyer, "Digital Computer Solution of Electromagnetic Transients in Single and Multi-phase Networks", *IEEE Trans. On PAS.*, 1969, Vol.18, pp.388-399

[127] Femlab, Online: http://www.femlab.com

[128] Matlab, Online: http://www.mathworks.com

[129] Masvik, E., “Diagnosis of transformers with frequency response analysis”, Diploma thesis (Norwegian) 2003, Norwegian University of Science and Technology, Dept. for Electrical power engineering.

[130] Moses, A. J., "Electrical steels: past, present and future developments", *IEE Proc.*, Vol. 137, Pt. A, No. 5, Sept. 1990

[131] Heathcote, J. M., “J & P Transformer Book”, 12th ed., Newnes 1998, ISBN: 07506 1158 8

[132] Boon, C.R., Robey, J.A., “Effect of domain-wall motion on power loss in grain-oriented silicon-iron sheet”, *Proc. IEE*, Vol. 115, No. 10, October 1968.

[133] Pry, R.H., Bean, C.P., “Calculation of the energy loss in magnetic sheet materials using a domain model”, *Journal of Applied Physics*, 1958, 30, pp. 532-533

[134] Fergestad, P I, Henriksen, T, "Transient oscillations in multiwinding transformers", *IEEE Trans. On PAS*, Vol.93, Nr.3, 1974, pp. 500-509

[135] Bertotti, G., Fiorillo, F., Pasquale, M., “Reversible and irreversible magnetization in soft iron-based polycrystalline materials”, *Journal of Applied Physics*, 69(8) 15 April 1991, pp. 5930-5932

[136] Quintana, J A, "Detailed lossy transformer model", Doctoral thesis, Rensselaer Polytechnic Institute, Troy-New York, May 2000

[137] IEC Standard 60076-3 “Power transformers – Part 3: Insulation levels, dielectric tests and external clearances in air”

[138] Stoll, R. L., "The Analysis of Eddy Currents", Clarendon Press Oxford, 1974

[139] Hallén, E., “Elektrisitetslära”, Almqvist & Wiksells Boktrykkeri Aktiebolag, Uppsala, 1953

[140] “Electrical Steels, Grain-oriented, Unisil, Unisil-H, ASTM-grades”, Cogent Power Ltd. (Surahammar), 2003, Online: http://www.cogent-power.com

[141] Coombs, A., Lindenmo, M., Snell, D., Power, D., “Latest Developments in Insulating Coatings on Nonoriented Electrical Steels”, *IEEE Trans. on Mag*., Vol. 37, No. 1, Jan. 2001

[142] IEC Standard 60404-11, “Magnetic Materials. Part 11: Method of test for the determination of surface insulation resistance of magnetic sheet and strip”, 1998

[143] ASTM A717/A717M-01 “Standard Test Method for Surface Insulation Resistivity of Single-Strip Specimens”, 2001

[144] Franklin, R.F., “Measurement and control of interlaminar resistance of laminated magnetic cores”, *ASTM Bulletin*, n° 144, January 1947, p. 57.

[145] Lin, K. C., Su, J-S., “Selection of Silicon Steel for Transformer Cores”, *Proc. from the El. Ins. & El. Manufact. & Coil Winding Conf.*, 18-21 Sept. 1995, pp. 147-152

[146] “Selection of Electrical Steels for Magnetic Cores”, Product data bulletin, AK Steel Corp., 2000, Online: http://www.aksteel.com/

[147] “Steel products manual on flat-rolled electrical steel,” American Iron Steel Inst. (AISI), Washington, D.C., Jan. 1983.

[148] Coombs, A., Lindenmo, M., Snell, D., Power, D., “Review of the Types, Properties, Advantages, and Latest Developments in Insulating Coatings on Nonoriented Electrical Steels”, *IEEE Trans. on Mag.*, Vol. 37, No. 1, January 2001, pp. 544-557

[149] Tavner, P.J., Jackson, R.J., “Coupling of discharge currents between conductors of electrical machines owing to laminated steel core”, *IEE Proc.* Vol. 135, Pt. B, No. 6, November 1988

[150] Clark, F. M., “Insulating Materials for Design and Engineering Practice”, John Wiley & Sons, New York, 1962, 1218 pages

[151] Whitehead, J.B., “Impregnated Paper Insulation - The inherent Electrical Properties”, John Wiley & Sons, New York, 1935.

[152] Sierota, A., Rungis, J., “Electrical Oils Part I: Characterization and Pre-treatment of New Transformer Oils”, *IEEE El.Ins.Mag*., Jan./Feb. 1995 Vol.11, No.1.

[153] Bartnikas, R., “Dielectric loss in insulation liquids”, *IEEE Trans. on El.Ins*., Vol.EI-2, No.1, April 1967, pp. 33-54

[154] Emsley, A.M., Xiao, X., Heywood, R.J., Ali, M., “Degradation of cellulosic insulation in power transformers. Part 2: Formation of furan products in insulating oil”, *IEE Proc. Sci. Meas. Technol.*, Vol. 147, No. 3, May 2000, pp. 110-114

[155] Morgan, V.T. “Effects of Frequency, Temperature, Compression and Air-Pressure on the Dielectric Properties of a Multilayer Stack of Dry Kraft Paper”, *IEEE Trans. on Diel. and El. Ins*., Vol. 5, No. 1, February 1998, pp. 125-131

[156] Race, H.H., Hemphill, R.J., Endicott H.S., “Important Properties of Electrical Insulating Papers”, *General Electric Review* Vol.43, 1940, pp. 492-499

[157] Jonscher, A.K., “Universal relaxation law”, ISBN 0-9508711-2-5, London, Chelsea Dielectric Press, 1996, 415 pages.

[158] Bartnikas, R., “Dielectric loss in solid-liquid insulating systems - Part I”, *IEEE Trans. on El.Ins*., Vol. EI-5, No. 4, December 1970, pp. 113-121

[159] Batruni, R., Degeneff, R.C., Lebow, M.A., “Determining The Effect Of Thermal Loading On The Remaining Useful Life Of A Power Transformer From Its Impedance Versus Frequency Characteristic”, *IEEE Trans. on PD,* Vol. 11, No. 3, July 1996

[160] Gäfvert, U., Adeen, L., Tapper, M., Ghasemi, P., Jönsson, B., “Dielectric Spectroscopy in Time and Frequency Domain Applied to Diagnostics of Power Transformers”, *Proc. Int. Conf. on Prop.&Appl. of Diel. Mat*., June 21-26, 2000, China.

[161] Linhjell, D., Gäfvert, U., Lundgaard, L., “Dielectric response of oil-impregnated paper insulation: variation with humidity and ageing level”, *conf. on El. Ins. & Diel. Phenomena*, CEIDP '04, 17-20 Oct. 2004, pp.262-266.

[162] Schaumburg, G., “New integrated dielectric analyzer extends accuracy and impedance range for material measurements”, *Dielectric Newsletter,* No. 11, 1999, Novocontrol Technologies

[163] Abri, V., Jorendal, G., “Relationship between the paper covering thickness of the electrode and the development of the surface flashover at impulse voltages” 1998, ICSD '98. *Proceedings of the 1998 IEEE 6th International Conference on Conduction and Breakdown in Solid Dielectrics*, 22-25 June 1998, pp.473-476

[164] Bayless, R.S., Selman, J.D., Truax, D.E., Reid, W.E., “Capacitor Switching and Transformer Transients”, *IEEE Trans. on PD*, Vol. 3, No. 1, January 1988

[165] Sokolov, V., “Experience with the refurbishment and life extension of large power transformers”, *Minutes of the sixty-first Annual International Conference of Doble Clients*, 1994, Doble Engineering Company, Watertown, Massachusetts, USA.

[166] Hässig, M., Bräunlich, R., “Technique and evaluation of FRA-measurements on large power transformers”, *Proc. of the 13th Int. Symp. on High-Voltage Engineering (ISH2003),* Netherlands 2003.

References in appendix:

[167] Waters, M ., “The Short-Circuit Strength of Power Transformers”, Macdonald & Co. Ltd., 1966

[168] Karsai, K., Kerenyi, D., Kiss, L., ”Large Power Transformers”, Elsevier, Amsterdam, 1987

[169] IEC 60599:1999, “Mineral Oil-Impregnated Electrical Equipment in Service – Guide to the interpretation of dissolved gasses”

[170] Allan, D.J., “Power Transformers - the second century”, *Power Eng. J*., Vol.5, Issue 1, Jan. 1991, pp. 5 -14

[171] T. P. Huges, “Networks of Power”, The John Hopkins University Press, Baltimore, 1993.

[172] Abetti, P.A., “Bibliography on the surge performance of transformers and rotating machines”, *AIEE Trans.*, vol.77, pt.III Dec. 1958, pp. 1150-68.

[173] Abetti, P.A., “Bibliography on the surge performance of transformers and rotating machines”, First suppl., *AIEE Trans.*, vol.81, pt. III, Aug. 1962, pp. 213-219.

[174] Abetti, P.A., “Bibliography on the surge performance of transformers and rotating machines”, Second suppl., *IEEE Trans*., vol. PAS-83, Aug. 1964, pp. 855-58.

[175] Abetti, P.A., “Survey and Classification of Published Data on the Surge Performance of Transformers and Rotating Machines”, *AIEE Trans*., vol. 77, 1959, pp. 1403-14.

[176] Abetti, P.A., “Transformer models for the determination of transient voltages”, *AIEE Trans*., vol.72, pt.III, June 1953, pp. 468-80.

[177] Abetti, P.A., Maginnis, F.J, “Natural frequencies of coils and windings determined by equivalent circuit”, *AIEE Trans*., Col.72, pt.III ,June 1953, pp. 495-504.

[178] Sommerfeld, A., “Static Strains in High Tension Circuits and the Protection of Apparatus”, *AIEE Trans*., Vol.19, 1902, pp. 213-76

[179] Rüdenberg, R., “Origin and Propagation of Electric Surge-Waves”, Elektrotechnik und Maschinenbau, Vol.32, 1914, pp. 729-33

[180] Rüdenberg, R., “Electric Transients”, (book in German) Julius Springer, Berlin, Germany, 1st ed., 1923, pp. 446 ff, third edition, 1933, pp. 528 ff

[181] Wagner, K.W., “Oscillations due to Traveling Waves in Transformer Windings”, *Arch. Elektrotech*., Vol.6, 1918, pp. 301-26

[182] Wagner, K.W., “Observations on my paper: Oscillations due to Traveling Waves in Transformer Windings”, *Arch. Elektrotech*., Vol.7, 1919, pp. 32-35

[183] Rosa, E.B., “Calculation of the Self-inductance of single-layer coils”, *Bulletin of the Bureau of Standards*, Vol. 2, No. 2, 1906, pp. 161-187

[184] Roth, E., “Magnetic Leakage Inductance in Transformers with Cylindrical Windings and Forces Acting on the Windings”, *Revue Générale de L'Électricité*, Paris, France, Vol. 40, 1936, pp.291-303, 323-336

[185] Grover, F.W., Inductance Calculations. “Working Formulas and Tables”, D. van Nostrand company Inc., 1946.

[186] Kirchoff, G., “Gesammelte Abhandlungen”, p. 177

[187] Lyle, Phil. Mag., Vol. 3, 1902, p. 310

[188] Maxwell, J.C., “A Treatise on Electricity and Magnetism”, Vol. II, (3rd ed.) Oxford At the Clarendon Press, 1904

[189] Abramowitz, M. and I.A. Stegun, "Handbook of Mathematical Functions", Dover Publications, 1965, 17.6.

[190] Del Vecchio, R. M., Poulin, B., Ahuja, R., “Calculation and Measurement of Winding Disk Capacitances with Wound-in-Shields”, IEEE Trans. on PD, Vol. 13, No. 2, April 1998, pp. 503-509

[191] SuperLU, Online: http://crd.lbl.gov/~xiaoye/SuperLU/

[192] Scilab, Online: http://scilabsoft.inria.fr/

[193] Davis, T. A., “UMFPACK Version 4.3 User Guide”, Revision of Technical report TR-03-008, Online: http://www.cise.ufl.edu/research/sparse/umfpack/v4.3/UMFPACKv4.3/UMFPACK/Doc/UserGuide.pdf

[194] James W. Demmel, Stanley C. Eisenstat, John R. Gilbert, Xiaoye S. Li, Joseph W. H. Liu "A Supernodal Approach to Sparse Partial Pivoting", SIMAX Vol. 20 Number 3 pp. 720-755. 1999

[195] Spooles v.2.2 Online: http://www.netlib.org/linalg/spooles/spooles.2.2.html

13 INDEX

13 INDEX